

INVESTIGATING OUR DYNAMIC  
SOLAR CORONA FROM NEAR SUN  
TO 1 AU

Jaz Pearson

A THESIS SUBMITTED IN PARTIAL FULFILMENT  
OF THE REQUIREMENTS FOR THE DEGREE OF  
DOCTOR OF PHILOSOPHY

Jeremiah Horrocks Institute for Astrophysics and Supercomputing  
University of Central Lancashire

March 2011

# Declaration

The work presented in this thesis was carried out in the Jeremiah Horrocks Institute for Astrophysics and Supercomputing, University of Central Lancashire.

I declare that while registered as a candidate for the research degree, I have not been a registered candidate or enrolled student for another award of the University or other academic or professional institution.

I declare that no material contained in the thesis has been used in any other submission for an academic award and is solely my own work.

# Abstract

In this thesis, we study two areas of high interest in solar physics: the propagation of coronal mass ejections (CMEs); and the heating and thermal evolution of coronal loops.

In our study of CMEs, two separate techniques are employed to derive the three-dimensional (3-D) position angles and kinematic profiles of three separate CME events as they propagate through the heliosphere and into interplanetary space.

By analysing observations from two vantage points of Sun-centred, and coronagraph stereoscopic data, provided by the NASA STEREO spacecraft, a triangulation technique is used to pin-point the location of the CME's leading edge in 3-D space. The resulting direction of the CME is compared with that derived from a method which employs the construction of "j-maps"; continuous running-difference height-time maps of coronal ejecta displaying solar transients along a selected radial path as they propagate from the Sun. This technique uses the assumption that a CME will experience no change in velocity or direction once it has reached the field of view of STEREO's Heliospheric Imager (HI). It is found that the two methods agree well for fast CMEs (propagating faster than the ambient solar wind speed), but there is a large discrepancy in the slow CME (propagating slower than the ambient solar wind speed), which is due to the longitudinal deflection of the CME by the interplanetary magnetic field. Also, the analyses show that the CME experiences both a latitudinal and longitudinal deflection early in its acceleration / propagation phase.

The study of coronal loops consists of two parts; hydrodynamics and hydrostatics.

Firstly, a 1-D hydrodynamic Lagrange re-map code is employed to numerically model a 10 Mm coronal loop which is split into many sub-resolution strands. Each strand is heated impulsively, by localised discrete energy bursts, and the strands are then amalgamated to form a global loop system. The effects of changing the parameters of the simulation upon the temperature and velocity profiles of the loop are examined and compared to observations. It is found that the multi-strand model can accurately match synthetic velocity observations to those from spectroscopic satellite observations from Hinode EIS, say.

Finally, a phase plane analysis is introduced to study the temperature structure along 1-D hydrostatic coronal loops. Using a new four-range optically thin radiative loss function, it is possible to analytically solve the thermal equilibrium equation and investigate the resulting solution space. It is found that the new radiative function produces many new solutions to the phase plane with a subsequent impact on coronal loop thermal equilibria.

# Contents

<b>Declaration</b>	<b>2</b>
<b>Abstract</b>	<b>3</b>
<b>Acknowledgements</b>	<b>24</b>
<b>1 Introduction</b>	<b>26</b>
1.1 Solar Atmosphere . . . . .	26
1.2 Coronal Loops . . . . .	28
1.2.1 Coronal Heating . . . . .	31
1.3 Other Features on the Solar Disk . . . . .	32
1.3.1 Sunspots . . . . .	32
1.3.2 Filaments and Prominences . . . . .	33
1.3.3 Coronal Holes . . . . .	33
1.4 Hydrostatics . . . . .	34
1.5 Hydrodynamics . . . . .	35
1.6 Explosive Events . . . . .	36
1.6.1 Coronal Mass Ejections . . . . .	36
1.6.2 Flares . . . . .	36
<b>2 Instrumentation</b>	<b>38</b>
2.1 STEREO . . . . .	38

2.1.1	SECCHI . . . . .	39
2.1.2	PLASTIC and IMPACT . . . . .	64
2.2	SOHO . . . . .	64
2.2.1	LASCO . . . . .	64
2.2.2	MDI . . . . .	64
2.2.3	EIT . . . . .	65
2.3	OMNI Combined Data . . . . .	66
2.4	TRACE . . . . .	68
2.5	Yohkoh (SXT) . . . . .	68
2.6	Hinode . . . . .	69
<b>3</b>	<b>The Theory of Coronal Mass Ejections: Initiation and Propagation</b>	<b>72</b>
3.1	CME Initiation . . . . .	73
3.2	CME Acceleration and Propagation . . . . .	82
<b>4</b>	<b>STEREO Observations of Coronal Mass Ejections</b>	<b>87</b>
4.1	CME Observations . . . . .	87
4.1.1	Solar Coordinate Systems . . . . .	88
4.1.2	Geometry . . . . .	92
4.1.3	Stereoscopic Triangulation . . . . .	98
4.1.4	J-maps . . . . .	104
4.2	3rd December 2007 CME . . . . .	107
4.2.1	Observations . . . . .	108
4.2.2	Triangulation method with COR-1 and COR-2 data . . . . .	113
4.2.3	Calculating $\beta$ from the HI-1 and HI-2 j-map data . . . . .	116
4.2.4	Kinematics . . . . .	116
4.2.5	Discussion . . . . .	119
4.3	25th March 2008 CME . . . . .	124

4.3.1	Observations . . . . .	129
4.3.2	Triangulation method with EUVI, COR-1 and COR-2 data . .	130
4.3.3	Calculating $\beta$ from the HI-1 and HI-2 j-map data . . . . .	131
4.3.4	Kinematics . . . . .	133
4.3.5	Discussion . . . . .	133
4.4	3rd April 2010 CME . . . . .	138
4.4.1	Observations . . . . .	141
4.4.2	Triangulation method with COR-1 and COR-2 data . . . . .	143
4.4.3	Calculating $\beta$ from the HI-1 and HI-2 j-map data . . . . .	146
4.4.4	Kinematics . . . . .	147
4.4.5	Discussion . . . . .	151
4.5	Results and Discussion . . . . .	153
<b>5</b>	<b>Multi-strand 1-D Hydrodynamic Coronal Loop Simulations</b>	<b>156</b>
5.1	Single Strand Model . . . . .	158
5.1.1	Numerical Model of a Single Strand . . . . .	158
5.1.2	Plasma Response in a Single Strand to a Discrete Energy Burst	161
5.2	125 Multi-Strand Model - Varying the Spatial Distribution of the Discrete Energy Bursts . . . . .	162
5.2.1	Effect on Loop Temperature . . . . .	167
5.2.2	Effect on Loop Line-of-Sight Velocity . . . . .	169
5.2.3	Discussion . . . . .	177
5.3	Changing $E_{Total}$ . . . . .	179
5.3.1	Effect on Loop Temperature . . . . .	180
5.3.2	Effect on Loop Line-of-Sight Velocity . . . . .	183
5.3.3	Discussion . . . . .	187
5.4	Changing the Number of Strands . . . . .	188
5.4.1	Effect on Loop Temperature . . . . .	189

5.4.2	Effect on Loop Line-of-Sight Velocity . . . . .	191
5.4.3	Discussion . . . . .	192
5.5	Changing the Number of Discrete Energy Bursts Per Strand . . . . .	197
5.5.1	Effect on Loop Temperature . . . . .	199
5.5.2	Effect on Loop Line-of-Sight Velocity . . . . .	204
5.5.3	Discussion . . . . .	205
5.6	Conclusions . . . . .	206
<b>6</b>	<b>Phase Plane Analysis of the Temperature Structure Along 1-D Hydrostatic Coronal Loops</b>	<b>209</b>
6.1	Basic Equations . . . . .	211
6.2	Analytical Solutions to the Phase Plane . . . . .	221
6.2.1	Thermal Equilibrium and the Four Range Radiative Loss Function . . . . .	221
6.2.2	Dependence of the summit temperature upon the length of the loop . . . . .	236
6.3	Conclusions . . . . .	240
<b>7</b>	<b>Future Work</b>	<b>242</b>
7.1	CME Observations . . . . .	242
7.2	Multi-Strand Coronal Loop Simulations . . . . .	243
7.3	Phase Planes . . . . .	243
	<b>Appendices</b>	<b>247</b>
<b>A</b>	<b>Critical Point Analysis</b>	<b>247</b>
A.1	Analysis of $y = y_{crit1}$ and $y = y_{crit3}$ . . . . .	248
A.2	Analysis of $y = y_{crit2}$ and $y = y_{crit4}$ . . . . .	248

<b>B</b>	<b>Analytical Solutions for the Dependence of the Summit Temperature upon the Length of the Loop</b>	<b>250</b>
B.1	Region 1: $T_0 \leq T_a$ . . . . .	250
	B.1.1 For $T \leq T_a$ . . . . .	250
B.2	Region 2: $T_a \leq T_0 \leq T_b$ . . . . .	253
	B.2.1 For $T_a \leq T \leq T_b$ . . . . .	253
	B.2.2 For $T \leq T_a$ . . . . .	256
B.3	Region 3: $T_b \leq T_0 \leq T_r$ . . . . .	258
	B.3.1 For $T_b \leq T \leq T_r$ . . . . .	258
	B.3.2 For $T_a \leq T \leq T_b$ . . . . .	259
	B.3.3 For $T < T_a$ . . . . .	260
B.4	Region 4: $T_0 \geq T_r$ . . . . .	263
	B.4.1 For $T \geq T_r$ . . . . .	263
	B.4.2 For $T_b \leq T \leq T_r$ . . . . .	265
	B.4.3 For $T_a \leq T \leq T_b$ . . . . .	267
	B.4.4 For $T \leq T_a$ . . . . .	269

# List of Tables

1.1	From Reale (2010): Typical X-ray coronal loop parameters . . . . .	29
1.2	From Reale (2010): Thermal coronal loop classification . . . . .	29
2.1	Main EUVI telescope properties . . . . .	41
2.2	Main COR-1 performance properties . . . . .	49
2.3	COR-1 comparison with LASCO C2 and MLSO Mk4 . . . . .	51
2.4	COR-2 Performance Characteristics . . . . .	56
2.5	HI Performance Characteristics . . . . .	59
2.6	From Delaboudinière et al. (1995): EIT Bandpasses . . . . .	67
2.7	Key Science Parameters for the TRACE satellite . . . . .	68
2.8	Key Science Parameters for EIS . . . . .	71
4.1	Table indicating the times the leading edge of the CME is visible in the SECCHI instruments . . . . .	109
4.2	Table showing the Stonyhurst and Heliocentric Earth Ecliptic (HEE) positions of STEREO-A, STEREO-B and the Earth on 3rd December 2007 at 22:00:00UT . . . . .	110
4.3	Table comparing results from this analysis and previous author's. . .	121
4.4	Table indicating the times the leading edge is visible in each instrument	126
4.5	Table showing the Stonyhurst and Heliocentric Earth Ecliptic (HEE) positions of STEREO-A, STEREO-B and the Earth on 25th March 2008 at 18:42:15UT . . . . .	127

4.6	Table comparing results from this analysis and previous author's. . . . .	136
4.7	Table indicating the times the leading edge of the CME is visible in the SECCHI instruments . . . . .	139
4.8	Table showing the Stonyhurst and Heliocentric Earth Ecliptic (HEE) positions of STEREO-A, STEREO-B and the Earth on 3-Apr-2010 at 00:00:00UT . . . . .	140
4.9	Table summarising the results found from all three CME examples . . . . .	154
5.1	Chianti contribution lines . . . . .	172
5.2	Changing $E_{Total}$ : simulation parameters . . . . .	181
5.3	Changing the number of strands: simulation parameters . . . . .	189
5.4	Changing the number of energy bursts: simulation parameters . . . . .	197
5.5	Summary of results in Chapter 5 . . . . .	208

# List of Figures

1.1	Figure showing the solar atmospheres and features on the solar disk. . .	27
1.2	Coronal loops shown in X-ray (left) from Yohkoh SXT, and in EUV (right) from TRACE. . . . .	28
1.3	Loop apex temperature and velocity profile for a 1 stranded loop . . .	30
1.4	Figure showing a large sunspot group on the 29th March 2001, taken by MDI on-board the SOHO spacecraft . . . . .	32
1.5	Figure showing a filament and a prominence . . . . .	33
1.6	Figure showing a large coronal hole, as the dark feature running from the north pole, near the middle of the image, towards the equator. (From <a href="http://jtintle.wordpress.com/category/planets/sun/page/2/">http://jtintle.wordpress.com/category/planets/sun/page/2/</a> ) . .	34
1.7	Standard flare model diagram (Hirayama, 1974) . . . . .	37
2.1	EUVI telescope cross-section (Wuelser et al., 2004) . . . . .	40
2.2	EUVI effective area . . . . .	42
2.3	EUVI response function . . . . .	43
2.4	Layout of the COR-1 instrument (Thompson and Reginald, 2008) . .	44
2.5	COR-1 vignetting . . . . .	47
2.6	COR-1 scattered light and average radial profiles . . . . .	48
2.7	Estimated signal-to-noise ratios for a modeled K corona for an exposure time of 1 second, with 2 x 2 pixel binning (Howard et al., 2008) . . . . .	49

2.8	COR-1 total brightness comparison with LASCO C2 . . . . .	52
2.9	COR-1 polarized brightness comparison with MLSO Mk4 . . . . .	53
2.10	Layout of the COR-2 instrument (Howard et al., 2008) . . . . .	54
2.11	COR-2 flat field response and vignetting pattern . . . . .	55
2.12	COR-2 stray light performance . . . . .	56
2.13	The HI design concept (Howard et al., 2008) . . . . .	58
2.14	HI schematic side view of the optical configuration . . . . .	59
2.15	The geometrical layout of the HI fields of view and the major intensity contributions (based upon a figure from Socker et al., 2000). . . . .	60
2.16	HI-1A pointing . . . . .	61
2.17	Schematic cross section of the Guide Telescope (Howard et al., 2008) . . . . .	62
2.18	Example of a LASCO C3 image. A CME is clearly visible. . . . .	65
2.19	Example of an MDI magnetogram. . . . .	66
2.20	Example EIT image of the Sun in 304 Å . . . . .	67
2.21	Example of a TRACE image, displaying coronal loops at 171 Å . . . . .	69
2.22	Yohkoh SXT image of the solar corona from the 12th November 1991 11:28:20 UT. . . . .	70
2.23	Example EIS image . . . . .	71
3.1	Mechanical analogue of the thermal blast model. Figure taken from UCLan course notes. . . . .	74
3.2	Mechanical analogue of the dynamo model. Figure taken from UCLan course notes. . . . .	75
3.3	Mechanical analogue of the mass loading model. Figure taken from UCLan course notes. . . . .	76
3.4	Mechanical analogue of the tether release model. Figure taken from UCLan course notes. . . . .	77
3.5	Forbes and Isenberg (1991) CME model . . . . .	79

3.6	Mechanical analogue of the tether straining model. Figure taken from UCLan course notes. . . . .	80
3.7	Magnetic breakout model . . . . .	81
3.8	Sheeley et al. (1999) CME acceleration and propagation profiles . . .	82
3.9	Parker spiral configuration . . . . .	84
3.10	Current sheet in the inner heliosphere, illustrating the ballerina skirt effect . . . . .	84
3.11	From Wang et al. (2004): Schematic pictures of (a) slow and (b) fast CME propagation in the interplanetary medium. . . . .	86
3.12	From Wang et al. (2004): The deflection angle ( $\delta\phi$ ) in the ecliptic plane at 1 AU versus the radial speed ( $V_r$ ) of CMEs. . . . .	86
4.1	Solar coordinates: heliocentric Cartesian, and Stonyhurst . . . . .	89
4.2	HEE and HEEQ coordinates example . . . . .	90
4.3	Heliocentric-radial coordinates . . . . .	90
4.4	HI-1A image with HPC (left) and HPR (right) contours . . . . .	91
4.5	HI-2A image, highlighting the spherical nature of the observations. . .	92
4.6	Triangulation geometry from Aschwanden et al. (2008) . . . . .	99
4.7	Epipolar geometry . . . . .	102
4.8	Screenshot of scc_measure . . . . .	103
4.9	HI-1 and HI-2 combined j-map, from the 25th March 2008. . . . .	105
4.10	EUVI 304 Å data from the 3rd December 2007 . . . . .	107
4.11	MDI magnetogram data for the 4th December 2007 . . . . .	108
4.12	Location of the STEREO spacecraft in HEEQ coordinates in the 4th December 2007 . . . . .	111
4.13	Running difference images of COR-1 data (left: STEREO-B, right: STEREO-A). Contours of elongation are drawn at intervals of $0.25^\circ$ .	112

4.14	Running difference images of COR-2 data (left: STEREO-B, right: STEREO-A). Contours of elongation are drawn at intervals of $1^\circ$ . . .	112
4.15	Running difference images of HI-1B (left) and HI-2B (right) data, with contours of PA and elongation. Contours of elongation are drawn at intervals of $5^\circ$ and $20^\circ$ for HI-1B and HI-2B respectively. . . . .	114
4.16	Latitude and longitude of the CME's leading edge. The solid line (if present) shows a best fit of the form $f(x) = ae^{bx} + c$ . . . . .	115
4.17	Figure showing the 3-D leading edges from COR-1 and COR-2 triangulated data. The HEEQ Y-X plane is shown (bottom) and the HEEQ Y-Z plane (top), with the projected CME direction indicated by the red line. . . . .	115
4.18	J-map from STEREO-B HI-1 ( $4 - 24^\circ$ ) and HI-2 ( $24 - 60^\circ$ ) from the 4th December 2007 00:00UT to 10th December 2007 00:00UT, along a constant PA of $273^\circ$ . The red line shows the track being analysed. .	117
4.19	Elongation (top-left) and distance (top-right) plots, along a PA of $\psi = 273^\circ$ , as a function of time. The stars represent the data taken from the associated j-map, and the solid line represents the fitted data from Section 4.2.3. Velocity (bottom-left) and acceleration (bottom-right) plots of the CME's leading edge, along a PA of $\psi = 273^\circ$ , as a function of radial distance. The solid line represents an angle of $\beta = 62^\circ$ , and the dashed line an angle of $\beta = 97^\circ$ . . . . .	118
4.20	In-situ data from STEREO-B (blue), OMNI (green), and STEREO-A (red), displaying (from top to bottom): solar wind speed; proton density; temperature; magnetic field magnitude; elevation angle; azimuth angle. . . . .	120
4.21	EIT image from SOHO on the 8th December 2007 11:48:09 UT, displaying an equatorial coronal hole. . . . .	122

4.22	MDI magnetogram data for the 25th March 2008 . . . . .	124
4.23	Plot showing the location of the STEREO spacecraft in relation to the Sun and Earth, in HEEQ coordinates at 18:42:15UT. The dotted lines indicate the HI FOV for each spacecraft. . . . .	125
4.24	Running difference images of EUVI 171 Å data (left: STEREO-B, right: STEREO-A). Contours of elongation are drawn at intervals of 0.1° . . . . .	125
4.25	Running difference images of COR-1 data (left: STEREO-B, right: STEREO-A). Contours of elongation are drawn at intervals of 0.25°. The red circle outlines the solar limb. . . . .	127
4.26	Running difference images of COR-2 data (left: STEREO-B, right: STEREO-A). Contours of elongation are drawn at intervals of 1°. The red circle outlines the solar limb. . . . .	128
4.27	Running difference images of HI-1A (left) and HI-2A (right) data. Contours of elongation are drawn at intervals of 5° and 20° respectively.	128
4.28	Latitude and longitude of the CME's leading edge. The solid line (if present) shows a best fit of the form $f(x) = ae^{bx} + c$ . . . . .	131
4.29	Figure showing the 3-D leading edges from EUVI, COR-1 and COR-2 triangulated data. The HEEQ Y-X plane is shown (top) and the HEEQ Y-Z plane (bottom), with the longitudinal and latitudinal projected CME direction indicated by the arrows, respectively. . . . .	132
4.30	J-map from STEREO-A HI-1 (4 – 24°) and HI-2 (24 – 50°) from the 25th March 2008 00:00UT to 29th March 2008 00:00UT, along a constant PA of 102° . . . . .	132

4.31	Elongation (top-left) and distance (top-right) plots, along a PA of $\psi = 102^\circ$ , as a function of time. The stars represent the data taken from the associated j-map, and the solid line represents the fitted data from Section 4.3.3. Velocity (bottom-left) and acceleration (bottom-right) plots of the CME's leading edge, along a PA of $\psi = 102^\circ$ , as a function of radial distance. The dashed line represents an angle of $\beta = -109^\circ$ , and the solid line represents an angle of $\beta = -114^\circ$ . . . . .	134
4.32	MDI Magnetogram Data for the 3rd April 2010 . . . . .	138
4.33	Plot showing the location of the STEREO spacecraft in relation to the Sun and Earth, in HEEQ coordinates on 3rd April 2010 09:15:00 UT. The dotted lines indicate the HI FOV for each spacecraft . . . . .	140
4.34	Running difference images of EUVI 195Å data, with contours of PA and elongation. Contours of elongation are drawn at $0.1^\circ$ intervals. . . . .	141
4.35	Running difference images of COR-1 data (left: STEREO-B, right: STEREO-A). Contours of elongation are drawn at intervals of $0.25^\circ$ . . . . .	142
4.36	Running difference images of COR-2 data (left: STEREO-B, right: STEREO-A). Contours of elongation are drawn at intervals of $1^\circ$ . The red circle outlines the solar limb. . . . .	143
4.37	Running difference images of HI-1 data (left: STEREO-B, right: STEREO-A). Contours of elongation are drawn at intervals of $5^\circ$ . . . . .	144
4.38	Running difference images of HI-2 data (left: STEREO-B, right: STEREO-A).. Contours of elongation are drawn at intervals of $20^\circ$ . . . . .	144
4.39	Latitude and longitude of the CME's leading edge . . . . .	145
4.40	Figure showing the 3-D leading edges from COR-1 and COR-2 stereoscopic triangulated data. The HEEQ Z-X plane is shown (right) and the HEEQ Y-X plane (left), with the longitudinal and latitudinal projected CME direction indicated by the arrow. . . . .	146

4.41	STEREO-A J-map for PA = 105° . . . . .	148
4.42	STEREO-B J-map for PA = 257° . . . . .	148
4.43	STEREO-A elongation (top-left) and distance (top-right) plots, along a PA of $\psi = 105^\circ$ , as a function of time. The stars represent the data taken from the associated j-map, and the solid line represents the fitted data from the j-map analysis. Velocity (bottom-left) and acceleration (bottom-right) plots of the CME's leading edge, as a function of radial distance. The dashed line represents an angle of $\beta = 71^\circ$ , and the solid line represents an angle of $\beta = 68^\circ$ . . . . .	149
4.44	STEREO-B elongation (top-left) and distance (top-right) plots, along a PA of $\psi = 257^\circ$ , as a function of time. The stars represent the data taken from the associated j-map, and the solid line represents the fitted data from the j-map analysis. Velocity (bottom-left) and acceleration (bottom-right) plots of the CME's leading edge, as a function of radial distance. The dashed line represents an angle of $\beta = 73^\circ$ , and the solid line represents an angle of $\beta = 72^\circ$ . . . . .	150
4.45	In-situ data taken from the OMNI data. From top-to-bottom: solar wind speed, proton density, temperature, magnetic field magnitude, elevation, and azimuth. . . . .	152
5.1	Snapshots of the strand evolution in temperature (left) and velocity (right) in response to a discrete energy burst containing $1.049 \times 10^{24}$ erg of energy being deposited at a position $s = -2.5$ Mm. . . . .	163
5.2	Evolution of the strand apex temperature (left) and density (right) after the discrete energy burst . . . . .	164
5.3	Histogram showing the spatial energy distribution for ADH (blue), SUH (green) and FDH (red) heating. . . . .	165

5.4	Energy histograms for the three different cases of spatial heating, with straight lines fitted to show the power-law slope, which has a value of $\alpha = 2.3$ in all cases. . . . .	166
5.5	Line of sight velocity . . . . .	168
5.6	Time evolution of the emission measure weighted temperature at the loop apex for 125 stranded loop with apex (left), footpoint (right) and uniform (bottom) heating. . . . .	168
5.7	Average temperature of the loop for each of the spatial heat inputs (0 Mm = loop apex). . . . .	170
5.8	From Del Zanna (2008): Monochromatic (negative) images and dopplergrams ( $\text{km s}^{-1}$ ) of NOAA 10926 in Fe VIII, Fe XII, Fe XV . . . . .	170
5.9	Chianti contribution functions for Si VII, Fe XI, and Fe XV . . . . .	172
5.10	Si VII line-of-sight blue/red shifts for the three cases of spatial heating (left), their corresponding histograms (centre), and the time-averaged mean blue/red $V_{cf}$ along the loop (right). . . . .	174
5.11	Fe XI line-of-sight blue/red shifts for the three cases of spatial heating (left), their corresponding histograms (centre), and the time-averaged mean blue/red $V_{cf}$ along the loop (right). . . . .	175
5.12	Fe XV line-of-sight blue/red shifts for the three cases of spatial heating (left), their corresponding histograms (centre), and the time-averaged mean blue/red $V_{cf}$ along the loop (right). . . . .	176
5.13	Comparison of Tripathi et al. (2009) average footpoint velocities (left) and the average simulation $V_{cf}$ at $s = 4.5$ Mm (right). . . . .	177
5.14	Energy histograms for three different total energy ranges, with straight lines fitted to show the power-law slop, which has a value of $\alpha = 2.3$ in all cases. . . . .	180

5.15	Emission measure weighted temperature at loop apex for different levels of $E_{Total}$ : $0.001E_{Total}$ , $0.1E_{Total}$ and $10E_{Total}$ (SUH). . . . .	181
5.16	Average emission measure weighted temperature of the loop for different levels of $E_{Total}$ : $0.001E_{Total}$ , $0.1E_{Total}$ and $10E_{Total}$ (SUH). . . . .	182
5.17	Average emission measure weighted temperature at the loop apex (left), and the average deviation of the temperature along the loop apex, over a range of total energy inputs . . . . .	182
5.18	Si VII line-of-sight blue/red shifts for the three selected cases of $E_{Total}$ (left), their corresponding histograms (centre), and the time-averaged mean blue/red $V_{cf}$ along the loop (right). For SUH only. . . . .	184
5.19	Fe XI line-of-sight blue/red shifts for the three selected cases of $E_{Total}$ (left), their corresponding histograms (centre), and the time-averaged mean blue/red $V_{cf}$ along the loop (right). The top row of diagrams can be ignored, but are included for completeness. For SUH only. . . . .	185
5.20	Fe XV line-of-sight blue/red shifts for the three selected cases of $E_{Total}$ (left), their corresponding histograms (centre), and the time-averaged mean blue/red $V_{cf}$ along the loop (right). The top row of diagrams can be ignored, but are included for completeness. For SUH only. . . . .	186
5.21	Percentage of red shifted pixels (left column), maximum mean velocity ranges (centre column), and average velocity deviation (right column) over a range of total energy inputs, and line filters. From top-to-bottom: Si VII, Fe XI, Fe XV . . . . .	187
5.22	Comparison of Tripathi et al. (2009) average footpoint velocities (left) and the average simulation $V_{cf}$ at $s = 4.5$ Mm (right) for 0.1 and 0.5 $E_{Total}$ . . . . .	188
5.23	Energy histograms for three different cases of strand number, with straight lines fitted to show the power-law slope ( $\alpha$ ). . . . .	190

5.24	Emission measure weighted temperature of the loop apex for 5 strand (left), 125 strand (right) and 2000 strand (bottom) loop. . . . .	190
5.25	Average temperature along the loop of a 5, 125 and 2000 strand loop.	191
5.26	Average apex emission measure weighted temperature (left) and the average deviation of the apex temperature (right) as a function of strand number. . . . .	192
5.27	Si VII line-of-sight blue/red shifts for the three selected cases of strand number (left), their corresponding histograms (centre), and the time-averaged mean blue/red $V_{cf}$ along the loop (right). . . . .	193
5.28	Fe XI line-of-sight blue/red shifts for the three selected cases of strand number (left), their corresponding histograms (centre), and the time-averaged mean blue/red $V_{cf}$ along the loop (right). . . . .	194
5.29	Fe XV line-of-sight blue/red shifts for the three selected cases of strand number (left), their corresponding histograms (centre), and the time-averaged mean blue/red $V_{cf}$ along the loop (right). . . . .	195
5.30	Percentage of red shifted pixels (left column), maximum mean velocity ranges (centre column), and average velocity deviation (right column) over a range of number of strands, and line filters. From top-to-bottom: Si VII, Fe XI, Fe XV . . . . .	196
5.31	Energy histograms for 11, 114 and 1140 energy bursts per strand. . .	198
5.32	Emission measure weighted temperature of the loop apex for 11 energy bursts (left), 114 energy bursts (right) and 1140 energy burst (bottom) per strand in a 125 strand loop. . . . .	198
5.33	Average temperature along a 125 strand loop with 11, 114 and 1140 discrete energy bursts per strand . . . . .	199

5.34	Average apex emission measure weighted temperature (left) and the average deviation of the apex temperature (right) as a function of number of energy bursts per strand. . . . .	200
5.35	Si VII line-of-sight blue/red shifts for the selected cases of number of energy bursts per strand (left), their corresponding histograms (centre), and the time-averaged mean blue/red $V_{cf}$ along the loop (right). . . . .	201
5.36	Fe XI line-of-sight blue/red shifts for the three cases of spatial heating (left), their corresponding histograms (centre), and the time-averaged mean blue/red $V_{cf}$ along the loop (right). . . . .	202
5.37	Fe XV line-of-sight blue/red shifts for the three cases of spatial heating (left), their corresponding histograms (centre), and the time-averaged mean blue/red $V_{cf}$ along the loop (right). . . . .	203
5.38	Percentage of red shifted pixels (left column), the minimum and maximum velocity (centre column), and the average deviation of the velocity (right column) as a function of energy bursts per strand. From top-to-bottom: Si VII, Fe XI, Fe XV . . . . .	204
6.1	Comparison of the radiative loss function $Q(T)$ from Hildner (1974), Rosner et al. (1978), and Cook et al. (1989). . . . .	216
6.2	An example of a magnetic flux tube through surfaces $S_1$ and $S_2$ . . . . .	217
6.3	Colgan et al. (2008) radiative losses . . . . .	222
6.4	Figure showing the non-dimensional four-range radiative loss function (solid line), Walsh et al. (1995) (dot-dash line) and Hildner (1974) (dashed line) optically thin radiative loss functions, with temperature ( $T$ ) displayed in dimensionless units. . . . .	224
6.5	Levels of uniform heating for the phase planes displayed in Figures 6.6 to 6.13, for $T_a = 0.07, T_b = 0.1, T_r = 0.15$ . . . . .	226
6.6	Phase planes for $H_0 = 5$ . . . . .	227

6.7	Phase planes for $H_0 = 6.69$ . . . . .	230
6.8	Phase planes for $H_0 = 7.5$ . . . . .	231
6.9	Phase plane for $H_0 = \sqrt{\frac{3(y_a^{1/2} - y_b^{1/2})y_b^3}{(y_a^{3/2} - y_b^{3/2})y_r^3}}$ . . . . .	232
6.10	Phase planes for $H_0 = 10$ . . . . .	233
6.11	Phase plane for $H_0 = 12.49$ . . . . .	234
6.12	Phase plane for $H_0 = 15$ . . . . .	235
6.13	Phase plane for $H_0 = 27.66$ . . . . .	235
6.14	Variation of length of loop parameter, $L$ , for the case with the double separatrix at $H_0 \sim 8.58$ . . . . .	236
6.15	Summit temperature for increasing $H_0$ for loops with a footpoint tem- perature of $T_e = 0.01$ MK, and $L = 2$ , with $T_a = 0.07, T_b = 0.1, T_r =$ $0.15$ . . . . .	237
6.16	Dependence of the summit temperature $T_0$ (in units of $10^6$ K upon the parameter $L$ for different values of $H_0$ , for a footpoint temperature of $T_e = 0.01$ MK . . . . .	241
7.1	Si VII (top row), Fe XI (middle row) and Fe XV (bottom row) line- of-sight blue/red shifts for a 1125 strand loop, with 57 energy bursts per strand and $0.1E_{Total}$ (left column), their corresponding histograms (centre column), and the time-averaged mean blue/red $V_{cf}$ along the loop (right column). . . . .	244
7.2	Phase volume displaying the separatrix curve for increasing $H_0$ with $L = 1, T_a = 0.07, T_b = 0.1$ , and $T_r = 0.15$ . The double separatrix is illustrated by the blue contours. . . . .	246

# Acknowledgements

I would like to express my extreme gratitude towards my supervisor, Robert Walsh, whose incredible enthusiasm and support was truly appreciated, and to the rest of my supervisory team; Danielle Bewsher and Dan Brown. With wonderful support also from Jackie Davies, who spent countless hours helping me through my struggles, and also to Aveek Sarker.

To my father, Roger, who has given me fantastic support throughout my life, and in particular this last year, offering me accommodation and financial support when I have needed it most. I can never thank you enough. To my mother, whose unquestionable love and faith shown in me, will never be forgotten, and to my step-father, Geoff, who has been an amazing role model. You have all given me so much, and yet asked for nothing in return. Words cannot express the gratitude I have, and I could not have wished for better parents. My only wish is to make you all proud.

To my girlfriend, Sheila, who has had to endure me at my worst, showing me wonderful patience, love, and understanding. During times when I have needed someone the most, you have been there.

To my wonderful family: Cherry and Harris; Fran and Lindsey; Sue and Keith; Sheila and Ray. Whether it be financial support, emotional support, or just a friendly word of advice; you have always been there for me and I know you always will. Your support has meant so much.

To all my friends who I have neglected whilst undertaking this project.

My thanks go to the staff at the University of Central Lancashire, where I have

spent over eight years, having arrived with barely any qualifications. The time I have spent there has been amongst my most enjoyable and fulfilling, throughout both my under-graduate and post-graduate studies. I have achieved things I never thought possible, and leave with great pride and wonderful memories.

I would like to thank my institution, the Jeremiah Horrocks Institute for Astrophysics and Supercomputing, for funding me for three years of my research, and for helping fund trips, in particular, to the USA and China, and for providing me with the chance to reach my academic potential.

Finally, to my dearly missed grandparents; Nan Irene, Nanna Pickles, and Grandad Ramsden. You never stopped believing in me, never stopped supporting me, and gave me joy throughout my life. I write this thesis for you. I only wish you were here to read it.

# Chapter 1

## Introduction

This thesis concerns two topics of high interest in the field of solar physics: the role of coronal loops in heating up the corona; and the 3-D propagation of coronal mass ejections (CMEs) into the heliosphere.

The Sun is our nearest star and contains  $\sim 99.8\%$  of the total mass in the Solar System. It has been the subject of our attention for centuries, with the earliest known observations of sunspots made by the Chinese in 364 BC. In 1610, sunspots were first observed by Galileo with the use of a telescope. From this simple instrument, a wide range of earth-based and space-based instruments has evolved, which provide data covering a wide range of particle energetics and electromagnetic wavelengths.

### 1.1 Solar Atmosphere

The photosphere is the visible surface of the Sun, and is one of four layers of the solar atmosphere. It has an average temperature of  $\sim 5800$  K, while dropping to  $\sim 4500$  K in sunspot regions. It is approximately 0.5 Mm in depth, and has a number density of  $\sim 10^{17}$  cm $^{-3}$ . Immediately above the photosphere, lies the  $\sim 2$  Mm thick chromosphere. The density number drops to  $\sim 10^{11}$  cm $^{-3}$ , while the temperature

## CHAPTER 1

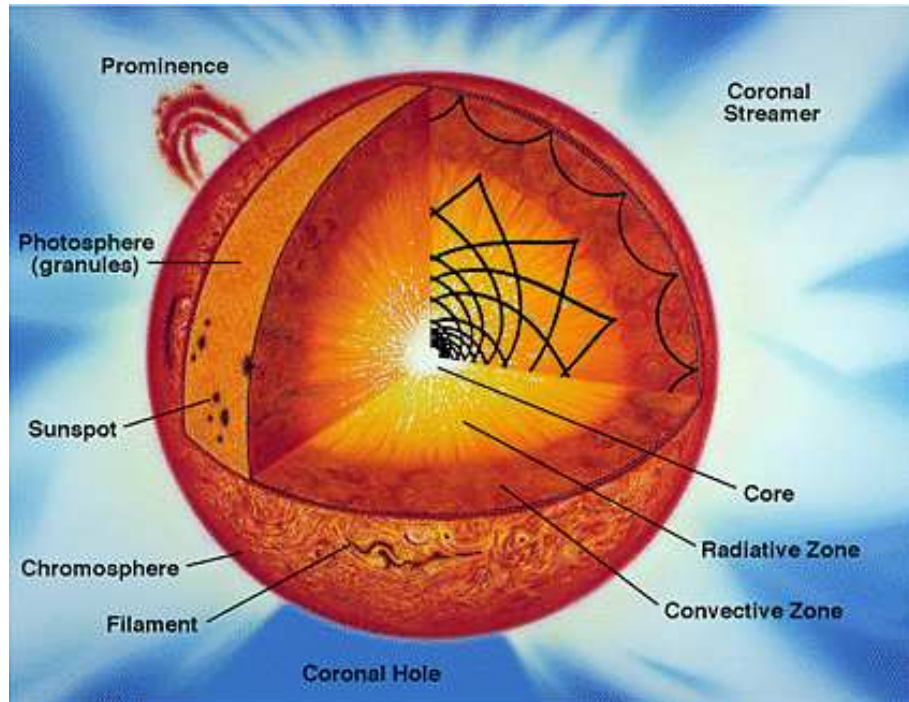


Figure 1.1: Figure showing the solar atmospheres and features on the solar disk.

rises slowly to  $\sim 20,000$  K. There is then a sudden jump in temperature, in an area  $< 100$  km thick, known as the transition region. The temperature increases significantly, from chromospheric temperatures up to 2 MK, into the Sun's outer atmosphere, known as the corona. The corona extends for millions of kilometres into interplanetary space, and has an average number density of  $\sim 10^9$   $\text{cm}^{-3}$  in the lower corona.

The corona is the laboratory within which the research in this thesis is predominantly based. It is a low plasma-beta ( $\beta$ ) environment, where  $\beta$  is the ratio of the plasma pressure to the magnetic pressure. A low  $\beta$  (i.e.  $\beta < 1$ ) indicates that the magnetic pressure force is greater than the plasma pressure force, and therefore the plasma follows the motion of the magnetic field.

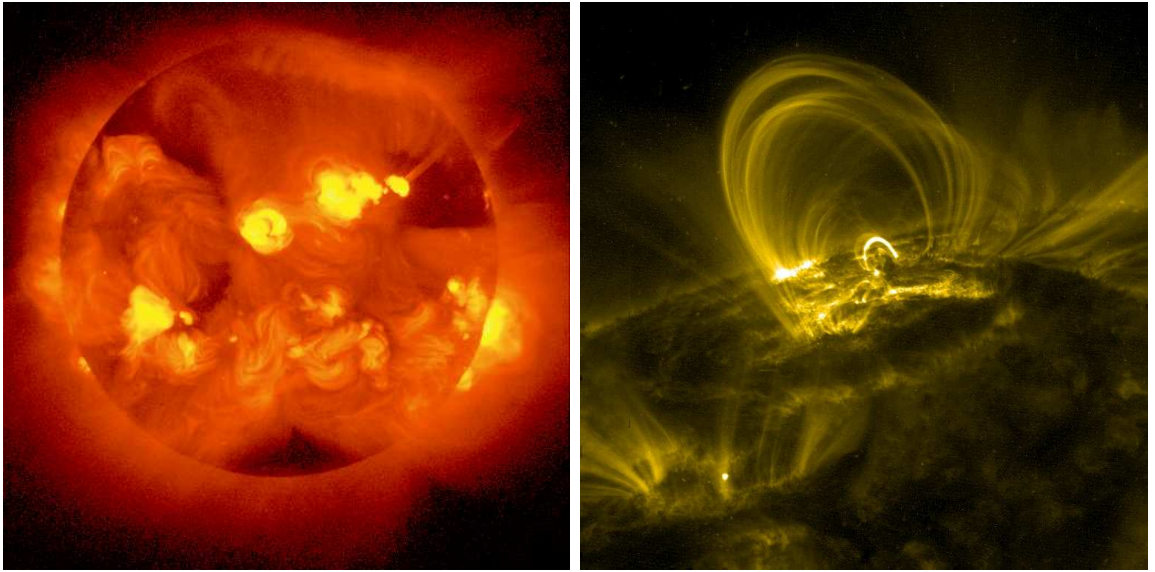


Figure 1.2: Coronal loops shown in X-ray (left) from Yohkoh SXT, and in EUV (right) from TRACE.

## 1.2 Coronal Loops

X-ray observations of the Sun's million degree outer atmosphere, the corona, show that it is made up almost entirely of loop-like structures which typically follow the Sun's magnetic field topology (see Figure 1.2, left). These coronal loops can also be observed in fine detail in the EUV band (see Figure 1.2, right), but the majority of loops are observed in the X-ray band, at temperatures of over 2 MK. Extensive research has gone into understanding the dynamical system of coronal loops, because it is believed that they hold a big key in solving the coronal heating problem, for example.

Coronal loops are characterised by an arch-like shape which are seen over a wide range of dimensions, and can be split into four categories (in terms of size): giant arches ( $\sim 10^{11}$  cm); active region loops ( $\sim 10^{10}$  cm); small active region loops ( $\sim 10^9$  cm); and bright points ( $\sim 10^8$  cm). Table 1.1 describes typical loop parameters, dependent upon the length of the loop. Most of the thermal energy is

## CHAPTER 1

Table 1.1: From Reale (2010): Typical X-ray coronal loop parameters

Type	Length ( $10^9$ cm)	Temperature (MK)	Density ( $10^9$ cm $^{-3}$ )	Pressure (dyne cm $^{-2}$ )
Bright points	0.1 - 1	2	5	3
Active region	1 - 10	3	1 - 10	1 - 10
Giant arches	10 - 100	1-2	0.1 - 1	0.1
Flaring loops	1 - 10	> 10	> 50	> 100

Table 1.2: From Reale (2010): Thermal coronal loop classification

Type	Temperature (MK)
Cool	0.1 - 1
Warm	1-1.5
Hot	$\geq 2$

conducted along the magnetic field lines by the magnetised plasma. As a result of high thermal insulation, coronal loops can have varying temperatures, with loops classed thermally as: cool (0.1 - 1 MK); warm (1 - 1.5 MK); and hot ( $\geq 2MK$ ). This thermal classification is displayed in Table 1.2.

It is widely believed that these features coincide with magnetic flux tubes, and occur because plasma and thermal energy flow along the magnetic field (Sarkar and Walsh, 2008). However, at this time, it is still not clear whether or not a coronal loop is one single loop, or in fact contains an amalgamation of many sub-resolution strands within one bright uniform structure, as investigated by Cargill (1994) and Cargill and Klimchuk (1997). Each strand could have a wide range of temperatures occurring across the structure, and could operate in thermal isolation from each other. Figure 1.3 displays the apex temperature and the line-of-sight

## CHAPTER 1

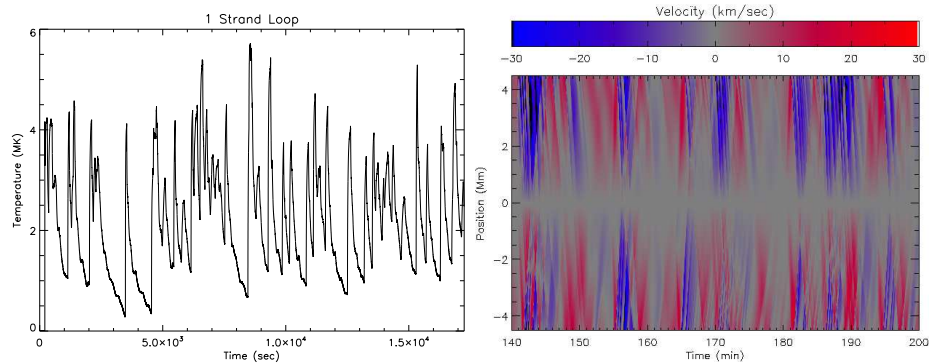


Figure 1.3: Loop apex temperature (left) and the Si VII line-of-sight velocities (right) from a 1 stranded loop heated by 57 discrete energy bursts. Taken from preliminary work in Chapter 5.

velocities of a 1 stranded loop, heated by 57 discrete energy bursts. It is clear to see, that a 1 stranded loop heated in this manner does not accurately reproduce loop observations found from satellite data. If we examine the apex temperature, we see that the loop apex temperature has huge variation as it is continually heated and then cooled, which do not accurately match the observations since we would see constant flashing and dimming over the time scales presented here. If we now examine the loop line-of-sight velocity, we see that there is no predomination of red or blue shift, which we would expect to see (Del Zanna, 2008; Hara et al., 2008; Tripathi et al., 2009). However, upon splitting up the loop into many strands, and combining them to form a global loop, it is possible to reproduce more accurately the temperature and velocity profiles (Sarkar and Walsh, 2008, 2009).

In Chapter 5, we take a 10 Mm long coronal loop, and split it into many, thermally isolated, strands, heated by localised discrete energy bursts. We then combine all the strands together, to form one single loop, and investigate the temperature and velocity profiles associated with the simulation parameters employed.

### 1.2.1 Coronal Heating

The coronal heating problem is one of the biggest mysteries in solar physics. Whilst the temperature of the Sun's surface, the photosphere, is  $\sim 6000$  K, the corona is over a million degrees hotter. By the laws of thermodynamics, the temperature of the corona should be lower than that of the photosphere. So the question is posed: what is heating the corona?

It is widely accepted that the source of the energy must come from mechanical motions in and below the photosphere. From these motions, the footpoints of a coronal loop are displaced. Magnetic disturbances propagate from the photosphere to the corona at the Alfvén speed. If the time-scale of the motions is much longer than the Alfvén travel time, the loop is able to adjust to the changing conditions in a quasi-static way. This dissipation of magnetic stresses is known as direct current (DC) heating. Conversely, if the time-scale of the motions is much shorter, then the loop experiences, for example, wave dissipation referred to as alternating current (AC) heating.

#### AC Heating

p (eg. Alfvén, acoustic, fast and slow magnetosonic waves) are generated in the photosphere, and propagate upwards into the corona. The waves are able to transfer energy, and thus heat, into coronal loops. AC heating is not considered in this thesis.

#### DC Heating

Heating by nanoflares is one possible mechanism to explain the heating of the corona (eg. Parker 1988). Here, the plasma is heated by the cumulative effects of many random time distributed pulses, deposited in the loop. In Chapter 5, a 1-D hydrodynamic simulation is used, which uses the principles of this type of DC heating, to investigate the temperature structure, and the line-of-sight Doppler velocities

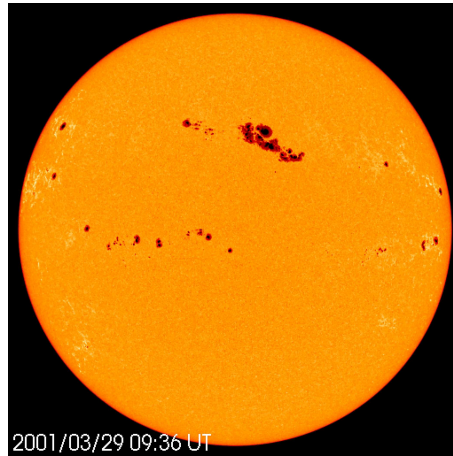


Figure 1.4: Figure showing a large sunspot group on the 29th March 2001, taken by MDI on-board the SOHO spacecraft. (Taken from <http://sohowww.nascom.nasa.gov/gallery/images/bigspotfd.html>)

associated with the random energy bursts.

## 1.3 Other Features on the Solar Disk

As well as coronal loops, several other solar features exist on the solar disk, and some of these are discussed here.

### 1.3.1 Sunspots

Sunspots appear on the photosphere as a dark spot, because they are cooler than their surroundings. They vary greatly in size, ranging from around 600 to 12,000 km in diameter, and can last from anything from 1 hour to half a year. Sunspot numbers also vary with the solar cycle, which has an average periodicity of about 11 years. During solar maximum, when the Sun's activity is at its peak, more sunspots are observed. Conversely, during solar minimum, the number of sunspots decreases. The latitudinal variation of sunspots also changes with the solar cycle. At the start of the solar cycle, sunspots will appear as low/high as  $40^\circ$  latitude, but new sunspots

## CHAPTER 1

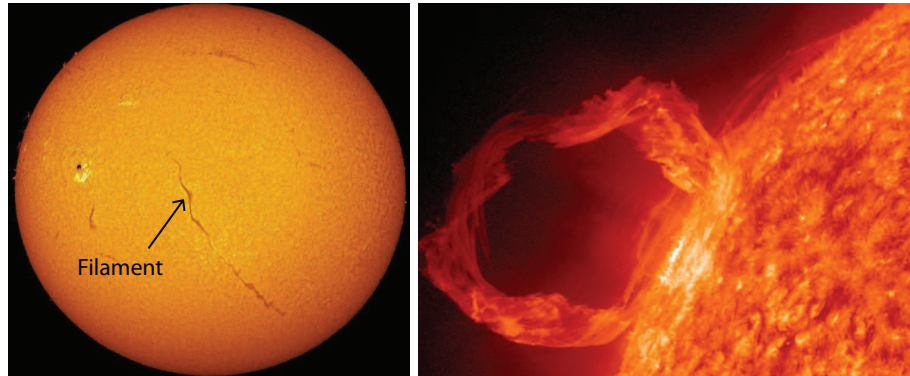


Figure 1.5: Figure showing a filament (left) observed on the solar disk, and a prominence (right) observed off the solar limb. Images taken from <http://www.universetoday.com/wp-content/uploads/2009/12/SolarFilament.jpg> (left image), and <http://sdo.gsfc.nasa.gov/gallery/> (right).

will emerge at latitudes closer to the equator as the cycle progresses. An example of several sunspots and sunspot groups is shown in Figure 1.4.

### 1.3.2 Filaments and Prominences

Filaments and prominences are large regions of very dense, cool gas, which are held in place by the Sun's magnetic field. Filaments will appear long, thin, and darker than the surrounding material (see Figure 1.5 (left)). They appear darker because they are cooler than their surroundings. A prominence is the same thing as a filament, but from the observer's perspective is seen off-disk, and as such appears extremely bright against the darker background (see Figure 1.5).

### 1.3.3 Coronal Holes

Coronal holes are areas of the Sun, when observed in EUV and X-ray, that appear darker than the surrounding coronal material. These darker regions are slightly cooler than the surrounding plasma, and are dominated by open magnetic field

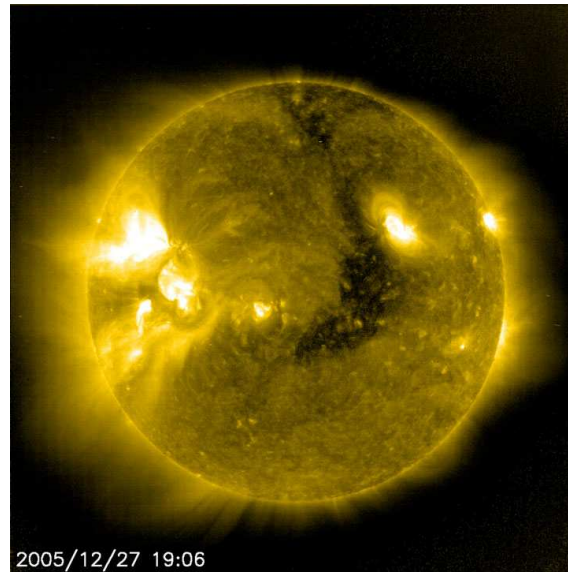


Figure 1.6: Figure showing a large coronal hole, as the dark feature running from the north pole, near the middle of the image, towards the equator. (From <http://jtintle.wordpress.com/category/planets/sun/page/2/>)

lines, and are the source of the fast solar wind. Figure 1.6 displays a large coronal hole.

## 1.4 Hydrostatics

The physics of hydrostatics provides a description of the density and pressure variation with height, and this strongly depends upon the temperature of the coronal plasma. Strictly speaking, hydrostatics is only applicable to static (or quasi-static) structures. This indeed does apply to most dynamic solar features, since they spend most of their time in a quasi-stationary state, evolving from a stable equilibrium. Chapter 6 uses a phase plane analysis to explore the temperature structure of a 1-D hydrostatic coronal loop.

A phase plane displays a visual representation of solutions to a differential equation. In Chapter 6, the hydrostatic equation for thermal equilibrium is solved analytically, with possible solutions illustrated within phase plane diagrams, and in phase volumes (a 3-D form of a phase plane).

## 1.5 Hydrodynamics

It is currently believed that most coronal structures which appear to be static are probably controlled by plasma flows. However, it is not a trivial task to observe, measure, and track these flows. A moving plasma blob travelling along a coronal loop may be easy to track, because it is a turbulent flow, and has increased contrast to that of the surroundings. Most flows in a coronal loop are thought to behave as a laminar flow, where a fluid flows in parallel layers and with no disruption between the layers. This makes a laminar type flow very difficult to measure. It is possible, though, to measure the line-of-sight Doppler shift velocities of the flows. Therefore, it is appropriate to consider hydrodynamics applied to coronal plasma.

Chapter 5 takes 1-D hydrodynamic equations, using a 1-D Lagrange re-map (Arber et al., 2001) code, to simulate plasma flows along individual plasma strands, within a global loop system. Random, localised heating events (eg. nanoflares) are released into the loop, and the temperature, density and Doppler shift line-of-sight velocities are recorded and compared to observations.

The Lagrange re-map code is particularly useful because it deals very well with shock fronts, which are important in fluid dynamics. The code solves the Euler equations, updating the variables in time and space on a Lagrangian grid, automatically conserving mass, momentum, and thermal energy, before remapping back on to a standard Eulerian grid.

## 1.6 Explosive Events

### 1.6.1 Coronal Mass Ejections

Coronal mass ejections (CMEs) are huge eruptions of plasma from the corona into interplanetary space, typically ejecting  $10^{14} - 10^{16}$  g of coronal material at speeds of  $100 - 2000$  km s<sup>-1</sup>. When directed towards the Earth, they can have very serious implications; causing damage to satellites, be potentially fatal to astronauts, and cause severe magnetic storms, so it is very important to understand what are the largest eruptive events in the solar system. CME initiation, acceleration and propagation theory is discussed in more detail in Chapter 3, whilst three separate CME events are analysed and discussed in Chapter 4.

### 1.6.2 Flares

Many CMEs are associated with solar flares, and as such, several CME models require a solar flare as part of the initiation process. The most widely accepted flare model, is the CSHKP model, which has evolved from the work of Carmichael (1964); Sturrock (1966); Hirayama (1974); Kopp and Pneuman (1976), and this is briefly described here.

A flare is defined as a sudden increase in brightness, and occurs when magnetic energy is suddenly released in the solar atmosphere. Radiation is emitted through much of the entire electromagnetic spectrum, from radio waves, through optical, X-rays, and gamma rays.

A rising prominence above the neutral line is the initial driver of the flare process, shown in Figure 1.7a. This then stretches a current sheet above the neutral line, and magnetic reconnection is thought to occur at the X-point. This X-point reconnection region is assumed to be the location of major magnetic energy dissipation, accelerating particles and heating the nearby plasma.

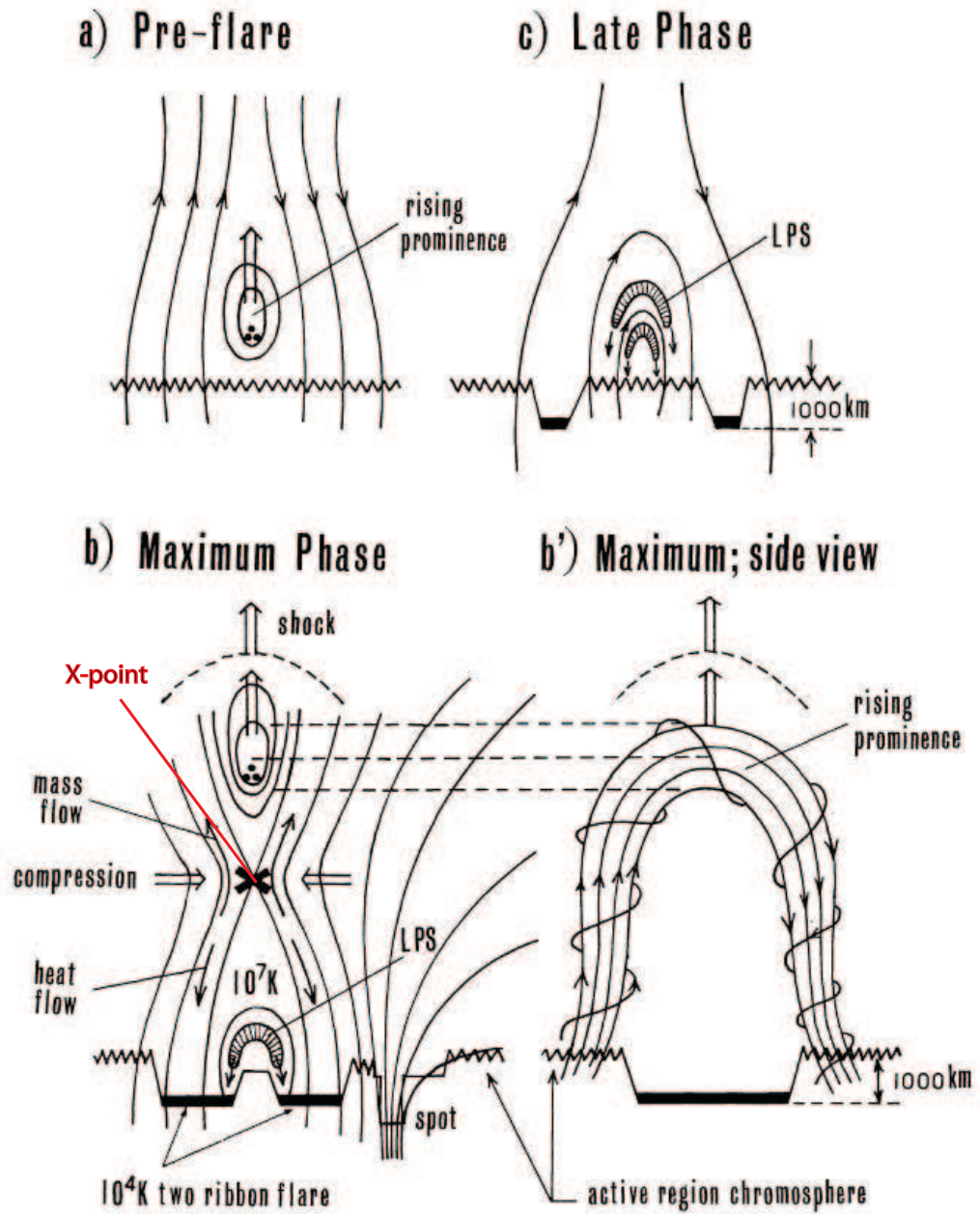


Figure 1.7: From Aschwanden (2005): Temporal evolution of a flare according to the model of Hirayama (1974), which starts from a rising prominence (a), triggers X-point reconnection beneath an erupting prominence (b), shown in side-view (b'), and ends with the draining of chromospheric evaporated, hot plasma from the flare loops (c).

# Chapter 2

## Instrumentation

The research conducted in this thesis has been assisted by several instruments, and these are discussed in this chapter. By far, the most significant research has been conducted in collaboration with the STEREO satellite pair.

### 2.1 STEREO

The pair of near-identical NASA Solar Terrestrial Relations Observatory (STEREO) spacecraft were launched in October 2006 into a near-ecliptic heliocentric orbit of 1 AU. STEREO-B (Behind) lags behind the Earth in its orbit, while STEREO-A (Ahead) leads the Earth in its orbit, providing us with a unique view of the Sun. The spacecraft separate from Earth at around  $22^\circ$  each year.

Each STEREO spacecraft consists of range of four instrument suites, including: the Sun Earth Connection and Heliospheric Investigation (SECCHI); Plasma and Supra-Thermal Ion Composition Investigation (PLASTIC); In-situ Measurements of Particles and CME Transients (IMPACT); and SWAVES (this instrument is not used in the work presented in this thesis).

### 2.1.1 SECCHI

The Sun Earth Connection and Heliospheric Investigation (SECCHI) (Howard et al., 2008) instruments are a suite of five telescopes on-board the Solar TERrestrial RElations Observatory (STEREO), that observe the solar corona and inner heliosphere, out to 1 AU, and consists of an EUV imager, two white-light coronagraphs, and two heliospheric imagers which observe along the Sun-Earth line. As the name suggests, one of SECCHI's main objectives is to advance our understanding of the Sun-Earth connection. The STEREO mission hopes to learn more about the origin and evolution of CMEs, and their interaction, in particular, with the Earth. The SECCHI suite of instruments is now providing unique observations of CMEs, from multiple vantage points. The work presented here, uses the full range of SECCHI observations, and tries to provide evidence to further understand the 3-D propagation and evolution of these huge events. This section draws heavily upon the work presented in Howard et al. (2008).

#### **Extreme UltraViolet Imager (EUVI)**

The Extreme UltraViolet Imager (EUVI) (Wuelser et al., 2004) is a normal incidence extreme ultraviolet (EUV) Sun-centred telescope, which observes the chromosphere and low corona at four distinct EUV emission lines; Fe IX (171 Å), Fe XII (195 Å), Fe XV (284 Å) and He II (304 Å), out to  $1.7R_{\odot}$ , and spans a temperature range from 0.1 to 20MK. The instrument also offers a substantial improvement in image resolution and cadence over its predecessor EIT on-board the SOHO spacecraft.

EUV radiation enters the telescope through a thin (150 nm) metal film filter of aluminium, which helps to suppress most of the UV, visible, and IR radiation, and also helps to keep any heat out of the telescope. The radiation then passes through the quadrant sector, to one of the four quadrants of the optics. Each quadrant of the primary and secondary mirror is coated with a multi-layered, narrow-band

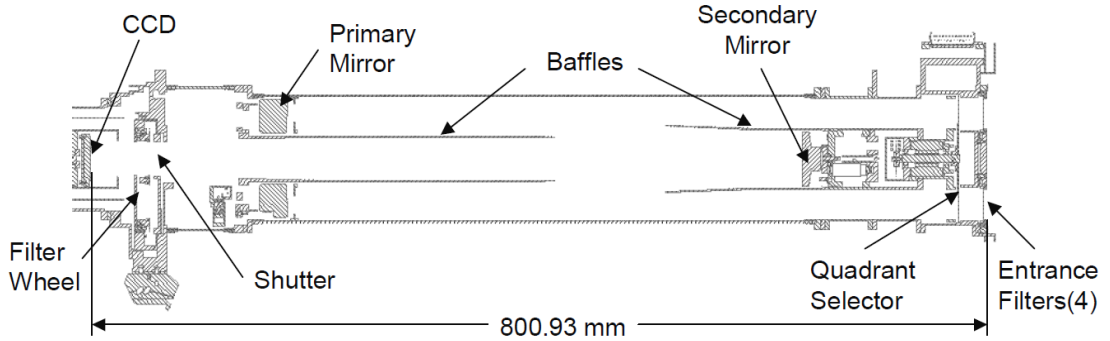


Figure 2.1: EUVI telescope cross-section (Wuelser et al., 2004)

reflective coating, optimised for one of the four EUV lines. The radiation bounces off the primary and secondary mirror, before passing through a filter wheel, which has redundant thin-film aluminium filters to remove the remainder of the visible and IR radiation. The rotating shutter blade is responsible for controlling the exposure times, and the image is formed on a charge-coupled device (CCD) detector. Figure 2.1 shows a cross section through the telescope, and the main properties of the telescope are featured in Table 2.1.

### Calibration and Predicted Response to Solar Phenomena

The EUVI mirrors were calibrated at the synchrotron of the Institut d'Astrophysique Spatiale in Orsay, as pairs. In the same geometry as the EUVI telescope, the mirrors were arranged, and illuminated by a nearly collimated beam from a monochromator attached to the synchrotron, and each telescope quadrant was measured individually. Wavelength scans were performed with the telescope in the beam, and also without, with the absolute total reflectivity of the mirror pairs being provided by the measured ratio of these wavelength scans. Each coating performed well both in terms of high reflectivity and proper wavelength of peak reflectivity. For 284 Å, the coating was optimised for rejecting the strong He II line at 304 Å. The result of this, is that it produces a lower peak reflectivity. The CCDs were calibrated at the

## CHAPTER 2

Table 2.1: Main EUVI telescope properties

Instrument type	Normal incidence EUV telescope (Ritchey-Chretien)
Wavelengths	He II 304 Å; Fe IX 171 Å; Fe XII 195 Å; Fe XV 284 Å
Characteristic Temperature (in relative order of wavelengths above)	0.06-0.08 MK; 1 MK; 1.4 MK; 2.2 MK
Aperture	98 mm at primary mirror
Effective focal length	1750 mm
Field of view	Circular full sun field of view to $\pm 1.7R_{\odot}$
Spatial resolution	1.6 arc second pixels
Detector	Backside illuminated CCD, 2048 x 2048 pixels

## CHAPTER 2

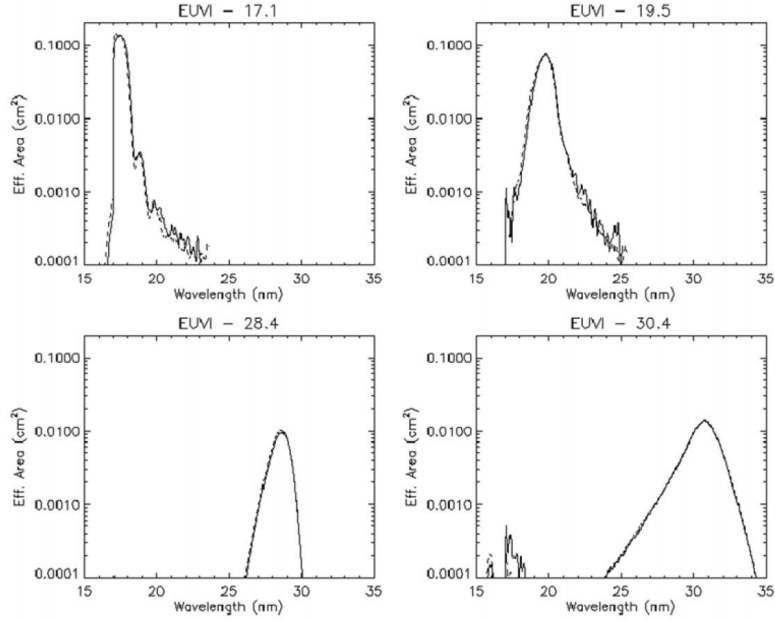


Figure 2.2: EUVI effective area (Howard et al., 2008). The solid lines are for the EUVI-A, the dashed lines for the EUVI-B.

Brookhaven synchrotron and at the LMSAL XUV calibration facility. The entrance and focal plane filters were also calibrated at the LMSAL XUV calibration facility. The results of those measurements were used to fit CCD and filter response models. The calibration curves of the individual components were combined to obtain the EUVI effective area as a function of wavelength. The effective area is defined by the product of the optical efficiency and the telescope area. The results are shown in Figure 2.2. The two telescopes (EUVI-A and EUVI-B) were found to have very similar responses.

Using the calibration results, the response of the EUVI to typical solar plasmas was then predicted. Using typical differential emission measure distributions (DEMs), the resulting solar spectral line emission was predicted using the CHIANTI software (Dere et al., 1997; Young et al., 2003), and the results were combined with the calibration data. Figure 2.3 shows count rates (in photons per pixel per second) predicted for isothermal plasmas (for an EM of  $10^{11} \text{ cm}^{-5}$ ) as a function of plasma

## CHAPTER 2

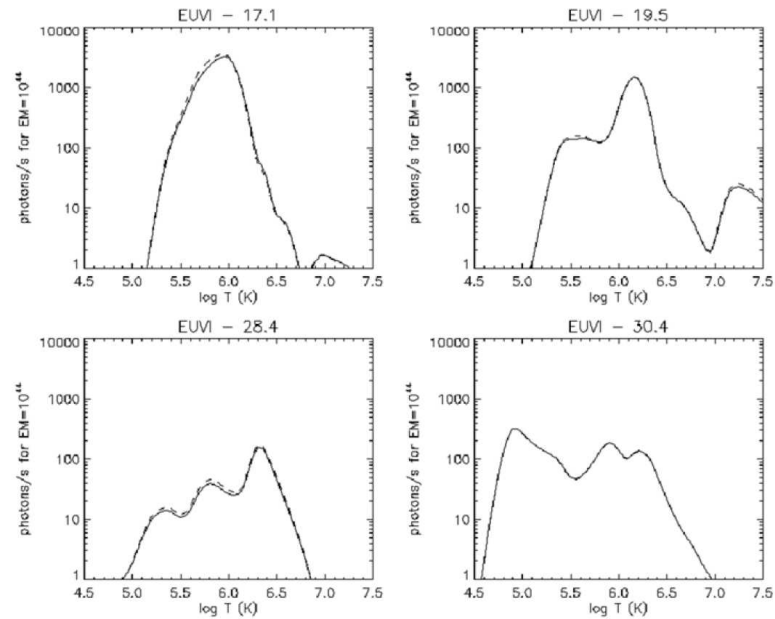


Figure 2.3: The response of the EUVI as a function of solar plasma temperature (Howard et al., 2008). The solid lines are for the EUVI-A, the dashed lines for the EUVI-B.

temperature.

### Coronagraphs

There are two coronagraphs on-board each STEREO spacecraft; the inner coronagraph (COR-1), and the outer coronagraph (COR-2). These visible light Lyot (Lyot, 1939) instruments measure the weak light from the solar corona originating from scattered light from the solar photosphere, allowing observations of the inner and outer corona from  $1.4R_{\odot}$  to  $15R_{\odot}$ . Due to the large radial gradient of coronal brightness in this height range, two different types of coronagraphs are required in order to fully exploit the potential observations.

The coronagraphs on STEREO owe much to the huge success of the LASCO coronagraphs on-board SOHO.

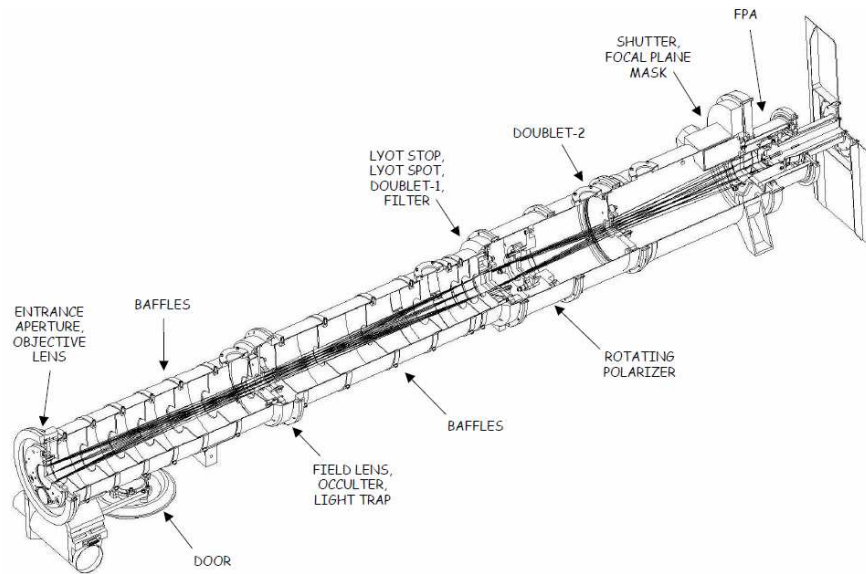


Figure 2.4: Layout of the COR-1 instrument (Thompson and Reginald, 2008)

### Inner Coronagraph (COR-1)

COR-1 (Thompson and Reginald, 2008) is the inner of the two coronagraphs, observing the corona from  $1.4R_{\odot}$  to  $4R_{\odot}$ . It is a classic Lyot internally occulting refractive coronagraph, and is the first internally occulting coronagraph of its kind currently in space. The internal occultation enables a better spatial resolution closer to the limb than an externally occulted design, as it eliminates more sources of stray light. The COR-1 signal is dominated by instrumentally scattered light, which is removed to measure the underlying coronal signal. This stray light cannot be removed by the Lyot principles but is largely unpolarised and is therefore greatly reduced by making polarised observations in three states of linear polarisation and calculating the polarised brightness (pB). To achieve this separation, there must be a high enough signal to noise ratio, even in the presence of the large scattered light noise, and this is partly achieved by performing on-board binning of the pixels.

The instrument layout is shown in Figure 2.4. Sunlight enters through the front

## CHAPTER 2

aperture, and is focused onto the internal occulter, by the objective lens, to remove the direct photospheric light. As a result of the occulter being mounted onto the field lens, no occulter stem appears in the image. The field lens re-images the front aperture onto a Lyot stop to remove any diffracted light, and a series of lenses refocus the coronal light onto a cooled CCD detector. Diffracted light is removed from the first occulter by a secondary occulter, known as the focal plane mask, which sits just in front of the detector. This has the net effect of giving a field of view which ranges from  $1.4$  to  $4R_{\odot}$ . A bandpass filter restricts the wavelength range to a region  $22.5$  nm wide, centred on the  $H\alpha$  line at  $656$  nm. A Corning Polarcor linear polariser within the beam allows one to derive both total and polarised brightness. The polariser is always in the optical path, and is rotated to sample different polarisation states. A contrast ratio in excess of  $10,000:1$  provides completely polarised images to all practical purposes, as was confirmed during ground testing. Three images are taken in rapid sequence at polarizer angles of  $0^{\circ}$ ,  $120^{\circ}$ , and  $240^{\circ}$ . The total brightness ( $B$ ) and polarised brightness ( $pB$ ) can then be derived via Equations 2.1 and 2.2 (Thompson and Reginald, 2008)

$$B = \frac{2}{3}(I_0 + I_{120} + I_{240}) \quad (2.1)$$

$$pB = \frac{4}{3}\sqrt{(I_0 + I_{120} + I_{240})^2 - 3(I_0I_{120} + I_0I_{240} + I_{120}I_{240})} \quad (2.2)$$

which are adopted from Billings (1966).

To produce calibrated data, the following steps are taken with each COR-1 image:

1. A correction is done for certain numerical operations applied on board the spacecraft to keep the data within the valid range of the compression algorithm.

## CHAPTER 2

2. A CCD bias derived from the overscan pixels is subtracted, and the data are divided by the exposure time.
3. A flat field image, which includes vignetting effects, is divided into the image, and is derived from observations using an opal window built into the aperture door.
4. The data are multiplied by a calibration factor to convert from data numbers per second ( $\text{DN s}^{-1}$ ) to mean solar brightness (MSB) units. These factors are applied to each of the individual polarisation components  $I_0$ ,  $I_{120}$ , and  $I_{240}$  in Equations 2.1 and 2.2.

Vignetting occurs near the edge of the occulter. The same calibration factor is used regardless of the polarisation angle, since the polariser never leaves the beam; it rotates about the optical axis. All of these calibration factors are applied through the IDL routine *secchi\_prep.pro* in the *SolarSoft* (Freeland and Handy, 1998) library. COR-1 is internally occulted, and as such, the images are dominated by light scattered from the front objective. To derive useful data, additional steps must be taken to remove the background. Throughout the work presented in this thesis, running difference images are used, as described in Section 4.1.

### Pointing Calibration

The simultaneous images from each STEREO spacecraft must be co-aligned in order to compare the data correctly. The SECCHI Guide Telescope, the star tracker, and the Inertial Measurement Unit (IMU) (Driesman et al., 2008) control the attitude of the STEREO spacecraft. The Guide Telescope provides the primary Sun pointing information, and this is mounted on the same optical bench as EUVI, COR-1, and COR-2. The spacecraft roll is controlled by the star tracker and IMU. The SECCHI FITS headers contain the attitude information, and is based upon telemetry from

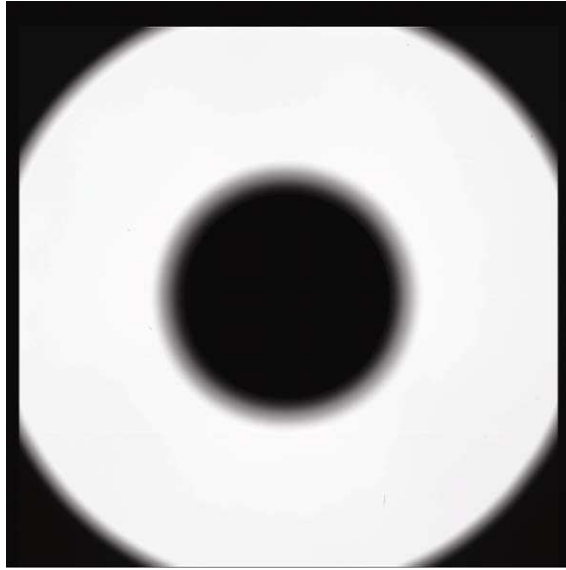


Figure 2.5: Flat field response and vignetting function of the COR-1A instrument (Howard et al., 2008)

the Guide Telescope, and the STEREO Mission Operations (SMO) which provides the attitude history data based on the star tracker and IMU.

### Calibration and Performance Results

The vignetting function and flat field response of the instrument is demonstrated in Figure 2.5. The field is unvignetted except for a small area around the edge of the occulter, and near the field stop in the corners of the image. (The dim spot in the center of the occulter shadow is caused by scattering within the instrument.) Only the Ahead data are shown, as the Behind response is virtually identical.

Figure 2.6 shows the measured COR1 scattered light performance for the Ahead and Behind instruments. The average radial profile is well below  $10^{-6}B/B_{\odot}$  for both instruments. There are discrete ring-shaped areas of increased brightness, which can climb to as high as  $1.4 \times 10^{-6}B/B_{\odot}$  for the Behind instrument. It has been determined that these are caused by features on the front surface of the field lens. However, after the thermal vacuum testing of the STEREO spacecraft, some

## CHAPTER 2

contamination was found on the COR-1 Behind objective lens. As a result, the objective was cleaned and re-installed, and may therefore have a slightly different performance to that shown in Figure 2.6

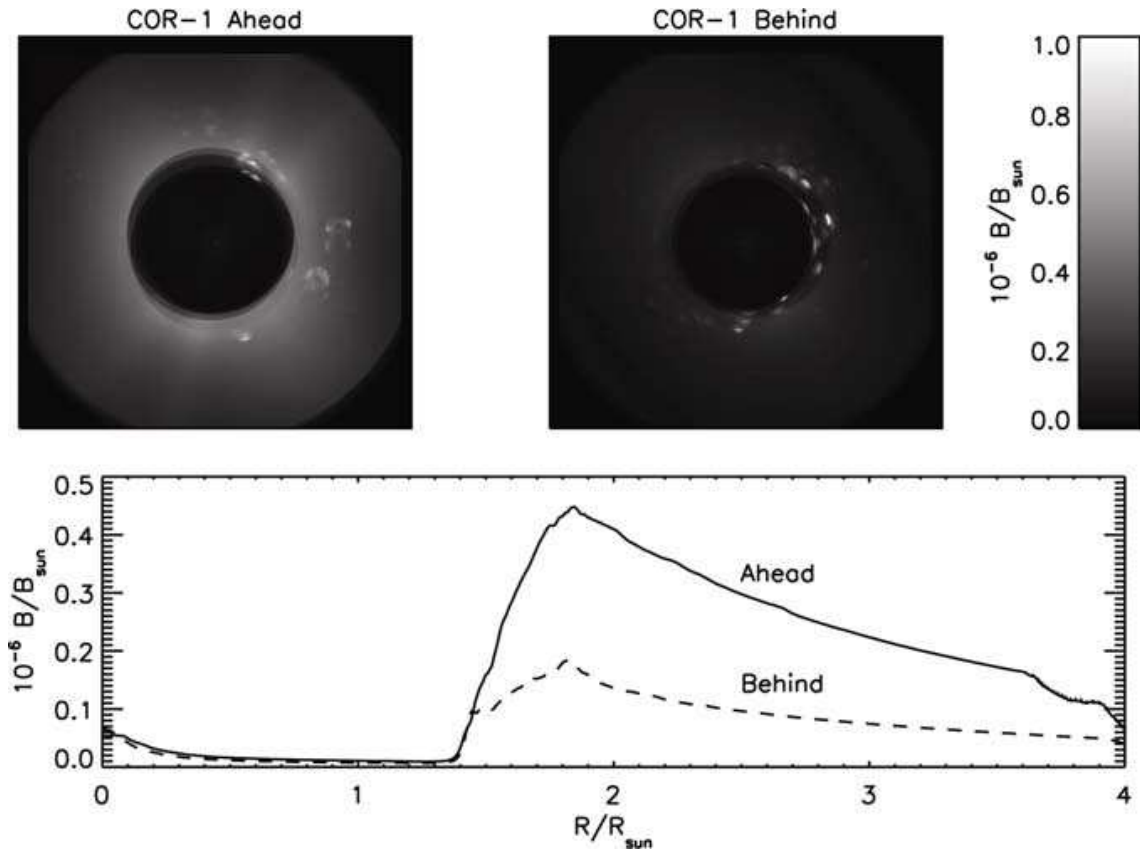


Figure 2.6: Measured scattered light images and average radial profiles for the COR-1 Ahead (solid) and Behind (dashed) instruments (Howard et al., 2008)

Using a model of the K corona polarised brightness, based upon the model found in Gibson (1973), with the data from Figures 2.5 and 2.6, allows one to estimate the signal-to-noise ratios seen during the mission, and the results of this, is shown in Figure 2.7 The coronal model, which is valid from 1.4 to  $4\odot$  has the functional form:

$$\log_{10}(pB) = -2.65682 - 3.55169(R/R_{\odot}) + 0.459870(R/R_{\odot})^2 \quad (2.3)$$

The main performance properties of the COR-1 instruments are shown in Table

CHAPTER 2

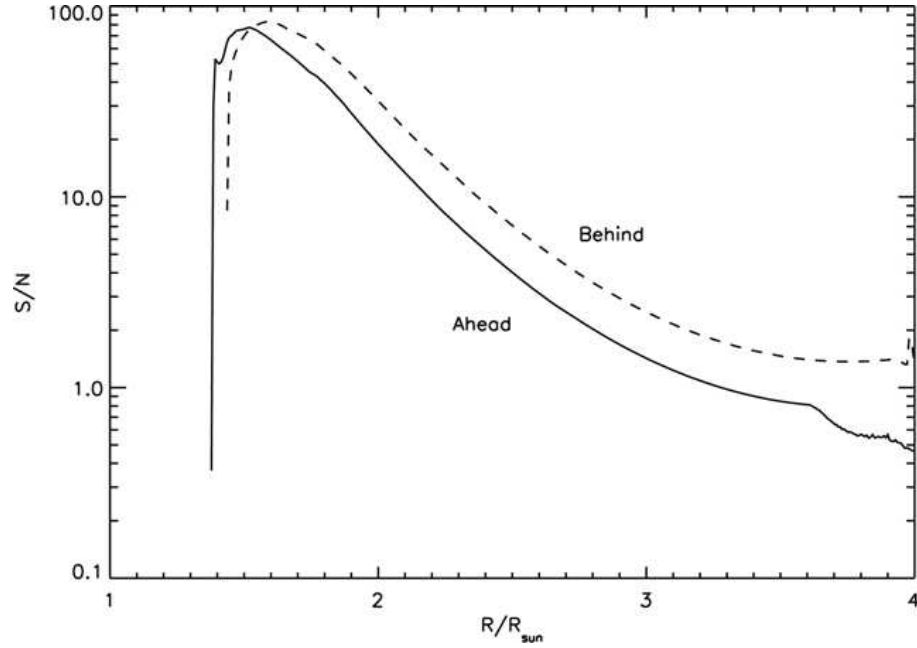


Figure 2.7: Estimated signal-to-noise ratios for a modeled K corona for an exposure time of 1 second, with 2 x 2 pixel binning (Howard et al., 2008)

Table 2.2: Main COR-1 performance properties

Property	Units	Ahead	Behind
Pixel size, full resolution	arcsec	3.75	3.75
Pixel size, 2 × 2 binned	arcsec	7.5	7.5
Planned exposure time	s	1	1
Polariser attenuation	-	$10^{-4}$	$10^{-4}$
Photometric response	$B_{\odot}/DN$	$7.1 \times 10^{-11}$	$5.95 \times 10^{-11}$
Time to complete pB sequence	s	11	11
Image sequence cadence	min	8	8

## CHAPTER 2

2.2. To increase the signal to noise ratio, the full resolution 3.75 arcsec square pixels are summed together into  $2 \times 2$  bins, to form 7.5 arcsec pixels.

Due to dynamic changes in the corona, it is essential to take the three images in a polarisation sequence as quickly as possible, so that any changes are kept to a minimum. Each set of three images makes up a complete observation, and the cadence of observations is the time between each polarisation set and the next.

### **Comparison with other Coronagraphs**

The coronagraphs on STEREO, above all, offer continuous observations of the solar corona, from a different vantage than the Earth. COR-1, LASCO C2 and MLSO Mk4 all observe a similar region of the solar corona, and Table 2.3 presents a comparison in cadence, pixel resolution, field of view, and CCD size. COR-1 offers a higher cadence, and better pixel resolution than LASCO C2, and observes the corona at a lower height. LMSO MK4 has a higher cadence and pixel resolution than COR-1, but has a smaller field of view. Mk4 is also based upon Earth, and so cannot observe 24 hours a day like COR-1 and C2. Being on Earth has other disadvantages too, such as having to deal with the Earth's atmosphere, weather and other such phenomena.

Figures 2.8 and 2.9 show a comparison of the COR-1 telescopes with two previously existing coronagraphs; the LASCO (Brueckner et al., 1995) C2 telescope on-board SOHO, and the Mk4 K-coronameter at the MLSO (Elmore et al., 2003). C2 observes total brightness, and Mk4 polarised brightness, and thus comparisons are made with COR-1 in their respective observed total / polarised brightness.

Figure 2.8 shows the comparison of COR-1 with the LASCO C2 telescope for two strong CMEs that occurred on the 24th and 30th of January 2007, when the two STEREO spacecraft were only  $0.5^\circ$  to  $0.6^\circ$  apart. Evidently the co-alignment of the three telescopes is quite good. The bottom two panels show the signal as a

## CHAPTER 2

Table 2.3: COR-1 comparison with LASCO C2 and MLSO Mk4

Instrument	Cadence (mins)	Pixel Resolution (arcsec)	Field of View ( $R_{\odot}$ )	CCD size
COR-1	8	7.5	1.4 to 4.0	2048 × 2048
LASCO C2	20	23.8	2 to 6	1024 × 1024
LMSO Mk4	3	5.95	1.14 to 2.86	960 × 960

function of position angle, averaged between  $2.5R_{\odot}$  and  $2.7R_{\odot}$  to reduce the noise. The COR-1 Ahead and Behind telescopes follow each other extremely closely and are practically indistinguishable from each other. The LASCO C2 data is  $\sim 20\%$  lower than the COR-1 data.

The MLSO Mk4 is compared with COR-1, with a CME from 9 February 2007, when the spacecraft were separated by  $0.7^{\circ}$ . The results of this are shown in Figure 2.9. The overall appearance is the same from all three telescopes, but the Mk4 data is  $\sim 50\%$  higher than the COR-1 data, and there may also be a slight offset in position angle between the Mk4 data and COR-1. Overall though, the COR-1 and Mk4 observations are in good agreement.

### Outer Coronagraph (COR-2)

The outer coronagraph, known as COR-2 is an externally occulted Lyot coronagraph, observing the weak coronal signal in visible light. The externally occulted design shields the objective lens from direct sunlight, and therefore enables a lower stray light level than COR-1, thus achieving observations to further distances from the Sun. COR-2 is complementary to COR-1; while COR-1 observes closer to the Sun,

CHAPTER 2

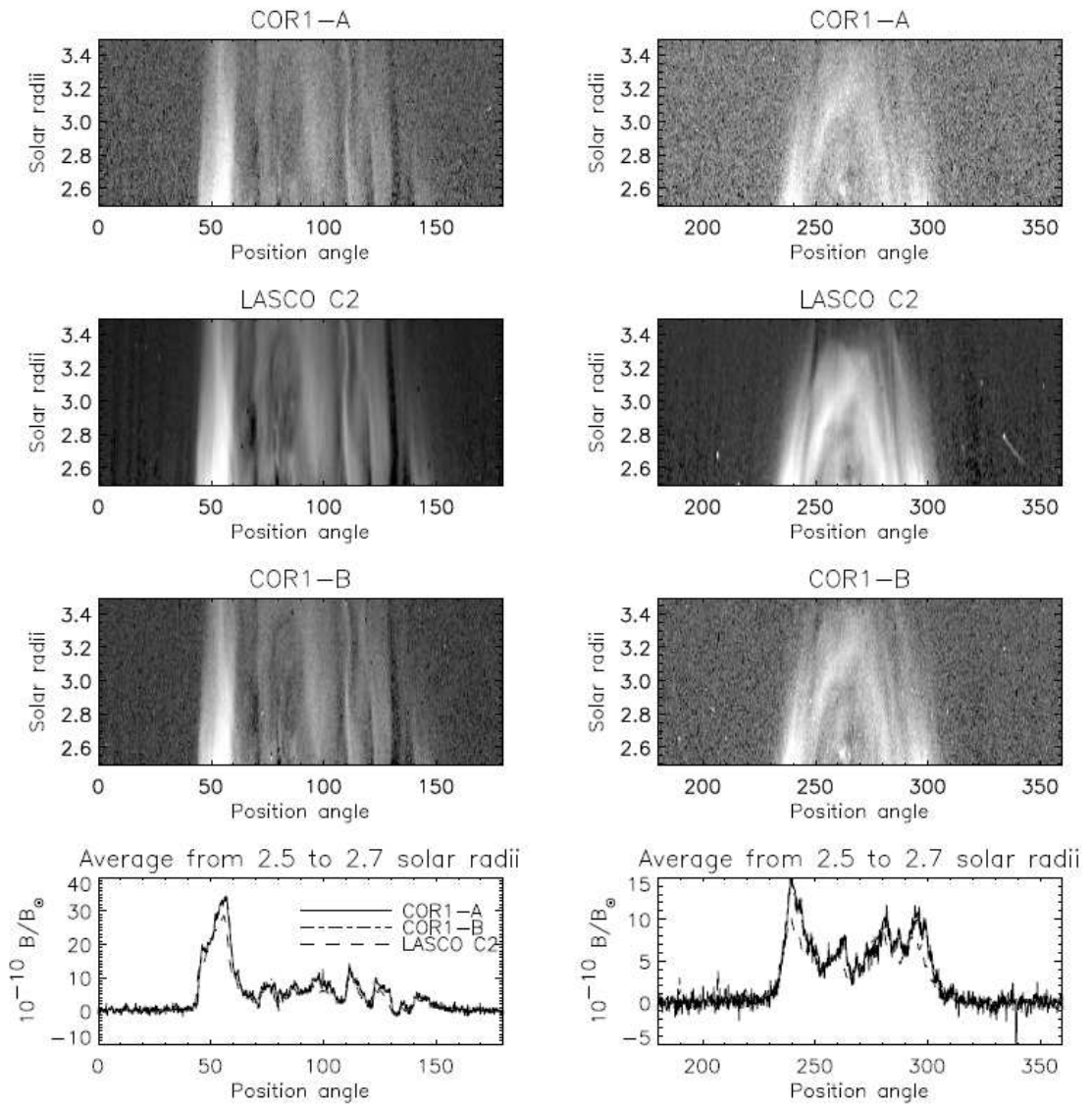


Figure 2.8: Comparison of COR-1 total brightness measurements with LASCO C2. The left panels show observations of a CME that occurred on the east limb on 24 January 2007, and the right panels show a CME from 30 January 2007 on the west limb (Thompson and Reginald, 2008)

## CHAPTER 2

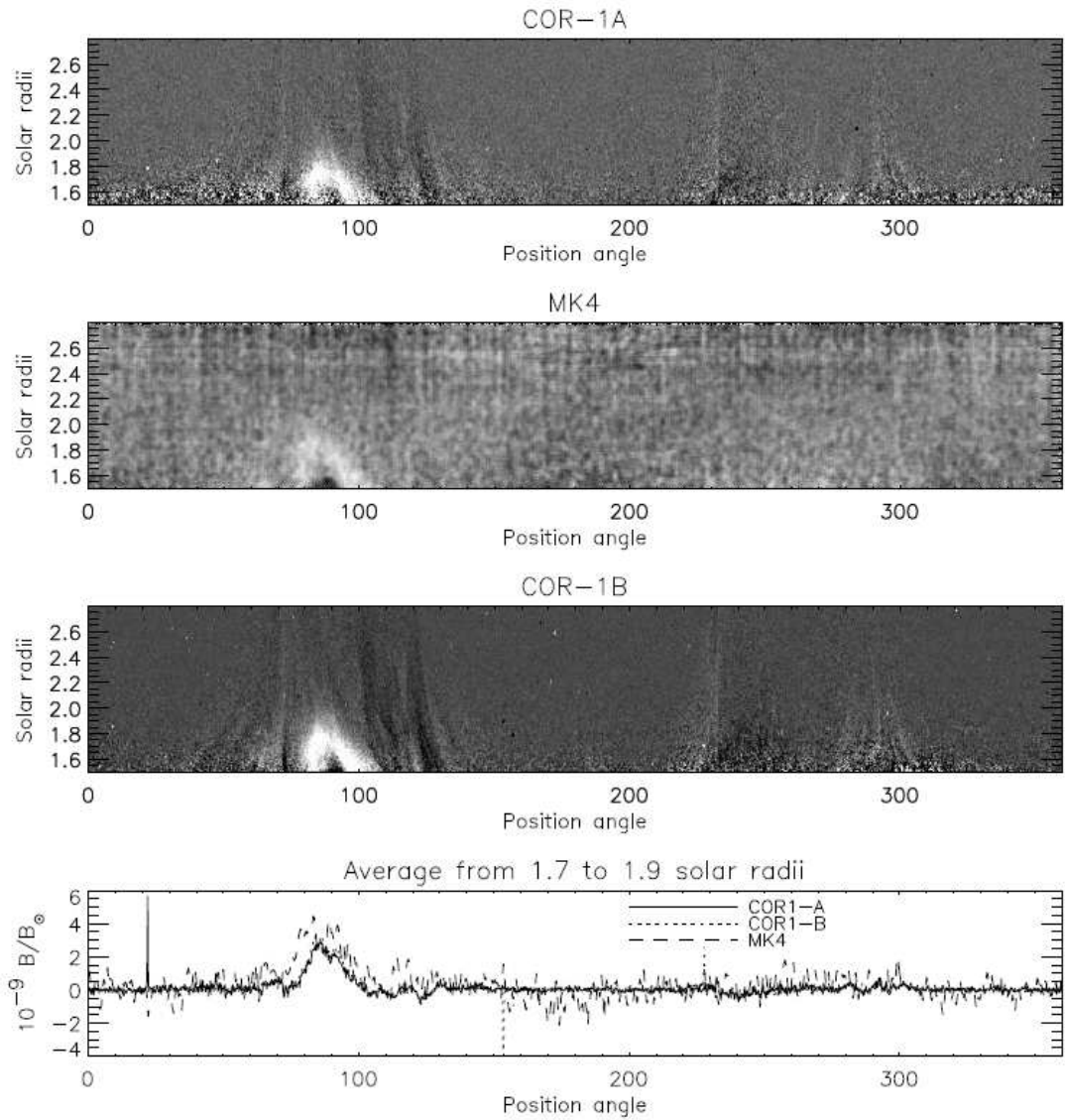


Figure 2.9: Comparison of COR-1 polarized brightness measurements with the MLSO Mk4 (second panel) for a CME on the east limb on 9 February 2007. Some smoothing has been applied to the Mk4 data to reduce the noise (Thompson and Reginald, 2008)

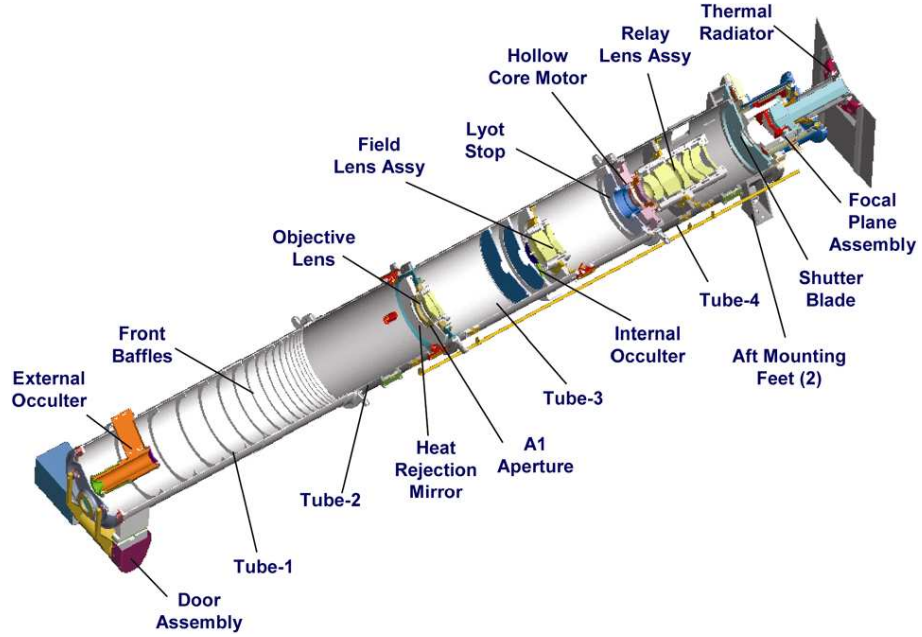


Figure 2.10: Layout of the COR-2 instrument (Howard et al., 2008)

COR-2 observes at longer distances, from 2 to  $15R_{\odot}$ . There is thus an overlap with COR-1, between the region of 2 to  $4R_{\odot}$ . COR-2 was designed so that it would build upon the success of the LASCO C2 and C3 coronagraphs. In order to accomplish this, COR-2 has a better spatial resolution, a higher cadence, and a shorter exposure time than either of C2 and C3, whilst observing similar fields of view.

Figure 2.10 displays the layout of the COR-2 instrument. As radiation enters into the coronagraph through the A0 aperture, a three-disk external occulter keeps the objective lens shaded from direct solar radiation, and creates a deep shadow at the objective lens aperture. Any incident solar radiation is reflected back through the entrance aperture by a heat rejection mirror.

### Calibration and Performance Results

The flat field response and vignetting pattern for the COR-2 Ahead telescope is shown in Figure 2.11. Each image is vignettted throughout the field of view, reaching a minimum of 20% at about  $10R_{\odot}$ , before increasing again towards the edge. Around

## CHAPTER 2

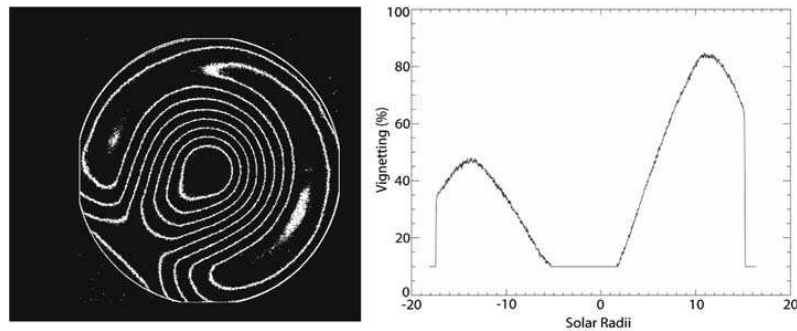


Figure 2.11: Flat field response and vignetting pattern (left) for COR-2A. The plot on the right is an intensity cut diagonally from the lower left to the upper right, through the pylon (Howard et al., 2008)

the occulter pylon, the vignetting is about 40 - 50%, which means the pylon is invisible in the images. The COR-2 Behind instrument has similar results.

During stray light tests, the instrument performance exceeded the design requirements, and allows detailed images of the extended corona, as shown in Figure 2.12. The image on the left of Figure 2.12 shows back-reflections onto baffles in the chamber, taken during the stray light test. The plot on the right shows the intensity along the radial track (the line in the lower right of Figure 2.12 (left)), compared to the K- and F-coronae and stray light recorded by LASCO C2, and for the Saito et al. (1977) (SPM) model of the K-corona.

The general performance characteristics of the COR-2 instruments are shown in Table 2.4.

COR-2 only acquires polarised images of the corona because the polariser is always in the beam, and takes three sequence images, similar to COR-1. These images are transmitted to the ground, and then processed to produce total and polarised brightness, as described previously with COR-1. Also, an alternative observation mode is used, which takes two images at  $0^\circ$  and  $90^\circ$  in quick succession, without reading out the CCD in between exposures. This produces a “double” exposure image, corresponding to a total brightness image. These images are sent to the ground

## CHAPTER 2

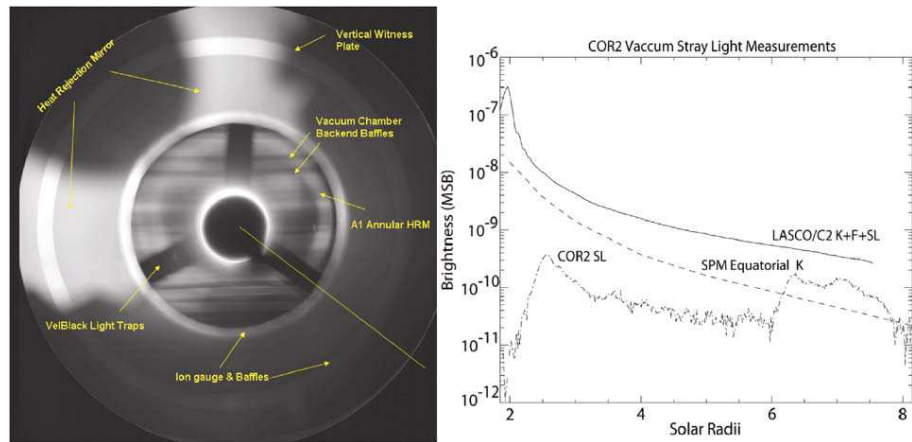


Figure 2.12: Stray light performance of the COR-2A instrument. The image on the left is an image taken during the stray light test, whilst the plot on the right shows the intensity along the radial track along the line in the in the lower right of the image as a dot-dash. The brightness is given in units of Mean Solar Brightness (Howard et al., 2008)

Table 2.4: COR-2 Performance Characteristics

Property	Units	Ahead	Behind
Field of View	$R_{\odot}$	$2-15R_{\odot}$	$2-15R_{\odot}$
Pixel size, full resolution	arcsec	14.7	14.7
Planned Exposure Time	sec	< 4	< 4
Photometric Response	$B_{\odot}/DN$	$1.35 \times 10^{-12}$	$1.25 \times 10^{-12}$
Time to complete pB sequence	sec	11	11
Image sequence cadence	min	15	15

## CHAPTER 2

as a single image, which helps to reduce telemetry, and increase image cadence for special observations.

### **The Heliospheric Imagers**

The Heliospheric Imager consists of two wide-angle telescopes, pointing off-limb (with a combined field of view of about 4 to 89° elongation), meaning that the Sun is not in the instrument's field of view. It is mounted on the side of each STEREO spacecraft, viewing the region between the Sun and the Earth; the so-called Sun-Earth line. HI-1 is the inner-most of the imagers, and has a field of view extending from 4 to 24°, whilst HI-2 has a field of view extending from about 17 to 89°. The concept behind the HI instrument was originally derived from laboratory measurements of Buffington et al. (1996), who determined that the scattering rejection was a function of the number of occulters and the angle below the occulting edge. This suggested that a simple telescope in a small package could achieve the required levels of rejection by proper occulting and by putting the telescope aperture sufficiently in the shadow of the occulter; a similar method can be used when observing the night sky once the Sun has dipped below the horizon.

So far, two similar instruments (previous to HI) have been used before, and have validated the ability to measure the electron scattered component against the strong stellar background and zodiacal light; the Zodiacal Light Photometer (Pitz et al., 1976) on-board the Helios spacecraft (launched 1974), and from the Solar Mass Ejection Imager (SMEI) instrument (Eyles et al., 2003) on-board the Coriolis spacecraft (launched 2003). Both of these instruments have demonstrated that a properly baffled instrument can detect CMEs against the more intense background (Tappin et al., 2004), and it is the primary objective of HI to study CMEs, as they propagate out into the heliosphere. HI is also capable of providing measurements of the F and K corona, interplanetary dust, comets, near-Earth objects, and stellar

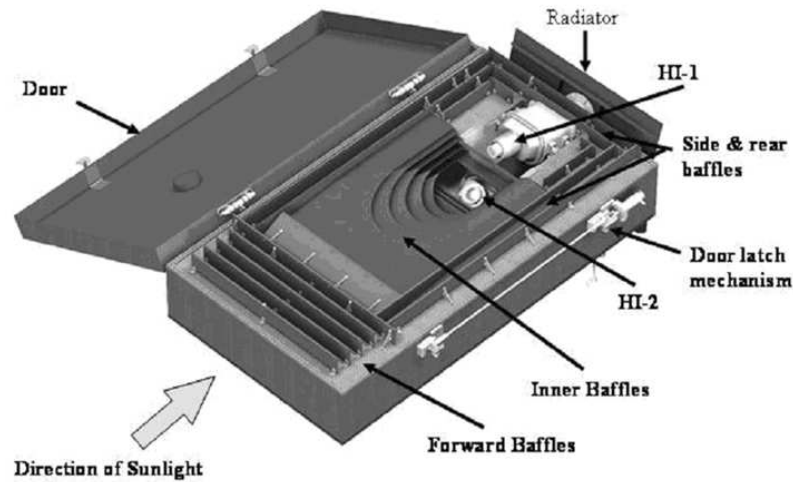


Figure 2.13: The HI design concept (Howard et al., 2008)

variability studies.

The design concept for HI can be seen in Figure 2.13. The instrument is a box shape, about 0.7 m long. During launch, and the initial cruise phase activities, a door covers the optical and baffle systems. Once HI reached its heliocentric orbit, the door was permanently opened. The HI telescopes are buried within the baffle system, as shown in Figures 2.13 and 2.14. The direction of sunlight is shown, and the design results in the Sun keeping below the vanes of the forward baffle system. The detectors are CCD devices, and are passively cooled by radiating the heat into deep space.

Table 2.5 shows the performance specifications for HI. The HI-1 and HI-2 telescopes are directed to angles of about  $13^\circ$  and  $53^\circ$  from the principal axis of the instrument, which in turn is tilted upwards by  $0.33^\circ$  to ensure that the Sun is sufficiently below the baffle horizon. Thus, the two fields of view are nominally set to about  $14^\circ$  and  $54^\circ$  from the Sun, along the ecliptic line, with fields of view of  $20^\circ$  and  $70^\circ$ , respectively, which means there is an overlap of approximately  $5^\circ$ .

The top-half of Figure 2.15 shows the geometrical layout of the fields of view HI instruments, as shown by the respective circles, and provides a view along the

CHAPTER 2

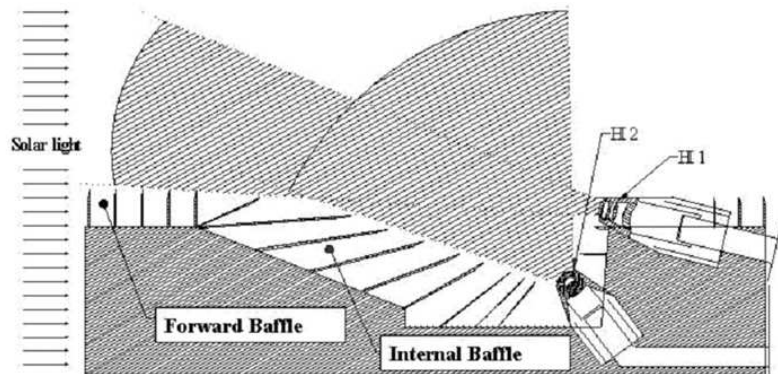


Figure 2.14: A schematic side view of the optical configuration, demonstrating the two fields of view of the instrument. (Howard et al., 2008)

Table 2.5: HI Performance Characteristics

	Units	HI-1	HI-2
Direction of centre of field of view	degrees	13.98	53.68
Angular field of view	degrees	20	70
Angular range	degrees	3.98 – 23.98	18.68 – 88.68
Image array ( $2 \times 2$ binning)	pixels	$1024 \times 1024$	$1024 \times 1024$
Image pixel size		70 arcsec	4 arcmin
Spectral bandpass	nm	630 – 730	400 – 1000
Nominal exposure time	sec	12 – 20	60 – 90
Typical exposures per image		150	100
Nominal image cadence	min	60	120
Brightness sensitivity	$B_{\odot}$	$3 \times 10^{-15}$	$3 \times 10^{-16}$

## CHAPTER 2

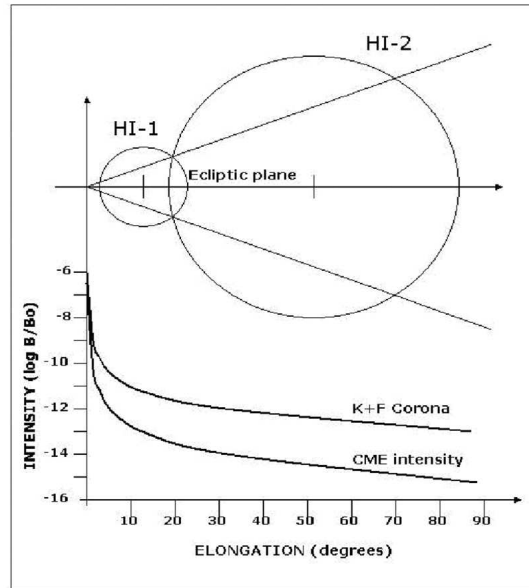


Figure 2.15: The geometrical layout of the HI fields of view and the major intensity contributions (based upon a figure from Socker et al., 2000).

Sun-Earth line, extending from the COR-2 outer limit. The bottom-half of Figure 2.15 shows the major contributions to the observed intensities, as a function of elongation. As shown, the brightness of a CME is some two orders of magnitude dimmer than the sum of the F-corona and K-corona. In order to extract the CME signal, the signal-to-noise ratio must be increased over a single exposure, and is accomplished by summing individual exposures on-board. Prior to this summing, and to the  $2 \times 2$  pixel binning, the individual exposures must be scrubbed for cosmic rays. Also, during the readout, a smearing occurs because there is no shutter. This is accounted for in *secchi\_prep*.

### Calibration and Pointing

The calibration of the pointing and optical parameters is derived by comparing the locations of stars identified in each HI image, with known star positions predicted from the star catalogue “NOMAD”, the Naval Observatory Merged Astrometric

## CHAPTER 2

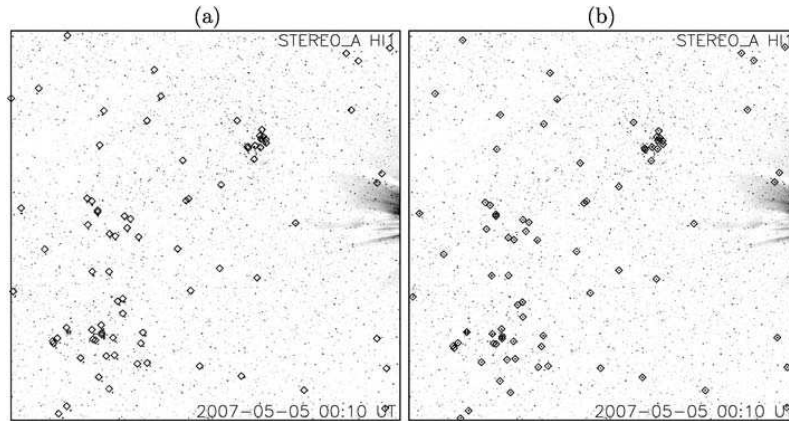


Figure 2.16: HI-1A images from May 2007 with catalogue stars overplotted as diamonds. Ideally, each diamond should contain a “dot” representing a star in the image. Image (a) uses the nominal pointing to find star locations, and image (b) uses the optimised pointing. For both images, the F corona has been subtracted Brown et al. (2009)

Dataset, by Brown et al. (2009). The pointing and optical parameters are varied in an autonomous way, in order to minimise the discrepancy between the observed and predicted positions of the stars. In order to determine the location of a solar transient, such as a CME, the pointing attitudes of the HI cameras must be accurately determined.

Attempts were initially made with the nominal preflight offsets between the HI cameras and spacecraft coordinates, together with the provided spacecraft attitude solutions. These spacecraft attitude solutions are derived from the error signals from the Guide Telescope, and the roll angle from the spacecraft star trackers. However, Brown et al. (2009) show in Figure 2.16a, that over-plotting the expected star positions on a HI image using the attitude solutions derived in this manner, shows an obvious discrepancy with the background star field observed by HI.

Inaccuracies in the attitude solutions can be contributed by many factors, such as errors in the spacecraft pointing solutions of the yaw, pitch and roll, and deviations

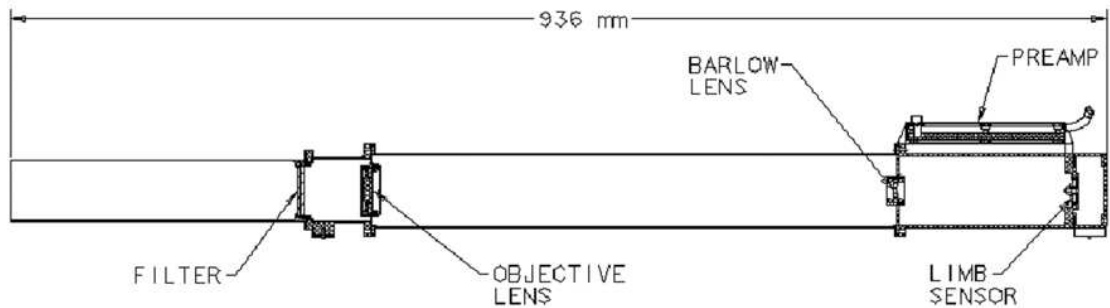


Figure 2.17: Schematic cross section of the Guide Telescope (Howard et al., 2008)

of the nominal instrument offsets from the spacecraft axes, and from any changes in the offsets since the spacecraft was launched. Brown et al. (2009) use an alternative method for deriving the attitude solutions, by matching known catalogue stars with those identified in the background star field, and by perturbing the pointing parameters to optimise the fit between the predicted and observed star positions.

Figure 2.16(b) shows that this method shows an excellent correspondence between the background stars and the catalogue stars. The photometric calibration and large scale flat field of HI-1 is discussed in Bewsher et al. (2010).

### The Guide Telescope

The Guide Telescope (GT) is mounted on the SCIP, and has two many functions; to act as the spacecraft fine Sun sensor, and to provide the error signal for the EUVI fine pointing system.

The concept of the GT is based upon the guide telescope from the TRACE mission. The GT images the Sun onto an occulter. Due to the size of this occulter, most of the solar disk is blocked, with only the limb just being passed, and the intensity of the limb is measured by photodiodes. These intensities are then used to calculate pitch and yaw pointing error signals.

## CHAPTER 2

### **Flight Software**

The SECCHI flight software runs on a multi-tasking, real-time, VxWorks operating system. This provides all the software services for all the instruments, including the image processing tasks. The flight software also includes handling commands from the spacecraft, heater control, guide telescope control, housekeeping and science telemetry to the spacecraft, instrument control, and image scheduling.

### **Image Processing**

After an image is taken, it requires processing before downlink. It is moved from the camera buffer memory to the computer, and into a queue of images ready to be processed. There are 27 camera buffers, and so it is possible for image taking to take data faster than it can be processed.

The image processing comprises of 120 different functions, including cosmic ray scrubbing, automatic compression control, automatic exposure control, image compression, event detection and reporting, occulter and region of interest masks, adding and subtracting images, and the ability to send images down any four channels (real-time, space weather, solid state recorder 1, solid state recorder 2).

Of these processes, the image compression is the most important feature. Four types of compression are used, including no compression. The Rice method is a lossless compression providing about a factor of 2.2 times compression. H-Compression is a lossy wavelet image compression with a variable image compression. ICER is a lossy wavelet image compression, which has the advantage of being able to specify the desired output size, and can produce useful images with a compression factor of up to 20 times.

## CHAPTER 2

### 2.1.2 PLASTIC and IMPACT

In-situ data is collected from both STEREO spacecraft from a range of two instrument suites. PLASTIC measures the density, speed, flow, and material of the solar wind, while IMPACT measures its electrons, embedded magnetic fields, and more energetic particles.

## 2.2 SOHO

The STEREO spacecraft owes much of its heritage to the success of the Solar and Heliospheric Observatory (SOHO). SOHO is a satellite observing the Sun, based at the L1 Lagrangian point, and was launched on the 2nd December 1995. The satellite consists of a suite of twelve instruments, including: the Large Angle and Spectrometric Coronagraph (LASCO); the Michelson Doppler Imager (MDI); and the Extreme ultraviolet Imaging Telescope (EIT).

### 2.2.1 LASCO

The LASCO instrument consists of three coronagraphs: C1 (no longer operational), which observed in the range 1.1 to  $3R_{\odot}$ ; C2, which observes from 1.5 to  $6R_{\odot}$ ; C3, which observes from 3.5 to  $30R_{\odot}$ .

Figure 2.18 shows an example of a LASCO C3 image, and clearly shows a CME. The COR instrument on-board STEREO offers similar imaging capabilities and FOV, but has an increased cadence and pixel resolution.

### 2.2.2 MDI

CMEs are often associated with regions of intense magnetic field, called active regions. It can therefore be useful to locate the source region of a CME. A useful way of detecting an active region is through the use of magnetogram data.

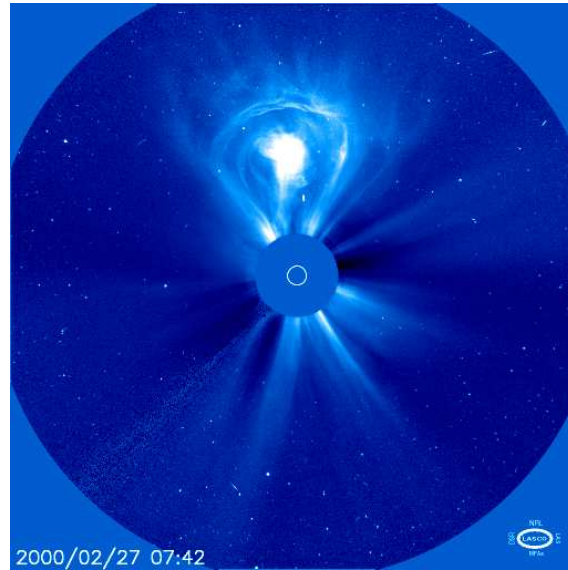


Figure 2.18: Example of a LASCSCO C3 image. A CME is clearly visible.

Magnetograms measure the line-of-sight magnetic field in the solar atmosphere, and are produced by the MDI instrument (Scherrer et al., 1995). This is done by measuring the spectral line splitting, known as the Zeeman effect. In a magnetogram, grey areas indicate regions with closely packed positive and negative small-scale magnetic fields. Black and white areas indicate regions where there is a strong negative and positive magnetic field, respectively. Figure 2.19 shows an example of a magnetogram, where there appears to be two active regions on the solar disk. The dark areas are regions of inwardly directed magnetic field, and the whiter regions are outwardly directed magnetic field.

If an active region is identified as the source region of a particular CME, it can then be used to give Stonyhurst coordinates, for example, for the source region of the CME; a useful tool for the analysis of the close-to-Sun propagation of CMEs.

### 2.2.3 EIT

The EIT (Delaboudinière et al., 1995) provides wide-field images of the solar corona and transition, from the solar disk, to  $1.5R_{\odot}$ . It observes in a range of spectral

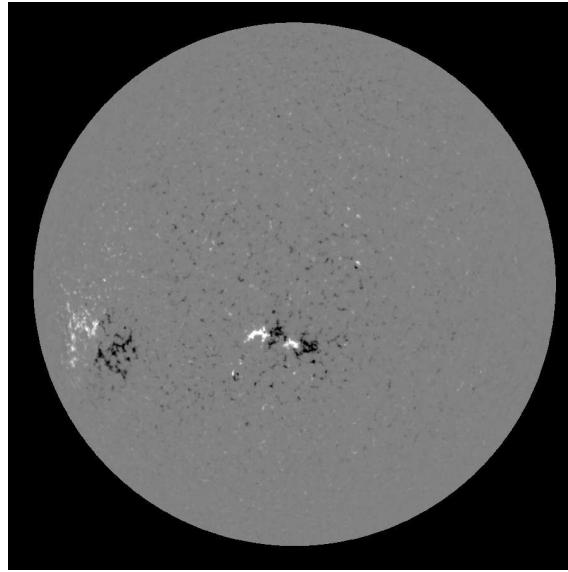


Figure 2.19: Example of an MDI magnetogram.

lines: Fe IX (171 Å); Fe XII (195 Å); Fe XV (284 Å); He II (304 Å), which provide observations in a temperature range of 80,000 - 2,000,000 K (see Table 2.6). The telescope provides a spatial resolution of approximately 5 arcsecs, with a 45x45 arcmin field of view. The EUVI instrument on-board STEREO provides data from the same range of wavelengths, but offers increased cadence and resolution over EIT.

Figure 2.20 shows an EIT image of the Sun (with a large erupting prominence) taken from September 1999, in 304 Å.

## 2.3 OMNI Combined Data

OMNI combined data is a collaboration of near-Earth satellite data, which includes satellites such as the Advanced Composition Explorer (ACE) and WIND. These satellites contain instruments which measure properties of energetic particles near the Earth. The majority of the energetic particles come from the solar wind. If a CME is directed towards Earth, OMNI in-situ measurements of the CME are able to be recorded.

## CHAPTER 2

Table 2.6: From Delaboudinière et al. (1995): EIT Bandpasses

Wavelength	Ion	Peak Temperature	Observational Objective
304 Å	He II	$8.0 \times 10^4$ K	chromospheric network; coronal holes
171 Å	Fe IX-X	$1.3 \times 10^5$ K	corona / transition region boundary; structures inside coronal holes
195 Å	Fe XII	$1.6 \times 10^6$ K	quiet corona outside coronal holes
284 Å	Fe XV	$2.0 \times 10^6$ K	active regions

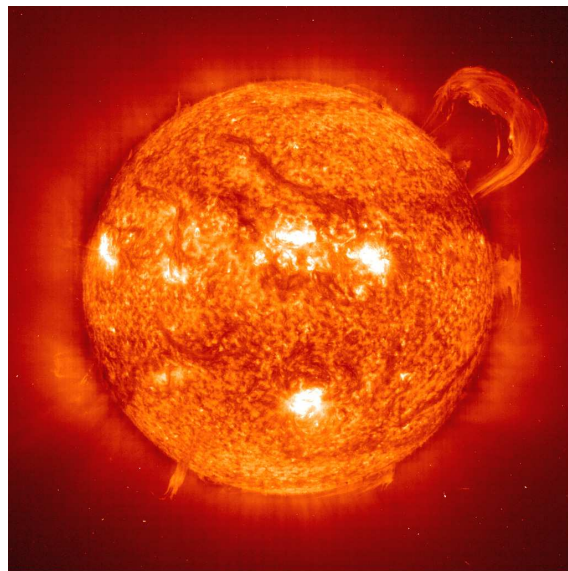


Figure 2.20: Example EIT image of the Sun in 304 Å

## CHAPTER 2

Table 2.7: Key Science Parameters for the TRACE satellite

---

Wavelength	171 Å (Fe IX); 195 Å (Fe XII); 284 Å (Fe XV); 1216 Å (H I); 1550 Å (C IV); 1600 Å (continuum)
Spatial Resolution	1 arc second; 0.5 arc second pixels
Temporal Resolution	< 1 s; 0.5 arc second pixels
Exposure Time	2 ms - 260 s
Field of View	8.5.5 arc minutes

---

### 2.4 TRACE

The Transition Region And Coronal Explorer (TRACE) was launched on the 2nd April 1988 (Strong et al., 1994). It was designed to investigate the relationship between diffusion of the surface magnetic fields and the changes in heating and structure throughout the transition region and corona, by providing high resolution images. Table 2.7 describes the key science parameters, and Figure 2.21 shows an example image of coronal loops, taken by TRACE.

### 2.5 Yohkoh (SXT)

Yohkoh (also known as Sunbeam) is a Japanese satellite that was launched on the 31st August 1991 (Ogawara, 1987). The scientific objective was to observe the energetic phenomena taking place on the Sun, specifically solar flares in X-ray and

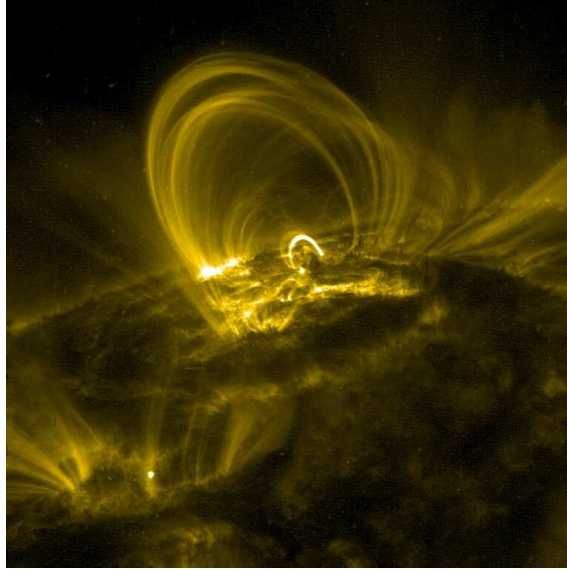


Figure 2.21: Example of a TRACE image, displaying coronal loops at  $171 \text{ \AA}$  gamma-ray emissions, and contains a range of four instruments, including the Soft X-ray Telescope (SXT)

The SXT imaged X-rays in the  $0.25 - 4.0 \text{ keV}$  range. It used thin metallic filters to acquire images in restricted portions of this energy range. Information about the temperature and density of the plasma emitting the observed X-rays was obtained by comparing images acquired with the different filters. Flare images could be obtained every 2 seconds. Smaller images with a single filter could be obtained as frequently as once every 0.5 seconds.

Figure 2.22 shows an SXT image of the solar corona from the 12th November 1991.

## 2.6 Hinode

Hinode (also known as Sunrise) is a Japanese satellite, and was launched on the 22nd September 2006 (Kosugi et al., 2007). It is a follow-on to the Yohkoh mission. Hinode consists of a coordinated set of optical, EUV, and X-ray instruments that

## CHAPTER 2



Figure 2.22: Yohkoh SXT image of the solar corona from the 12th November 1991 11:28:20 UT.

investigates the interaction between the Sun's magnetic field and its corona. In particular, and of interest to the research presented in Chapter 5, it contains the EUV imaging spectrometer (EIS) providing monochromatic images of the transition region and corona at high cadence, and high spectral resolution images. Table 2.8 displays the EIS science parameters.

## CHAPTER 2

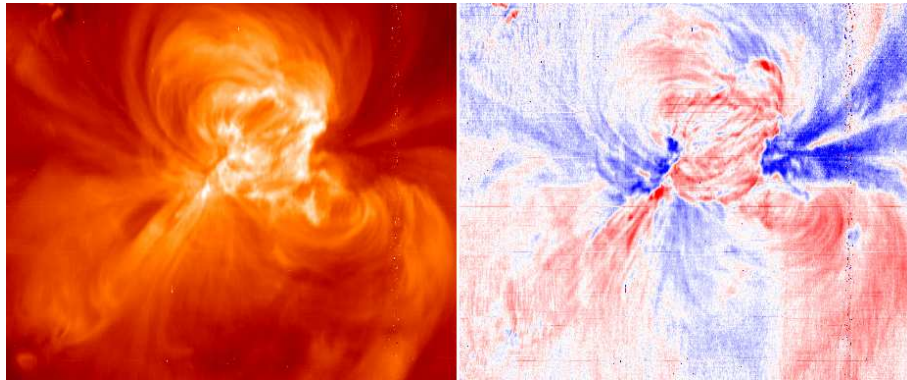


Figure 2.23: Taken from [http : //msslxr.mssl.ucl.ac.uk : 8080/SolarB/Solar – B.jsp](http://msslxr.mssl.ucl.ac.uk:8080/SolarB/Solar-B.jsp): EIS intensity map (left) vs velocity map (right) on the 11th December 2007, of active region coronal loops Credit: K Dere.

Table 2.8: Key Science Parameters for EIS

---

Wavelength Range	170 – 210 Å and 250 – 290 Å
Spatial Resolution	2 arc seconds. Four slit/slot positions are available: 1 and 2 arc second slits; 40 and 266 arc second slots
Velocity Resolution	3 km/s for Doppler velocities; 20 km/s for line widths
Temporal Resolution	In spectroscopy mode: < 1 s in dynamic events ~ 10 s in active regions In imaging mode: monochromatic imaging of an active region ( 4x4 arc min) in 3 s for dynamic events, 10 s otherwise
Field of View	360 × 512 arc seconds

---

## Chapter 3

# The Theory of Coronal Mass Ejections: Initiation and Propagation

As stated in Chapter 1, CMEs are huge eruptions of plasma and magnetic field from the solar corona, and play an important part in the role in space weather. In Chapter 4, we observe and analyse the acceleration and propagation phase of 3 CMEs. Firstly, though, we give a brief overview of the CME initiation models in Section 3.1.

Sheeley et al. (1999) propose two types of CME:

1. impulsive CMEs, which are often associated with a flare, and have speeds in excess of  $750 \text{ km s}^{-1}$ , and are observed to have a constant velocity or decelerate at distances greater than  $2R_{\odot}$
2. gradual CMEs, which appear to form from prominences whose cavities rise up from below coronal streamers (a wisp-like stream of particles travelling through the solar corona), with speeds typically in the range  $400 - 600 \text{ km s}^{-1}$ , and gradual acceleration up to distances of  $30R_{\odot}$

## CHAPTER 3

However, Moon et al. (2004); Vršnak et al. (2005); Zhang et al. (2004), amongst others, provide evidence for the continuity between slow and fast CMEs, thus arguing against the existence of two such distinct CME classes.

Zhang et al. (2001) describes the evolution of a CME in three phases: the initiation; the acceleration; and the propagation phases.

### 3.1 CME Initiation

The subject of how a CME is initiated is a topic of hot debate. There are five major CME models; the thermal blast model, the dynamo model, the mass loading model, the tether release model, and the tether straining model. These are briefly discussed here, with these discussions drawing upon those in Klimchuk (2001) and Aschwanden (2005).

#### Thermal Blast Model

The thermal blast model proposes that the main mechanism for the driving force of a CME is produced by a flare.

In this model the coronal magnetic field is rooted deep in the photosphere, and the thermal pressure force of a resulting flare event destabilises the magnetic field, and the plasma can no longer be contained, and thus a CME is quickly formed and able to propagate into the heliosphere.

Figure 3.1 shows a mechanical analogue to the thermal blast model, where a bomb explosion (i.e. a flare) causes an overpressure, and forces the spring to recoil outwards.

However, many CMEs have been recorded without a flare having occurred, or even where a CME has launched first before a flare has happened, as discovered in Harrison (1986), amongst others.

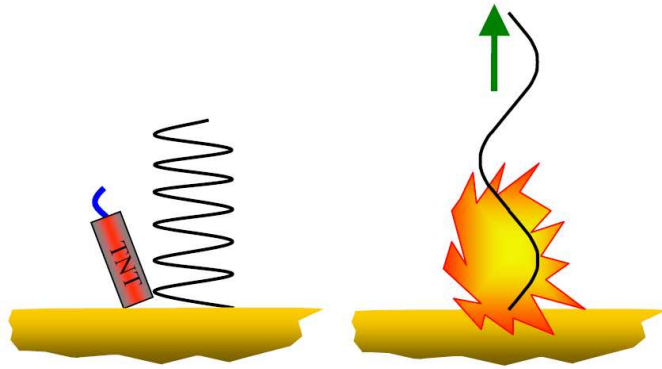


Figure 3.1: Mechanical analogue of the thermal blast model. Figure taken from UCLan course notes.

### Dynamo Model

The dynamo model proposes that the main mechanism of a dynamo-driven CME is due to a rapid generation of magnetic flux by the stressing of the magnetic field. Extra magnetic field is added to the existing field from an external source, such as from the emergence of more magnetic field through the photosphere into an active region. This injection of magnetic flux would therefore increase the strength of the magnetic field, inflating it outwards.

A mechanical analogue is displayed in Figure 3.2, and shows how through some external source, extra tension is added to the spring, stretching the spring outwards.

A theoretical study by Klimchuk (1990) showed that shearing of a coronal loop arcade always leads to an inflation of the entire magnetic field. A fast enough driver would therefore mean it would be possible to produce a CME through this mechanism. In simulations, such as those undertaken in Chen (2001), such a driver mechanism is called a flux injection, which can correspond to either:

1. pre-existing coronal field lines become twisted. However, Krall et al. (2000) show that the required footpoint motion needs to be at least two orders of magnitude faster than what is observed.

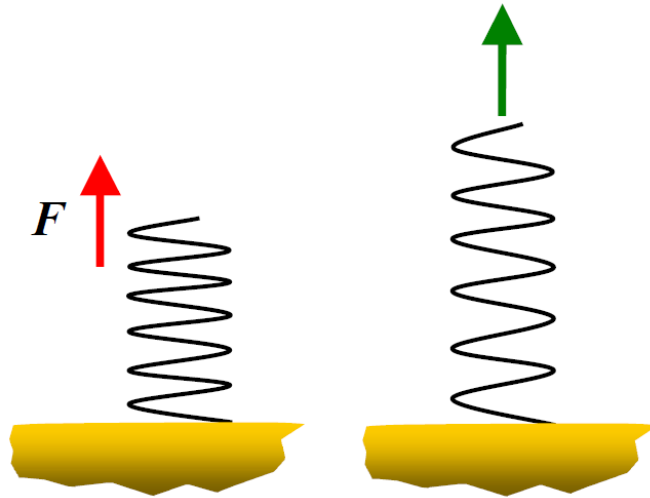


Figure 3.2: Mechanical analogue of the dynamo model. Figure taken from UCLan course notes.

2. new ring-shaped field lines detach from the photosphere and rise upward into the corona. This is unlikely, since the amount of entrained mass has never been observed, whilst there is no obvious force that is known to exist that can lift the mass.
3. new arch-shaped field lines stay anchored in the photosphere and emerge into the corona. This emerging flux is theoretically more plausible, but there are issues arising when trying to match this theory with the observations, and whether or not the required increase in vertical flux through the photosphere can be matched.

### Mass Loading Model

The main mechanism of the mass loading model is the loading of the magnetic field with a large mass, such as a prominence, straining the magnetic field in the process. A magnetic instability can then move (drain) the prominence, and the surrounding field erupts, expelling any remaining prominence material.

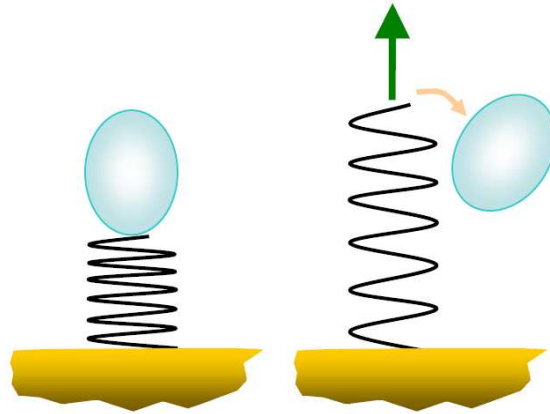


Figure 3.3: Mechanical analogue of the mass loading model. Figure taken from UCLan course notes.

A mechanical analogue is displayed in Figure 3.3, and shows a heavy mass being placed upon the spring, which explosively recoils when this mass is moved to one side.

Theoretical studies, such as Low (1996), Guo and Wu (1998) and Wolfson and Saran (1998), have demonstrated this possible transition from a higher to a lower state, by comparing the total magnetic energy in pre-eruption and post-eruption equilibrium configurations. Mass loading can come in two forms:

1. by prominences, which have a chromospheric temperature, are extremely dense and are contained in a compact volume. This is supported by observations, for example, in Low (1996), with coincident starts of prominence eruptions and CMEs. Zhang and Low (2004) show that the mass of the prominence is crucial.
2. by a relatively higher electron density distributed over a large volume, which is unstable to the Kruskal-Schwarzschild or Rayleigh-Taylor instability, if it overlays a volume of lower density. This is supported by observations of CMEs from helmet streamers, which contain lower density cavities, such as those discussed in Hundhausen (1999). However, there are many examples where

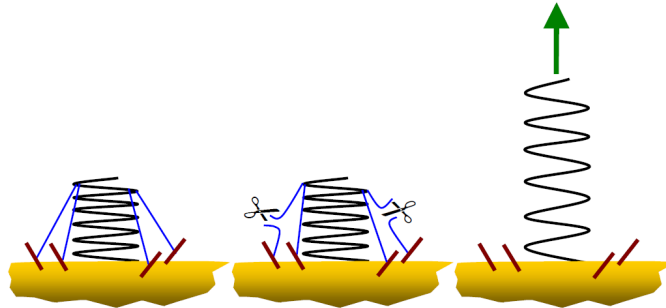


Figure 3.4: Mechanical analogue of the tether release model. Figure taken from UCLan course notes.

this is not the case, with CMEs launching without any signs of internal low-density regions.

### Tether Release Model

The tether release model proposes that the main mechanism is the gradual releasing of magnetic field lines, which are acting as tethers, in a downward-directed force of magnetic tension, and are holding down the upward-directed force of magnetic pressure. Once the tethers are released, one after another, the tension on the remaining tethers increases, until the strain becomes too much, and the remaining tethers start to release. It must be noted, however, that once a pair of field lines become free, they reconnect at a point of contact to produce two new field lines with a different topology from the original pair. Mass plays no significant role.

A mechanical analogue is displayed in Figure 3.4. This shows a spring compressed by tethers, and as each tether is cut, the tension on the remaining tethers increases, until all the tethers have broken, and the spring is allowed to recoil outwards.

The 2.5-D translationally-symmetric model of Forbes and Isenberg (1991) is an example of a tether release model, which consists of an infinitely long flux rope and an overlying arcade. The arcade field lines act as tethers and thus prevent the flux rope from rising. By converging flow in the photosphere, the opposite

## CHAPTER 3

magnetic polarity foot points are slowly brought together, and when they meet at the neutral line, they reconnect to form a short loop between the nearest foot points, which may submerge, and a long helical field line which is disconnected from the photosphere, as shown in Figure 3.5. In this model, there is a transition through a sequence of equilibria, which is driven by converging footpoint motion, until there is a sudden loss of equilibrium, and the X-point jumps discontinuously upward into a new equilibrium position. During this loss-of-equilibrium stage, a break-off of the tethers would result (in a non-ideal MHD situation), resulting in the launch of a CME (eg. Amari et al., 2000)

For a full eruption, however, the reconnection necessary has an important observational consequence, producing closed loops below the erupting flux rope. However, in many examples, only post-eruption arcades are observed.

### **Tether Straining Model**

The tether straining model is a slight adaptation to the tether release model. In the tether release model, the force upon the tethers remains approximately constant, but this force becomes distributed to fewer and fewer tethers, as the tethers break. However, in the tether straining model, the number of tethers remains the same, but the total stress increases, until the tethers eventually break.

A mechanical analogue is displayed in Figure 3.6. Here a spring is held on a platform, and is held down by the tethers. As the platform is gradually raised, the strain on the tethers increases, until they finally break.

### **Magnetic Breakout Model**

The magnetic breakout model of Antiochos et al. (1999) is one such physical model of tether straining, and is described by Figure 3.7, where there are four distinct flux systems which are quadrupolar in nature. The blue lines indicate the central

## CHAPTER 3

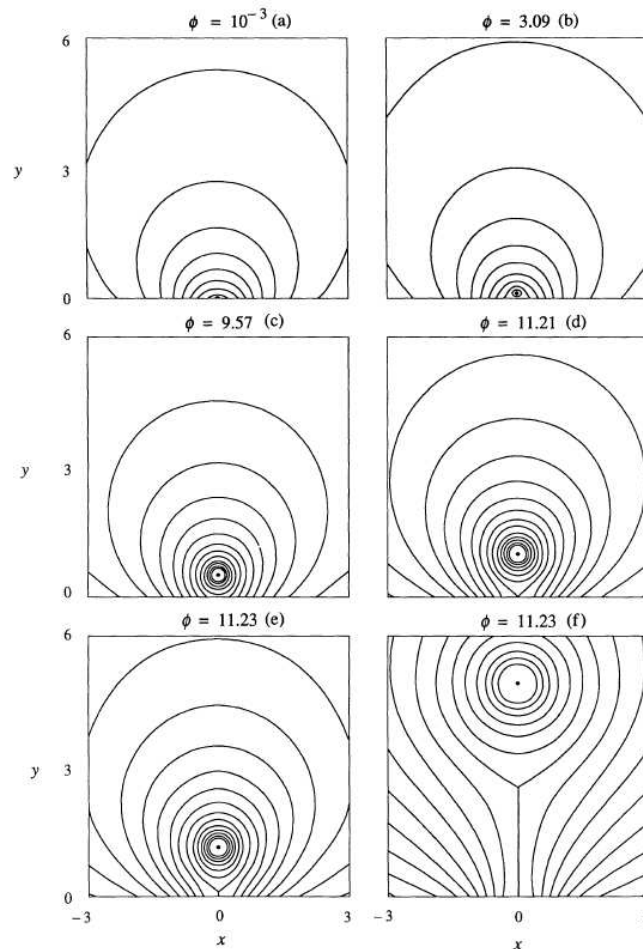


Figure 3.5: From Forbes and Isenberg (1991): Contours of the vector potential for the normalised filament radius of  $10^{-5}$ . The six different configurations shown correspond to different locations on the equilibrium curve. The contour levels are not the same for all panels, and the field lines near the current filament are omitted. The parameter  $\phi$  is the flux between the filament and the base. In (a) the dipole background field completely dominates. Reconnection in the photosphere causes  $\phi$  to continually increase in (b) and (c), and this increase eventually leads to the formation of a neutral line in (d) and a current sheet in (e). However, when  $\phi$  reaches 11.23, the equilibrium height jumps discontinuously from  $h = 1, 1$  to  $h = 4.90$ , as shown in (e) and (f).

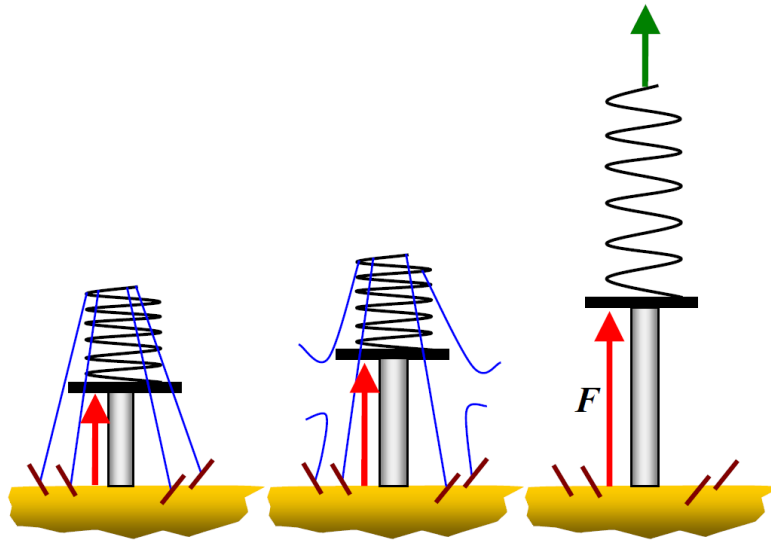


Figure 3.6: Mechanical analogue of the tether straining model. Figure taken from UCLan course notes.

arcade, the red is the overlying field, and the green are two side arcades. Near to the equator, shearing motions stretch the inner field lines of the central arcade in an east-west direction, as shown by the thicker blue lines, which could be associated with a prominence. The core of the central arcade inflates as a result of enhanced magnetic pressure due to the shear. The overlying field and unshered central arcade help to counter this effect. However, as the system becomes gradually more and more stressed, the magnetic X-point above the central arcade distorts, and forms a horizontal region of enhanced electric current. As the stress keeps building, and the current layer becomes thinner, the adjacent overlying field and central arcade field lines reconnect to form side arcades which pull away from the X-point, resulting in fewer tethers. This causes the central arcade to bulge, and so an eruption ensues.

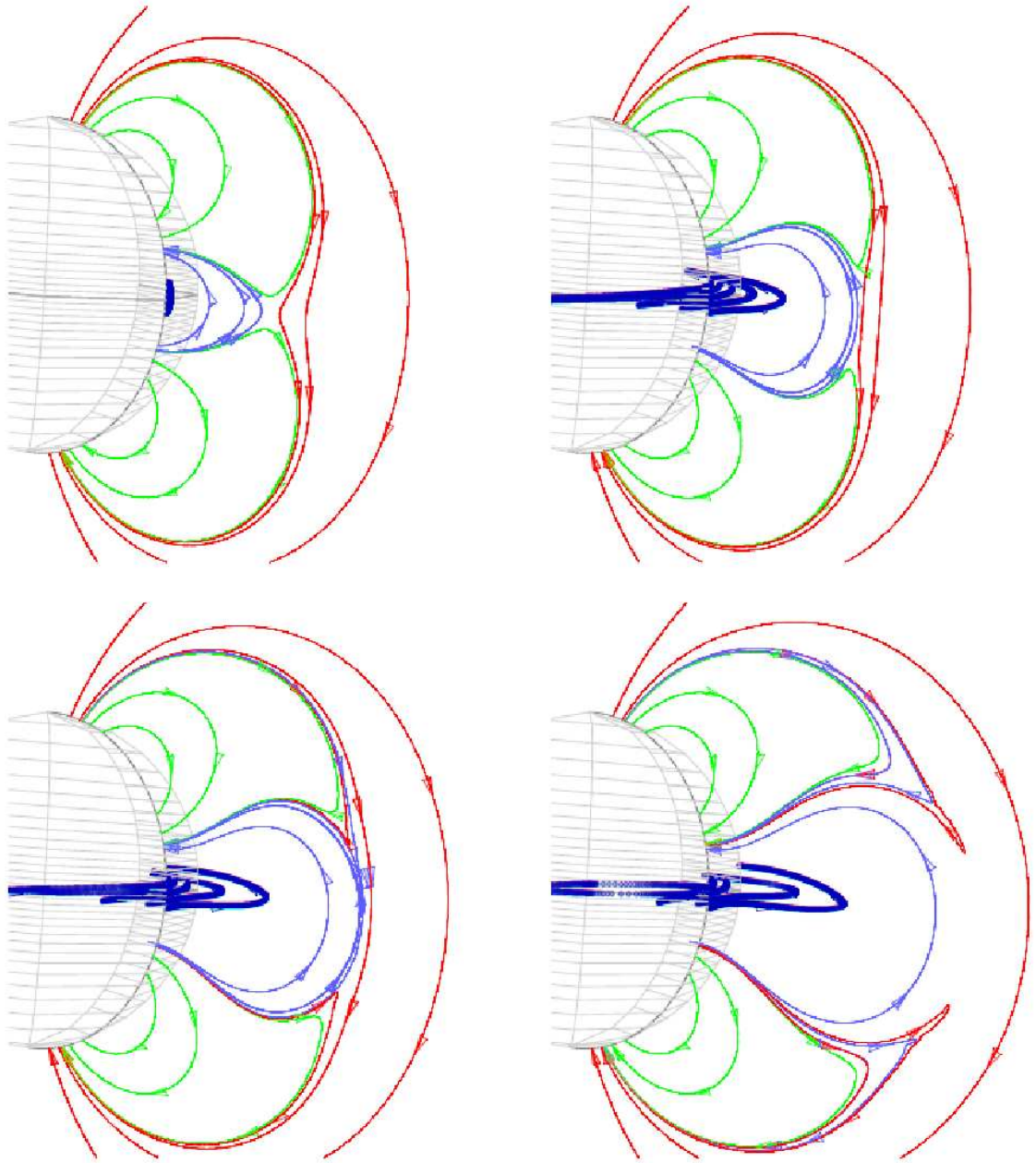


Figure 3.7: Magnetic breakout model showing the evolution of a quadrupolar system in which the inner part of the central arcade are sheared by antiparallel footpoint motions near the neutral line (equator). The field bulges slowly, until the red and blue field lines begin to reconnect, and a runaway eruption ensues (Klimchuk, 2001)

## CHAPTER 3

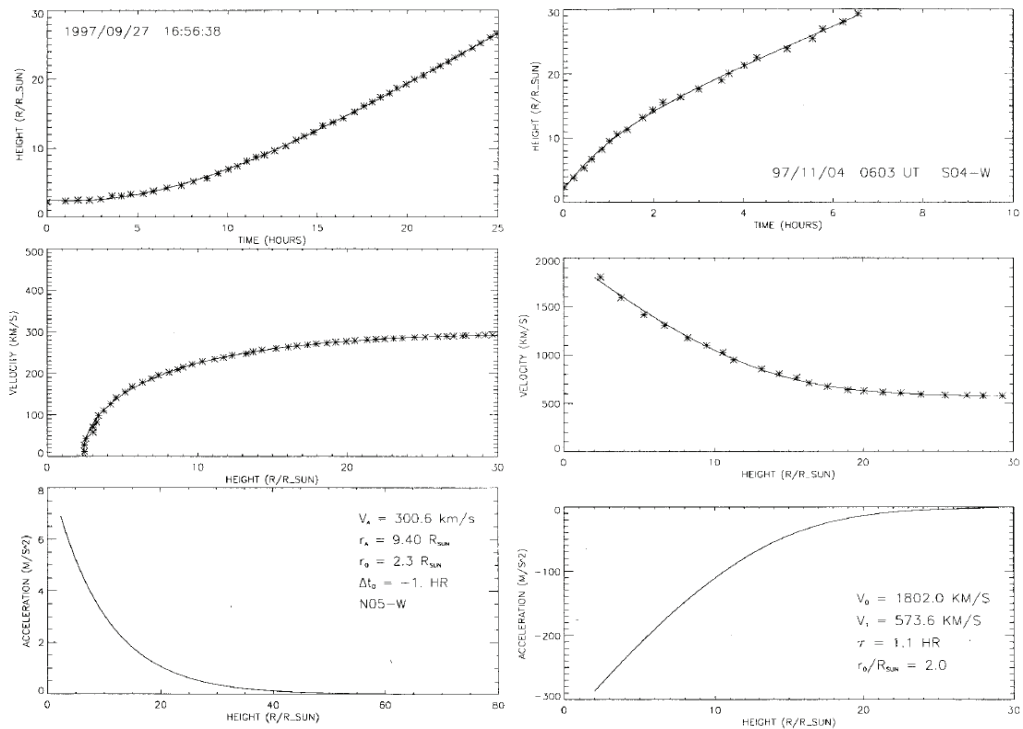


Figure 3.8: From Sheeley et al. (1999): Height-time plot (top), velocity (middle) and acceleration profiles (bottom) shown for the two different classes of CME: gradual CME (left), and an impulsive CME (right), taken from C2 and C3 LASCO observations.

### 3.2 CME Acceleration and Propagation

By calculating the height, velocity and acceleration profiles of a CME, it may be possible to shed some light upon the drivers of a CME, and it is the acceleration phase which can help do this. By calculating when the acceleration phase ends (when the CME is no longer experiencing any acceleration), this will indicate at what height range the acceleration forces operate. Figure 3.8 attempts to show this, and suggests that the acceleration profile of a CME can be approximated by either an exponentially increasing or decreasing function.

Liu et al. (2010) report that all CMEs should undergo a west-ward deflection during their acceleration phase. This westward motion can be explained by the

## CHAPTER 3

magnetic field connection the Sun and the CMEs. The magnetic field is frozen in the CME plasma, and so the Sun and CME are coupled together by the magnetic field, out to a distance. Therefore, the westward deflection of CMEs is caused by the rotation of the Sun when the motion of CMEs is still heavily influenced by the magnetic field. The force is known as the Lorentz force. The distance at which this occurs is known as the Alfvén radius, and is found to occur at distances of  $10 - 20R_{\odot}$ .

In terms of latitudinal deflections, Gopalswamy et al. (2003) and Byrne et al. (2010) report that CMEs experience a deflection from high latitude source regions, into regions of lower latitude, particularly during solar minimum. This has been attributed to the magnetic field from polar coronal holes guiding the CMEs towards the equator, although other models may indicate otherwise. For example, Cremades and Bothmer (2004) show that the internal configuration of the erupting flux rope will determine where magnetic reconnection is more likely to occur, thus having a significant effect on its propagation through the corona. The magnetic configuration will therefore guide the CME towards the equator or towards the pole.

Once a CME leaves the acceleration phase (if indeed it actually does), it then enters the propagation phase. During the propagation phase one important question is left to be answered: does a CME travel in a constant direction, or will it be affected by the interplanetary magnetic field (IMF)?

The IMF is defined by the flow of the solar wind between the planets near the ecliptic plane, and has the form of a spiral shape, as defined in Parker (1958), and this is displayed in Figure 3.9. The resulting spirals cross the orbit of the Earth at an angle  $\approx 45^{\circ}$ .

Measurements of the magnetic field direction at Earth orbit reveal a four-sector pattern during solar minimum, and a two-sector pattern during the period of declining solar activity, with oppositely directed magnetic field vectors in each sector.

CHAPTER 3

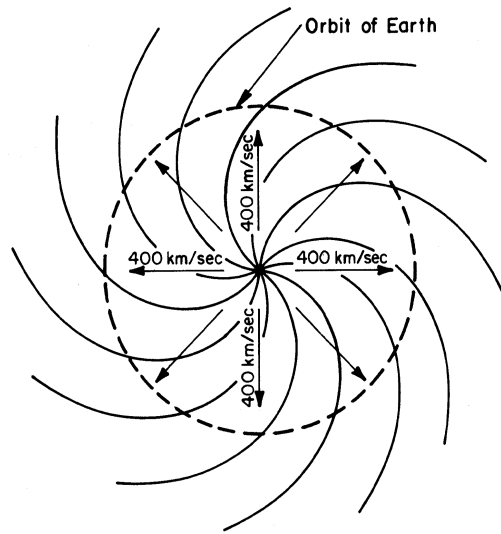


Figure 3.9: From Kivelson and Russell (1995): A sketch of the Parker spiral configuration of the IMF. The footpoints of the field lines stay attached to the Sun, and the field lines and plasma are carried away from the Sun, and are wound into a spiral by the Sun's rotation.

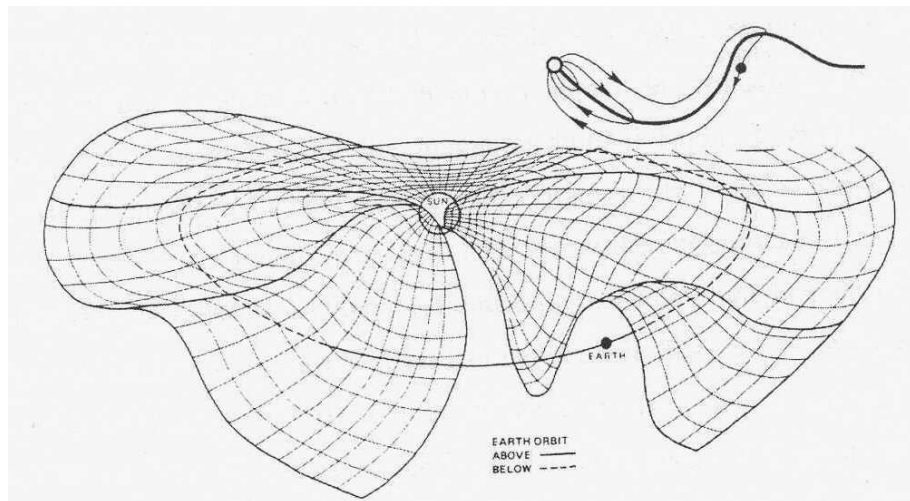


Figure 3.10: From Kivelson and Russell (1995): Current sheet in the inner heliosphere where the effect of the tilt of the solar magnetic axis with respect to the rotation axis produces the “ballerina skirt” effect.

## CHAPTER 3

Figure 3.10 shows an ecliptic cut of the warped heliospheric current sheet, which shows the shape to be like a ballerina skirt. The strength of the IMF depends on the solar cycle, where the IMF is stronger during solar maximum, and weakest during solar minimum.

The IMF can be heavily disturbed by CMEs propagating into the heliosphere. However, it is not well understood how the IMF affects the propagation of a CME.

Wang et al. (2004) provide evidence for the longitudinal deflection of CMEs in the IMF. Figure 3.11 displays a schematic diagram showing how slow CMEs (where a slow CME is a CME propagating at speeds slower than the solar wind) can be expected to experience a west-ward deflection. Conversely, a fast CME (where a fast CME is a CME travelling at speeds faster than the solar wind) can be expected to experience an east-ward deflection. Figure 3.12 shows the predicted deflection angle for a CME as a function of the CME's speed.

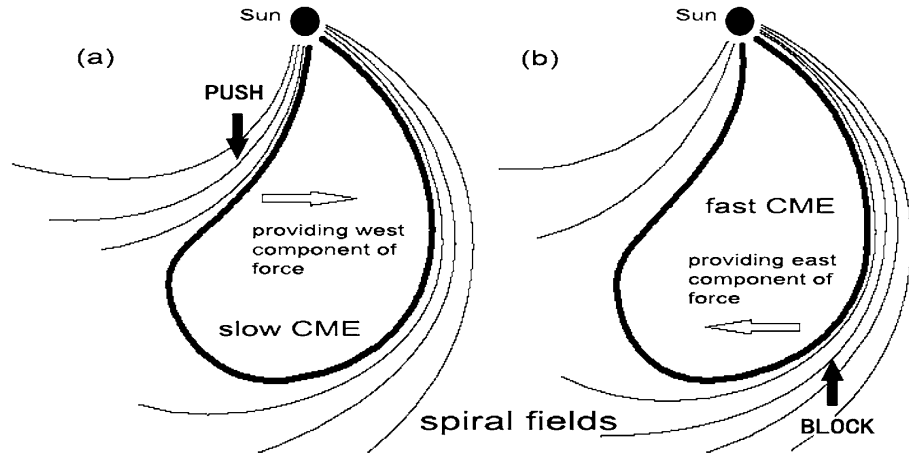


Figure 3.11: From Wang et al. (2004): Schematic pictures of (a) slow and (b) fast CME propagation in the interplanetary medium.

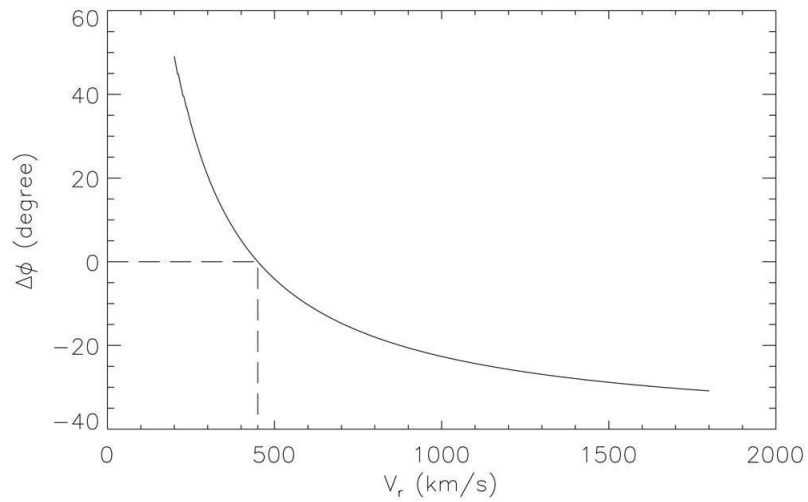


Figure 3.12: From Wang et al. (2004): The deflection angle ( $\delta\phi$ ) in the ecliptic plane at 1 AU versus the radial speed ( $V_r$ ) of CMEs.

# Chapter 4

## STEREO Observations of Coronal Mass Ejections

### 4.1 CME Observations

The SECCHI data was calibrated using *secchi\_prep.pro* from the SolarSoft library (Freeland and Handy, 1998). The COR-1 and COR-2 data was further reduced by taking three polarized brightness images for each particular time stamp and creating a single, total brightness image. This was done by using the keyword *polariz\_on* within *secchi\_prep.pro*. Also, for COR-2, the “img” files were used, as well as the total brightness images. A standard running difference technique was employed for the EUVI, COR-1 and COR-2 data sets only, such that the previous image is subtracted from the current image. Where the image appears black or dark grey implies a reduction of intensity with respect to the previous image. Conversely, white and light grey areas show an increase in intensity. A somewhat modified running difference technique was used with the HI data, in which the contribution from the background star-field was reduced (as discussed by Davies et al. 2009). A star will move approximately one pixel to the right, in each subsequent HI image.

## CHAPTER 4

Therefore, the modified running difference technique takes this account, and shifts each image to be subtracted by one pixel to the left. The pointing calibration of Brown et al. (2009) was used to provide the accurate pointing information necessary to perform a successful star-field removal.

### 4.1.1 Solar Coordinate Systems

There are many different coordinate systems employed throughout the fields of solar and space physics, so it is important to understand and use the most suitable one for the task at hand. Throughout this thesis, angles are presented in Stonyhurst coordinates, but the conversion from pixel coordinates from the observations into Stonyhurst coordinates is not a trivial matter, and this is discussed in Section 4.1.2.

#### Heliocentric Cartesian Coordinates

Heliocentric Cartesian coordinates  $(x,y,z)$  provide the spatial position of a feature in physical units from the centre of the Sun. In this coordinate system, the y-axis is defined along the central meridian, pointing towards the north-pole. The z-axis runs along the Sun-observer line, pointing towards the observer, whilst the x-axis is perpendicular to both the y and z-axis, pointing towards the western limb. This is displayed in Figure 4.1 (left).

Heliocentric Earth Equatorial (HEEQ) coordinates are an example of heliocentric Cartesian coordinates. In this coordinate system, the y-axis lies along the solar equatorial plane, pointing towards the western limb. The z-axis lies along the central meridian as seen from Earth, pointing towards the north-pole, and the x-axis is perpendicular to the y and z-axis, pointing towards the observer. Figure 4.2 (left, top-right panels) displays the location of the Sun, Earth and STEREO satellites on the 24th October 2008 in HEEQ coordinates.

Stonyhurst coordinates are the spherical polar equivalent of HEEQ, and are

## CHAPTER 4

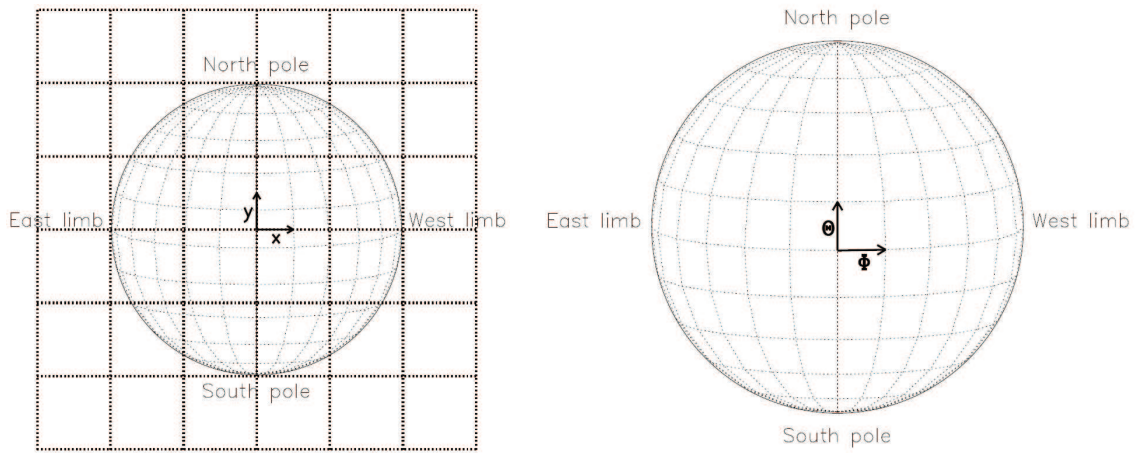


Figure 4.1: From Thompson (2006): Left - A diagram of the Sun, with lines of constant heliocentric Cartesian position ( $x$ ;  $y$ ) overlaid. The  $z$  axis points out of the page. Right - A diagram of the Sun, showing lines of constant Stonyhurst heliographic longitude and latitude on the solar disk. The origin of the coordinate system is at the intersection of the solar equator and the (terrestrial) observers central meridian. This representation is also known as a Stonyhurst grid.

displayed in Figure 4.1 (right). Angles are given in terms of Stonyhurst longitude ( $\Phi$ ) and latitude ( $\Theta$ ).

Figure 4.2 (bottom-right panel) displays the location of the Sun and Earth in X-Z heliocentric Earth ecliptic (HEE) coordinates. In this coordinate system, the X-axis lies along the Sun-Earth line, pointing towards the Earth. The Z-axis points towards ecliptic north, and the Y-axis lies along the ecliptic plane, as seen from Earth.

### Heliocentric Radial Coordinates

An alternative to the Cartesian coordinate system is the heliocentric-radial (HCR) system. Position angle ( $\psi$ ) is measured in degrees, anti-clockwise from the projection of the north-pole. The  $z$ -axis points towards the observer, and  $\rho$  is a measure of radial distance from the  $z$ -axis. This is displayed in Figure 4.3.

## CHAPTER 4

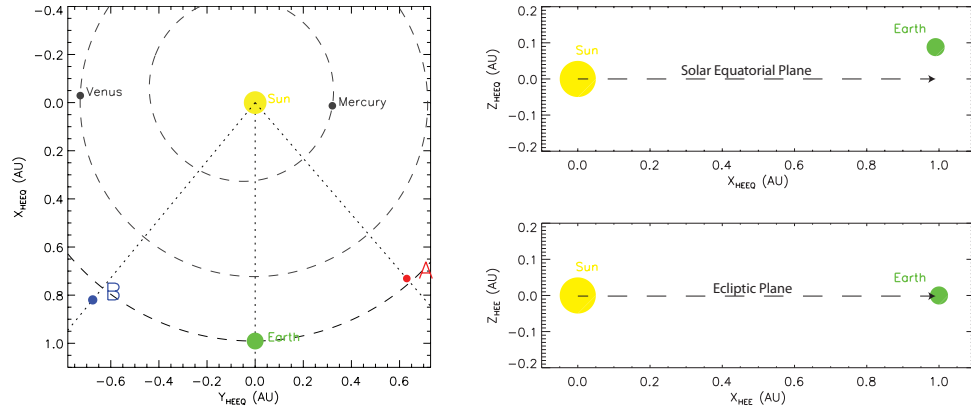


Figure 4.2: Figure displaying the positions of the Sun, Earth and STEREO satellites on the 24th October 2008. The HEEQ Y-X (left) and X-Z (top-right) positions are displayed, along with the X-Z HEE positions of the Earth and Sun (bottom-right).

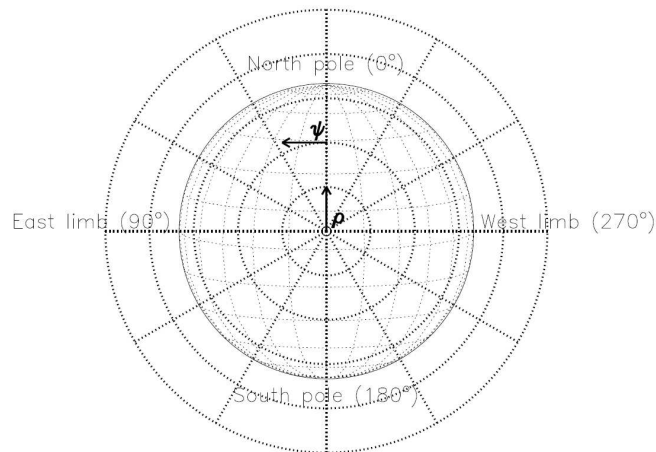


Figure 4.3: A diagram of the Sun demonstrating heliocentric-radial coordinates, with lines of constant impact parameter ( $\rho$ ) and position angle ( $\psi$ ) overlaid. The value of  $\psi$  at each of the four compass points is also shown. The z axis points out of the page.

## CHAPTER 4

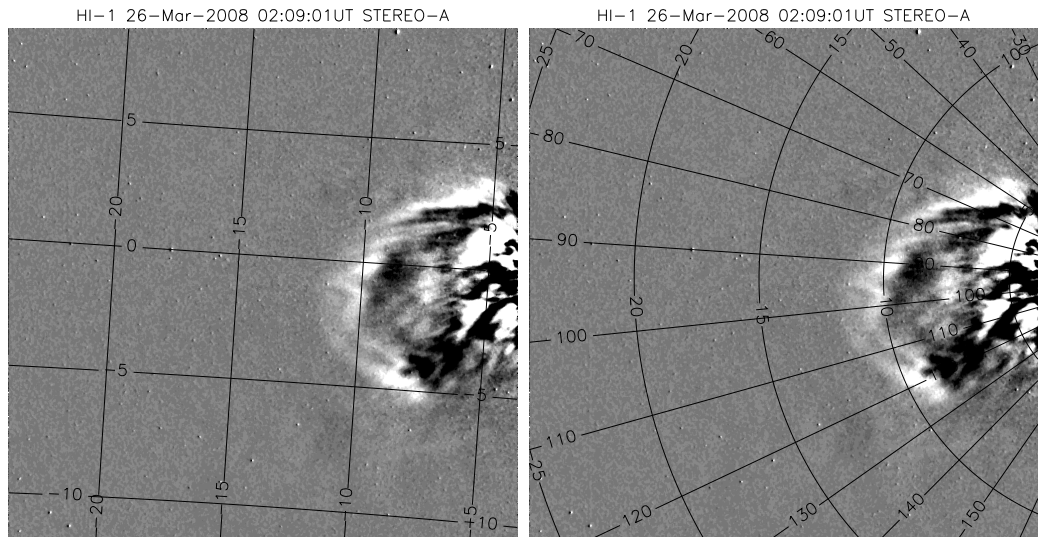


Figure 4.4: HI-1A image with HPC (left) and HPR (right) contours

### Helioprojective Coordinates

If only two of the positions  $(x,y)$  are known, then projected coordinates are more suitable. In helioprojected coordinate systems, the origin is located at the observer, with the  $z$ -axis along the Sun-observer line. The projective equivalent of heliocentric Cartesian coordinates, are helioprojected Cartesian coordinates (HPC). The distance parameters  $(x,y)$  are replaced by the angles  $\theta_x$  (which is HPC longitude), and  $\theta_y$  (which is HPC latitude), respectively. Figure 4.4 (left) shows contours of HPC overlaid.

The projected equivalent of HCR is helioprojective-radial (HPR) coordinates.  $\rho$  is replaced by  $\theta_p$ , and is a measure of angular distance from Sun-centre (by the observer), also known as elongation. Constant values of  $\theta_p$  are shown in Figure 4.4 (right) as the ( $\sim$ ) circles.  $\psi$  is a measure of position angle, which is shown in Figure 4.4 (right) as the radial lines, originating from Sun-centre.  $\psi$  is measured anti-clockwise from the projection of the north-pole.

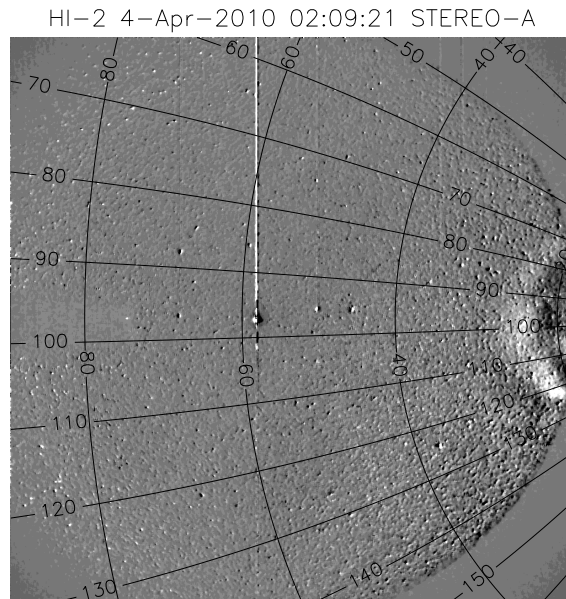


Figure 4.5: HI-2A image, highlighting the spherical nature of the observations.

### 4.1.2 Geometry

It is important to fully understand the 3-dimensional nature of the STEREO observations undertaken. When observing features close to the Sun, projection effects are minimal, and plane-of-sky assumptions are often made. However, when dealing with the propagation of CMEs into the heliosphere, and in particular, using HI observations, plane-of-sky assumptions no longer hold. Figure 4.5 shows how, for example, constant lines of PA are not straight lines; this is mainly due to the spherical nature of the coordinate system. Therefore, full 3-D angles must be calculated in order to derive solar transient properties. HI observations are spherically projected, and so when converting from pixel coordinates into solar coordinates, such as the Stonyhurst coordinate system, this needs to be accounted for. This is done with use of the FITS World Coordinate System (WCS), as discussed in Thompson and Wei (2010).

EUVI, COR-1 and COR-2 pixels are converted into WCS coordinates via a multi-step process. The simplest spherical projection is the TAN (also known as Gnomonic

## CHAPTER 4

projection) projection, which is where the pixel position scales as the tangent of the angle away from a central reference point. Firstly, pixel coordinates are transformed into a measure of distance (eg. degrees), and thus into intermediate coordinates (Maloney et al., 2009), given by

$$x_i = s_i \sum_{j=1}^N m_{ij} (p_j - r_j) \quad (4.1)$$

where  $r_j$  is the reference pixel,  $m_{ij}$  is a linear transformation matrix,  $p_j$  are the pixel coordinates, and  $s_i$  is a scale function, where  $i$  refers to pixel axes and  $j$  refers to coordinate axes. To convert to Helioprojective-Cartesian (HPC) coordinates (where  $\theta_x$  is HPC longitude, and  $\theta_y$  is HPC latitude), a reference coordinate,  $c_i$  is introduced into the intermediate coordinates, such that  $x_i = x_i + c_i$ , where ( $x_0 = \theta_x$  and  $x_1 = \theta_y$ ). The HPC coordinate system can thus be described as

$$\theta_x \approx \left( \frac{180^\circ}{\pi} \right) \frac{x}{D_\odot} \approx \left( \frac{180^\circ}{\pi} \right) \frac{x}{d} \quad (4.2)$$

$$\theta_y \approx \left( \frac{180^\circ}{\pi} \right) \frac{y}{D_\odot} \approx \left( \frac{180^\circ}{\pi} \right) \frac{y}{d} \quad (4.3)$$

where  $d$  is the observer-feature distance, and  $D_\odot$  is the Sun-observer distance.

However, when observing out to much larger distances, the TAN projection is insufficient to properly describe the coordinates. The transformation of pixel coordinates into HPC coordinates for HI images is more complicated, and relies on the azimuthal (or zenithal) perspective (AZP) projection, where an additional parameter,  $\mu$ , measuring the distortion, or the deviation away from TAN is introduced. To convert from pixel coordinates, into HPC, the pixel coordinates are converted into intermediate coordinates as described by Equation 4.1, and then by the following (Maloney et al., 2009):

$$\phi = \tan^{-1}(x/y - \cos(\gamma)) \quad (4.4)$$

$$\theta = \begin{cases} \psi - \omega \\ \psi + \omega + 180^\circ \end{cases} \quad (4.5)$$

## CHAPTER 4

where

$$\psi = \tan^{-1}(1/\rho) \quad (4.6)$$

$$\omega = \sin^{-1}\left(\frac{\rho\mu}{\sqrt{\rho^2 + 1}}\right) \quad (4.7)$$

$$\rho = \frac{R}{\frac{180^\circ}{\pi}(\mu + 1) + y \sin(\gamma)} \quad (4.8)$$

$$R = \sqrt{x^2 + (y \cos(\gamma))^2} \quad (4.9)$$

where  $\gamma$  is the look-angle. Once  $\theta$  and  $\phi$  are calculated, they can then be rotated into HPC. This can be done by converting each SECCHI header into a WCS (Thompson, 2006) structure with the use of *fitshead2wcs.pro*. Using this WCS structure, together with the pixel positions, one is able to use *wcs\_get\_coord.pro* to convert the pixel position into HPC coordinates easily. The conversion into HPR coordinates is obtained through Equations 4.10 and 4.11.

$$\theta_p = \arg\left(\cos \theta_y \cos \theta_x, \sqrt{\cos^2 \theta_y \sin^2 \theta_x + \sin^2 \theta_y}\right) \quad (4.10)$$

$$\psi = \arg(\sin \theta_y, -\cos \theta_y \sin \theta_x) \quad (4.11)$$

$$\text{where } \arg(x, y) = \begin{cases} \tan^{-1}(y/x), & \text{if } x > 0 \\ \pi + \tan^{-1}(y/x), & \text{if } x < 0 \text{ and } y \geq 0 \\ \tan^{-1}(y/x) - \pi, & \text{if } x < 0 \text{ and } y < 0 \\ \pi/2, & \text{if } x = 0 \text{ and } y > 0 \\ -\pi/2, & \text{if } x = 0 \text{ and } y < 0 \\ \text{undefined,} & \text{if } x = 0 \text{ and } y = 0 \end{cases}$$

However, in order to calculate the full 3-D position of the CME, we need a further

## CHAPTER 4

parameter;  $d$ .

$$d = \frac{D_{\odot} \sin \beta}{\sin (\beta + \theta_p)} \quad (4.12)$$

where  $d$  is the distance from the observer to the leading edge. The angle  $\beta$  is the angle between the transient and the Sun-observer line, and is a convolution of Stonyhurst longitude difference ( $\Phi_D$ ), latitude ( $\Theta$ ) and the heliographic latitude of the observer ( $B_0$ ), where  $\Phi_D$  is the Stonyhurst longitude difference between the observer and the leading edge (Rouillard et al., 2009) .

$$\sin^2 \beta = \cos^2 \Theta \sin^2 \Phi_D + [\sin \Theta \cos B_0 - \cos \Theta \cos \Phi_D \sin B_0]^2 \quad (4.13)$$

It is also possible to directly calculate the position angle (PA or  $\psi$ ) from the heliographic latitude and longitude difference of the leading edge and heliographic latitude of the observer (Rouillard et al., 2009)

$$\psi = \arg (\sin \Theta \cos B_0 - \cos \Theta \cos \Phi_D \sin B_0, \cos \Theta \sin \Phi_D) \quad (4.14)$$

Solutions to Equations 4.13 and 4.14, are given by Equations 4.15 and 4.16.

$$\Theta = \sin^{-1} (\cos B_0 \cos \delta \cos \psi + \sin B_0 \sin \delta) \quad (4.15)$$

$$\Phi_D = \arg (\cos B_0 \sin \delta - \cos \delta \cos \psi \sin B_0, \sin \psi \cos \delta) \quad (4.16)$$

where  $\delta$  is the angle of the transient out of the sky plane, as seen by the observer. If the transient is travelling in the plane of the sky, in relation to the observer, then  $\delta = 0^\circ$ . For  $\delta = 90^\circ$ , this indicates the transient is travelling directly towards the observer, and conversely, for  $\delta = -90^\circ$ , the transient is travelling directly away from the observer.

The conversion from Stonyhurst longitude and latitude into HEEQ is then given by Thompson (2006):

$$X_{HEEQ} = r \cos \Theta \cos \Phi \quad (4.17)$$

## CHAPTER 4

$$Y_{HEEQ} = r \cos \Theta \sin \Phi \quad (4.18)$$

$$Z_{HEEQ} = r \sin \Theta \quad (4.19)$$

where  $r$  is the radial distance from Sun-centre, and can be derived by:

$$r = \frac{D_{\odot} \sin \theta_p}{\sin(\theta_p + \beta)} \quad (4.20)$$

The conversion back in Stonyhurst coordinates from HEEQ is thus given by Thompson (2006):

$$\Theta = \tan^{-1} \left( Z_{HEEQ} / \sqrt{X_{HEEQ}^2 + Y_{HEEQ}^2} \right) \quad (4.21)$$

$$\Phi = \arg(X_{HEEQ}, Y_{HEEQ}) \quad (4.22)$$

$$r = \sqrt{X_{HEEQ}^2 + Y_{HEEQ}^2 + Z_{HEEQ}^2} \quad (4.23)$$

### Coordinate Transformation

Due to the dynamic nature of the solar system, and the many different sun-centred coordinate systems in use, it is essential that when comparing similar work, that one must be able to directly compare one set of results to another. If the coordinate systems differ, then it is necessary to rotate the coordinate systems accordingly. Since the results presented in this work use HEEQ coordinates, we describe how to transform from HEEQ into other solar coordinate systems, such as Heliocentric Earth Ecliptic (HEE), by using the 3-D rotation matrices in Equations 4.24 to 4.29

$$R_x = \begin{bmatrix} 1 & 0 & 0 \\ 0 & \cos a & -\sin a \\ 0 & \sin a & \cos a \end{bmatrix} \quad (4.24)$$

CHAPTER 4

$$R_y = \begin{bmatrix} \cos b & 0 & \sin b \\ 0 & 1 & 0 \\ -\sin b & 0 & \cos b \end{bmatrix} \quad (4.25)$$

$$R_z = \begin{bmatrix} \cos c & -\sin c & 0 \\ \sin c & \cos c & 0 \\ 0 & 0 & 1 \end{bmatrix} \quad (4.26)$$

These matrices represent anti-clockwise rotations of an object relative to fixed coordinate axes, by an angle of  $a, b$  and  $c$ .  $R_x$  rotates the  $Z_{HEEQ}$  axis towards the  $X_{HEEQ}$  axis (where  $a$  represents the latitudinal rotation),  $R_y$  rotates the  $X_{HEEQ}$  axis towards the  $Y_{HEEQ}$  axis (where  $b$  represents the longitudinal rotation), and  $R_z$  rotates the  $Y_{HEEQ}$  axis towards the  $Z_{HEEQ}$  axis (where  $c$  represents the roll-angle rotation).

Finally, to put into the HEE coordinate system, for example, we use Equations 4.27 - 4.29 to rotate the system accordingly. Information on the position of the spacecraft is held in the WCS structure file.

$$\mathbf{A} = R_z R_y R_x \quad (4.27)$$

$$\mathbf{v} = \begin{bmatrix} X_{HEEQ} \\ Y_{HEEQ} \\ Z_{HEEQ} \end{bmatrix} \quad (4.28)$$

$$\mathbf{v}_{new} = \mathbf{A}\mathbf{v} \quad (4.29)$$

where  $\mathbf{v}_{new} = \begin{bmatrix} X_{HEE} & Y_{HEE} & Z_{HEE} \end{bmatrix}^T$ .

### 4.1.3 Stereoscopic Triangulation

The STEREO spacecraft gives us a unique opportunity to observe solar phenomena from two separate vantage points. As a result of this, it is possible to stereoscopically triangulate a solar feature, such as the leading edge of a CME, to give its full 3-D coordinates. This section relies heavily on the work presented in Aschwanden et al. (2008).

Firstly, it is practical to co-align the image pair. This is done by co-aligning, rescaling, and rotating the images, into the STEREO spacecraft-plane, which is defined by the positions of the two spacecraft and Sun-centre, using the information stored within the SECCHI header structure files of each image. Each image is centred on Sun-centre, and the pixels are rebinned to an equal size, which is dependent on the distance of each spacecraft from the Sun ( $1/D_{\odot}$ ). The images are then rotated by the spacecraft roll angles into the plane defined by the STEREO spacecraft and Sun centre.

The separation angle between the two spacecraft ( $\alpha_{sep}$ ) can also be derived from the heliographic longitudes and latitudes:

$$\alpha_{sep} = \cos^{-1} [\cos(l_A - l_B) \cos(b_A - b_B)] \quad (4.30)$$

Once the image-pair are properly co-aligned, it is possible to obtain the 3-D position of a solar feature through stereoscopic triangulation, also known as tie-pointing.

A coordinate system that has an origin  $O$  at Sun centre, a Z-axis which is the line of sight from STEREO-A to Sun centre, an X-Z plane which is the plane of the two spacecraft (as shown in Figure 4.6) is defined as  $(X, Y, Z)$ .

The point  $P$  has 3-D coordinates  $(x, y, z)$ , or heliographic longitude  $\gamma$  and latitude difference  $b$ , with respect to the central meridian defined by the line-of-sight from STEREO-A.

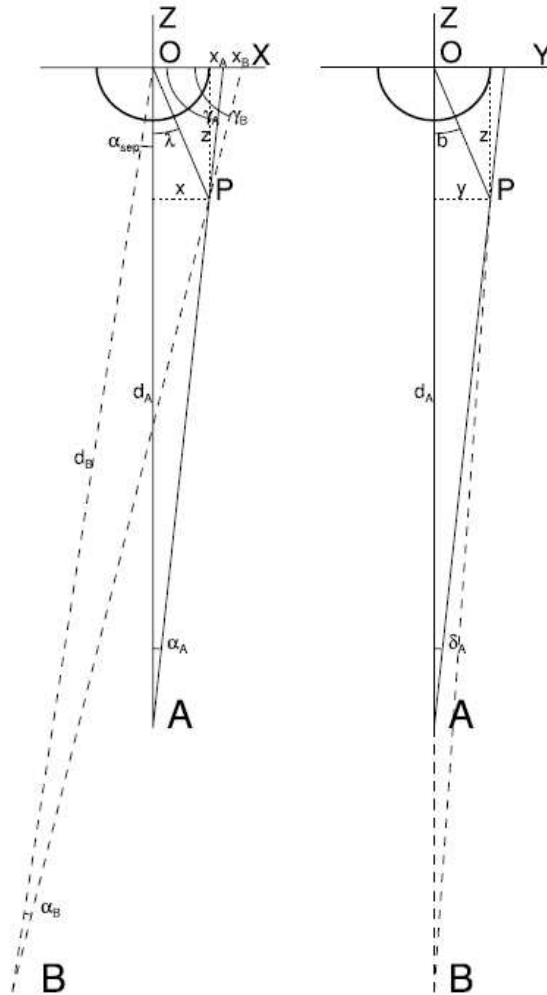


Figure 4.6: Taken from Aschwanden et al. (2008): Geometry of triangulation or projecting a point  $P$  from spacecraft  $A$  and  $B$ , where the  $X$ - $Z$  plane is coincident with the Sun centre position  $O$ , and the two spacecraft positions  $A$  and  $B$  (left), while the vertical  $Y$ - $Z$  plane is perpendicular (right). The distances of the spacecraft from the Sun are  $d_A$  and  $d_B$ , the observed angles of point  $P$  with respect to the Sun centre  $O$  are  $\alpha_A$  and  $\alpha_B$ , intersecting the  $X$ -axis at positions  $x_A$  and  $x_B$  with the angles  $\gamma_A$  and  $\gamma_B$ . The spacecraft separation angle is  $\alpha_{sep}$ . The point  $P$  has 3-D coordinates  $(x, y, z)$  and heliographic longitude  $\gamma$  and latitude  $b$ .

## CHAPTER 4

The distance of the spacecraft from Sun centre is defined as  $d_A$  and  $d_B$ , and they observe  $P$  at an angle of  $\alpha_A$  and  $\alpha_B$  in the X-direction from Sun centre, and at an angle of  $\delta_A$  and  $\delta_B$  in the Y-direction from Sun centre.

$x_A$  and  $x_B$  are the projected positions of the point  $P$  on the X-axis.

Thus, the requirement is to solve for  $(x,y,z)$ , using the angles which are already known.

Firstly, the angles  $\gamma_A$  and  $\gamma_B$  are easily calculated as:

$$\gamma_A = \frac{\pi}{2} - \alpha_A \quad (4.31)$$

$$\gamma_B = \frac{\pi}{2} - \alpha_B - \alpha_{sep} \quad (4.32)$$

From the sine rule, we can derive  $x_A$  and  $x_B$ :

$$x_A = d_A \tan(\alpha_A) \quad (4.33)$$

$$x_B = d_B \frac{\sin \alpha_B}{\sin \gamma_B} \quad (4.34)$$

Basic trigonometry allows the derivation of  $\gamma_A$  and  $\gamma_B$ :

$$\tan \gamma_A = \frac{z}{x_A - x} \quad (4.35)$$

$$\tan \gamma_B = \frac{z}{x_B - x} \quad (4.36)$$

Similarly, we can derive the  $x$ ,  $y$  and  $z$  coordinates<sup>1</sup>:

$$x = \frac{x_B \tan \gamma_B - x_A \tan \gamma_A}{\tan \gamma_B - \tan \gamma_A} \quad (4.37)$$

$$y = (d_A - z) \tan \delta_A \quad (4.38)$$

$$z = (x_A - x) \tan \gamma_A \quad (4.39)$$

---

<sup>1</sup>the x-coordinate should be derived first, then the z-coordinate, and finally the y-coordinate

## CHAPTER 4

The point  $P$  can then be described in heliographic coordinates  $(r, b, \gamma)$  as:

$$r = \sqrt{x^2 + y^2 + z^2} \quad (4.40)$$

$$b = \tan^{-1} \left( \frac{y}{z} \right) \quad (4.41)$$

$$\gamma = \tan^{-1} \left( \frac{x}{z} \right) \quad (4.42)$$

where  $r$  is the radius of the point from Sun centre,  $b$  is the heliographic latitude, and  $\gamma$  is the heliographic longitude.

### Procedure “`scc_measure`”

There exists a procedure in *SolarSoft* called *scc\_measure.pro* which conveniently allows the user to select, by eye, a particular feature from a pair of simultaneous STEREO images (see Figure 4.8). The user selects a point from the STEREO-A image, and the tool then computes an approximate epipolar line (Inhester, 2006), as shown in Figure 4.8, which constrains the user to select from a point along this epipolar line.

An epipolar line is the projection of the plane containing the two spacecraft positions and the feature to be triangulated, onto the opposing observer’s field of view. From Figure 4.7, if a point  $P$  is observed from STEREO-B, it is projected onto STEREO-B’s image plane as  $P'$ . The point  $A'$  is the projection onto STEREO-B’s image plane of the position of STEREO-A. The plane containing the positions of STEREO-B,  $P'$  and  $A'$  is known as the epipolar plane, and the projection of this plane onto the STEREO-A image plane is known as the epipolar line. Therefore, upon picking the same feature ( $P$ ) from STEREO-A, the feature will be positioned along the epipolar line, and so the problem of picking the same feature from both vantage points becomes a 1-D problem, rather than a 2-D problem.

This software was used to stereoscopically triangulate the leading edge of the

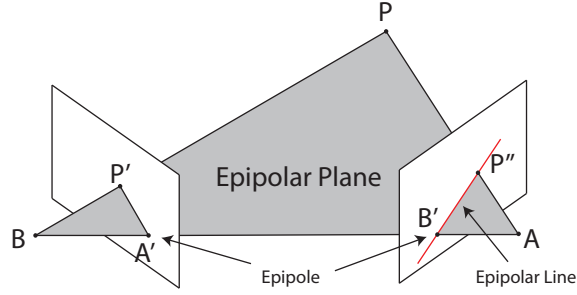


Figure 4.7: The points A and B denote STEREO-A and STEREO-B, respectively. The points P' and P'' are the projection onto STEREO-A's and STEREO-B's image plane, respectively, of point P. The point A' is the projection onto STEREO-B's image plane of STEREO-A. Similarly, the point B' is the projection onto STEREO-A's image plane of STEREO-B.

CMEs analysed in this thesis. Datasets from EUVI, COR-1, COR-2 and HI-1 were used, when the data was available.

The error in the 3-D triangulation decreases as the separation angle between the two spacecraft increases, for a constant error (Liewer et al., 2009). If the feature can be picked out to within a certain number of pixels ( $\Delta x$ ), then this leads to an error in the height of  $\Delta h \approx \Delta x / \sin \alpha_{sep}$ , where  $\alpha_{sep}$  is the separation angle of the two spacecraft. For each instrument, the error will also rely upon the pixel radius of the Sun, so that an error of 1 pixel is given by  $\Delta h / R_{\odot}$ . Using EUVI as an example,  $R_{\odot} \approx 700$  pixels, and assuming a separation angle of  $30^\circ$ , would give an error in height of  $\sim 0.3\%$ .

However, the ability to identify the same feature, within one pixel, is difficult. Since there are two different vantage points, features may appear different, and any changes in intensity could be a result of a line-of-sight integration effect, for example. The leading edge of a CME does not have a clearly defined boundary which negates any such effects, so there must be some degree of error in picking the location of the leading edge. In this work, to give an estimation of error, a 3 pixel margin of error

## CHAPTER 4

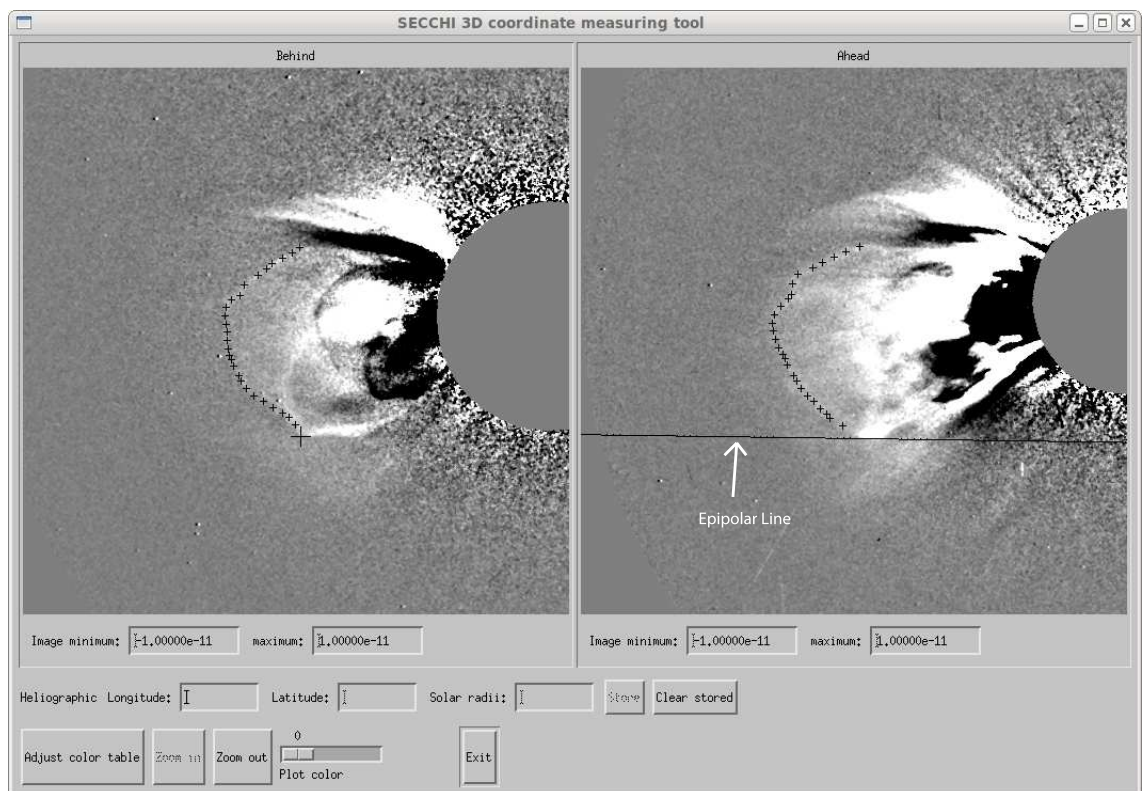


Figure 4.8: Screenshot of `scc_measure`. Points are selected on the STEREO-B image (left, indicated by the black crosses), and the epipolar line, corresponding to the largest black cross from the STEREO-B image, is displayed on the STEREO-A image (right).

## CHAPTER 4

for EUVI, COR-1 and COR2 images has been assumed, whilst a 5 pixel margin of error is assumed for HI. There is a larger error associated with HI, as the leading edge becomes more diffuse, and therefore harder to pick out.

Errors in latitude and longitude are found by calculating the maximum difference in longitude and latitude when triangulating from a derived point  $\pm$  the pixel error. For example, a point  $Q$  is selected from the STEREO-A image, and then triangulated by selecting the appropriate point on the corresponding STEREO-B image. The error is then found by altering the pixel position found from the STEREO-B image by the pixel errors, and those points then triangulated. The error is then the maximum difference between the original and the altered.

### 4.1.4 J-maps

The concept of the so-called j-map was originally devised by Sheeley et al. (1999), for use in tracking white-light coronal intensity features, by constructing continuous running difference height-time maps of coronal ejecta, from LASCO data. These height-time maps display solar transients along a selected radial path, as they propagate from the Sun. The work presented in this chapter uses this philosophy, but extends the observable range vastly, into the HI FOV.

Rouillard et al. (2008, 2010), and Davies et al. (2009), amongst others, apply the concept of the j-map to characterise outward-moving solar transients in HI data. Briefly, j-maps are usually created by extracting running difference HI-1 and HI-2 observations (in HPR coordinates) along a fixed solar radial (ie. along a constant PA - see Figure 4.4, right) from a series of HI images from a single STEREO spacecraft, and plotting them as a function of elongation (y-axis) and time (x-axis).

Such a plot format clearly identifies outward-propagating transient features, such as the leading edge of the CME (see Figure 4.30). A j-map instantly shows where a particular feature is in terms of its elongation at a certain time. There exists

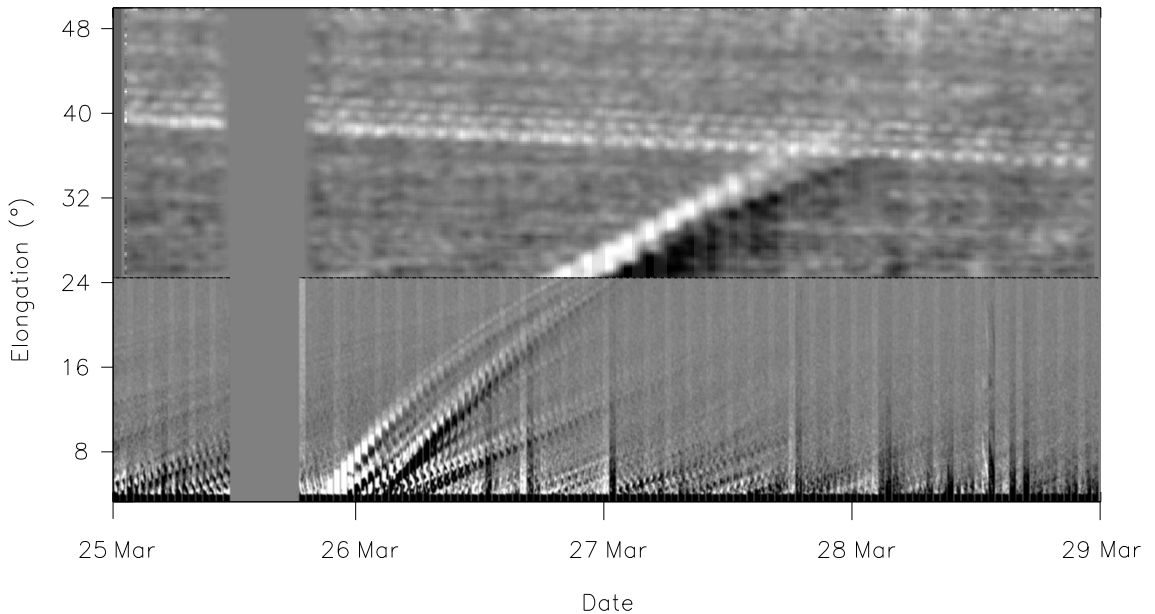


Figure 4.9: HI-1 and HI-2 combined j-map, from the 25th March 2008.

software within the *SolarSoft* library to create single instrument j-maps (*v2a.pro*), to combine these j-maps together (*wjmap-combine.pro*), and to take height-time points from the j-maps (*tool2a.pro*). It is then possible to use *jgraph.pro* which applies a similar fitting to that as described in Rouillard et al. (2009). To calculate the spacecraft-based longitudinal direction of the CME from these j-maps, via the Rouillard technique, requires the assumption that by the time the leading edge has entered the HI FOV, it is travelling at a constant radial velocity. This is achieved by applying a constant velocity to the HI data and fitting this with a constant radial direction, as described in Equation 4.43, which is derived from Equation 4.12.

$$\alpha(t) = \tan^{-1} \left( \frac{V_r(t) \sin \beta}{D_{\odot}(t) - V_r(t) \cos \beta} \right) \quad (4.43)$$

where  $\alpha(t)$  is the elongation variation,  $V_r$  is the radial velocity,  $D_{\odot}$  is the radial distance of the spacecraft, and  $\beta$  is the angle of the CME relative to the observer-Sun line.

## CHAPTER 4

A point and click method is used to select points on the j-map to determine its elongation variation with time. From the j-map, it is possible to extract the elongation of the leading edge of the CME, at any particular time. An example j-map is shown in Figure 4.9 for data from HI-1 from around  $4^\circ - 24^\circ$  and data from HI-2 from around  $24^\circ - 88^\circ$ .

Using the longitude difference ( $\Phi_D$ ) and latitude ( $\Theta$ ) with Equation 4.14 allows the PA to be derived. This is a useful check to compare the PA calculated via the triangulation technique to the HI observation.

Once  $\delta$  is known, Equations 4.15 and 4.16 can be used to calculate the Stonyhurst longitude and latitude.

Williams et al. (2009) state that a user should be able to pick out the leading edge of a CME from a j-map to within  $1^\circ$  elongation for HI-1 data, and  $2^\circ$  for HI-2 data. Therefore, to calculate errors from the j-maps, the height-time points are randomly adjusted within the accuracy declared by Williams et al. (2009), and the fitting process is repeated. The errors are then the difference between the original fitted data, and those of the adjusted fitted data.

Any apparent acceleration shown within the j-maps is likely to be a cause of projection geometry.

The basis of this technique makes two very large assumptions: that the CME propagates radially, and does not have any sort of deflection (within the HI FOV), thus maintaining a constant longitude and latitude; and that the CME experiences no acceleration within the HI FOV. If either of these two assumptions is incorrect, then this technique fails. However, there has been confirmation of the validity of this technique by comparing the velocities and angles calculated with in-situ data, in Rouillard et al. (2010).

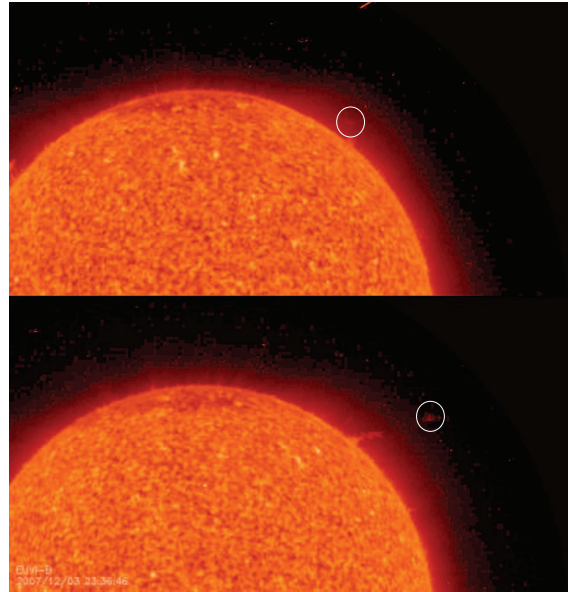


Figure 4.10: EUVI 304 Å STEREO-A (top) and STEREO-B (bottom) data on the 3rd December 2007 at 23:36UT. The circle highlights a prominence feature believed to be material from the CME as it leaves the Sun.

## 4.2 3rd December 2007 CME

A CME was launched from an unknown source region, from the western limb, at high latitude at a time between 12:00UT and 22:00UT on the 3rd December 2007. Figure 4.10 displays two snapshots of the solar disk in 304 Å. Circled, is a prominence type feature which starts to propagate outwards from the Sun, and it is this which is believed to be material from the CME subsequently tracked in the coronagraphs and heliospheric imagers. A magnetogram is shown in Figure 4.11, and this shows there to be no viable strong-field source region associated with a CME at this time.

Figure 4.12 displays the location of the STEREO spacecraft in relation to the Earth and Sun, in HEEQ coordinates. The CME is not observed in either HI-1A or HI-2A, but can be seen in HI-1B and HI-2B. As such, the CME must be propagating in the region marked “HI-B FOV” in Figure 4.12. Table 4.1 shows the time at which the CME leading edge enters and exits each instrument’s FOV, and

## CHAPTER 4

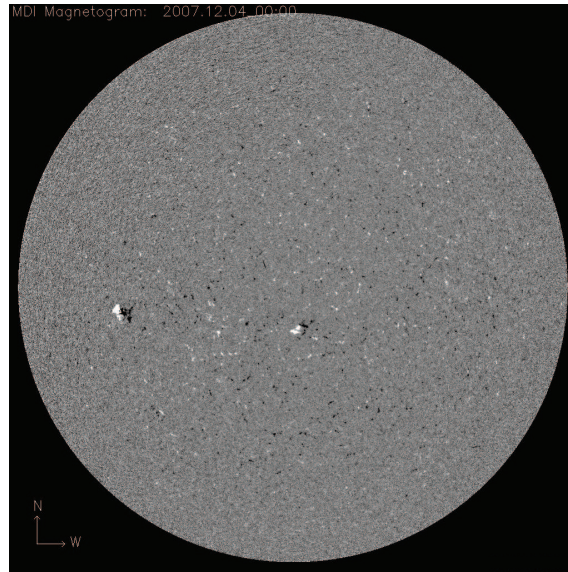


Figure 4.11: MDI magnetogram data for the 4th December 2007

Table 4.2 displays the location of the STEREO spacecraft and the Earth, in HEEQ coordinates.

### 4.2.1 Observations

#### **EUVI**

In the EUVI observations, what appears to be a flux rope (containing the prominence) is observed in  $171 \text{ \AA}$  and  $195 \text{ \AA}$  leaving the solar disk, at a high latitude, and at a time consistent with the observations in the subsequent COR-1 observations. Material is shown leaving the disk in  $304 \text{ \AA}$ , which is consistent with the other EUVI observations.  $284 \text{ \AA}$  does not appear to show any prominence type features, but does show very small flare-like events on the solar disk, which could be associated with the site of initiation. There is no well defined leading edge in the EUVI observations.

CHAPTER 4

Table 4.1: Table indicating the times the leading edge of the CME is visible in the SECCHI instruments

Instrument	Leading Edge Enters FOV BEHIND	Leading Edge Leaves FOV BEHIND	Leading Edge Enters FOV AHEAD	Leading Edge Leaves FOV AHEAD
EUVI	-	-	-	-
COR-1	3-Dec-2007 22:00:00UT	4-Dec-2007 08:50:30UT	4-Dec-2007 02:30:00UT	4-Dec-2007 09:40:00UT
COR-2	4-Dec-2007 06:52:31UT	4-Dec-2007 18:52:30UT	4-Dec-2007 07:52:00UT	4-Dec-2007 19:52:00UT
HI-1	4-Dec-2007 19:29:31UT	6-Dec-2007 21:29:31UT	- -	- -
HI-2	6-Dec-2007 04:09:21UT	9-Dec-2007 08:09:21UT <sup>1</sup>	- -	- -

<sup>1</sup> Time the leading edge becomes too faint to track

CHAPTER 4

Table 4.2: Table showing the Stonyhurst and Heliocentric Earth Ecliptic (HEE) positions of STEREO-A, STEREO-B and the Earth on 3rd December 2007 at 22:00:00UT <sup>1</sup>

	STEREO-B	Earth	STEREO-A
Heliocentric distance (AU)	1.028625	0.985649	0.966430
Stonyhurst longitude	-21.249°	0.000°	20.558°
Stonyhurst latitude	3.408°	0.527°	-2.166°
Earth Ecliptic (HEE) longitude	-21.427°	0.000°	20.729°
Earth Ecliptic (HEE) latitude	0.283°	0.000°	-0.105°
Roll from ecliptic north	0.726°		0.278°
Roll from solar north	7.274°		7.233°

<sup>1</sup> Note, these numbers change as the spacecraft orbit the Sun

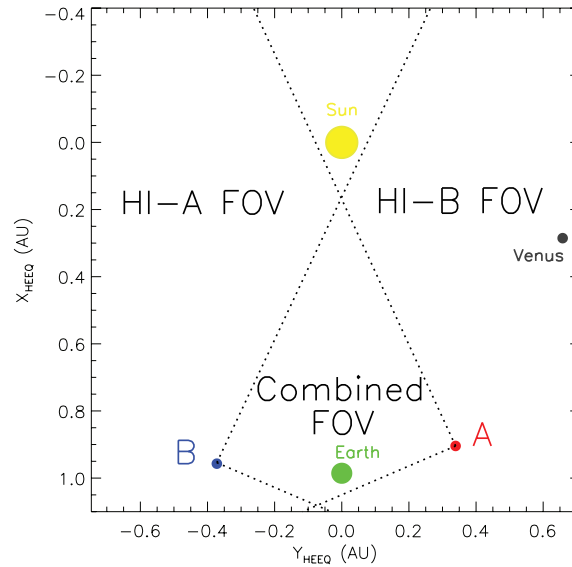


Figure 4.12: Plot showing the locations of the STEREO spacecraft in relation to the Sun and Earth, in HEEQ coordinates on 4th December 2007 05:55UT. The dotted lines indicate the HI FOV for each spacecraft

### COR-1 and COR-2

The CME leading edge is first seen by COR-1 on STEREO-B on the 3rd December 2007 at 22:00:00UT, four and a half hours before it is seen by the COR-1 instrument on-board STEREO-A. The CME remains in the COR-1B FOV for nearly eleven hours, and in the COR-1A for about seven hours, as it slowly propagates outwards from the Sun. The leading edge has a near semi-circular profile, with a flux rope which appears to twist as it follows, resulting in an appearance similar to a light bulb, as shown in Figure 4.13.

The leading edge enters the COR-2B FOV at 06:52:31UT on the 4th December 2007, where the leading edge remains in the FOV for twelve hours before exiting. The COR-2A observations show similar results but with a discrepancy of one hour, which is consistent with the COR-1 observations, and is due to the direction of the CME and the relative longitude of the two spacecraft. Figure 4.13 displays a snapshot of the CME in the COR-2 FOV.

## CHAPTER 4

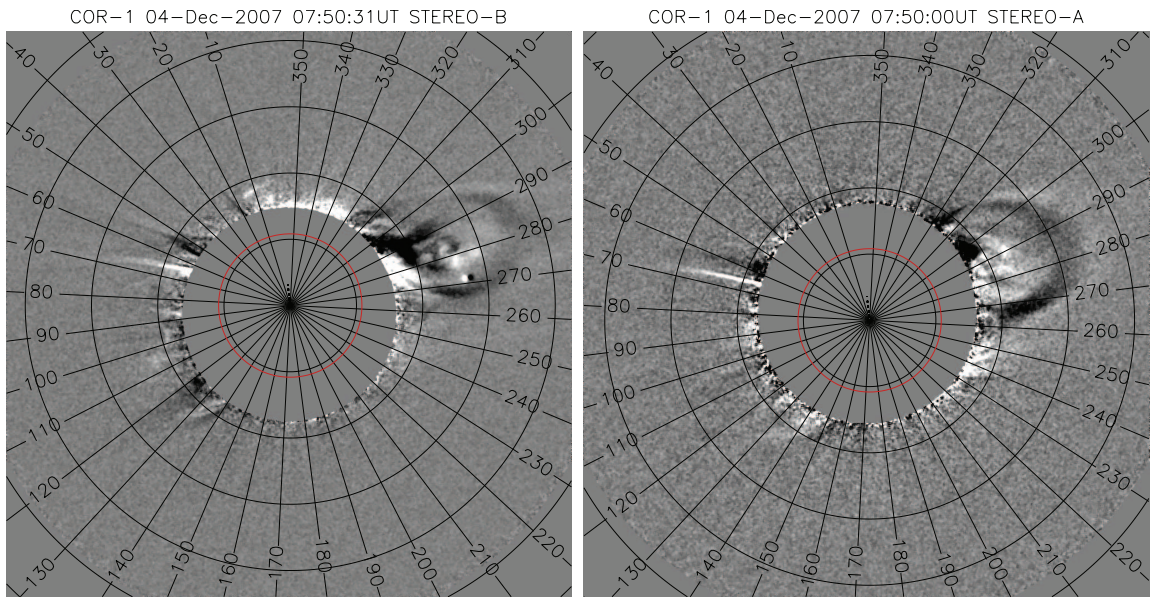


Figure 4.13: Running difference images of COR-1 data (left: STEREO-B, right: STEREO-A). Contours of elongation are drawn at intervals of  $0.25^\circ$

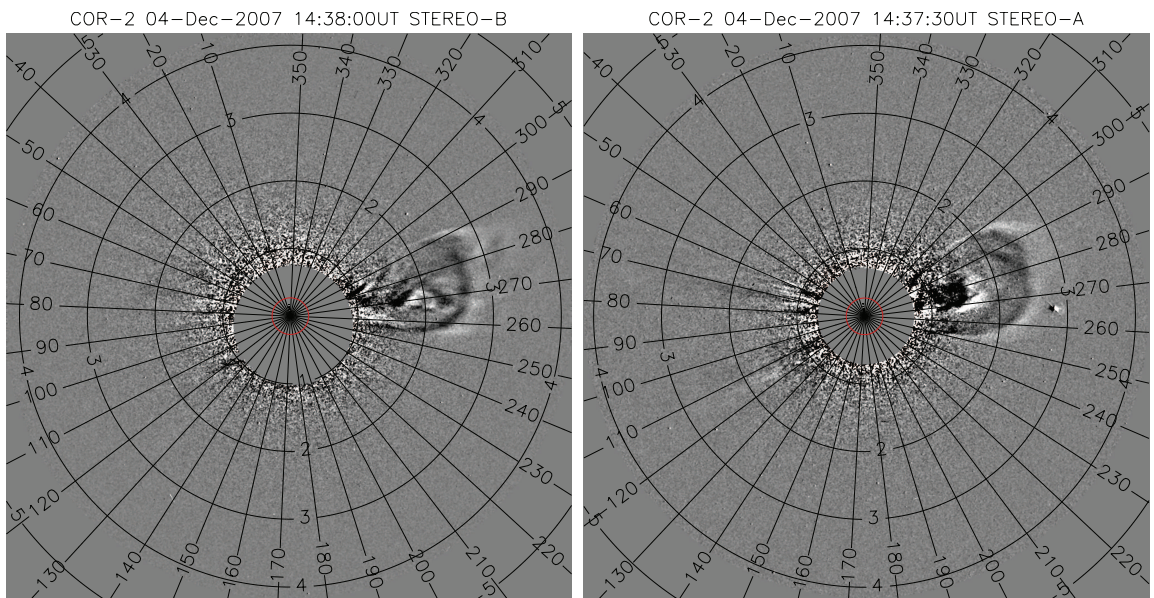


Figure 4.14: Running difference images of COR-2 data (left: STEREO-B, right: STEREO-A). Contours of elongation are drawn at intervals of  $1^\circ$

**HI-1 and HI-2**

Figure 4.15 displays modified running difference images for HI-1 and HI-2 from STEREO-B only. Given the fact that the CME is not observed in HI by STEREO-A, we already know that the CME is propagating at an angle that takes it beyond the Sun – STEREO-A line in the HI-B FOV.

The leading edge is first observed by HI-1B on the 4th December 2007 at 19:29:31UT, and can be observed for a further 50 hours until it exits the HI-1B FOV. During this stage of its evolution, the CME’s leading edge appears to lose its more uniform shape, and spread out more. There also appears to be another loop-like structure emerging at higher latitudes, in conjunction with the original leading edge. The CME core is still visible but is travelling at a latitude that appears to run parallel to the ecliptic plane.

As the leading edge enters the HI-2B FOV at 04:09:21UT on the 6th December 2007, the intensity of the leading edge begins to drop off, as it passes over Venus, until it becomes too faint to be detected by 08:09:21UT on the 9th December 2007.

**4.2.2 Triangulation method with COR-1 and COR-2 data**

Nine COR-1 and COR-2 stereoscopic triangulations were performed to reconstruct the 3-D geometric properties of the CME.

Figure 4.16 displays the latitude and longitude of the CME’s leading edge, and clearly shows a trend in both latitude and longitude, and has been fitted with a curve of the form  $f(x) = a \exp(bx) + c$ . There is a deflection of the CME in latitude; during the early phases of its evolution, in the COR-1 FOV, the central part of the leading edge deflects from an initial angle of  $\sim 13^\circ$  and rapidly drops to  $\sim 4^\circ$  latitude, where it would appear to plateau within  $5R_\odot$ , although without stereoscopic observations from the HI instruments, this is not certain.

## CHAPTER 4

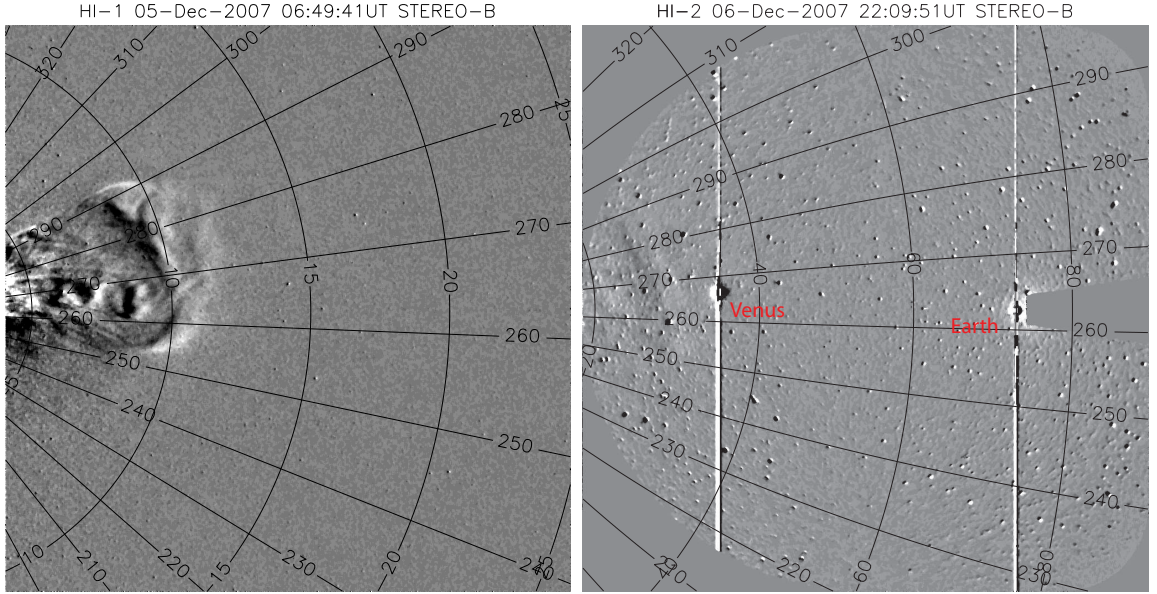


Figure 4.15: Running difference images of HI-1B (left) and HI-2B (right) data, with contours of PA and elongation. Contours of elongation are drawn at intervals of  $5^\circ$  and  $20^\circ$  for HI-1B and HI-2B respectively.

A rapid deflection in longitude also seems to exist, with the leading edge deflecting rapidly from  $\sim 69^\circ$  to approximately  $76^\circ$  where it again appears to plateau at around  $4R_\odot$ .

Single HI-1B and HI-2B observations show that the CME's leading edge follows along a central PA of  $\sim 273^\circ$ , which would agree with the longitude and latitude estimations.

Assuming a constant radial direction of the CME (after the initial deflections), the following Stonyhurst coordinates are derived:

$$\Theta = 4^\circ \pm 1^\circ$$

$$\Phi = 76^\circ \pm 2^\circ$$

To calculate the error from these angles, the average deviation was used:

$$\frac{1}{n} \sum_{i=1}^n |x_i - m(x)|$$

## CHAPTER 4

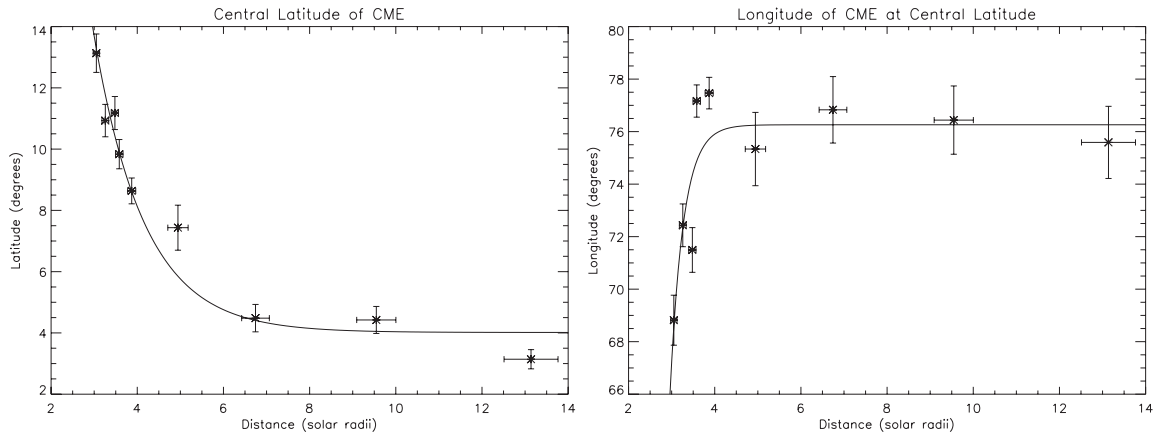


Figure 4.16: Latitude and longitude of the CME's leading edge. The solid line (if present) shows a best fit of the form  $f(x) = ae^{bx} + c$

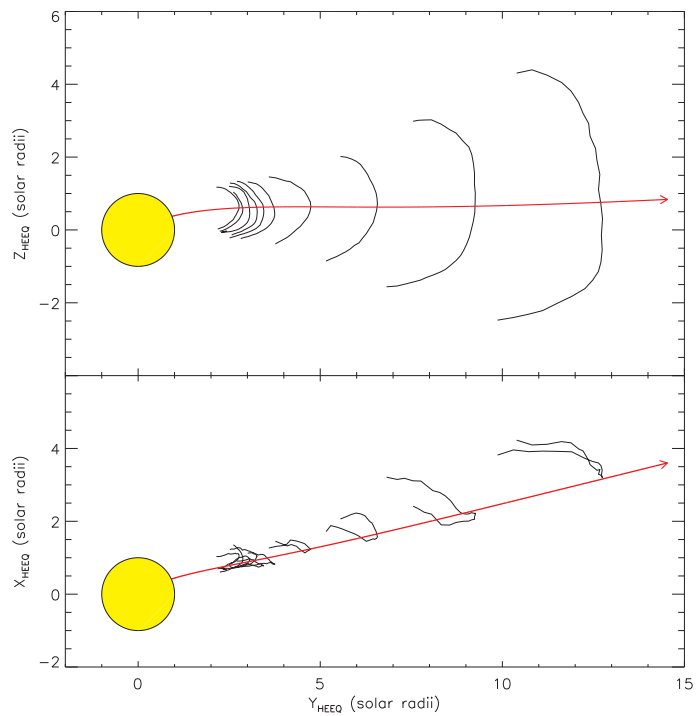


Figure 4.17: Figure showing the 3-D leading edges from COR-1 and COR-2 triangulated data. The HEEQ Y-X plane is shown (bottom) and the HEEQ Y-Z plane (top), with the projected CME direction indicated by the red line.

## CHAPTER 4

where  $m(x)$  is the chosen “mean”

Figure 4.17 displays the leading edge of the CME at different time intervals, in HEEQ coordinates. The functions fitted from the latitude and longitude are displayed as the red line.

### 4.2.3 Calculating $\beta$ from the HI-1 and HI-2 j-map data

Figure 4.18 displays a j-map created from HI data from the 4th - 10th December 2007, along a constant PA of  $273^\circ$ . The leading edge can be seen entering the HI-1 FOV on the 4th December, and can be seen out to about  $46^\circ$  by the 9th December 2007.

Using the fitting technique discussed in Section 4.1.4, this CME track is found to be travelling at a constant speed of  $290 \pm 10 \text{ km s}^{-1}$ , at a constant radial direction of  $\beta = 62^\circ \pm 5^\circ$ , along a PA of  $273^\circ$ .

This gives the following Stonyhurst coordinates:

$$\begin{aligned}\Theta &= 5^\circ \pm 1^\circ \\ \Phi &= 41^\circ \pm 5^\circ\end{aligned}$$

### 4.2.4 Kinematics

Height-time points taken from the j-map are shown in Figure 4.19 (top-left). The best-fit data is plotted top-right, with a constant angle of  $\beta = 62^\circ$  and velocity of  $291 \text{ km s}^{-1}$ , and from this angle, the CME is tracked out to  $\sim 170 R_\odot$ .

When the data is fitted with an angle of  $\beta = 97^\circ$  there is a significant change in the velocity profile of the CME. With this angle, the CME has an initial velocity of  $\sim 200 \text{ km s}^{-1}$  and accelerates at a constant rate of  $4.2 \text{ m s}^{-2}$  for the duration of the observations, with the CME being tracked out to  $240 R_\odot$ .

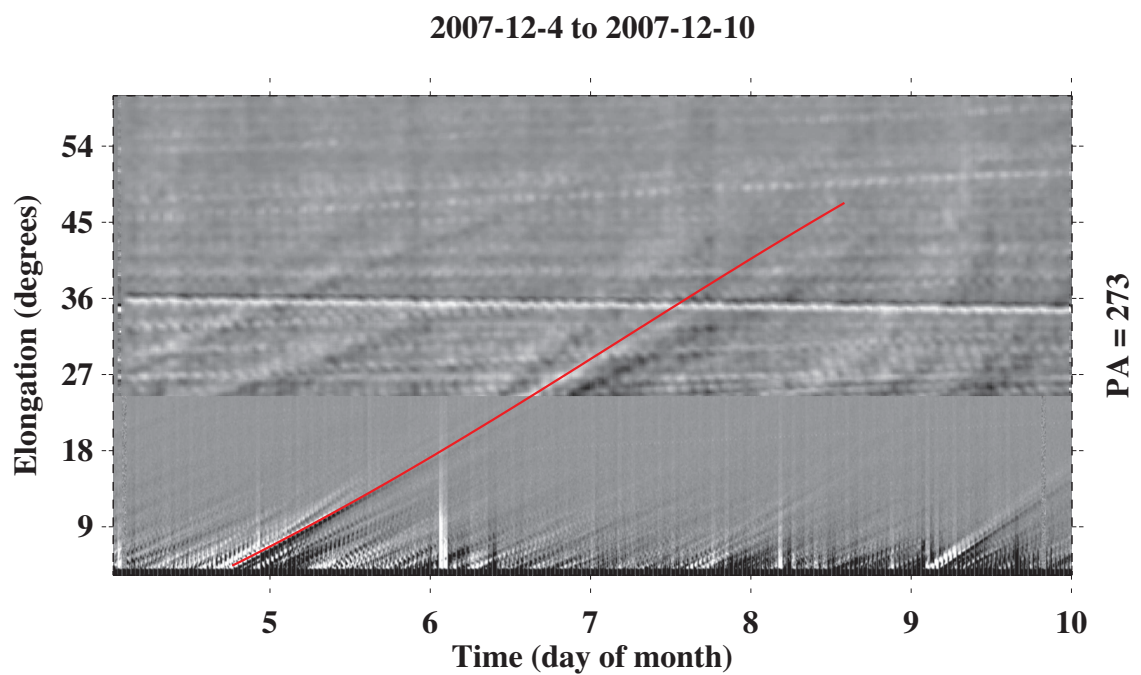


Figure 4.18: J-map from STEREO-B HI-1 ( $4 - 24^\circ$ ) and HI-2 ( $24 - 60^\circ$ ) from the 4th December 2007 00:00UT to 10th December 2007 00:00UT, along a constant PA of  $273^\circ$ . The red line shows the track being analysed.

## CHAPTER 4

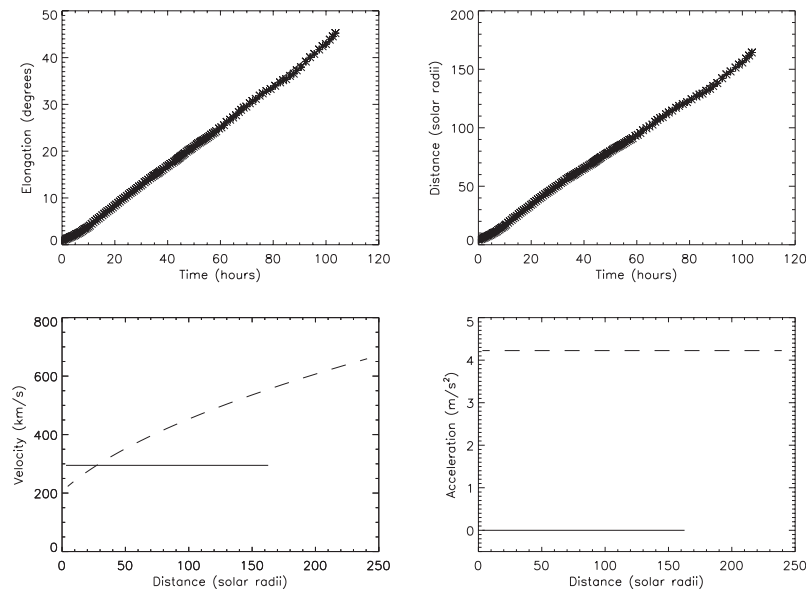


Figure 4.19: Elongation (top-left) and distance (top-right) plots, along a PA of  $\psi = 273^\circ$ , as a function of time. The stars represent the data taken from the associated j-map, and the solid line represents the fitted data from Section 4.2.3. Velocity (bottom-left) and acceleration (bottom-right) plots of the CME's leading edge, along a PA of  $\psi = 273^\circ$ , as a function of radial distance. The solid line represents an angle of  $\beta = 62^\circ$ , and the dashed line an angle of  $\beta = 97^\circ$ .

## CHAPTER 4

There is a discrepancy in the  $\beta$  angle of  $35^\circ$  calculated by the two different methods; a significant discrepancy which results in a totally different velocity and acceleration profile (see Figure 4.19, bottom panels) for the CME.

### 4.2.5 Discussion

The 3rd December 2007 CME was launched from an unknown source region from the western limb, and was tracked out to  $46^\circ$  elongation, over a duration of 105 hours. The stereoscopic triangulation produced a Stonyhurst latitude of  $\Theta = 4^\circ \pm 1^\circ$ , and a longitude of  $\Phi = 76^\circ \pm 2^\circ$ . The j-map tracking technique produces a Stonyhurst latitude of  $\Theta = 5^\circ \pm 1^\circ$  and a longitude of  $\Phi = 41^\circ \pm 5^\circ$ .

This significant discrepancy, of  $35^\circ$  in the longitude, results in a very different velocity profile for the CME, and raises several questions as to why this discrepancy exists.

The j-map fitting technique relies on the assumption that the CME has a constant radial direction. If this assumption is false, and the CMEs direction is influenced by, for example, the IMF, then the results from this fitting technique will be inherently flawed. The stereoscopic triangulation technique is very unlikely to produce errors  $> 30^\circ$  longitude.

Wang et al. (2004) discuss the deflection of CMEs in the heliosphere, and predict that CMEs with a velocity slower than the solar wind should have a west-ward deflection. The amount of deflection depends upon the velocity of the CME, and of the solar wind. As a general guide line, Wang et al. (2004) estimate that a CME travelling around  $300 \text{ km s}^{-1}$  should be deflected by  $\sim 25^\circ$  in a west-ward direction. However, if the j-map fitting technique is to be believed, the deflection would be east-wardly and there appears to be no plausible explanation for this to happen.

In-situ data covering the 1st - 26th December 2007 is displayed in Figure 4.20 from the STEREO-A, STEREO-B and OMNI-combined spacecraft. Although there

## CHAPTER 4

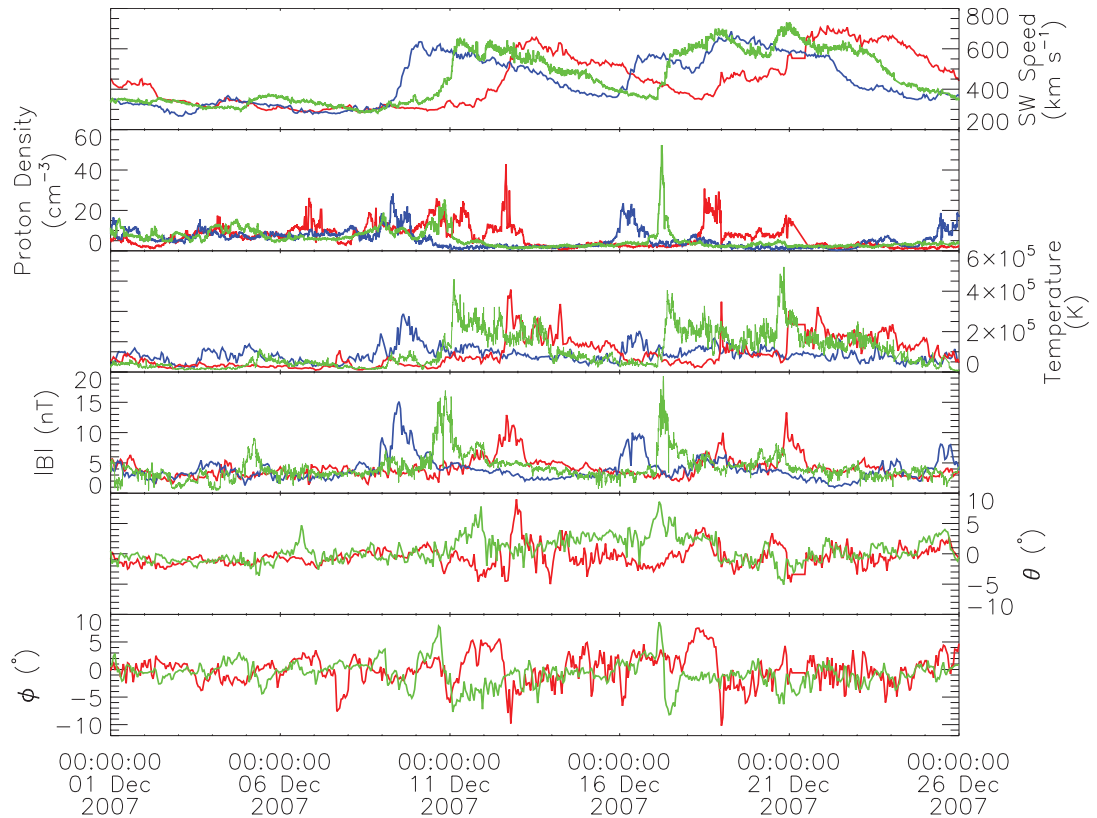


Figure 4.20: In-situ data from STEREO-B (blue), OMNI (green), and STEREO-A (red), displaying (from top to bottom): solar wind speed; proton density; temperature; magnetic field magnitude; elevation angle; azimuth angle.

appears to be a change in the solar wind speed, proton density, and magnetic field magnitude at approximately the estimated time of arrival of the CME at 1AU on the 9th-10th December in first STEREO-B, then OMNI-combined on the 11th December, and then STEREO-A on the 13th December, this is most certainly not from this CME. It is far more likely as a result of the fast solar wind originating from the equatorial coronal hole, displayed in Figure 4.21 on the 8th December 2007 11:48:09 UT. From the in-situ data, the solar wind speed increases to  $\sim 650 \text{ km s}^{-1}$ . At this constant speed, it would take  $\sim 2.5$  days to travel 1 AU, which would indicate this to be the case.

Several other authors have produced results for this particular event, and these

CHAPTER 4

Table 4.3: Table comparing results from this analysis and previous author's.

Author	Data Set	Stonyhurst Longitude	Stonyhurst Latitude	Velocity (km s <sup>-1</sup> )
Davis et al. (2009)	HI-1, HI-2	55° ± 2°	-7°	339 ± 8
Temmer et al. (2009)	COR-1, COR-2, C2, C3 <sup>1</sup>	62°	-	215
Thernisien et al. (2009)	COR-2	71°	4°	260
This work	COR-1, COR-2	76° ± 2°	4° ± 1°	200 – 300 <sup>2</sup>
This work	HI-1, HI-2	41° ± 5°	5° ± 1°	291 ± 21

<sup>1</sup> from LASCO

<sup>2</sup> velocity range from COR-1 and COR-2 data

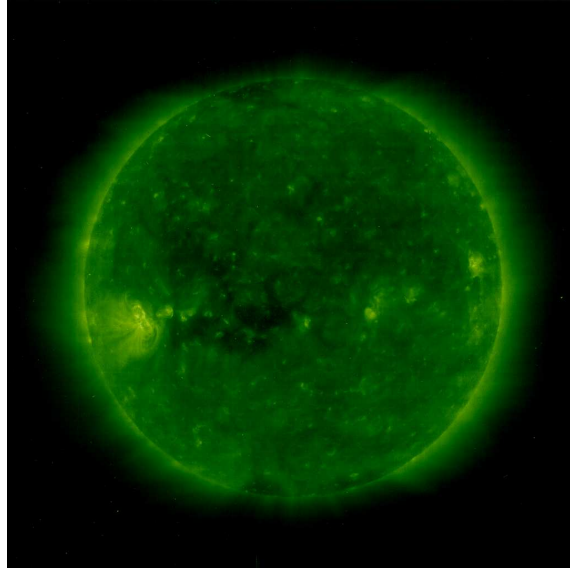


Figure 4.21: EIT image from SOHO on the 8th December 2007 11:48:09 UT, displaying an equatorial coronal hole.

are displayed in Table 4.3.

Davis et al. (2009) use HI-1 and HI-2 data, to produce j-maps along the ecliptic ( $\Theta \sim -7^\circ$ ), and then use a similar fitting technique to that in Section 4.1.4. With this technique, they produce a Stonyhurst longitude of  $\phi = 55^\circ \pm 2^\circ$ . There is a  $14^\circ$  discrepancy here, with the j-map technique used in this work. However, the discrepancy is likely to be caused by a different part of the leading edge being tracked.

Triangulation techniques are used by Temmer et al. (2009), with COR-1, and COR-2 data, as well as LASCO C2 and C3 data, so incorporating three separate vantage points. Temmer et al. (2009) record a Stonyhurst longitude of  $62^\circ$  using their triangulation method, and this compares to a longitude of  $76^\circ \pm 2^\circ$  with the triangulation technique applied from Section 4.1.3. However, rather than tracking the leading edge, Temmer et al. (2009), in this case, track a feature behind the leading edge. This could result in the  $14^\circ$  discrepancy, since the same features are not being tracked. However, Temmer et al. (2009) triangulate with different pairs,

## CHAPTER 4

choosing LASCO/STEREO-A and LASCO/STEREO-B. Since the angle between the two spacecraft is smaller, then the error is likely to be larger. Also, the image cadence of LASCO is smaller than that of STEREO, and so the number of images with a similar time-stamp will be smaller.

Thernisien et al. (2009) calculate a longitude of  $\phi = 71^\circ$  and a latitude of  $\theta = 4^\circ$ , from a forward modelling technique with COR-2 data. This compares more favourably with the longitude and latitude calculated from the COR-1 and COR-2 data calculated here, with only a discrepancy of  $5^\circ$  in the longitude.

There have been five separate analyses of this CME event, and all five results differ somewhat from each other. The techniques that have used COR data have found longitudes between  $62^\circ$  and  $76^\circ$ , whilst the j-map fitting techniques which use the HI data have found longitudes between  $41^\circ$  and  $55^\circ$ .

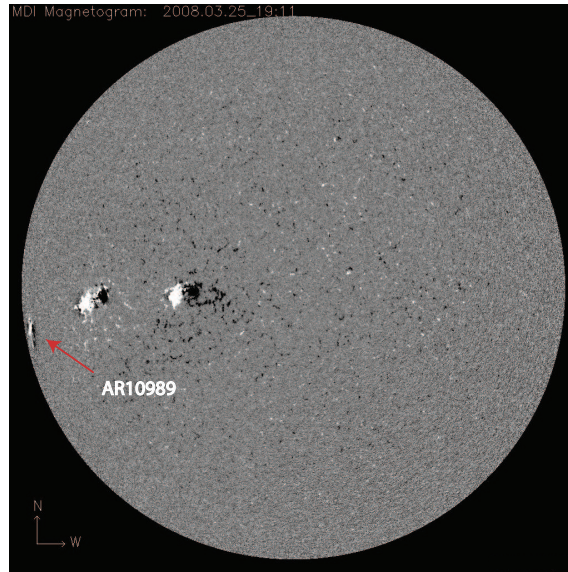


Figure 4.22: MDI magnetogram data for the 25th March 2008

### 4.3 25th March 2008 CME

On the 25th March 2008 (25-Mar-2008), a CME erupted from active region AR10989 (see Figure 4.22). Running difference images of the CME are presented, in each available SECCHI instrument in Figures 4.24 to 4.27, covering the CME’s evolution from initiation at 18:42UT on 25-Mar-2008 in EUVI, through to  $\sim$  00:09UT on 28-Mar-2008 when it becomes too faint to track by HI.

Table 4.4 shows the times at which the CME leading edge enters and exits the FOV of each instrument, and Table 4.2 displays the location of the STEREO spacecraft and the Earth, in HEEQ coordinates.

The CME leading edge has a nearly semi-circular profile during its evolution, consisting of a loop-like structure throughout. We do not observe the CME in HI on STEREO-B, and this already gives us an idea of the CME’s direction. The CME must have been propagating in the region marked “HI-1A FOV” (see Figure 4.23).

CHAPTER 4

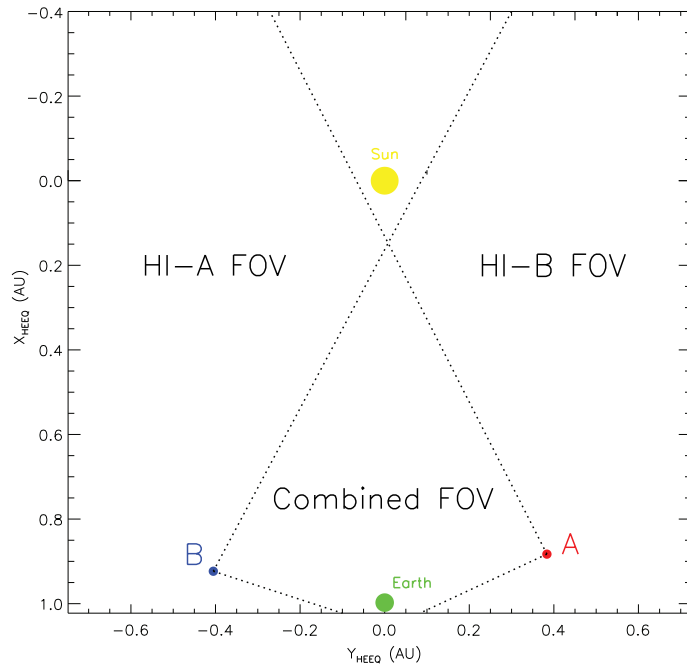


Figure 4.23: Plot showing the location of the STEREO spacecraft in relation to the Sun and Earth, in HEEQ coordinates at 18:42:15UT. The dotted lines indicate the HI FOV for each spacecraft.

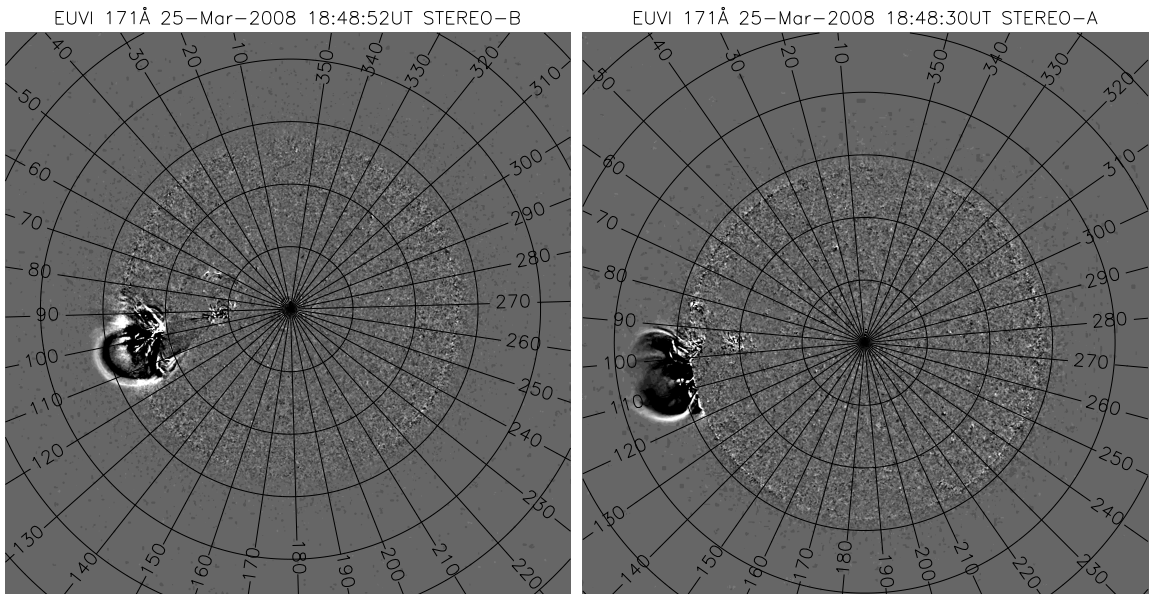


Figure 4.24: Running difference images of EUVI 171 Å data (left: STEREO-B, right: STEREO-A). Contours of elongation are drawn at intervals of  $0.1^\circ$

CHAPTER 4

Table 4.4: Table indicating the times the leading edge is visible in each instrument

Instrument	Leading Edge Enters FOV BEHIND	Leading Edge Leaves FOV BEHIND	Leading Edge Enters FOV AHEAD	Leading Edge Leaves FOV AHEAD
EUVI	25-Mar-2008 18:42:37UT	25-Mar-2008 18:57:37UT	25-Mar-2008 18:42:15UT	25-Mar-2008 18:54:45UT
COR-1	25-Mar-2008 18:55:22UT	25-Mar-2008 19:45:22UT	25-Mar-2008 18:55:00UT	25-Mar-2008 19:55:00UT
COR-2	25-Mar-2008 19:38:16UT	25-Mar-2008 22:08:16UT	25-Mar-2008 19:07:54UT	25-Mar-2008 22:07:54UT
HI-1	-	-	25-Mar-2008 20:49:01UT	26/03/2008 20:49:01UT
HI-2	-	-	26/03/2008 10:09:21UT	28/03/2008 00:09:21UT <sup>1</sup>

<sup>1</sup> Time the leading edge becomes too faint to track

CHAPTER 4

Table 4.5: Table showing the Stonyhurst and Heliocentric Earth Ecliptic (HEE) positions of STEREO-A, STEREO-B and the Earth on 25th March 2008 at 18:42:15UT

	STEREO-B	Earth	STEREO-A
Heliocentric distance (AU)	1.008326	0.997512	0.962606
Stonyhurst longitude	$-23.870^\circ$	$0.000^\circ$	$23.567^\circ$
Stonyhurst latitude	$-7.260^\circ$	$-6.828^\circ$	$-5.300^\circ$
Earth Ecliptic (HEE) longitude	$-23.691^\circ$	$0.000^\circ$	$23.482^\circ$
Earth Ecliptic (HEE) latitude	$-0.027^\circ$	$0.000^\circ$	$-0.013^\circ$
Roll from ecliptic north	$-0.063^\circ$		$0.027^\circ$
Roll from solar north	$0.454^\circ$		$-4.942^\circ$

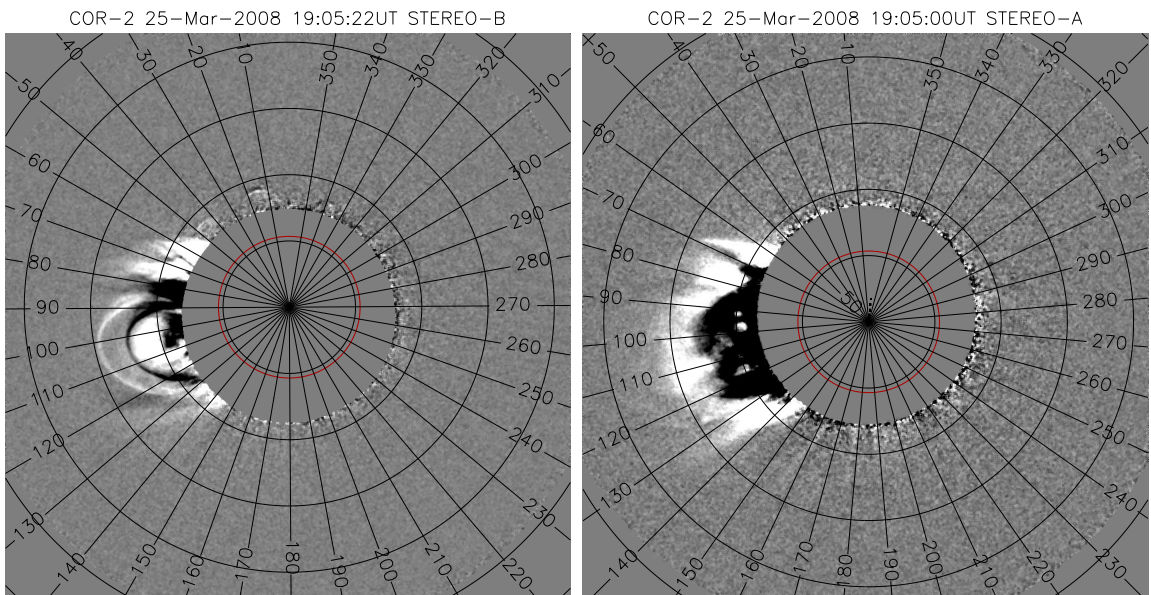


Figure 4.25: Running difference images of COR-1 data (left: STEREO-B, right: STEREO-A). Contours of elongation are drawn at intervals of  $0.25^\circ$ . The red circle outlines the solar limb.

## CHAPTER 4

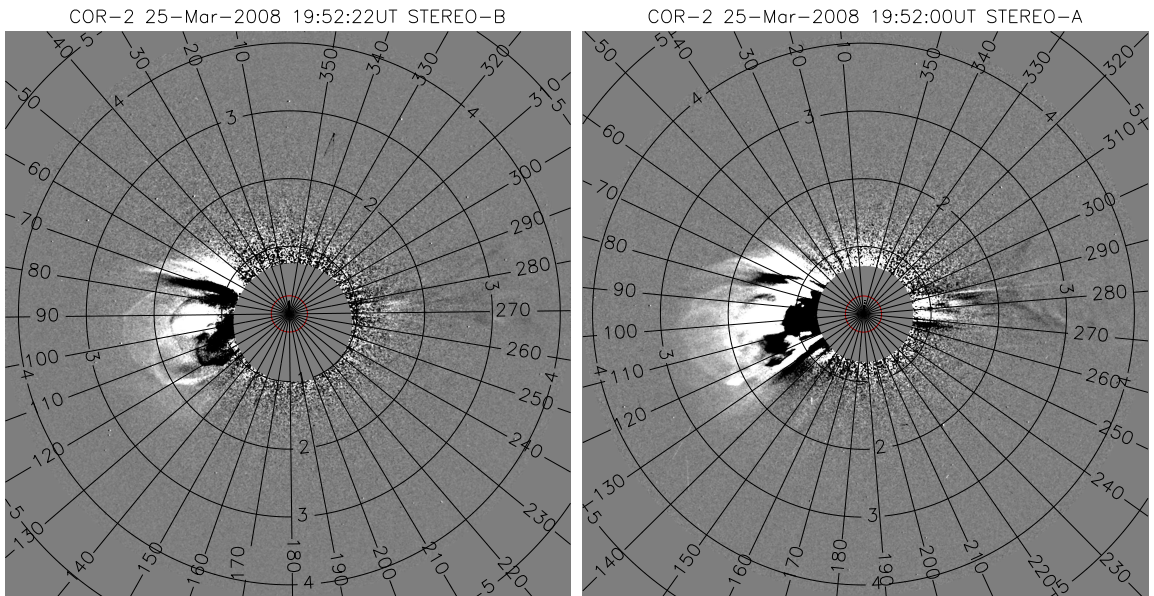


Figure 4.26: Running difference images of COR-2 data (left: STEREO-B, right: STEREO-A). Contours of elongation are drawn at intervals of  $1^\circ$ . The red circle outlines the solar limb.

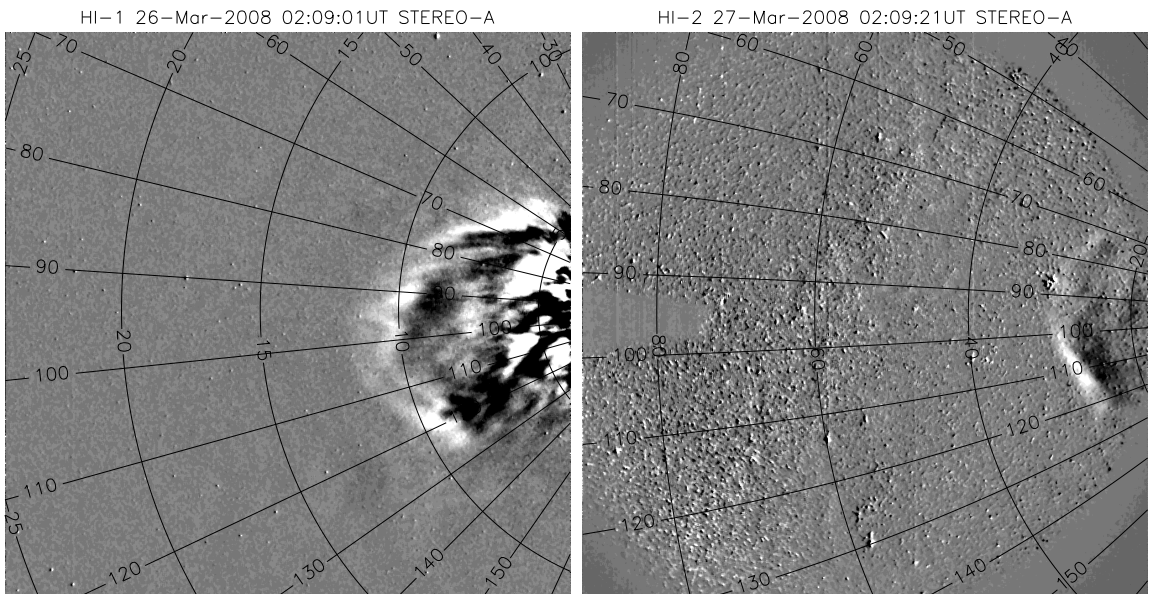


Figure 4.27: Running difference images of HI-1A (left) and HI-2A (right) data. Contours of elongation are drawn at intervals of  $5^\circ$  and  $20^\circ$  respectively.

### 4.3.1 Observations

#### **EUVI 171 Å**

Figure 4.24 displays an EUVI snapshot from both STEREO-A and STEREO-B during the initial phase of propagation of the CME through the lower corona, shortly after its eruption. A very clearly defined expanding leading edge, with a trailing cavity, is first viewed by the EUVI instruments at  $\sim 18:42$ UT. It takes only  $\sim 15$  minutes for the expanding CME leading edge to pass through the EUVI FOV. At this stage, it is already clear that the different viewing angles of STEREO-A and STEREO-B have a distinctly noticeable effect; from STEREO-A the CME appears to originate from close to or behind the limb, but from STEREO-B the CME appears to be front-sided. EUVI 171 Å observations were only used due to the high cadence at the time in this bandpass.

#### **COR-1 and COR-2**

The CME leading edge enters the COR-1A FOV first and then the COR-1B FOV. The same is true for COR-2 where the leading edge emerges from behind the occulter, first in COR-2A (at 19:07UT) and then later in COR-2B (at 19:38UT). The CME propagates outwards with the leading edge exiting the FOV of COR-1A by 19:55UT, and in COR-2A by 22:07UT. Figures 4.25 and 4.26 show a snapshot of the CME as the leading edge passes through the COR-1 and COR-2 FOV.

#### **HI-1 and HI-2**

Figure 4.27 displays running difference images for HI-1 and HI-2 from STEREO-A only. Given the fact the the CME is not observed in HI on STEREO-B, we already know that the CME is propagating at an angle that takes it beyond the Sun - STEREO-B line in the HI-A FOV.

The CME leading edge enters the HI-1A FOV at 20:49UT on 25-Mar-2008 and it

## CHAPTER 4

propagates radially through the HI-1A FOV before leaving twenty four hours later. Correspondingly, the CME leading edge is observed entering the HI-2A FOV at  $\sim 10:09$  on 26-Mar-2008 before it becomes too faint to identify unambiguously at  $\sim 00:09$  on 28-Mar-2008.

### 4.3.2 Triangulation method with EUVI, COR-1 and COR-2 data

Nine EUVI, COR-1 and COR-2 stereoscopic triangulations were performed to reconstruct the 3-D geometric properties of this CME. Figure 4.28 shows the longitude and latitude of the leading edge.

Figure 4.28 shows a trend in both latitude and longitude, and has been fitted with a curve, of the form  $f(x) = a \exp(bx) + c$ . There appears to be a deflection of the CME in latitude; during the initial phases of its evolution, in the EUVI, from an initial angle of  $\sim -16^\circ$ , up to  $10^\circ$  in the COR-2 FOV, where it appears to plateau after  $\sim 5R_\odot$ . There also appears to be a rapid deflection in longitude, with the longitude ranging from  $-78^\circ$  in the first EUVI observation, to  $-86^\circ$  after  $3R_\odot$ .

Single HI-1A and HI-2A observations show that the CME's leading edge follows along a central PA of  $\sim 102^\circ$ , which agree well with the longitude and latitude estimations calculated here.

Assuming a constant radial direction of the CME (after the initial deflectons), the following Stonyhurst coordinates are used:

$$\Theta = -10^\circ \pm 1^\circ \quad (4.44)$$

$$\Phi = -86^\circ \pm 1^\circ \quad (4.45)$$

Figure 4.29 displays the leading edge of the CME at different time intervals, in HEEQ coordinates. The functions fitted from the latitude and longitude are

## CHAPTER 4

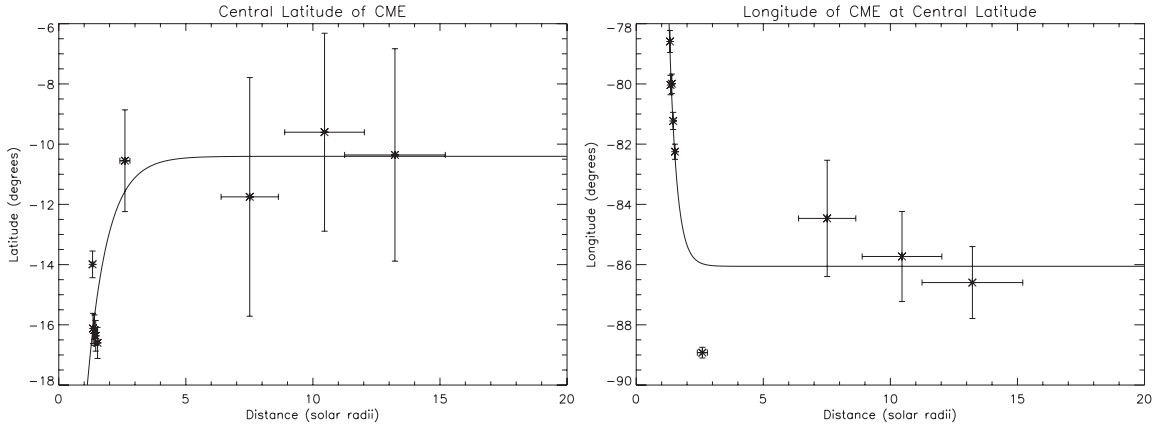


Figure 4.28: Latitude and longitude of the CME's leading edge. The solid line (if present) shows a best fit of the form  $f(x) = ae^{bx} + c$

displayed with a red line.

### 4.3.3 Calculating $\beta$ from the HI-1 and HI-2 j-map data

Figure 4.31 displays a j-map created from the HI data from the 25th - 29th March 2008, along a constant PA of  $102^\circ$ . The leading edge can be seen entering the HI-1 FOV on the 25th March, and can be seen propagating out to an elongation of  $\sim 36^\circ$  by the start of the 28th March.

Using the fitting technique discussed in Section 4.1.4, this CME track is found to be travelling at a constant speed of  $940 \pm 90 \text{ km s}^{-1}$ , at a constant radial direction of  $\beta = -114^\circ \pm 2^\circ$ , along a PA of  $102^\circ$ .

This yields the following Stonyhurst coordinates:

$$\Theta = -10^\circ \pm 1^\circ \quad (4.46)$$

$$\Phi = -91^\circ \pm 2^\circ \quad (4.47)$$

CHAPTER 4

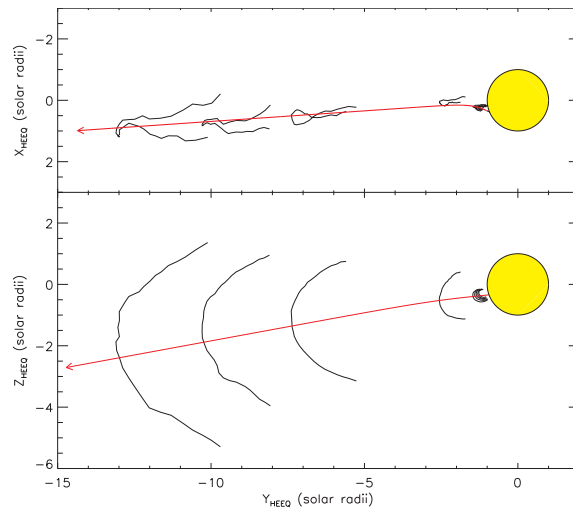


Figure 4.29: Figure showing the 3-D leading edges from EUVI, COR-1 and COR-2 triangulated data. The HEEQ Y-X plane is shown (top) and the HEEQ Y-Z plane (bottom), with the longitudinal and latitudinal projected CME direction indicated by the arrows, respectively.

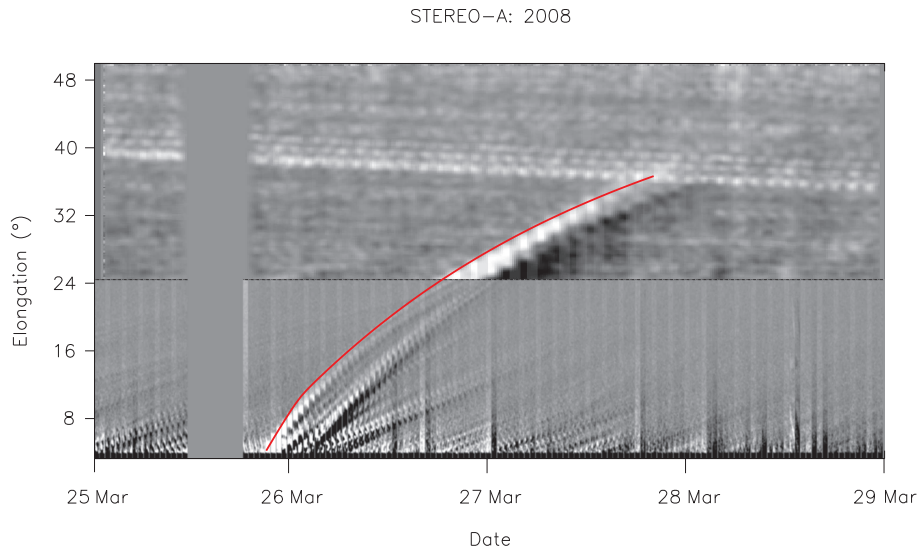


Figure 4.30: J-map from STEREO-A HI-1 ( $4 - 24^\circ$ ) and HI-2 ( $24 - 50^\circ$ ) from the 25th March 2008 00:00UT to 29th March 2008 00:00UT, along a constant PA of  $102^\circ$

### 4.3.4 Kinematics

J-maps were created for the EUVI-A, COR-1A and COR-2A data together, and time-elongation points were taken from these, as well as those taken from HI-1A and HI-2A. After calculating the constant velocity and longitudinal angle from the single spacecraft fitting technique based on HI data,  $\psi = 102^\circ$  and  $\beta = -114^\circ$  were used, from all the j-map data to calculate true distances, true velocity, and true acceleration (see Figure 4.31), which is shown by the solid line.

A square root function was fitted to the velocity and acceleration (see Figure 4.31, bottom panels), to show an overall decrease in velocity of  $\sim 1400 \text{ km s}^{-1}$  from its initiation until it reaches the HI FOV where the velocity then remains constant, at  $\sim 950 \text{ km s}^{-1}$ . From the initial eruption, the CME decelerates until  $\sim 30R_\odot$ , which corresponds to the end of the acceleration phase as noted in Sheeley et al. (1999). However, this indicates that the acceleration phase, in this instance, has not ended until approximately  $7^\circ$  elongation, which is well into the HI-1 FOV. As such, the j-map analysis was repeated, with elongations lower than  $7^\circ$  neglected, with the results agreeing within  $0.5^\circ$  of the full elongation analysis.

Similarly, the propagation angles calculated in Section 4.3.2 were applied, and the velocity and acceleration profiles were calculated, as shown by the dashed line in Figure 4.31. The PA remains the same, but  $\beta = -109^\circ$ . Due to this different angle, a different velocity and acceleration profile is seen, and a shorter distance is travelled. For  $\beta = -109^\circ$ , the CME has an initial velocity of  $\sim 1300 \text{ km s}^{-1}$ , before it decelerates and converges towards  $\sim 750 \text{ km s}^{-1}$ .

### 4.3.5 Discussion

A CME is observed by STEREO, and is tracked from its initiation, as observed by EUVI, and is followed through its evolution as it propagates through COR-1 and COR-2, and into HI-1 and HI-2.

## CHAPTER 4

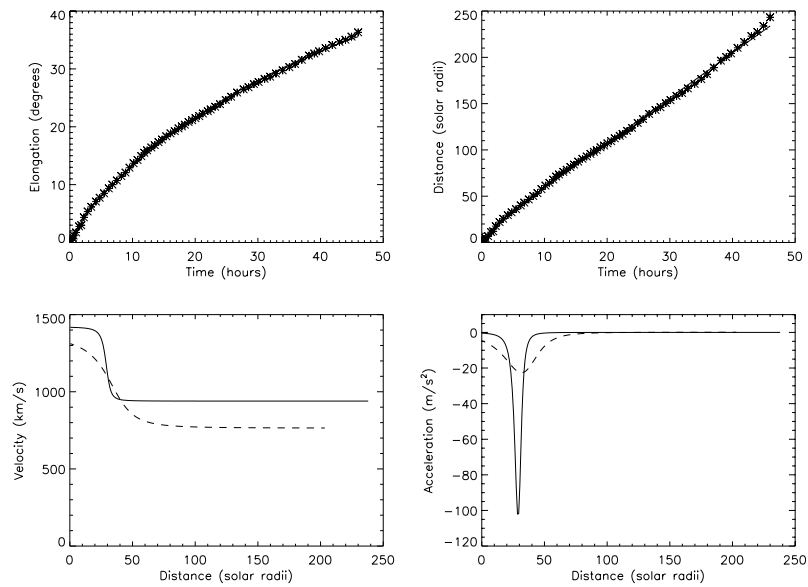


Figure 4.31: Elongation (top-left) and distance (top-right) plots, along a PA of  $\psi = 102^\circ$ , as a function of time. The stars represent the data taken from the associated j-map, and the solid line represents the fitted data from Section 4.3.3. Velocity (bottom-left) and acceleration (bottom-right) plots of the CME's leading edge, along a PA of  $\psi = 102^\circ$ , as a function of radial distance. The dashed line represents an angle of  $\beta = -109^\circ$ , and the solid line represents an angle of  $\beta = -114^\circ$

## CHAPTER 4

The results from the 3-D triangulation technique give a Stonyhurst longitude of  $\Phi = -86^\circ \pm 1^\circ$  and latitude of  $\Theta = -10^\circ \pm 1^\circ$ . The j-map technique provided estimates of  $\Phi = -91^\circ \pm 2^\circ$  and  $\Theta = -10^\circ \pm 1^\circ$ . The latitude angles are in agreement. However, the longitudinal directions differ by  $5^\circ$ . This could be attributed to a number of things. It is possible there could be an east-ward deflection of the CME in the HI observations compared to the close-to-the-Sun observations, as discussed in more detail in Wang et al. (2004). Williams et al. (2009) state that the accuracy of the technique employed in Section 4.3.3 deteriorates at elongations less than  $40^\circ$ , and as this CME is only observed out to  $36^\circ$  some caution must be attributed to this result. It must also be noted how the accuracy relies heavily on the number of data points taken from the j-map.

There have been a number of papers that have already obtained results for this particular event, and these are discussed, with reference to Table 4.6.

For the 25th March 2008 CME event, Davis et al. (2010) used HI data to create j-maps (along the ecliptic), to derive a constant velocity and direction. A Stonyhurst longitude angle of  $-93^\circ \pm 3^\circ$  from the Sun-Earth line, is derived by the authors, together with a velocity of  $1021 \pm 96 \text{ km s}^{-1}$ , which is in agreement with the longitude and velocity derived in this work. The ecliptic corresponds to a STEREO-A PA of  $95^\circ$  for this interval, an offset of some  $7^\circ$  to the PA we have used, which may account for some of the slight discrepancy between the latitude results from this work, and those of Davis et al. (2010).

For the same event, Maloney et al. (2009) use 3-D COR-1 and COR-2 triangulated data to calculate a latitude of  $-26^\circ$ . This is a significant difference from the latitudinal angle calculated in this work, with a difference of  $16^\circ$ . We assume that Maloney et al. (2009) follow the bright “plasma-blob” which appears along a PA of  $120^\circ$  in the STEREO-A observations. The latitudinal angle found in this work

Table 4.6: Table comparing results from this analysis and previous author's.

Author	Data Set	Stonyhurst Longitude (°)	Stonyhurst Latitude (°)	Velocity (km s <sup>-1</sup> )
Aschwanden (2009)	EUVI	-79 ± 1	-9 ± 1	
Colaninno and Vourlidas (2009)	COR-2	-78		
Davis et al. (2009)	HI-1, HI-2	-93 ± 3	-7°	1021 ± 96
Maloney et al. (2009)	COR-1, COR-2	-77	-26	1020
Mierla et al. (2010)	COR-1	-58 to -97	-12 to -15	
	COR-2	-50 to -92	-2 to -11	
Temmer et al. (2009)	COR, LASCO	-82 ± 7	-10 ± 0	1095 ± 5
Thernisien et al. (2009)	COR-2	-83	-12	1127
This work	EUVI, COR-1, COR-2	-85 ± 4	-10 ± 4	1310 ± 70 (initial)
	HI-1, HI-2	-91 ± 6	-9 ± 5	950 ± 90 (final)

## CHAPTER 4

follows the furthest point of the leading edge. Similarly, with the longitudinal direction, there are some discrepancies. Maloney et al. (2009) calculate their angle to be  $-74^\circ$ , which differs from our closest calculation angle of  $-86^\circ$ . They use a similar technique, using 3-D triangulated COR data, but calculate their angle from a single point along each front (which we believe to be the plasma-blob). It would seem likely that selecting only a single point would result in a greater need for accuracy, and could thus be a reason for any discrepancy, or that the plasma-blob may simply be traveling at a different longitude than the leading edge.

Thernisien et al. (2009) also present results from the COR-2 data set. They use a forward modeling method that calculates the direction of propagation, velocity and acceleration, by matching COR-2 observations to an assumed distribution of electrons around a flux rope. Both their longitudinal and latitudinal angles agree well.

Mierla et al. (2010) use a variety of techniques with COR data, including forward modeling, stereoscopic triangulation, and techniques based on the Thomson scattering properties. Mierla et al. (2010) produce results which have longitudes ranging from  $-50^\circ$  up to  $-97^\circ$ , and latitudes ranging from  $-2^\circ$  to  $-15^\circ$ . Aschwanden (2009), use stereoscopic EUVI data to derive Stonyhurst coordinates of the CME leading edge, while Temmer et al. (2009) use LASCO data with COR data to derive true propagation angles and velocities. Colaninno and Vourlidas (2009) use the Thomson scattering function to calculate the mass of the CME with COR-2 data, and deduce the longitudinal angle by comparing mass results from each image pair.

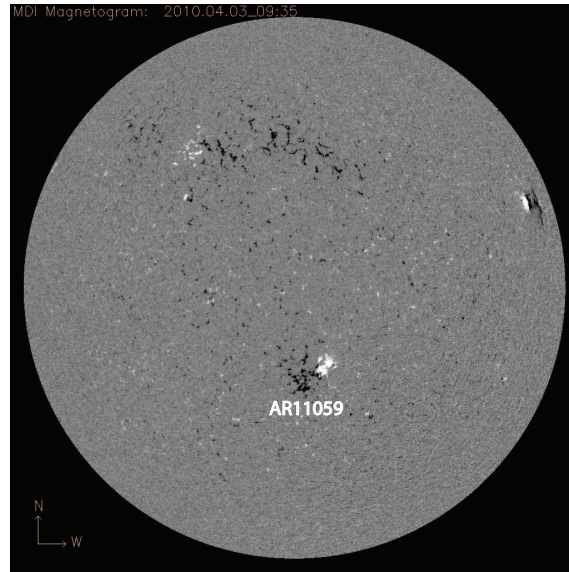


Figure 4.32: MDI Magnetogram Data for the 3rd April 2010

#### 4.4 3rd April 2010 CME

A CME was launched from AR11059 (see Figure 4.32) on the 3rd April 2010 at approximately 08:30UT as observed in both STEREO spacecraft with the EUVI instrument at  $195 \text{ \AA}$ , and then progressively into each SECCHI instrument as the CME propagates outwards from the Sun. The CME can be tracked until 5-Apr-2010 18:09:41UT by HI-2B out to approximately  $32^\circ$ , before it becomes too faint to track, but can be seen through the entire FOV of HI-2A.

Figure 4.33 displays the location of the STEREO spacecraft in relation to the Earth and Sun, in HEEQ coordinates. Table 4.7 shows the times at which the CME leading edge enters and exits the FOV of each instrument, and Table 4.8 displays the location of the STEREO spacecraft and the Earth, in HEEQ coordinates.

The CME is observed in both STEREO HI cameras, and so the CME must be propagating in the region marked “Combined FOV” (see Figure 4.33).

CHAPTER 4

Table 4.7: Table indicating the times the leading edge of the CME is visible in the SECCHI instruments

Instrument	Leading Edge	Leading Edge	Leading Edge	Leading Edge
	Enters FOV	Leaves FOV	Enters FOV	Leaves FOV
	BEHIND	BEHIND	AHEAD	AHEAD
EUVI <sup>1</sup>	-	-	-	-
	-	-	-	-
COR-1	3-Apr-2010	3-Apr-2010	3-Apr-2010	3-Apr-2010
	09:10:20UT	10:05:20UT	09:10:00UT	10:05:00UT
COR-2	3-Apr-2010	3-Apr-2010	3-Apr-2010	3-Apr-2010
	10:08:35UT	12:39:20UT	10:08:15UT	12:24:00UT
HI-1	3-Apr-2010	4-Apr-2010	3-Apr-2010	4-Apr-2010
	12:49:21UT	03:29:21UT	12:49:01UT	03:29:01UT
HI-2	4-Apr-2010	5-Apr-2010	4-Apr-2010	6-Apr-2010
	00:09:41UT	18:09:41UT <sup>2</sup>	00:09:21UT	14:09:21UT

<sup>1</sup> No discernible leading edge seen by EUVI

<sup>2</sup> Time the leading edge becomes too faint to track

CHAPTER 4

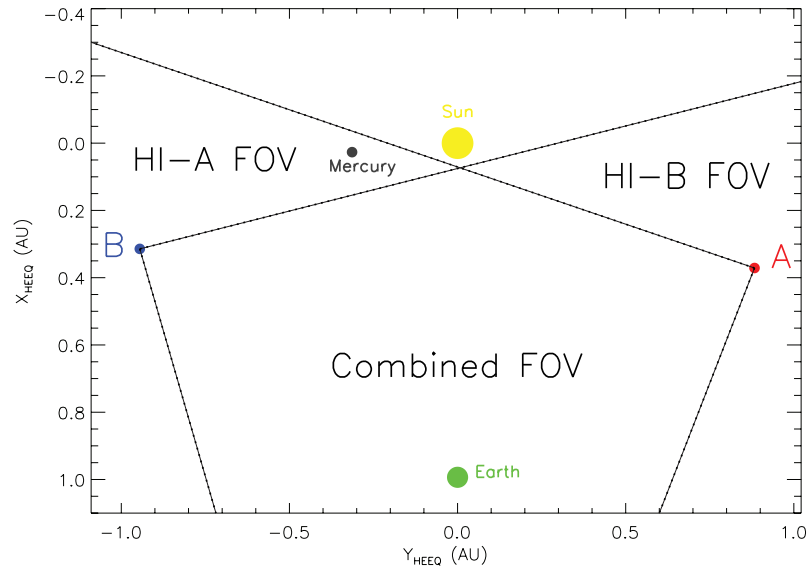


Figure 4.33: Plot showing the location of the STEREO spacecraft in relation to the Sun and Earth, in HEEQ coordinates on 3rd April 2010 09:15:00 UT. The dotted lines indicate the HI FOV for each spacecraft

Table 4.8: Table showing the Stonyhurst and Heliocentric Earth Ecliptic (HEE) positions of STEREO-A, STEREO-B and the Earth on 3-Apr-2010 at 00:00:00UT

	STEREO-B	Earth	STEREO-A
Heliocentric distance (AU)	0.999743	0.999689	0.958065
Stonyhurst longitude	$-71.605^\circ$	$0.000^\circ$	$67.180^\circ$
Stonyhurst latitude	$-5.045^\circ$	$-6.444^\circ$	$0.675^\circ$
Earth Ecliptic (HEE) longitude	$-71.202^\circ$	$0.000^\circ$	$67.416^\circ$
Earth Ecliptic (HEE) latitude	$0.0168^\circ$	$0.000^\circ$	$-0.013^\circ$
Roll from ecliptic north	$-0.063^\circ$		$0.027^\circ$
Roll from solar north	$0.454^\circ$		$-4.942^\circ$

## CHAPTER 4

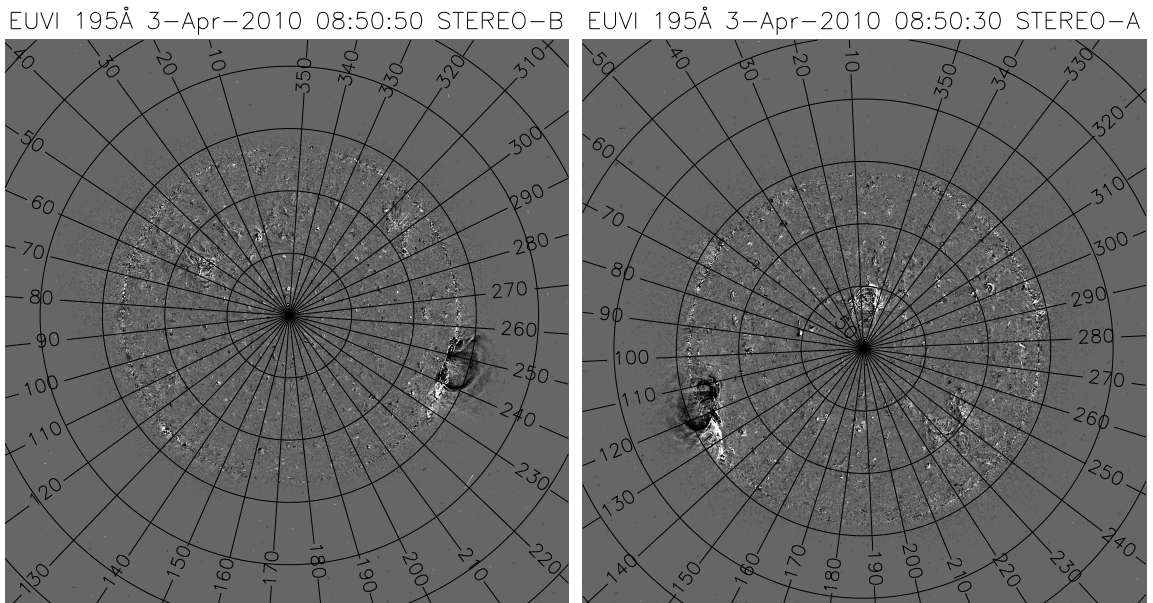


Figure 4.34: Running difference images of EUVI 195Å data, with contours of PA and elongation. Contours of elongation are drawn at  $0.1^\circ$  intervals.

### 4.4.1 Observations

#### EUVI 195Å

Figure 4.34 displays an EUVI snapshot from both STEREO-A and STEREO-B. A CME-type disturbance can be seen (although no discernible leading edge can be seen) on the south-western limb of STEREO-B, and on the south-eastern limb of STEREO-A.

#### COR-1 and COR-2

The CME leading edge is first observed by COR-1 on 3-Apr-2010 at 09:10UT by both STEREO spacecraft, and stays within the COR-1 FOV for 55 minutes. The features, and shape of the CME appear to be similar, from both vantage points, in an almost symmetrical fashion, as shown by Figure 4.35. The leading edge is then seen by both COR-2 instruments at 10:08UT, until 12:24:00UT by COR-2A, and 12:39:20 by COR-2B. The CME leading edge appears as if it is being slightly deflected in a

## CHAPTER 4

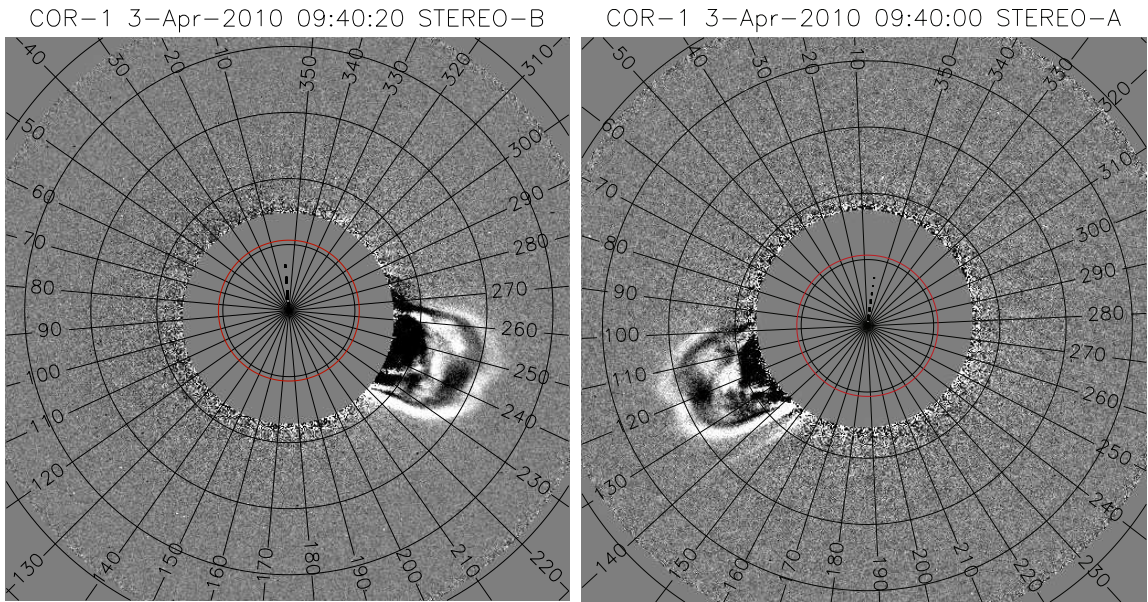


Figure 4.35: Running difference images of COR-1 data (left: STEREO-B, right: STEREO-A). Contours of elongation are drawn at intervals of  $0.25^\circ$

northerly direction in COR-2A, as shown by Figure 4.36. This deflection is not as noticeable in the COR-2B observations.

### HI-1 and HI-2

At 12:49UT on 3-Apr-2010, the leading edge of the CME enters both the HI-1B and HI-1A FOV. Again, the CME appears almost symmetrical, and can be seen until 03:29UT the next day. There also appears to be a second edge, which appears to be travelling at a similar velocity, but it is travelling at a higher PA, and has a fainter boundary than the leading edge being tracked in this study. This could be an associated shock-front. Mercury can be seen in HI-1A, as the bright saturated object.

The leading edge enters both HI-2 FOV at 00:09UT on 4-Apr-2010. However, the Milky Way is visible in HI-2B, and as a result, it becomes much more difficult to pick out the leading edge. In HI-2A, however, this is not the case, and the leading

## CHAPTER 4

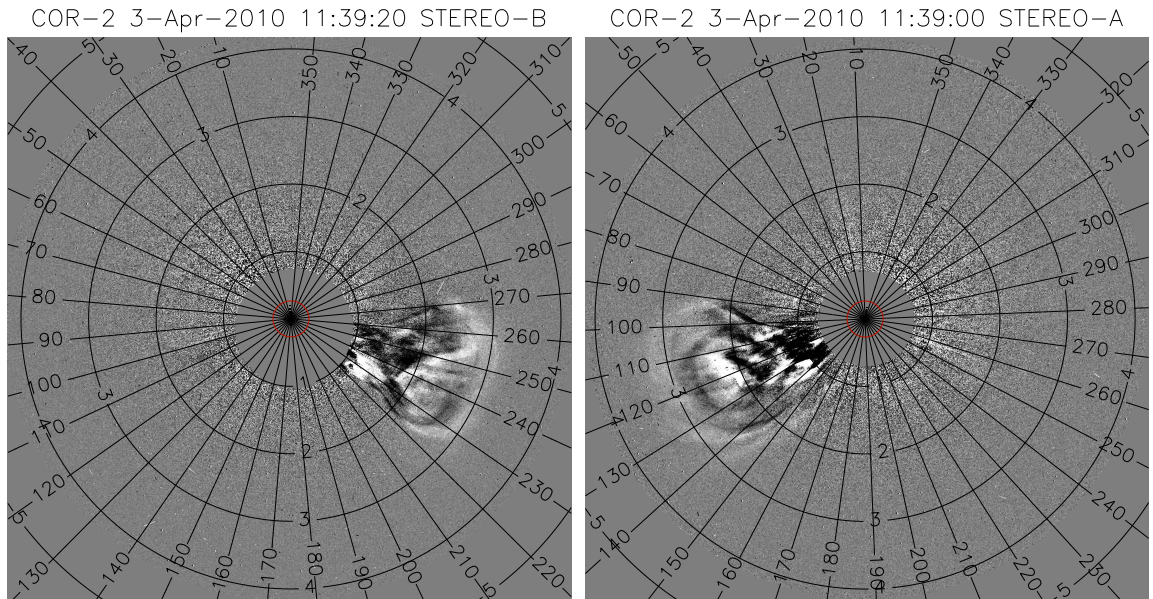


Figure 4.36: Running difference images of COR-2 data (left: STEREO-B, right: STEREO-A). Contours of elongation are drawn at intervals of  $1^\circ$ . The red circle outlines the solar limb.

edge is seen across almost the entire FOV, passing over Earth as it does so.

### 4.4.2 Triangulation method with COR-1 and COR-2 data

Although there are clear signs of CME-type activity from the EUVI observations, no clear leading edge is observed, and so no stereoscopic EUVI data is presented. Although the leading edge can be seen in both HI-2 cameras, it is quite diffuse. Since the Milky Way lies in the background of the HI-2B observations, no stereoscopic HI-2 data is presented.

Figure 4.39 shows the longitude and latitude of the leading edge. There appears to be a clear trend in the change in latitude and longitude; from low latitude, the CME appears to deflect north-wards by around  $10^\circ$ , towards the ecliptic, and around another  $10^\circ$  westward deflection in the CME's longitude, by  $50R_\odot$ .

## CHAPTER 4

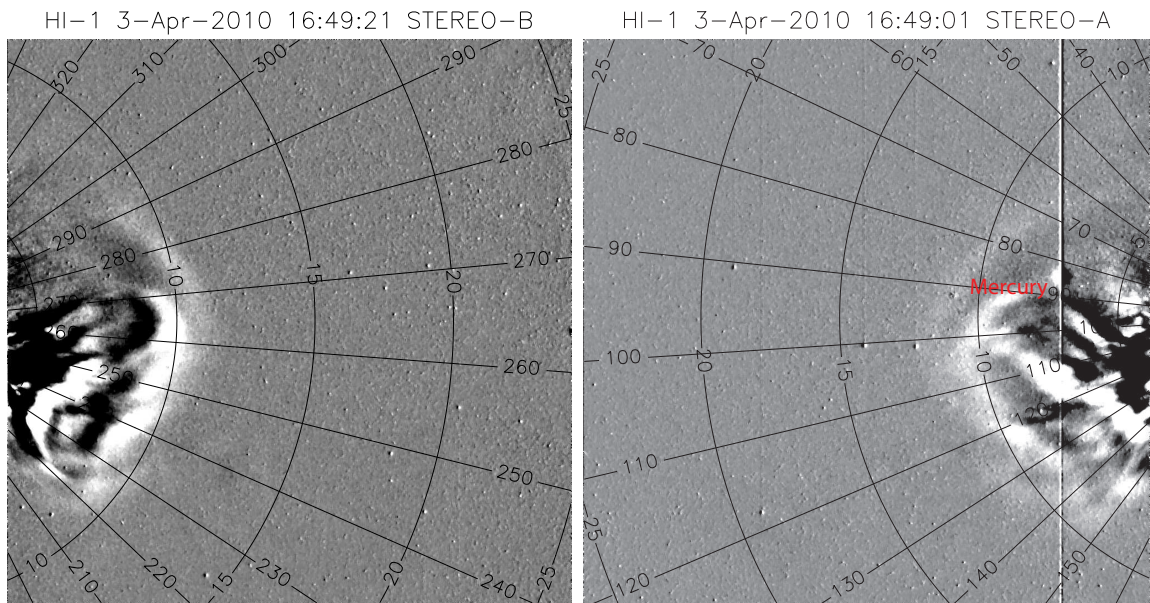


Figure 4.37: Running difference images of HI-1 data (left: STEREO-B, right: STEREO-A). Contours of elongation are drawn at intervals of  $5^\circ$

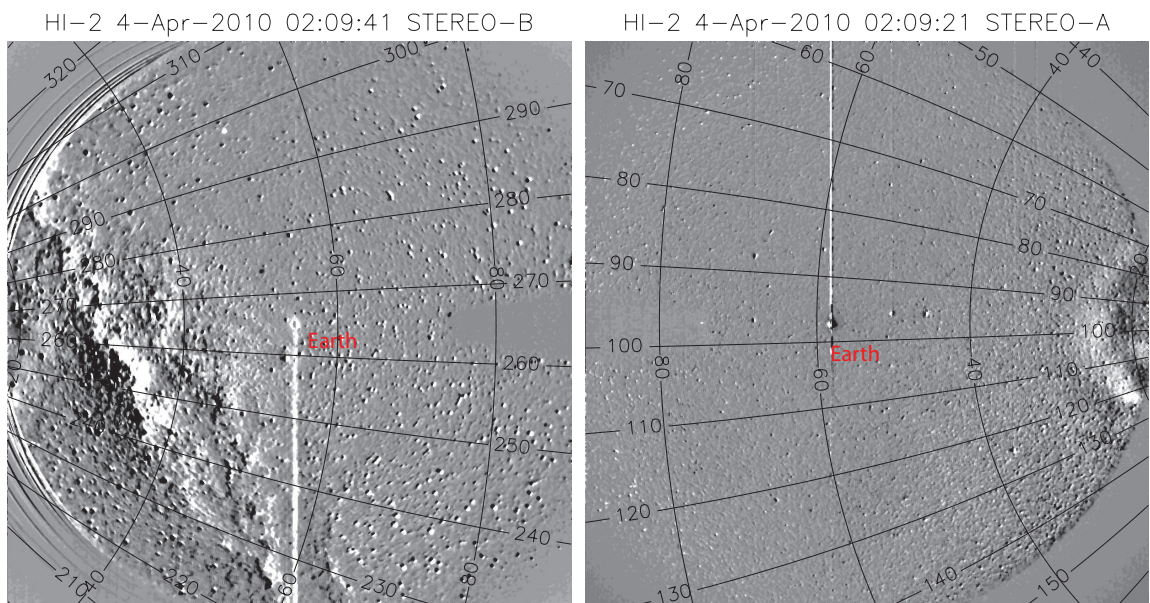


Figure 4.38: Running difference images of HI-2 data (left: STEREO-B, right: STEREO-A).. Contours of elongation are drawn at intervals of  $20^\circ$ .

## CHAPTER 4

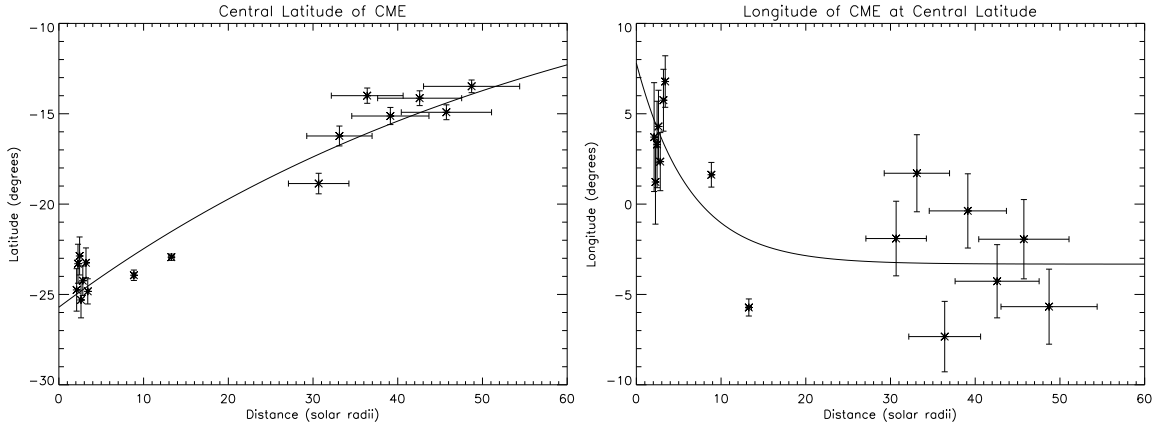


Figure 4.39: Latitude and longitude of the CME's leading edge

By fitting an exponential function to the latitude, it would appear that the latitude may converge to around  $8^\circ$  (if the function is extrapolated), and the longitude at around  $-3^\circ$ . This would give a PA of  $99^\circ$  and  $263^\circ$  for STEREO-A and STEREO-B respectively. From the HI observations, these PAs seem incorrect, as can be seen in Figure 4.38, where the central point of the leading edge appears to be travelling along PAs of  $105^\circ$  and  $257^\circ$  for STEREO-A and STEREO-B respectively.

Assuming the longitude remains approximately the same, then a latitude of  $-14^\circ$  would appear to give more suitable PAs from the HI observations. Indeed, the data points from Figure 4.39 (left) appear to be converging towards this figure, rather than that predicted by the fitted exponential curve.

Therefore, for this dataset, the following angles are given:

$$\Theta = -14^\circ \pm 2^\circ \quad (4.48)$$

$$\Phi = -3^\circ \pm 3^\circ \quad (4.49)$$

Figure 4.40 displays the stereoscopic triangulated data for the CME's leading edge, taken at different time points, in HEEQ coordinates. The data includes COR-1, COR-2, and HI-1. From the Y-X plane, the leading edge itself appears to rotate somewhat, in a clock-wise direction. This could be due to the affects of the Parker Spiral, or may be due to the higher errors with the HI data. The red line shows the

## CHAPTER 4

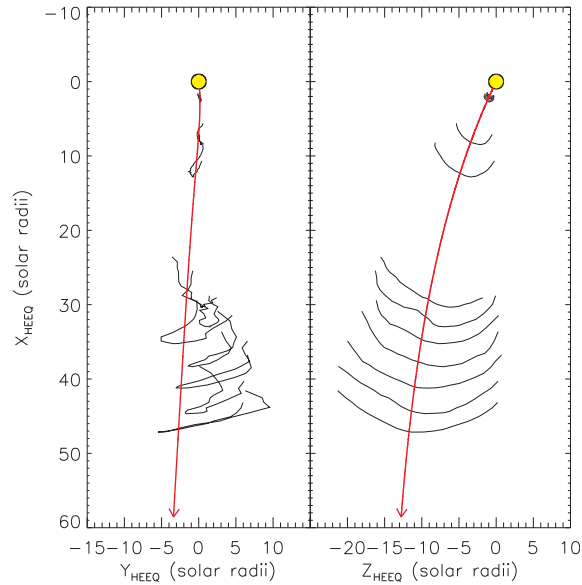


Figure 4.40: Figure showing the 3-D leading edges from COR-1 and COR-2 stereoscopic triangulated data. The HEEQ Z-X plane is shown (right) and the HEEQ Y-X plane (left), with the longitudinal and latitudinal projected CME direction indicated by the arrow.

fitted exponential curve.

### 4.4.3 Calculating $\beta$ from the HI-1 and HI-2 j-map data

Figure 4.41 displays j-maps from STEREO-A HI data and Figure 4.42 STEREO-B HI data.

The leading edge can be seen entering the HI-1A FOV at 12:49UT on the 4-Apr-2010, and is tracked along a PA of  $105^\circ$ , out to  $75^\circ$  elongation, at 14:09 on the 6-Apr-2010, before the leading edge becomes too faint to track.

Using the fitting technique discussed in Section 4.1.4, the CME is travelling at a constant speed of  $770 \pm 70 \text{ km s}^{-1}$ , and at a constant radial direction of  $\beta = 68^\circ \pm 3^\circ$ ,

## CHAPTER 4

along a PA of  $105^\circ$ , which yields the following Stonyhurst coordinates<sup>2</sup>:

$$\Theta_a = -14^\circ \pm 1^\circ \quad (4.50)$$

$$\Phi_a = 0^\circ \pm 2^\circ \quad (4.51)$$

Similarly, the leading edge can be seen entering the HI-1B FOV at 12:49UT on the 4-Apr-2010. It is tracked along a PA of  $257^\circ$ , until it becomes too faint to track at around  $32^\circ$ , at 18:09UT on the 5-Apr-2010. The constant speed is found to be  $810 \pm 110 \text{ km s}^{-1}$ , travelling at a constant radial direction of  $\beta = 72^\circ \pm 6^\circ$ . This yields the following Stonyhurst coordinates<sup>3</sup>:

$$\Theta_b = -14^\circ \pm 2^\circ \quad (4.52)$$

$$\Phi_b = -1^\circ \pm 6^\circ \quad (4.53)$$

### 4.4.4 Kinematics

Height-time points taken from Figure 4.41 are shown in Figure 4.43 (top-left). The best fit data is plotted top-right, to show distance as a function of time, and is tracked out to  $\sim 320R_\odot$ . The CME has an initial velocity of  $950 \text{ km s}^{-1}$ , before decelerating to  $870 \text{ km s}^{-1}$  after  $40R_\odot$ , as shown by the solid line (bottom-left). The dashed line shows the velocity profile of the CME when the  $\beta$  angle calculated in Section 4.4.2 is imposed; there is negligible difference between the two profiles.

Similarly, height-time plots are taken from Figure 4.42, and are shown in Figure 4.44. The leading edge is only tracked out to  $\sim 32^\circ$  and this equates to a distance of  $\sim 115R_\odot$ . It has an initial velocity of  $1000 \text{ km s}^{-1}$ , before decelerating to  $800 \text{ km s}^{-1}$  at  $20R_\odot$ . Imposing the  $\beta$  angle calculated in Section 4.4.2 produces a slightly different velocity and acceleration profile, with the acceleration phase ending by  $12R_\odot$ , and with a faster final velocity of  $860 \text{ km s}^{-1}$ .

---

<sup>2</sup> $\Theta_a$  and  $\Phi_a$  refer to the Stonyhurst latitude and longitude derived from STEREO-A jmaps respectively

<sup>3</sup> $\Theta_b$  and  $\Phi_b$  refer to the Stonyhurst latitude and longitude derived from STEREO-B jmaps respectively

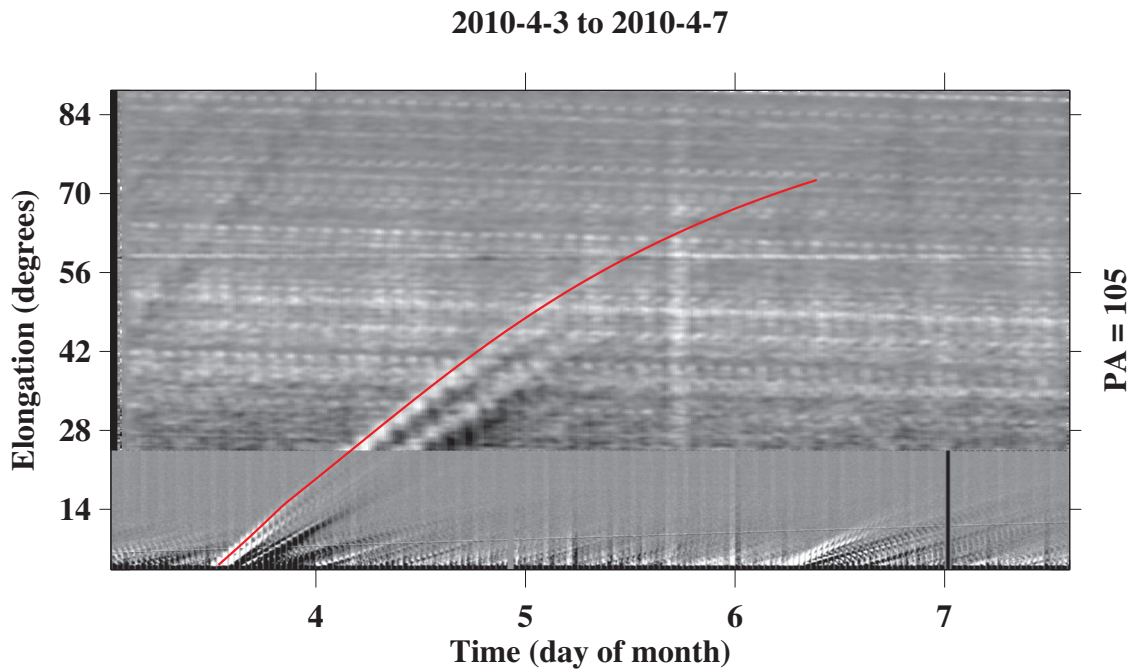


Figure 4.41: STEREO-A J-map for PA = 105°

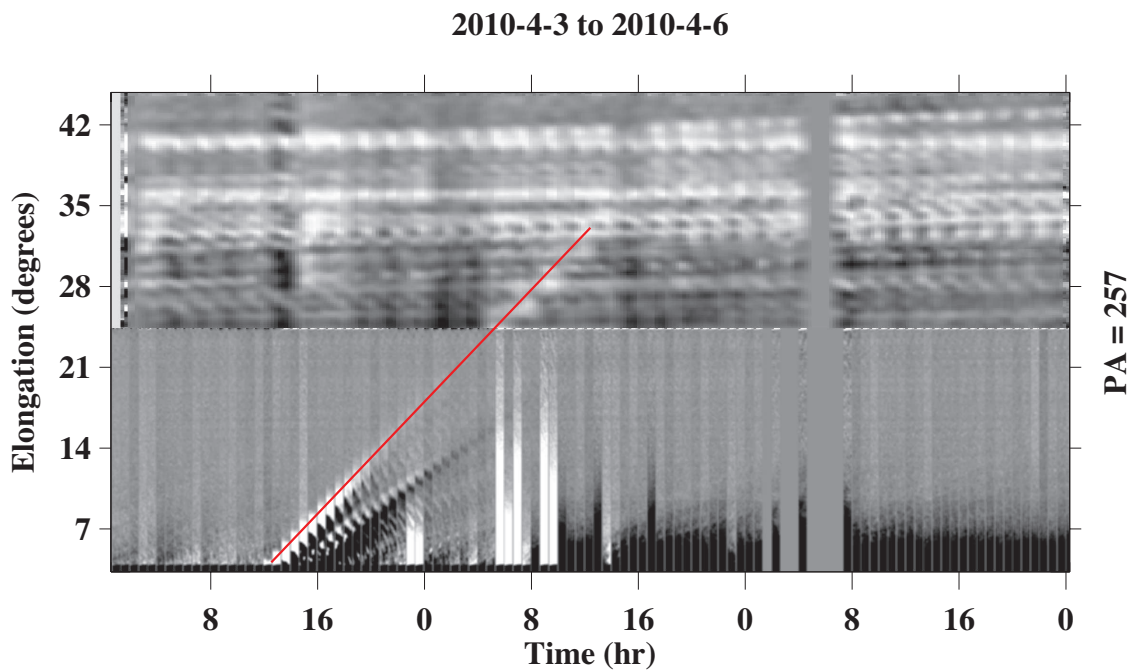


Figure 4.42: STEREO-B J-map for PA = 257°

CHAPTER 4

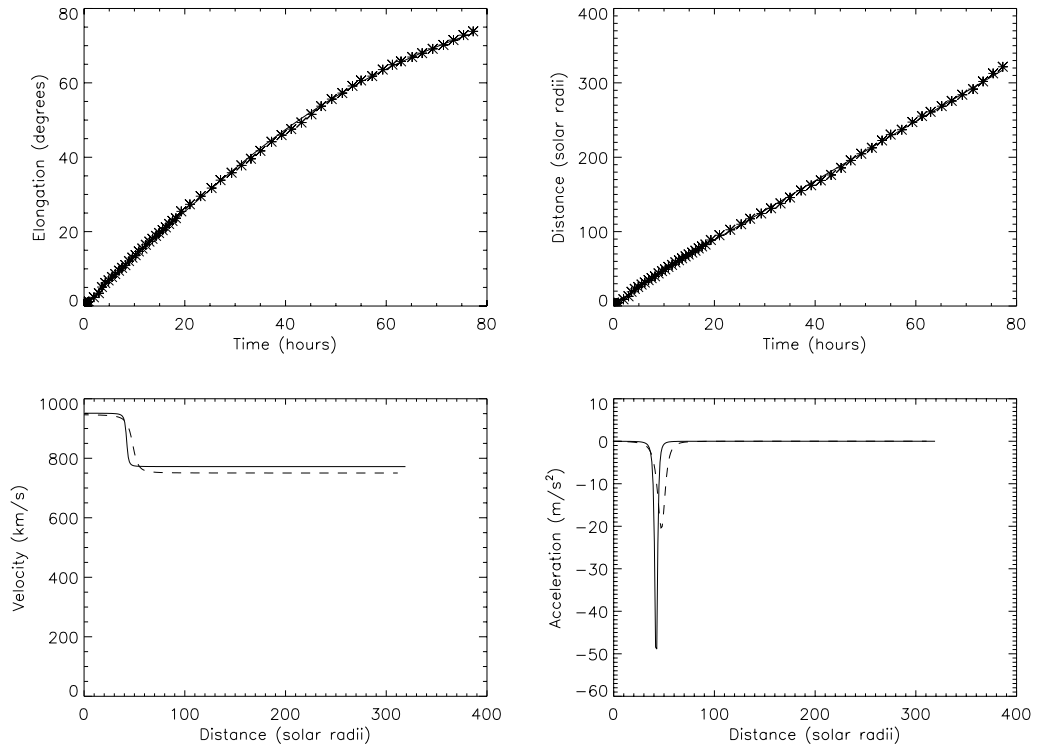


Figure 4.43: STEREO-A elongation (top-left) and distance (top-right) plots, along a PA of  $\psi = 105^\circ$ , as a function of time. The stars represent the data taken from the associated j-map, and the solid line represents the fitted data from the j-map analysis. Velocity (bottom-left) and acceleration (bottom-right) plots of the CME's leading edge, as a function of radial distance. The dashed line represents an angle of  $\beta = 71^\circ$ , and the solid line represents an angle of  $\beta = 68^\circ$

## CHAPTER 4

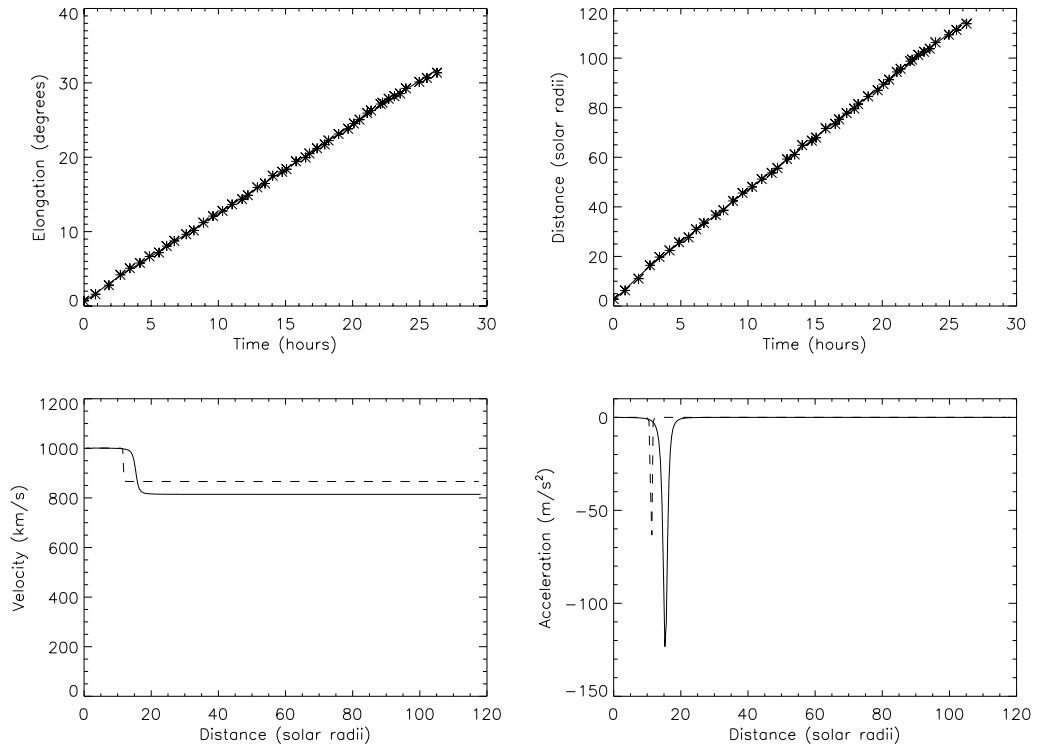


Figure 4.44: STEREO-B elongation (top-left) and distance (top-right) plots, along a PA of  $\psi = 257^\circ$ , as a function of time. The stars represent the data taken from the associated j-map, and the solid line represents the fitted data from the j-map analysis. Velocity (bottom-left) and acceleration (bottom-right) plots of the CME's leading edge, as a function of radial distance. The dashed line represents an angle of  $\beta = 73^\circ$ , and the solid line represents an angle of  $\beta = 72^\circ$

### 4.4.5 Discussion

The 3rd April 2010 CME was observed erupting by the STEREO EUVI instruments at approximately 08:30UT, and is subsequently tracked by the entire suite of SECCHI instruments out into the heliosphere to a distance of  $320R_{\odot}$  by HI-2A.

The two techniques used to derive the 3-D direction of the CME give similar results to each other, and imply that the CME is Earth-directed. Although the latitude of the leading edge is calculated to be  $\Theta = -14^{\circ}$ , this is only the central part of the leading edge, and as such, other parts of the leading edge (at higher latitudes) will pass over the Earth, and thus in-situ data is able to be taken, and the velocity and angular estimations can be verified.

Figure 4.45 shows in-situ data taken from OMNI. There is a significant change in the magnetic field strength, the plasma velocity, proton density, temperature, at around 08:00UT on the 5-Apr-2010. This concurs with the HI-2 observations, where the leading edge can be seen passing over Earth at a comparable time. This confirms that the longitude calculations from the two techniques agree well with the in-situ data, and verifies the applicability of using the j-map fitting technique as a tool for CME propagation.

The plasma velocity recorded by WIND increases from  $500 \text{ km s}^{-1}$  to around  $750 \text{ km s}^{-1}$  which again agrees well with the velocity derived within this work. From this particular CME event, the analytical methods used here have been verified by in-situ data.

One topic of interest is the deflection of the CME leading edge, which is illustrated in Figure 4.40. Within the HI-1 FOV, the leading edge appears to have rotated almost  $90^{\circ}$  by  $48R_{\odot}$ . Since the errors are much larger, due to difficulties in picking out the same feature, and due to the leading edge becoming more diffuse, it cannot be assumed that this particular feature is a true event. More CME events will be needed to fully analyse whether this particular rotation feature exists.

## CHAPTER 4

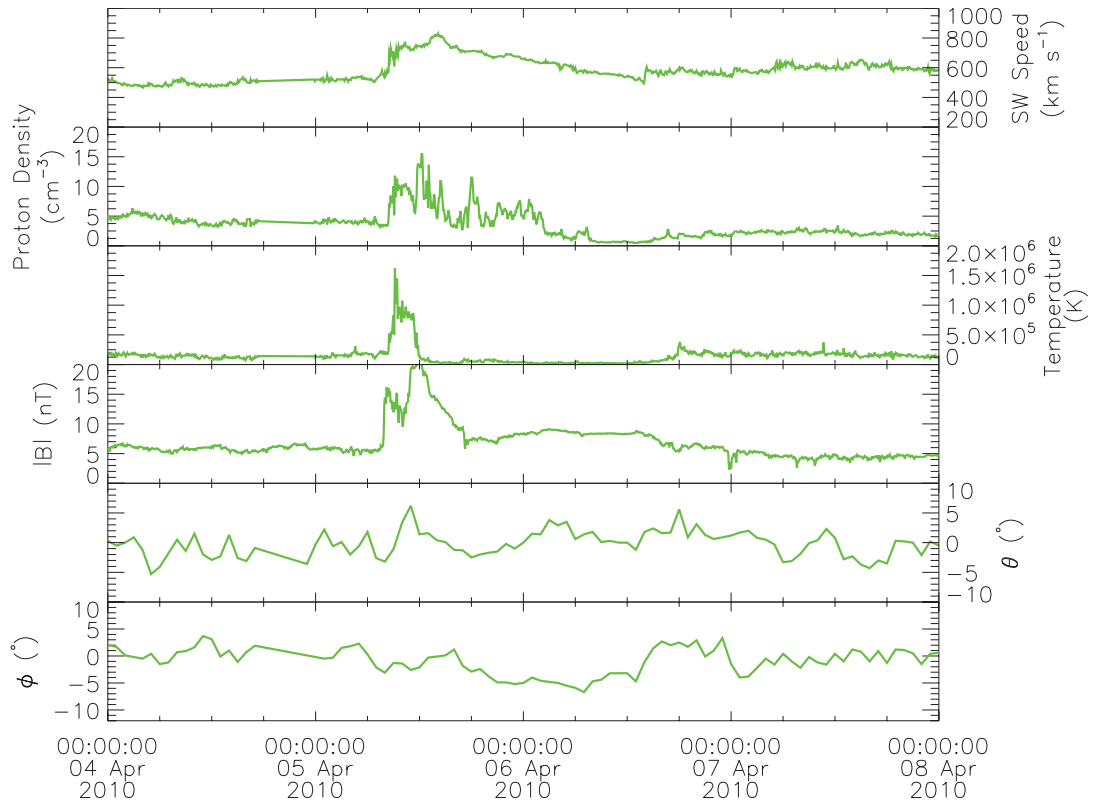


Figure 4.45: In-situ data taken from the OMNI data. From top-to-bottom: solar wind speed, proton density, temperature, magnetic field magnitude, elevation, and azimuth.

There has not been any other reported work done for this particular CME event, so no angular comparisons can be made.

## 4.5 Results and Discussion

Three CME events were analysed in this thesis, bringing together two separate techniques to calculate the 3-D propagation angle, and the kinematic profiles of each CME.

Firstly, each CME's leading edge was stereoscopically triangulated (when possible), and the 3-D position of the furthest point of the leading edge in each sequence recorded.

In each example, the leading edge would deflect from regions of high or low latitude towards the equatorial plane. This agrees well with the work presented in Gopalswamy et al. (2003); Byrne et al. (2010), who suggest that the over-expanding magnetic field from polar coronal holes guide a CME towards the equator. In two of the three examples, this latitudinal deflection occurs within  $3 - 4R_{\odot}$ , when the Sun is at solar minimum. In the 3rd April 2010 CME, this latitudinal deflection is found at a distance up to  $40R_{\odot}$ . However, in this case, HI-1 data was also used, and therefore the stereoscopic data was obtained for much longer distances than the previous two examples.

Each CME shows close-to-Sun ( $< 4R_{\odot}$ ) longitudinal deflections. The 2007 and 2010 CME examples experience rapid westward deflections due to the magnetic field connecting the Sun and the ejecta, as predicted by Liu et al. (2010). However, the 2008 CME experiences an eastward deflection which contradicts Liu et al. (2010). The predictions made by Wang et al. (2004) for fast CMEs indicate an overall eastward deflection at 1 AU, and this is the case for the two fast CMEs presented in this thesis, although the actual deflection is smaller in each case than that predicted by Wang et al. (2004).

Secondly, j-maps were created for each CME example. With the 2007 CME, there was a major discrepancy between the longitudes calculated between the two techniques; it is believed in this case that the j-map fitting technique did not produce

## CHAPTER 4

Table 4.9: Table summarising the results found from all three CME examples

Date	Speed	Region	Early $\Theta$ Deflection	Early $\Phi$ Deflection	2 Methods Agree?
3-Dec-2007	slow	Western limb	High $\rightarrow$ Equator	Westward	$\times$
25-Mar-2008	fast	Eastern limb	Low $\rightarrow$ Equator	Eastward	$\checkmark$
3-Apr-2010	fast	Earth-directed	Low $\rightarrow$ Equator	Westward	$\checkmark$

accurate results. The technique relies upon the assumption that the CME undergoes no acceleration in the heliosphere, and also travels in a constant radial direction. But, if the CME interacts with the faster solar wind, it is likely to be deflected (in a westward direction) to some extent, and also experience some acceleration. If this happens, then the assumptions needed for the technique to work become invalid. Also, the rotation of the spacecraft around the Sun is not taken into account. For slow CMEs, such as this example, this is likely to have a larger impact upon the analysis since the CME stays in the FOV for much longer, than for a much faster CME. There have been other examples, although none published to date, where slow CMEs do not work well with the j-map fitting method. However, for the fast CMEs (the 2008 and 2010 CMEs), the directions agreed well with the stereoscopic triangulation method.

These results are summarised in Table 4.9.

From these results alone, it can be seen that there is no one model that fits all. Each CME has brought up at least one contradiction from predictions in previous

## CHAPTER 4

research.

The assumption that a CME will propagate in a constant direction and constant velocity appears to have been validated, at least once the CME leaves the acceleration phase, by in-situ data. In-situ data is the only way of validating any results, and where it has been available, it has been in agreement, both in this work, and other's (eg. Rouillard et al. 2010).

### Summary

- CMEs will experience rapid latitude and longitude deflections close-to-the-Sun ( $< 4R_{\odot}$ )
- Fast CMEs work well with the j-map method; slow CMEs do not
- In-situ data verifies that fast CMEs approximately propagate in a constant direction at a constant velocity

## Chapter 5

# Multi-strand 1-D Hydrodynamic Coronal Loop Simulations

Coronal loops are the basic structural elements of the solar corona, and considerable effort has gone into the research to understand these phenomena. Of particular interest is the temperature structure along these plasma loops, and the heat input associated with that.

In order to reach the observed temperatures in coronal loops (1 MK+), a heating mechanism is required. Parker (1988) suggests the concept of nanoflares as one possible mechanism, where the plasma is heated by the cumulative effect of numerous small-scale, time-dependent, localised energy bursts of  $\sim 10^{24}$  erg per event.

The frequency of occurrence ( $f$ ) of larger solar flares has a dependence on their energy content ( $E$ ), and it follows the power law:

$$\frac{df}{dE} = E_0 E^{-\alpha} \quad (5.1)$$

where  $\alpha \sim 1.8$ . However, for the corona to be predominantly heated by nanoflare events, Hudson (1991) calculated that the power law slope should be steeper, with  $\alpha > 2$ . This steeper distribution has been noted from observed brightening in X-ray

## CHAPTER 5

and EUV by several authors, including Parnell and Jupp (2000) and Pauluhn and Solanki (2007).

In the studies by Cargill (1994); Cargill and Klimchuk (1997); Klimchuk and Cargill (2001); Cargill and Klimchuk (2004), the authors assumed that a coronal loop could be made out of many sub-resolution strands. Each strand could be represented by a single temperature and density value only, in a 0-D hydrodynamic simulation. In these simulations, each strand experiences impulsive nanoflare heating, where the energy deposition occurs on timescales much shorter than the plasma cooling time. The heated plasma is cooled firstly by conduction, and then by radiation. In this method, a loop consisting of many strands (500-5000) and its observables were calculated. The results indicated that by increasing the number of strands, the overall average temperature increases slightly, but the emission measure remains almost unaffected.

Patsourakos and Klimchuk (2005) used their multi-stranded, nanoflare-heated model to show that TRACE and Yohkoh SXT emission was only weakly affected by changing the location of the heat-inputs (i.e. apex dominated heating (ADH), spatially uniform heating (SUH), or footpoint dominated heating (FDH)). However, throughout this chapter, this suggestion is investigated and discussed.

The research in this chapter relies heavily upon, but extends further, the works of Sarkar and Walsh (2008), and Sarkar and Walsh (2009). However, during the course of the research undertaken in this chapter, an error in the work of Sarkar and Walsh (2008) and Sarkar and Walsh (2009) was discovered. This error was located in a part of the simulation which incorrectly interpreted the Rosner et al. (1978) radiative loss function. This was due to the radiation being undefined for temperatures lower than 20,000 K, and with a temperature at the footpoints set at 10,000 K, there was this large, and important, temperature range where there was no radiation. This error was the source of the large quantity of high-density, low-temperature

## CHAPTER 5

“plasmoids” found to occur throughout the loop structure. These plasmoids affected the temperature, velocity and density profiles of the loop. The work presented throughout this chapter uses the Hildner (1974) radiative loss function to correct for this error.

The work in this chapter further investigates the effects of changing the location of the energy bursts, upon the loop temperature. Furthermore, line-of-sight Doppler velocities are calculated along the loop, using a selection of CHIANTI emission lines. Also, the effects of changing the energy content of each energy burst, and therefore the effect of changing the overall total energy deposited in the system, is investigated and discussed, as well as investigating changing the number of strands in the loop system and the number of energy bursts per strand. These are then compared with observations to discuss the implications of the findings, and provide further evidence that loops can indeed be split into many sub-resolution strands. This is important to increase understanding of the underlying physics of coronal loops, and to match theory to observation.

### 5.1 Single Strand Model

The model in this chapter follows that of Sarkar and Walsh (2008). Consider a loop 10 Mm in length, with a cross-sectional radius of 1.1 Mm. Let us assume that the loop consists of 125 individual plasma strands that fill the loop volume, so that each strand radius is 0.098 Mm. Each strand is thermally independent, so therefore the dynamics along one strand do not affect any other.

#### 5.1.1 Numerical Model of a Single Strand

1-D hydrodynamics can be used to simulate the plasma in each strand. It is assumed that the corona is a highly conducting, low- $\beta$  medium, and therefore the magnetic

## CHAPTER 5

field confines the plasma along flux tubes. A Lagrange remap 1-D hydrodynamic code, adapted from Arber et al. (2001), is employed for the purpose of solving the following time-dependent 1-D differential equations of mass, momentum, and energy conservation:

$$\frac{D\rho}{Dt} + \rho \frac{\partial}{\partial s} v = 0 \quad (5.2)$$

$$\rho \frac{Dv}{Dt} = -\frac{\partial p}{\partial s} + \rho g + \rho \nu \frac{\partial^2 v}{\partial s^2} \quad (5.3)$$

$$\frac{\rho^\gamma}{\gamma - 1} \left( \frac{p}{\rho^\gamma} \right) = \frac{\partial}{\partial s} \left( \kappa \frac{\partial T}{\partial s} \right) - n^2 Q(T) + H(s, t) \quad (5.4)$$

$$p = \frac{R}{\bar{\mu}} \rho T \quad (5.5)$$

$$\text{where } \frac{D}{Dt} \equiv \frac{\partial}{\partial t} + v \frac{\partial}{\partial s}$$

Where,

- $\rho$  : is the mass density
- $p$  : is the pressure
- $n$  : is the particle density
- $v$  : is the velocity
- $T$  : is the temperature of the plasma
- $\nu$  : is the coefficient of kinematic viscosity, assumed to be uniform throughout the plasma

## CHAPTER 5

- $g$  : is assumed to be a constant, with  $g = 2.74 \times 10^4 \text{ s}^{-2}$  for all points along the loop
- $s$  : is the spatial coordinate along a 10 Mm strand so that  $-5 < s < 5$ , and is assumed to semi-circular.
- $\gamma$  : is the adiabatic index of the medium, with  $\gamma = 5/3$
- $\kappa$  : is the conductivity of the plasma in the direction of  $s$ , with  $\kappa = 9.2 \times 10^{-7} \text{ T}^{5/2} \text{ erg s}^{-1} \text{ cm}^{-1} \text{ K}^{-1}$
- $R$  : is the molecular gas constant, with  $R = 8.3 \times 10^7 \text{ erg mol}^{-1} \text{ K}^{-1}$
- $\bar{\mu}$  : is the mean molecular weight, with  $\bar{\mu} = 0.6 \text{ mol}^{-1}$
- $H(s, t)$  : is the spatially and temporally dependent coronal heating term
- $Q(T)$  : is the Hildner (1974) optically thin radiative loss function (see Figure 6.1)

$$\text{where } Q(T) \approx \begin{cases} 5.51 \times 10^{-30} T^{-1}, & T \geq 8 \times 10^5 \text{ K} \\ 3.94 \times 10^{-21} T^{-2.5}, & 8 \times 10^5 > T \geq 3 \times 10^5 \text{ K} \\ 8 \times 10^{-35} T^0, & 3 \times 10^5 > T \leq 8 \times 10^4 \text{ K} \\ 1.2 \times 10^{-43} T^{1.8}, & 8 \times 10^4 > T \leq 1.5 \times 10^4 \text{ K} \\ 4.92 \times 10^{-27} T^{7.4}, & T < 1.5 \times 10^4 \end{cases}$$

The loop is assumed to be symmetrical, and at the loop apex ( $s = 0$ ), initially:

$$\frac{\partial T}{\partial s} = \frac{\partial p}{\partial s} = 0 \quad (5.6)$$

The boundary conditions are:

$$T(-5, t) = T(5, t) = T_{ch} = 10^4 \text{ K} \quad (5.7)$$

$$p(-5, t) = p(5, t) = p_{ch} = 0.314 \text{ Pa} \quad (5.8)$$

which describe the temperature and pressure at the loop footpoints deep in the chromosphere (where  $T_{ch}$  and  $p_{ch}$  are the chromospheric temperature and pressure, respectively). The chromosphere has a depth of 0.4 Mm at the footpoint of each loop end. At the start of the simulation, the temperature along the strand is kept at  $10^4$  K (chromospheric value), and the velocity along the strand is set to zero. The density and pressure decrease exponentially towards the strand apex. As a result, the plasma is gravitationally stratified, and higher density plasma in the chromosphere is available for chromospheric evaporation.

The sudden release of nano-flare events produces a travelling shock front throughout the strand plasma. The Lagrange remap code (Arber et al., 2001) has been shown to cope well with resolving this type of front. To optimise the simulation in terms of a reasonable simulation run time, and the required resolution to track the dynamic features in the strand, an average grid spacing of 0.037 Mm was employed.

### 5.1.2 Plasma Response in a Single Strand to a Discrete Energy Burst

The response of the plasma in a single strand due to a single discrete energy burst (containing  $1.049 \times 10^{24}$  erg) is examined in Figure 5.1; this displays snapshots of the temperature and the density at different stages of the plasma evolution. The energy burst takes place after 50 seconds of the start of the simulation, and has a lifetime of  $\tau = 50$  seconds, at which point the heating is switched off. The heating is localised at  $s = -2.3$  Mm (which is 2.3 Mm to the left of the loop apex), and occurs over a length scale of 0.2 Mm.

The temperature of the strand firstly increases to  $\sim 4$  MK where the heating is localised, as shown by the snapshot at 51.75 seconds in Figure 5.1. The heat is then conducted throughout the rest of the strand, which reaches an overall temperature of up to 5 MK. As a result of this sudden heating, a shock front develops that

## CHAPTER 5

propagates along the strand with a velocity of up to  $160 \text{ km s}^{-1}$ , as shown in the velocity snapshots in Figure 5.1. A slight increase in temperature is observed with the propagation of the front, as expected from basic acoustic shock front physics where there is always an extremely rapid rise in pressure, temperature and density of the flow in front of the shock.

After 100 seconds, the heating is switched off. Sound waves bounce back and forth along the strand, reflecting off the high-density boundary of the chromosphere. Subsequently, the overall temperature starts to decrease, and the shock front begins to decay.

The dominant cooling mechanisms of conduction and radiation is determined automatically by solving the set of hydrodynamic equations. The model is also capable of transporting localised extra heat by means of mass flow through enthalpy flux. Figure 5.2 shows the evolution of the strand temperature and density at the strand apex ( $s = 0$ ) after the energy burst. The density evolution clearly shows chromospheric evaporation taking place at until approximately 350 seconds. The density then begins to decline as the plasma condenses back to the chromosphere. Small scale structures exist due to the flow of material along the loop as the plasma cools, and the evolution of this plasma flow is shown in Figure 5.1.

## 5.2 125 Multi-Strand Model - Varying the Spatial Distribution of the Discrete Energy Bursts

In this section, a loop consisting of 125 individual strands, which evolve hydrodynamically independently of each other is considered. However, it is important to note that the strands are related through the frequency distribution of the total energy input across the loop.

There are a number of fundamental aspects to the multi-strand heat deposition

## CHAPTER 5

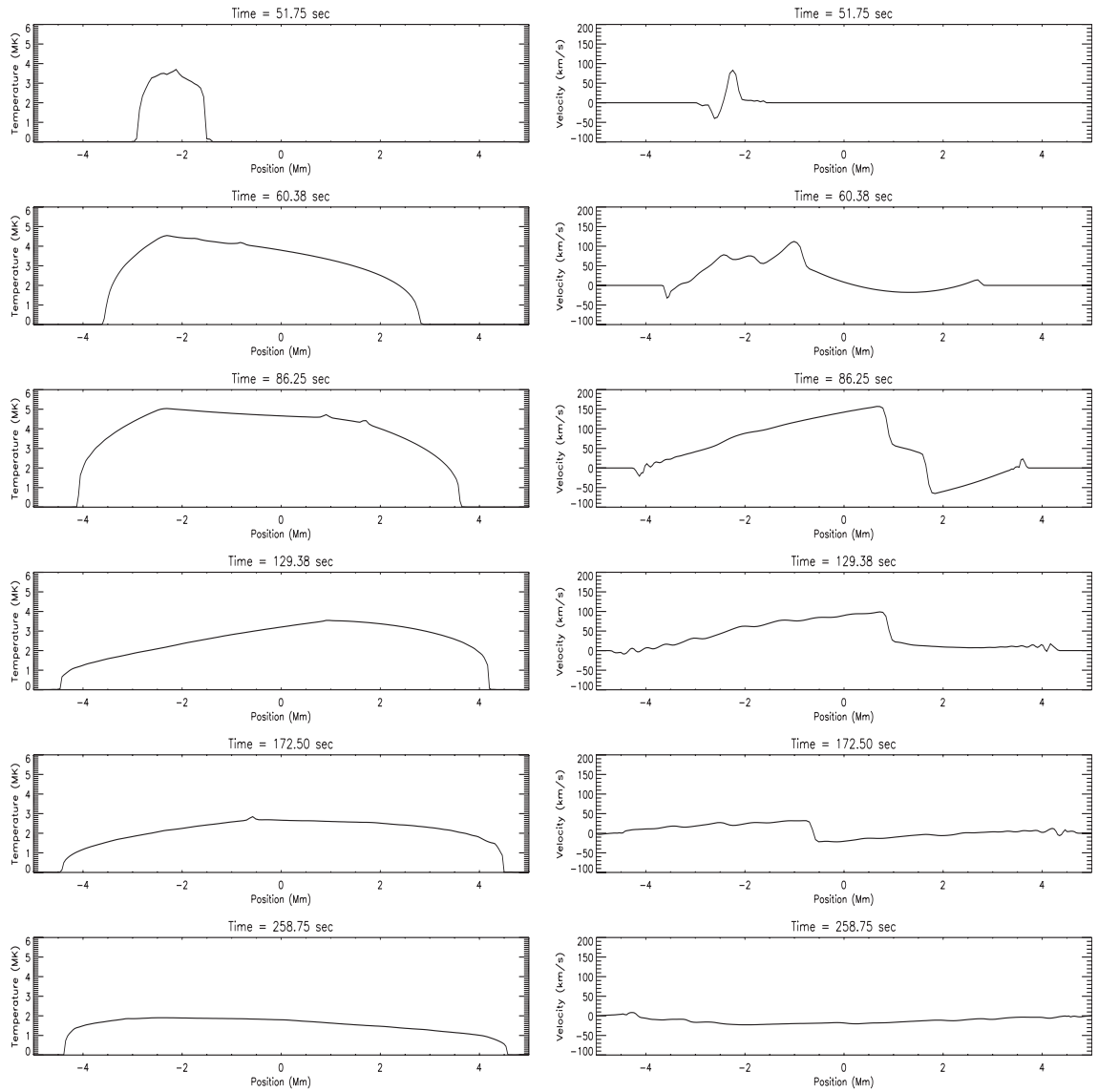


Figure 5.1: Snapshots of the strand evolution in temperature (left) and velocity (right) in response to a discrete energy burst containing  $1.049 \times 10^{24}$  erg of energy being deposited at a position  $s = -2.5$  Mm.

## CHAPTER 5

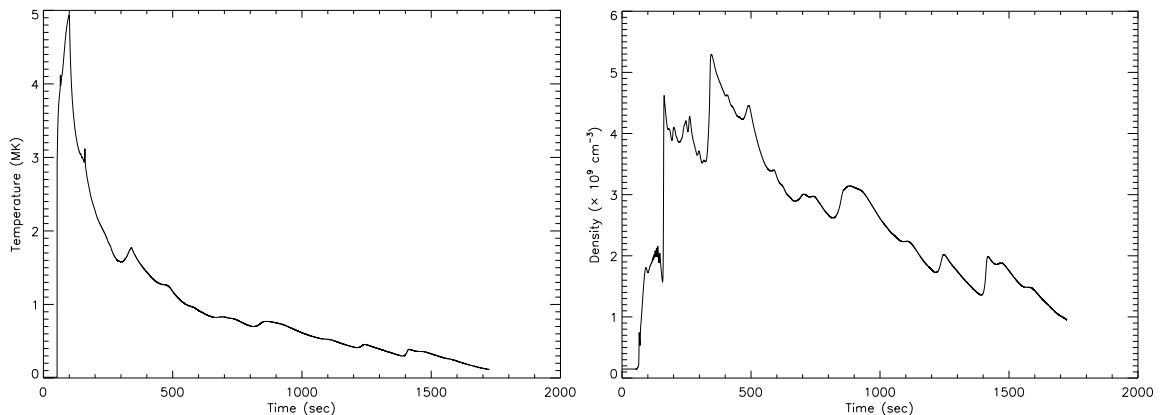


Figure 5.2: Evolution of the strand apex temperature (left) and density (right) after the discrete energy burst

mechanism that must be considered. The localised heat input  $H(s, t)$  from a discrete energy burst, which has a given amount of energy  $E$ , over an event lifetime  $\tau$  is chosen randomly in time, with constraints  $1.00 \times 10^{23} \text{ erg} \leq E \leq 5.38 \times 10^{24} \text{ erg}$ , and  $50 \text{ s} \leq \tau \leq 150 \text{ s}$ . The location of the heat input ( $S_L$ ) is kept in the range  $-4.44 \text{ Mm} \leq S_L \leq 4.44 \text{ Mm}$  so as to avoid the chromospheric part of the structure, while the events are released in an element length of  $0.2 \text{ Mm}$ . However, three spatial ( $H(s)$ ) cases of heat input are used separately throughout this section, namely: apex dominated heating (ADH), where the discrete energy bursts are concentrated towards the apex of each strand; spatially uniform heating (SUH), where the energy bursts are spread evenly over the length of the loop (excluding the chromospheric footpoints); footpoint dominated heating (FDH), where the energy bursts are located predominantly towards the loop footpoint, but outside of the chromospheric part of the loop. Figure 5.3 displays a histogram illustrating the spatial distribution of the energy bursts. Each strand experiences 57 energy bursts. The results in this chapter will investigate, amongst others, the impact of changing the spatial distribution of the energy bursts, upon the resulting thermal and velocity profiles.

The overall energy-release profile follows the power-law given in Equation 5.1,

## CHAPTER 5

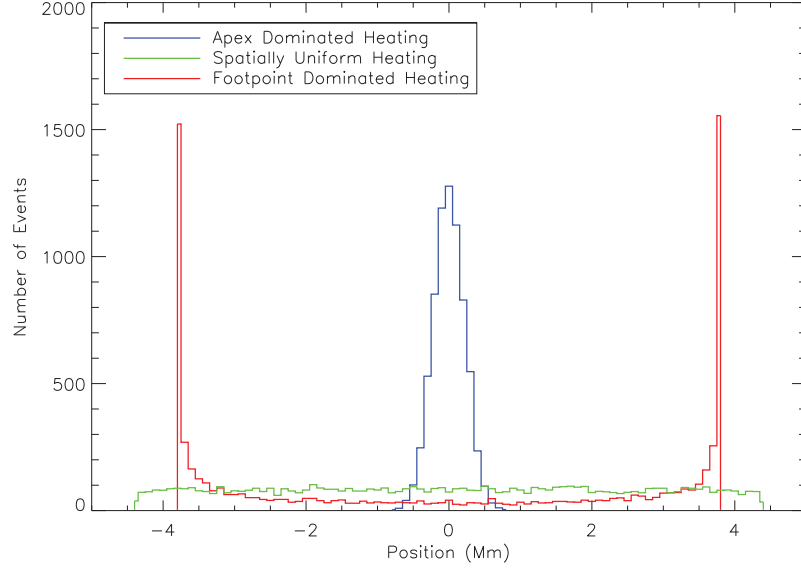


Figure 5.3: Histogram showing the spatial energy distribution for ADH (blue), SUH (green) and FDH (red) heating.

with a value of  $\alpha$  kept fixed at 2.3, as can be seen in Figure 5.4. The total energy input into the loop is also kept fixed throughout this section, with a value of  $4.5 \times 10^{27}$  erg; we will refer to this as  $E_{Total}$ .

All 125 strands are combined to form a global loop. Since individual strands are unresolved, the observed temperature is affected by the composite emission of all the strands together (Sarkar and Walsh, 2008). Therefore, it is important to include a weighting to the derived temperature, which depends upon the emission measure ( $EM$ ). The emission measure is defined as:

$$EM = \int_V n^2 dV \quad (5.9)$$

where  $V$  is the plasma volume.

The emission measure weighted temperature ( $T_{em}$ ), is therefore defined as:

$$T_{em}(s, t) = \frac{\sum_{i=1}^r n_i^2(s, t) T_i(s, t) dl(s)}{\sum_{i=1}^r n_i^2(s, t) dl(s)} \quad (5.10)$$

where  $r$  is the number of strands in the loop,  $n(s, t)$  is the density evolution in

## CHAPTER 5

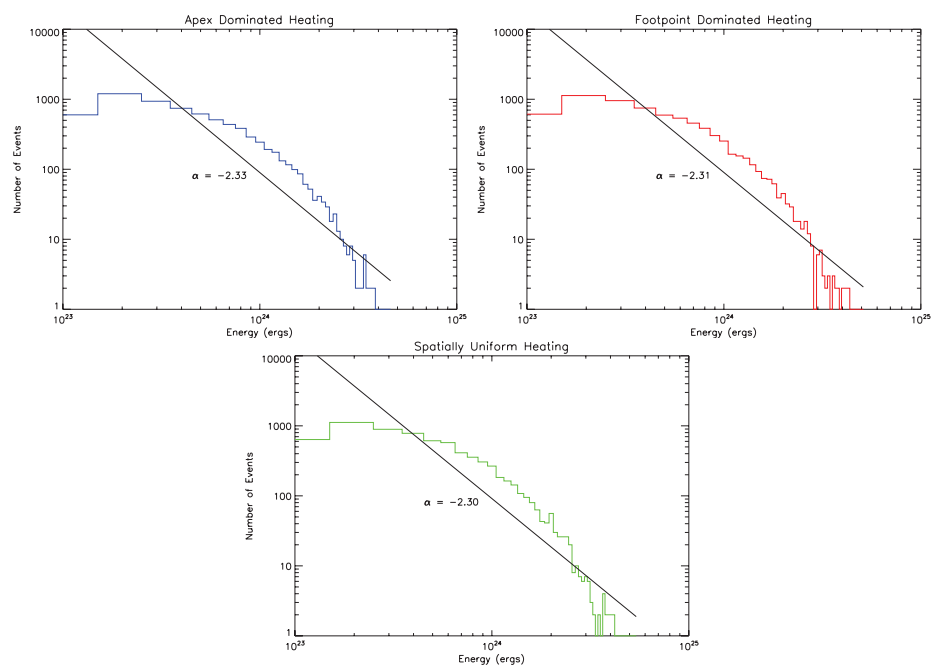


Figure 5.4: Energy histograms for the three different cases of spatial heating, with straight lines fitted to show the power-law slope, which has a value of  $\alpha = 2.3$  in all cases.

## CHAPTER 5

space ( $s$ ) and time ( $t$ ),  $T$  is the strand temperature, and  $dl(s)$  is the grid resolution.

Similarly, a line filtered emission measure weighted velocity ( $V_{cf}$ ) is also calculated, and this is defined as:

$$V_{cf}(s, t) = \frac{\sum_{i=1}^r n_i^2(s, t)C(T)v_i(s, t)dl(s)}{\sum_{i=1}^r n_i^2(s, t)C(T)dl(s)} \quad (5.11)$$

where  $v(s, t)$  is the velocity evolution, and  $C(T)$  is the contribution function of a particular spectral line. If one were to observe the plasma flow velocity in a coronal loop from a spacecraft observation, the line-of-sight velocity is what would be observed, and as such, this is used throughout this work. Any values with a positive value are thus travelling away from the observer (and towards the loop footpoints), and appear red-shifted. Conversely, values of a negative value would be travelling towards the observer (and towards the loop apex), and so would appear to be blue-shifted. Figure 5.5 illustrates this. The line-of-sight velocity is therefore calculated by multiplying the derived velocities by  $\sin \phi$ , so that at the loop apex,  $\sin(\phi = 0^\circ) = 0$ , and at the footpoints,  $\sin(\phi = 90^\circ) = 1$ .

The effect on the loop apex temperature by altering the spatial distribution of the energy bursts is analysed in Section 5.2.1, while the impact on the loop line-of-sight velocity is discussed in Section 5.2.2. In each simulation, the discrete energy bursts will release the same amount of energy, and at the same time during the simulation. The only difference is the locality of the energy bursts.

### 5.2.1 Effect on Loop Temperature

Figure 5.6 shows the time evolution of the emission measure weighted temperature at the loop apex for the three different cases of spatial heating. A period of 25 minutes is selected in all simulations ( $9900 \leq t \leq 11400$  s), and from this period, the mean temperature is calculated.

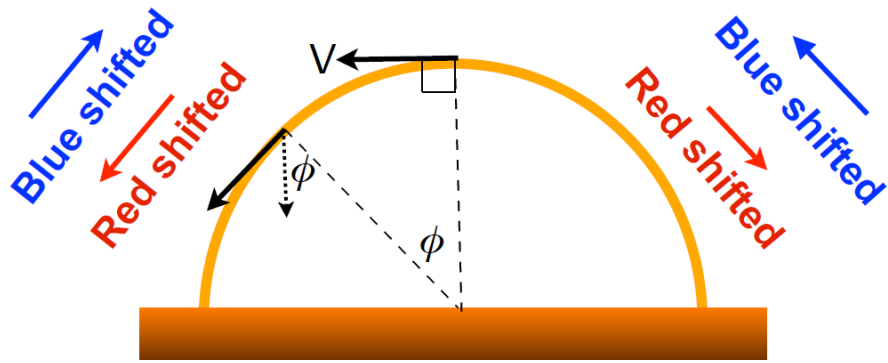


Figure 5.5: Line of sight velocity

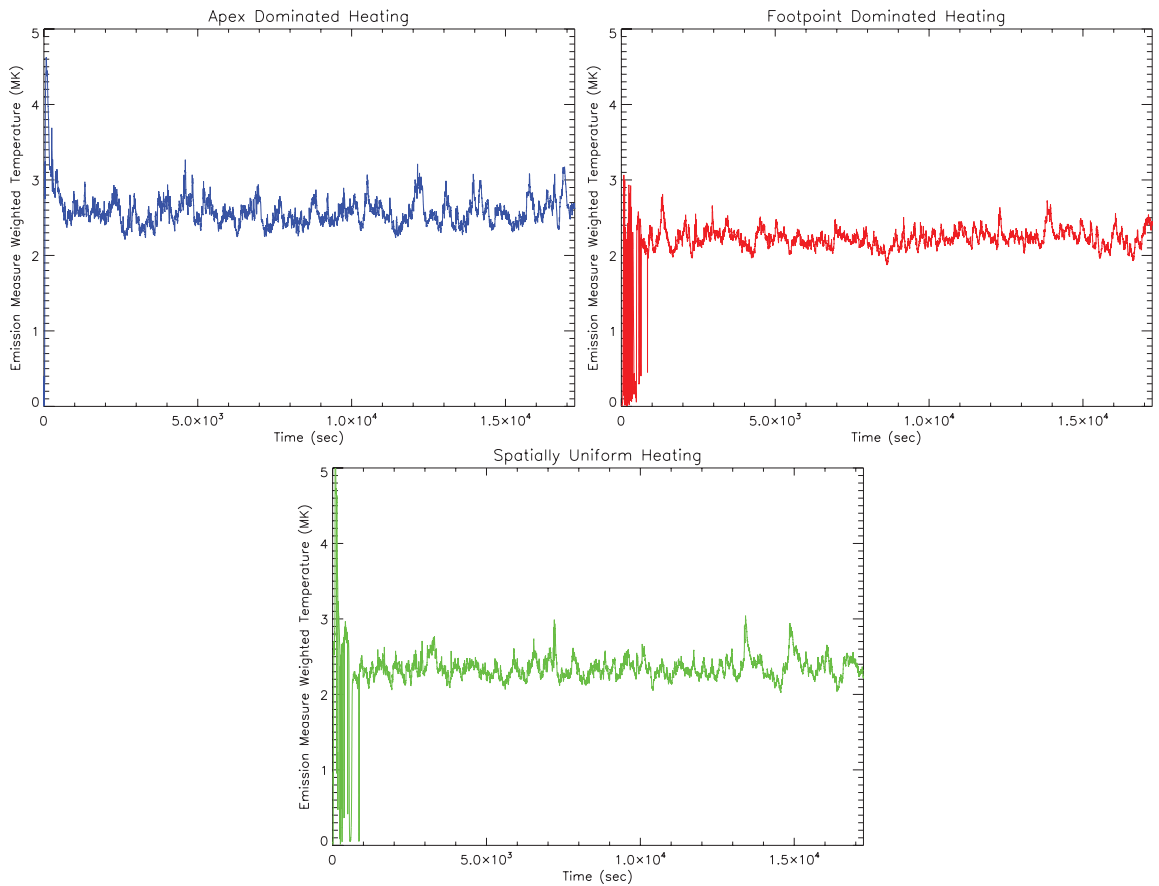


Figure 5.6: Time evolution of the emission measure weighted temperature at the loop apex for 125 stranded loop with apex (left), footpoint (right) and uniform (bottom) heating.

## CHAPTER 5

Figure 5.7 presents the time-averaged emission measure weighted temperature of the half-loop system. This shows there to be a notable difference in the temperature gradient from  $\sim -4$  Mm upwards, dependent on the location of the heat input. For the case with ADH, the apex temperature reaches a mean of 2.59 MK. The energy bursts occur at the loop apex, where thermal conduction dominates as the energy mechanism. As a result, the average temperature and the temperature gradient has to increase in order to account for the deposited heat, since radiation is so low. The SUH simulation presents a lower mean apex temperature of 2.31 MK. The energy bursts occur along the whole structure, and since there is a relatively flat coronal temperature gradient, there must be a balance between heating, conduction and radiation. FDH produces the lowest mean apex temperature of 2.23 MK. All the energy bursts are located towards the footpoint, where there is also high density, and so both radiation and conduction balance the heating. For the coronal part of the loop, the temperature gradient is very flat, and so therefore thermal conduction is negligible.

### 5.2.2 Effect on Loop Line-of-Sight Velocity

Observations of plasma up-flows and down-flows in coronal loop system, from satellites such as Hinode, with EIS (eg. Del Zanna, 2008) have shown clear evidence of:

1. red-shifted velocities in cooler lines, with typical speeds of  $20 - 30 \text{ km s}^{-1}$  in Fe VIII. Also, in the hotter Fe XII line, typical velocities reach  $5 - 10 \text{ km s}^{-1}$  (hot loop).
2. blue shifted velocities in the same locations, being predominantly seen in hotter lines, with typical ranges of  $5 - 20 \text{ km s}^{-1}$  in Fe XII (cooler loop) and  $10 - 30 \text{ km s}^{-1}$  in Fe XV.

## CHAPTER 5

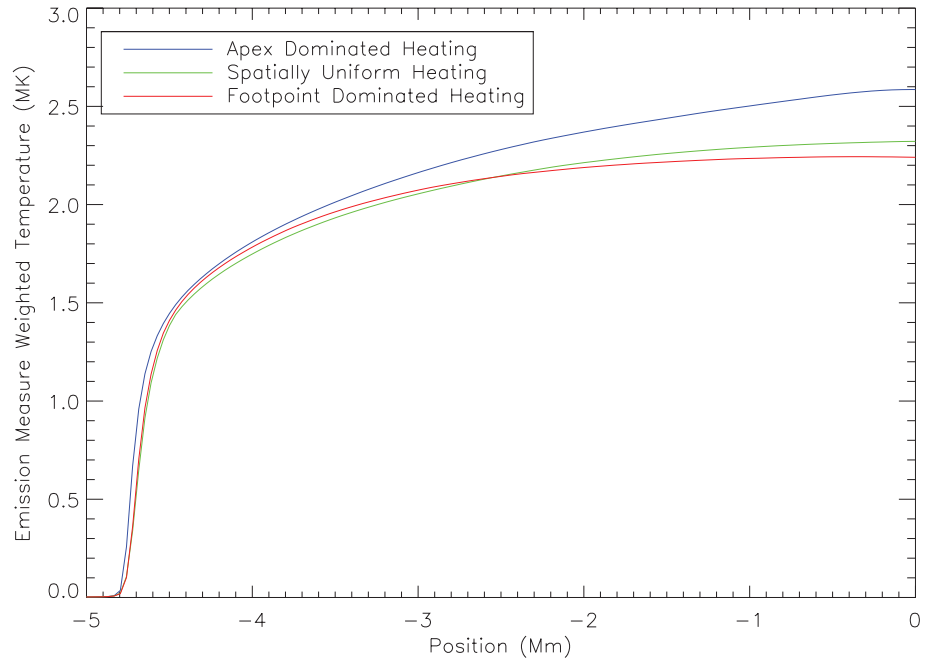


Figure 5.7: Average temperature of the loop for each of the spatial heat inputs (0 Mm = loop apex).

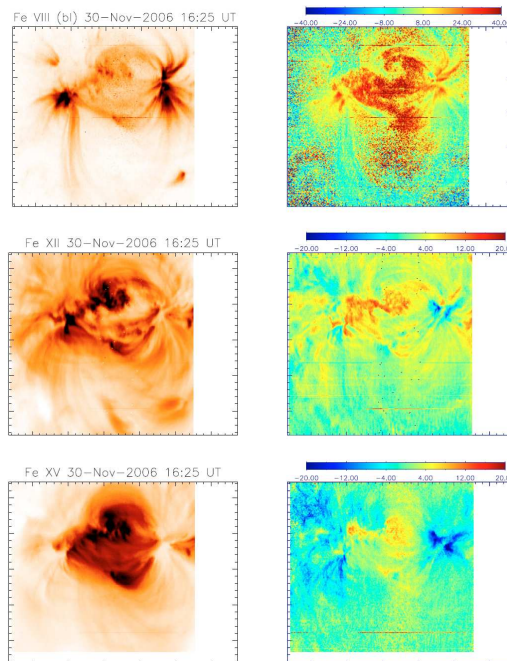


Figure 5.8: From Del Zanna (2008): Monochromatic (negative) images and dopplergrams ( $\text{km s}^{-1}$ ) of NOAA 10926 in Fe VIII, Fe XII, Fe XV

## CHAPTER 5

Del Zanna (2008) agree with previous observations that red shifts are greater in cooler lines. However, Del Zanna (2008) states that blue-shifts are located in boundary sharp regions and that the shifts are higher in higher-temperature coronal lines. The strongest blue shifts are in regions of low density, and are therefore difficult to observe.

Hara et al. (2008) observe moderate ( $5\text{-}10 \text{ km s}^{-1}$ ) blue shifts in coronal lines at the footpoints with EIS observations, whilst Tripathi et al. (2009) find that:

1. down-flows are predominantly seen in the core of the active region, and that up-flows are seen at the boundary of the active region in the low emission regions. As the temperature is increased, the regions showing red-shifted emission turn towards blue-shifted emission.
2. down-flows are observed all along the loop at all temperatures. In Si VII, the down-flows are seen only towards the foot-points, with velocities reaching  $\approx 60 \text{ km s}^{-1}$ . In the higher temperature lines of Fe X and Fe XII, the down-flows are localised towards the loop apex.

With the above in mind, the work presented in this section uses contribution functions, obtained from the CHIANTI database (Dere et al., 1997), for three emission lines spread over a range of (characteristic) temperatures, from  $0.63 - 2.0 \text{ MK}$ . In doing so, observables are produced from the simulation results, and line-of-sight velocities from each emission line are compared with each heating case, from the same 25 minute period previously used:  $9900 \leq t \leq 11400 \text{ s}$ . The contribution functions are plotted in Figure 5.9, and are also presented in Table 5.1.

### **Si VII 275.36 Å**

The coolest of the three lines, Si VII, has a characteristic temperature of  $0.63 \text{ MK}$ . Along the length of the loop, it is predominantly red shifted, as can be seen from

CHAPTER 5

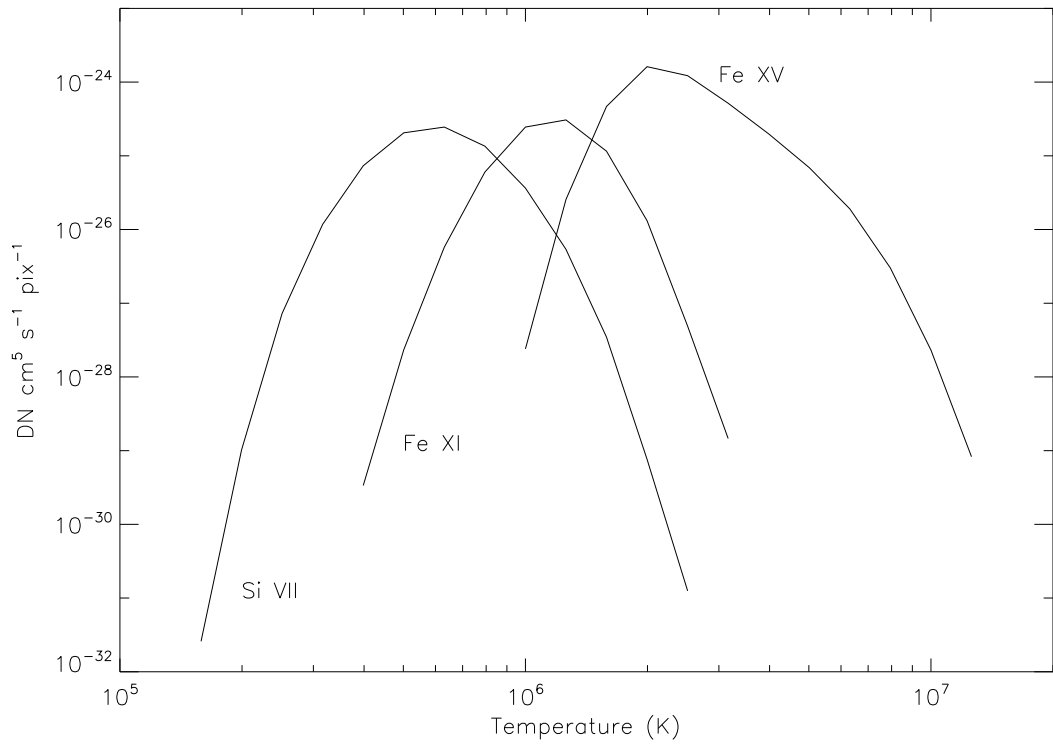


Figure 5.9: Chianti contribution functions for Si VII, Fe XI, and Fe XV

Table 5.1: Chianti contribution lines

Emission Line	Wavelength (Å)	Characteristic Temperature (MK)	Temperature Range (MK)
Si VII	275.36	0.63	0.16 - 2.51
Fe XI	188.23	1.26	0.40 - 3.16
Fe XV	284.16	2.00	1.00 - 12.59

## CHAPTER 5

Figure 5.10 (left-hand-side). Towards the loop apex, only red shifts are seen in the ADH case, whilst a small number of blue shifted pixels are seen in the SUH case, and more so in the footpoint case.

This line filter has the highest predominance of red shift of all the line filters used, with 96.10%, 92.94%, and 91.23% of pixels red shifted for the ADH, SUH, and FDH cases in Figure 5.10 (left-hand-side), respectively. Figure 5.10 (middle row) shows their respective histograms, which details the predominance of red shift. There is a bump in the red shifted data, which is caused by the line-of-sight effect. The higher velocities are located toward the footpoint, where the line-of-sight effect has less impact, and as a result we see this bump in the data.

Figure 5.10 (right-hand-side) displays the average blue and red shift velocities along the length of the loop. The mean velocity profiles show no blue shift in any of the three cases, whilst reaching a mean red shift velocity of  $2.3 - 2.6 \text{ km s}^{-1}$  towards each footpoint.

### **Fe XI 188.23 Å**

The Fe XI line filter has a characteristic temperature of 1.26 MK. The loop is slightly more blue shifted than the Si VII line, with 92.77%, 80.97% and 81.20% of the pixels being red shifted in the ADH, SUH and FDH cases respectively. The increase in blue shift is due to an increase in the temperature range of the line filter, with the majority of the blue shifts occurring towards the loop apex.

The mean velocity profiles (see Figure 5.11) show only red shifted velocities, in the range  $1.5 - 2 \text{ km s}^{-1}$ .

### **Fe XV 284.16 Å**

The hottest of the line filters, Fe XV, has a characteristic temperature of 2.00 MK. The loop is now predominantly blue shifted, with 56.62%, 55.72%, and 53.18% of

## CHAPTER 5

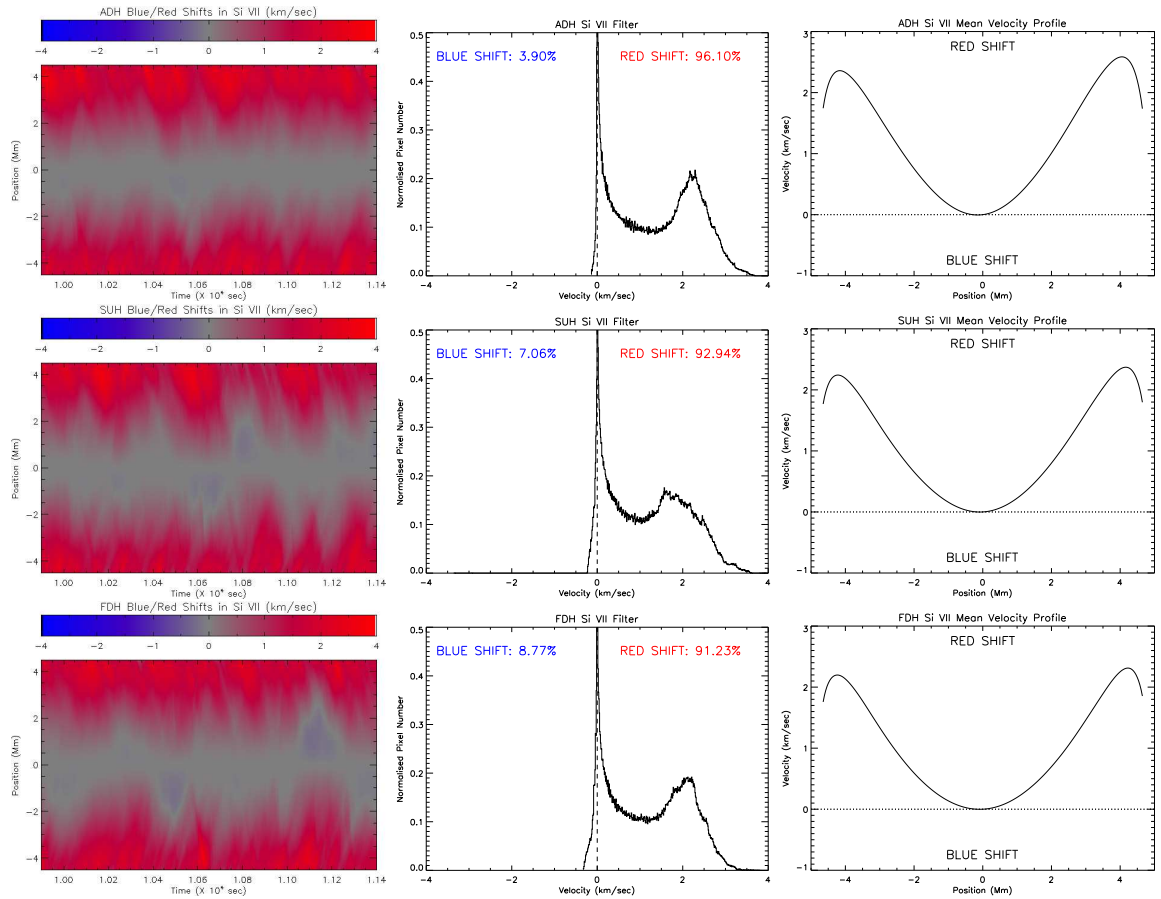


Figure 5.10: Si VII line-of-sight blue/red shifts for the three cases of spatial heating (left), their corresponding histograms (centre), and the time-averaged mean blue/red  $V_{cf}$  along the loop (right).

## CHAPTER 5

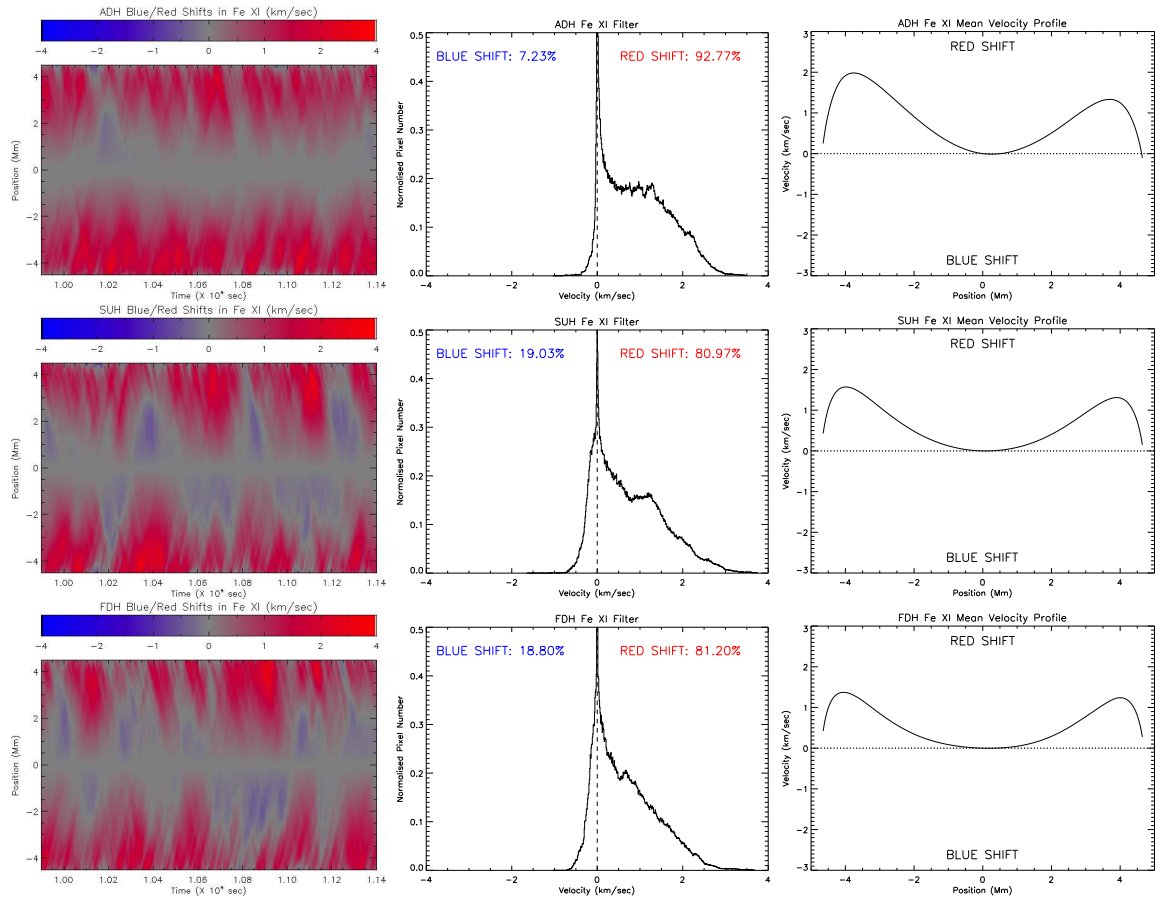


Figure 5.11: Fe XI line-of-sight blue/red shifts for the three cases of spatial heating (left), their corresponding histograms (centre), and the time-averaged mean blue/red  $V_{cf}$  along the loop (right).

## CHAPTER 5

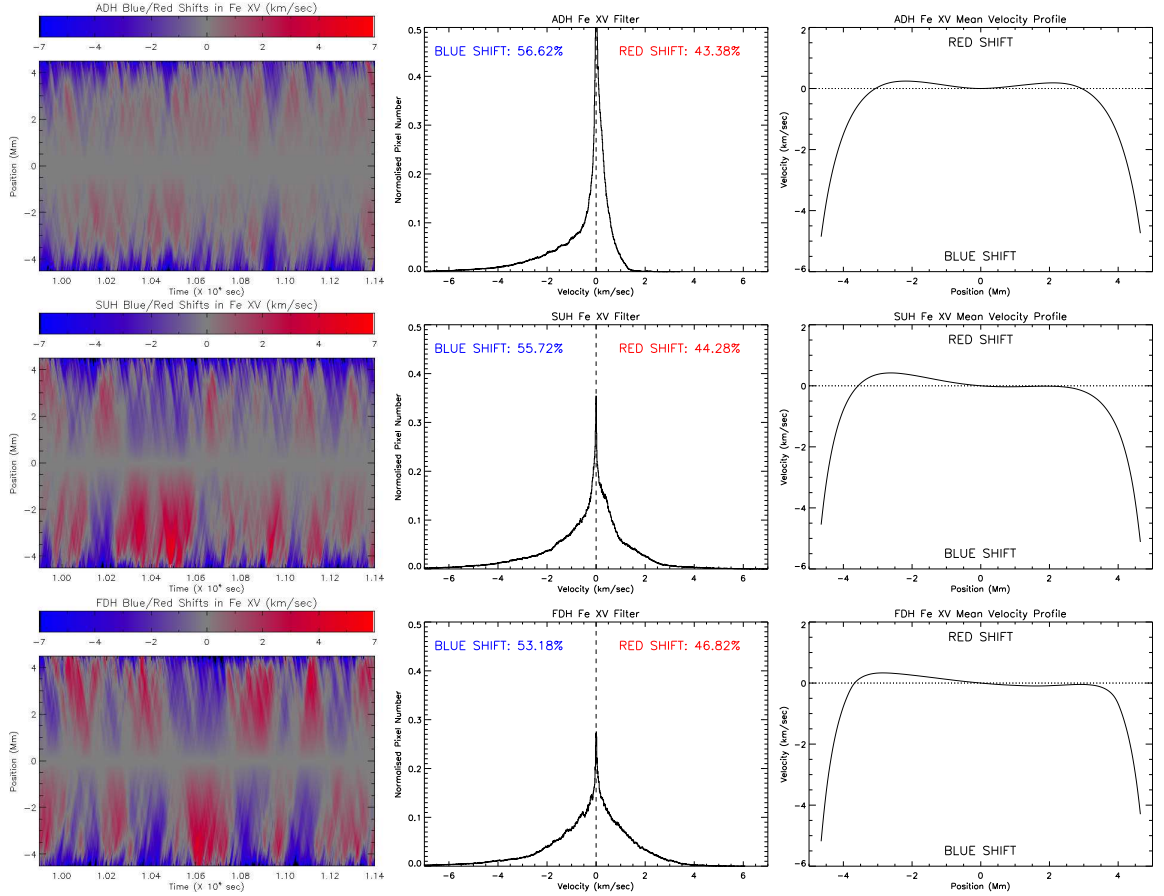


Figure 5.12: Fe XV line-of-sight blue/red shifts for the three cases of spatial heating (left), their corresponding histograms (centre), and the time-averaged mean blue/red  $V_{cf}$  along the loop (right).

pixels being blue shifted, in Figure 5.12 (left-hand-side) for the ADH, SUH, and FDH cases, respectively. The footpoints show a predominance of blue shift, while red and blue shifts are seen along the rest of the loop. Again, this increase in blue shift is due to the increase in temperature of the line filter, where hotter plasma is being evaporated towards the loop apex.

The mean velocity profiles show that footpoints are predominantly blue shifted with velocities reaching an average blue shift of  $4.5 - 5 \text{ km s}^{-1}$ . On either side, and close to the loop apex, the ADH case is red shifted on both sides. In the SUH and FDH cases, the loop apex is red shifted only on the left-hand-side, whilst slightly

## CHAPTER 5

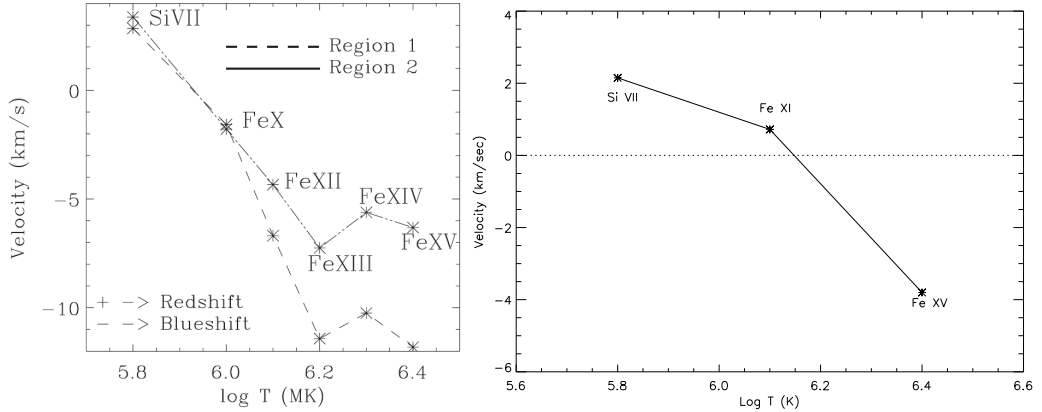


Figure 5.13: Comparison of Tripathi et al. (2009) average footpoint velocities (left) and the average simulation  $V_{cf}$  at  $s = 4.5$  Mm (right).

blue shifted on the right-hand-side. This discrepancy is likely to be caused by a slight asymmetry in the energy deposition throughout the loop, with fractionally more energy deposited on the right-hand-side of the loop.

### 5.2.3 Discussion

In this section, the effects of altering the localisation of the discrete energy bursts in a 10 Mm, 125 stranded loop was investigated. Patsourakos and Klimchuk (2005) suggest that the localisation of the heating has little effect on the emission. However, the work presented in this chapter suggests that it may not be quite so straightforward. FDH has a much flatter coronal temperature profile than that from ADH, where the temperature gradient is much steeper. However, with the current instrument resolution this difference may be difficult to detect.

Figure 5.13 shows a comparison between the average (weighted) footpoint velocities found in Tripathi et al. (2009) (left), and the average velocity at  $s = 4.5$  Mm from the Si VII, Fe XI and Fe XV lines. There is a clear shift towards blue-shift with increasing temperature with both the observations and the synthetic results. However, Tripathi et al. (2009) observe blue shift velocities in the Fe XI filter, whilst

## CHAPTER 5

red shifted velocities are obtained from the simulation results. The loop analysed in Tripathi et al. (2009) is slightly cooler, with a temperature range of  $0.8 - 1.5$  MK from the base of the loop to close to the apex. Since the red and blue shift velocities are heavily influenced by temperature, the effect of lowering the average loop temperature, by changing the energy content of each energy burst is investigated in the next section.

However, Del Zanna (2008) observe both red and blue shift velocities from their observations in the Fe XII, which has a characteristic temperature very similar to Fe XI. With Fe XII, red shifts are seen in the hot (3 MK) loops. The loops simulated in this section are approximately  $2.2 - 2.6$  MK, and are therefore also classed as hot loops, and so the red shifts we produce with the Fe XI filter, match those in Del Zanna (2008), although the actual values of the velocity disagree by several factors. But it is important to note, that where red shifts are expected, we have produced red shifts, and where blue shifts are expected blue shifts are also produced.

It must be remembered that the results from the simulations are for one particular coronal loop, with a number of parameters that are unknown, and are being compared with much longer loops, that have different temperature profiles. Therefore, it is important to understand that although the values of the velocities do not match accurately, the general relationship of the simulation results to the observations is in agreement; generally, where one expects to see red shifts, red shifts are seen, with the same also applicable to blue shifts. Using this multi stranded hydrodynamic approach is therefore a useful tool to investigate the physics of coronal loops. A single strand model would not produce results consistent with observations. Figure 1.3 (left) illustrates the apex temperature of a single strand as it evolves over time. There are large fluctuations in temperature as the strand is heated and cooled. From an observer's point-of-view, this would mean that the loop apex would keep brightening, and then dimming, as the loop is being heated and cooled. But this is

## CHAPTER 5

not the case, since a loop is observed to have a quasi-constant temperature during its observable lifetime (excluding large flare type events). Figure 1.3 (right) also shows the Si VII line-of-sight velocities from a single stranded loop. There is no clear predominance of red or blue shift, which we would expect to see from any line filtered velocities. However, by amalgamating all of the strands together, we have shown that we can reproduce expected temperature and velocity profiles which closely match observations.

As previously mentioned, we are investigating the heating of coronal loops through localised energy bursts. There are a number of parameters which are unknown, such as the number of strands in a loop, the number of discrete energy bursts in each strand, the spatial distribution of the energy bursts, and the energy content in each energy burst. Therefore, in the following sections, we will investigate each parameter, and see how this effects the temperature and velocity profiles of the global loop system.

### 5.3 Changing $E_{Total}$

So far, the total energy input has been kept fixed for all simulations. This section will investigate how altering the energy of each discrete energy burst, and thus  $E_{Total}$  affects the loop apex temperature for the three spatial heating cases. Logically, it would be expected that as more energy is released into the loop that the temperature will rise. Conversely, as energy is removed, the temperature will be expected to drop.

In this section, the number of strands is kept fixed at 125,  $\alpha$  (the power law index from Equation 5.1) is kept fixed at  $\alpha = 2.3$ , and the timing and locations of the energy bursts are kept the same. The only difference to the simulations in Section 5.2 is the energy content of each burst, thus meaning a change in  $E_{Total}$ . Only SUH is considered. Figure 5.14 displays the energy distributions for three ranges of  $E_{Total}$  from a selection of the simulations undertaken. The results of the same three

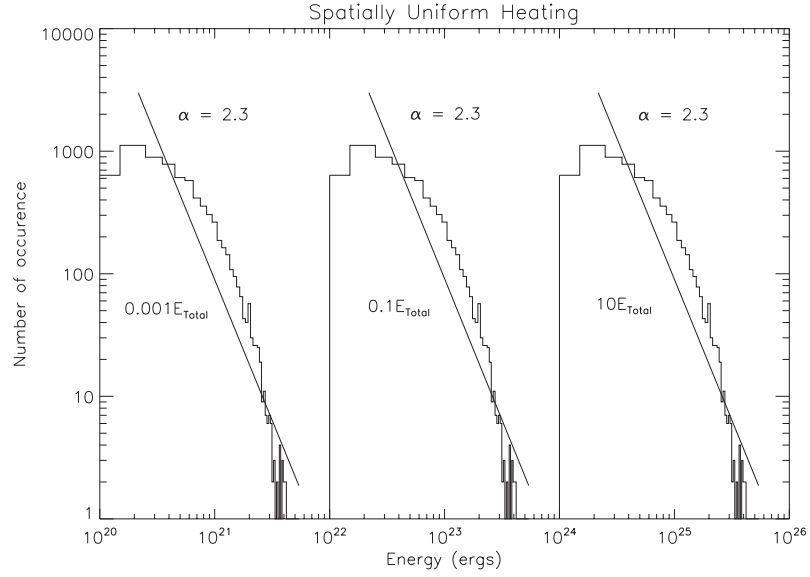


Figure 5.14: Energy histograms for three different total energy ranges, with straight lines fitted to show the power-law slop, which has a value of  $\alpha = 2.3$  in all cases.

simulations are shown throughout this section, with results for  $0.001E_{Total}$ ,  $0.1E_{Total}$  and  $10E_{Total}$ . Table 5.2 displays the simulation parameters used throughout this section.

### 5.3.1 Effect on Loop Temperature

Figure 5.15 displays the emission measure weighted apex temperature for the three different  $E_{Total}$  cases, whilst Figure 5.16 displays the mean temperature profile along the half-loop. With a total energy input of  $0.001E_{Total}$ , the mean apex temperature reaches approximately 0.3 MK. As the energy is increased to  $0.1E_{Total}$ , the mean apex temperature increases to 1.23 MK, and further to 3.69 MK for  $10E_{Total}$ .

So far in this section, only three different cases of total energy have been discussed. However, Figure 5.17 (left) displays the average loop apex temperature for a far greater number of simulations for the three spatial heating cases, in the range  $0.001E_{Total} \leq \text{Total Energy} \leq 10E_{Total}$ . This plot clearly identifies how the average loop apex temperature changes, as the total amount of energy deposited in the loop

CHAPTER 5

Table 5.2: Changing  $E_{Total}$ : simulation parameters

No. Strands	No. Bursts	Total Energy ( $\times E_{Total}$ erg)	Energy Range (erg)	Power Law Index ( $\alpha$ )
125	57	0.001	$1.00 \times 10^{20} - 5.38 \times 10^{21}$	-2.30
125	57	0.005	$5.00 \times 10^{20} - 2.69 \times 10^{22}$	-2.30
125	57	0.01	$1.00 \times 10^{21} - 5.38 \times 10^{22}$	-2.30
125	57	0.05	$5.00 \times 10^{21} - 2.69 \times 10^{23}$	-2.30
125	57	0.1	$1.00 \times 10^{22} - 5.38 \times 10^{23}$	-2.30
125	57	0.5	$5.00 \times 10^{22} - 2.69 \times 10^{24}$	-2.30
125	57	1.0	$1.00 \times 10^{23} - 5.38 \times 10^{24}$	-2.30
125	57	5.0	$1.00 \times 10^{23} - 2.69 \times 10^{25}$	-2.30
125	57	10.0	$1.00 \times 10^{24} - 5.38 \times 10^{25}$	-2.30

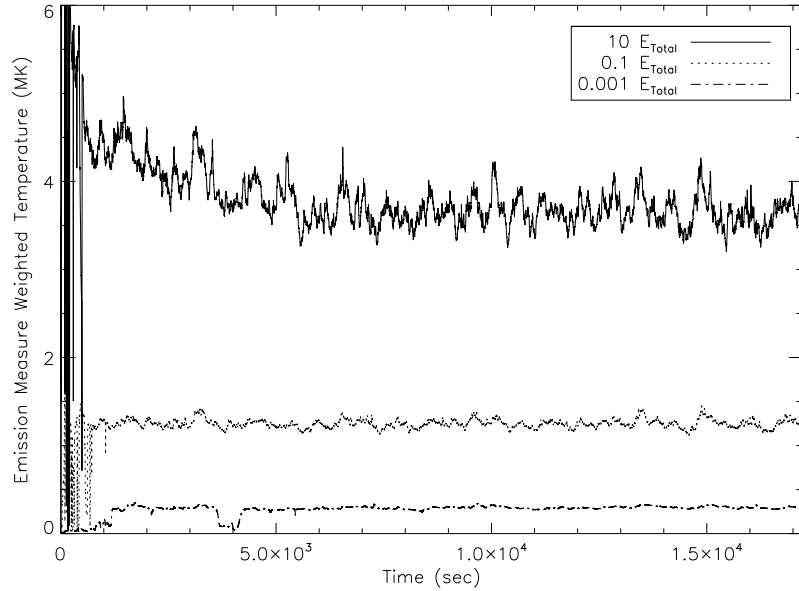


Figure 5.15: Emission measure weighted temperature at loop apex for different levels of  $E_{Total}$ :  $0.001E_{Total}$ ,  $0.1E_{Total}$  and  $10E_{Total}$  (SUH).

CHAPTER 5

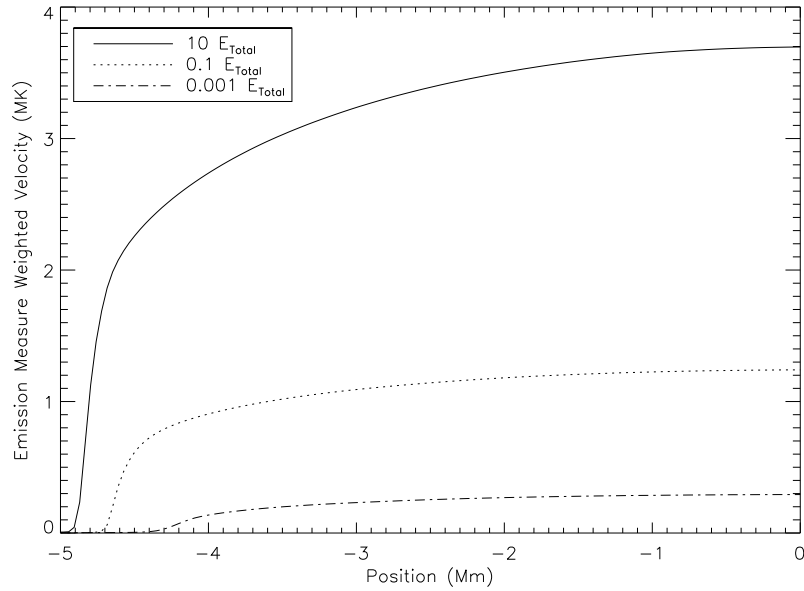


Figure 5.16: Average emission measure weighted temperature of the loop for different levels of  $E_{Total}$ :  $0.001E_{Total}$ ,  $0.1E_{Total}$  and  $10E_{Total}$  (SUH).

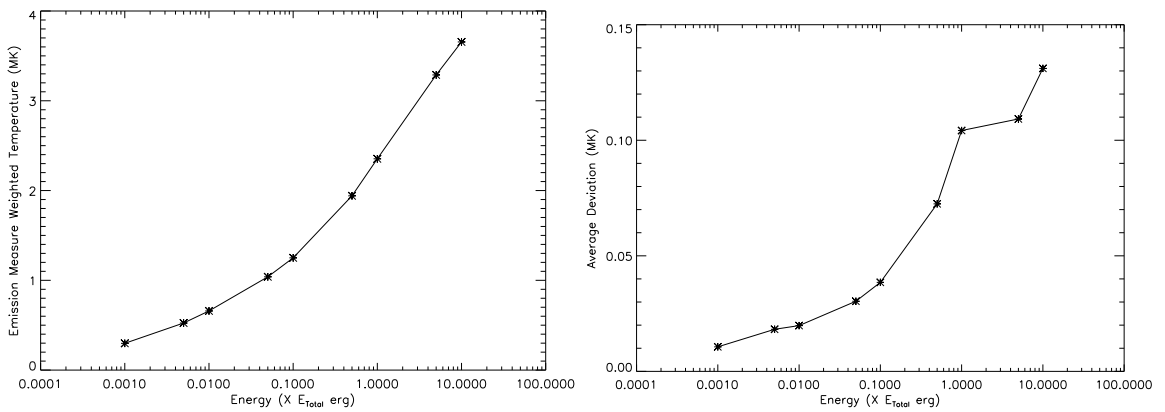


Figure 5.17: Average emission measure weighted temperature at the loop apex (left), and the average deviation of the temperature along the loop apex, over a range of total energy inputs

## CHAPTER 5

varies. The average absolute deviation (or average deviation) is used as a method to quantify the fluctuations in the mean temperature (and later, the mean velocity). As can be seen in Figure 5.15, the apex temperature corresponding to  $10E_{Total}$  has a much higher degree of variation than the the cooler temperatures displayed. At higher temperatures, the loop will cool at a much faster rate, whilst the higher energy content of the energy bursts will also heat the loop more rapidly, causing the higher level of fluctuations observed. Figure 5.17 (right) illustrates this, showing an increase in average deviation with increasing energy.

### 5.3.2 Effect on Loop Line-of-Sight Velocity

#### Si VII 275.36 Å

In the Si VII line filter, the  $0.001E_{Total}$  case is predominantly blue shifted (see Figure 5.18). We believe that this is caused because the loop is not being heated sufficiently by the low energy bursts, and a “one-way-traffic” situation occurs. Also, at this lower temperature, the density is much lower, and, as Del Zanna (2008) suggests, it is much easier to see blue shifts at lower densities. As the energy is increased, the loop becomes increasingly more red shifted, going from 20% red shifted at  $0.001E_{Total}$  to 95% at  $10E_{Total}$ .

The mean velocity moves from a blue shift of  $4 \text{ km s}^{-1}$  up to a red shift of  $3.5 \text{ km s}^{-1}$ .

#### Fe XI 188.23 Å

The Fe XI line filter has a temperature range of  $0.4 - 3.16 \text{ MK}$ , and therefore the  $0.001E_{Total}$  case is not within this range. At  $0.1E_{Total}$ , the footpoints are predominantly blue shifted, with red and blue shifts occurring along the rest of the loop length, with average blue shift velocities reaching  $3.5 \text{ km s}^{-1}$ . As the energy is increased further, the loop becomes predominantly red shifted (90%), with red shift

## CHAPTER 5

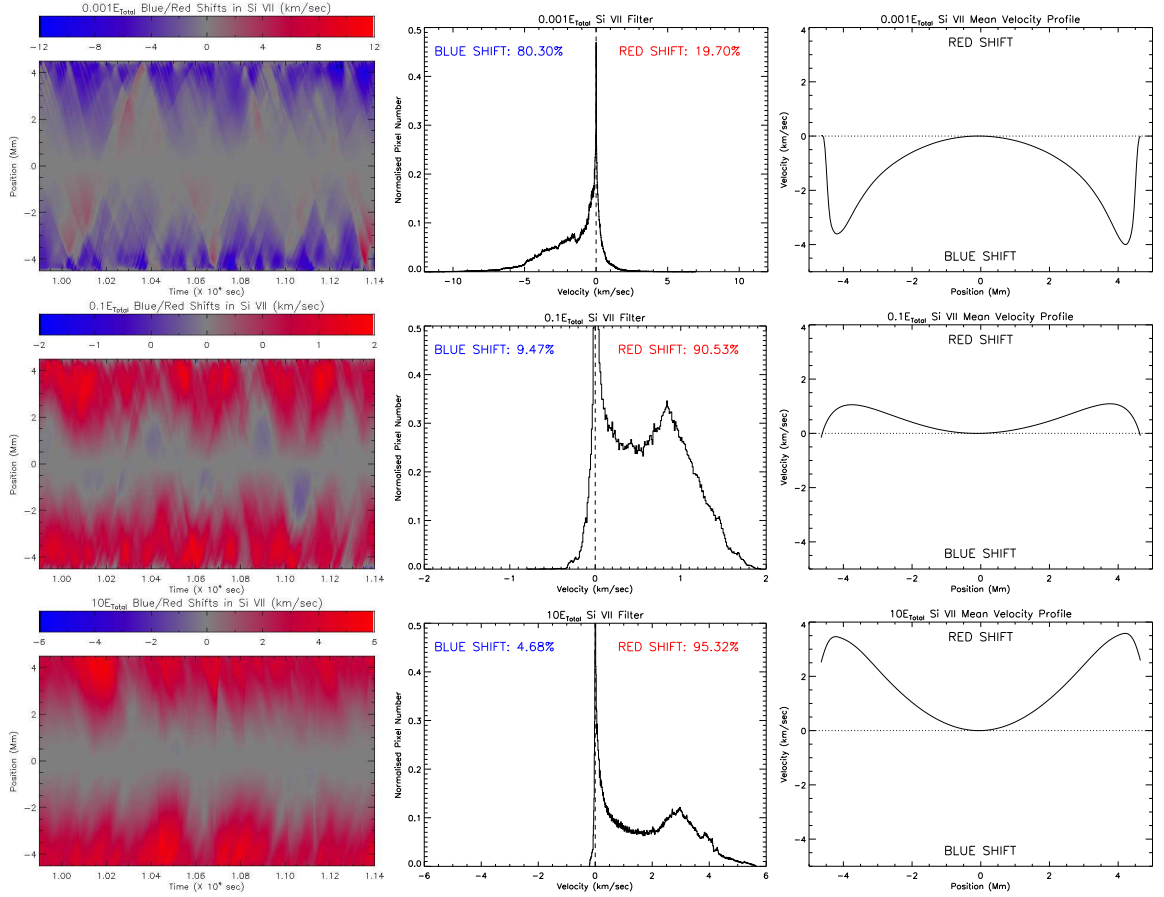


Figure 5.18: Si VII line-of-sight blue/red shifts for the three selected cases of  $E_{Total}$  (left), their corresponding histograms (centre), and the time-averaged mean blue/red  $V_{cf}$  along the loop (right). For SUH only.

## CHAPTER 5

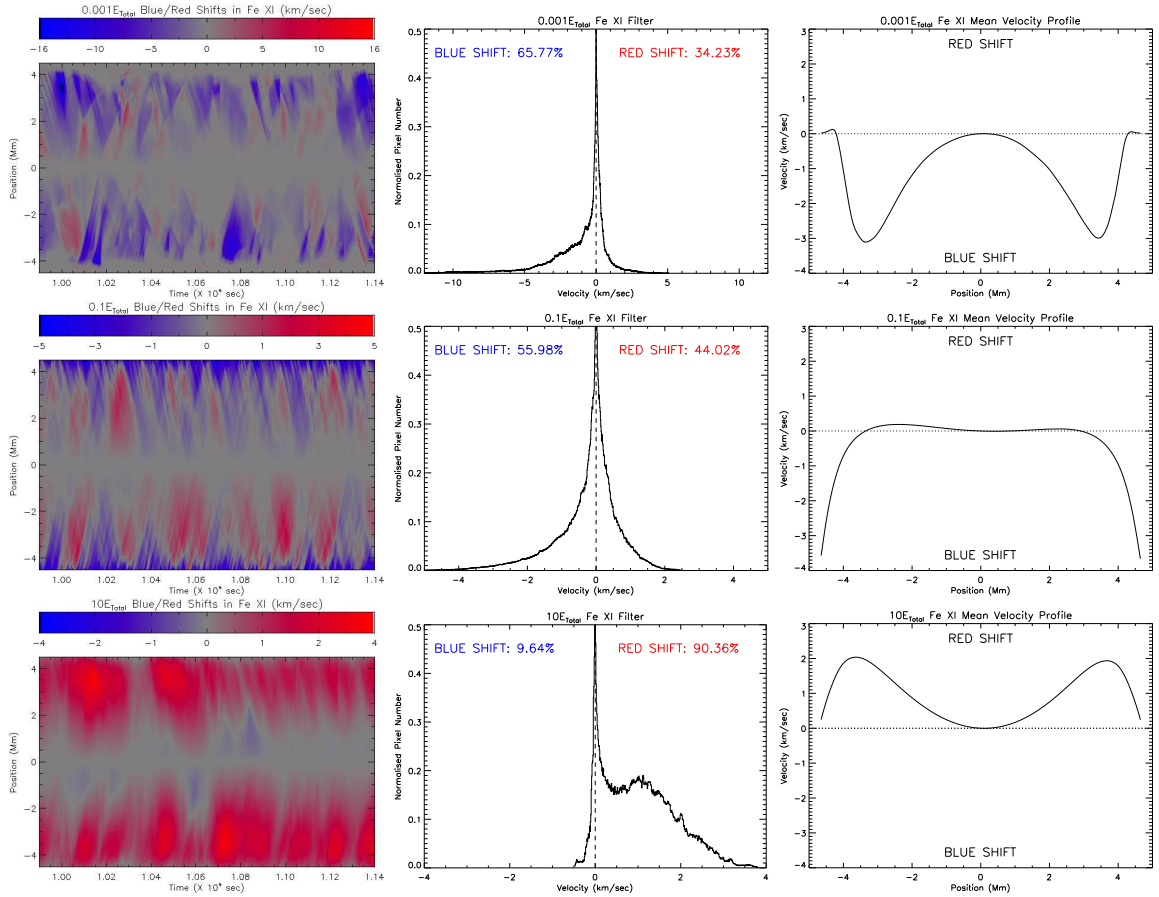


Figure 5.19: Fe XI line-of-sight blue/red shifts for the three selected cases of  $E_{Total}$  (left), their corresponding histograms (centre), and the time-averaged mean blue/red  $V_{cf}$  along the loop (right). The top row of diagrams can be ignored, but are included for completeness. For SUH only.

## CHAPTER 5

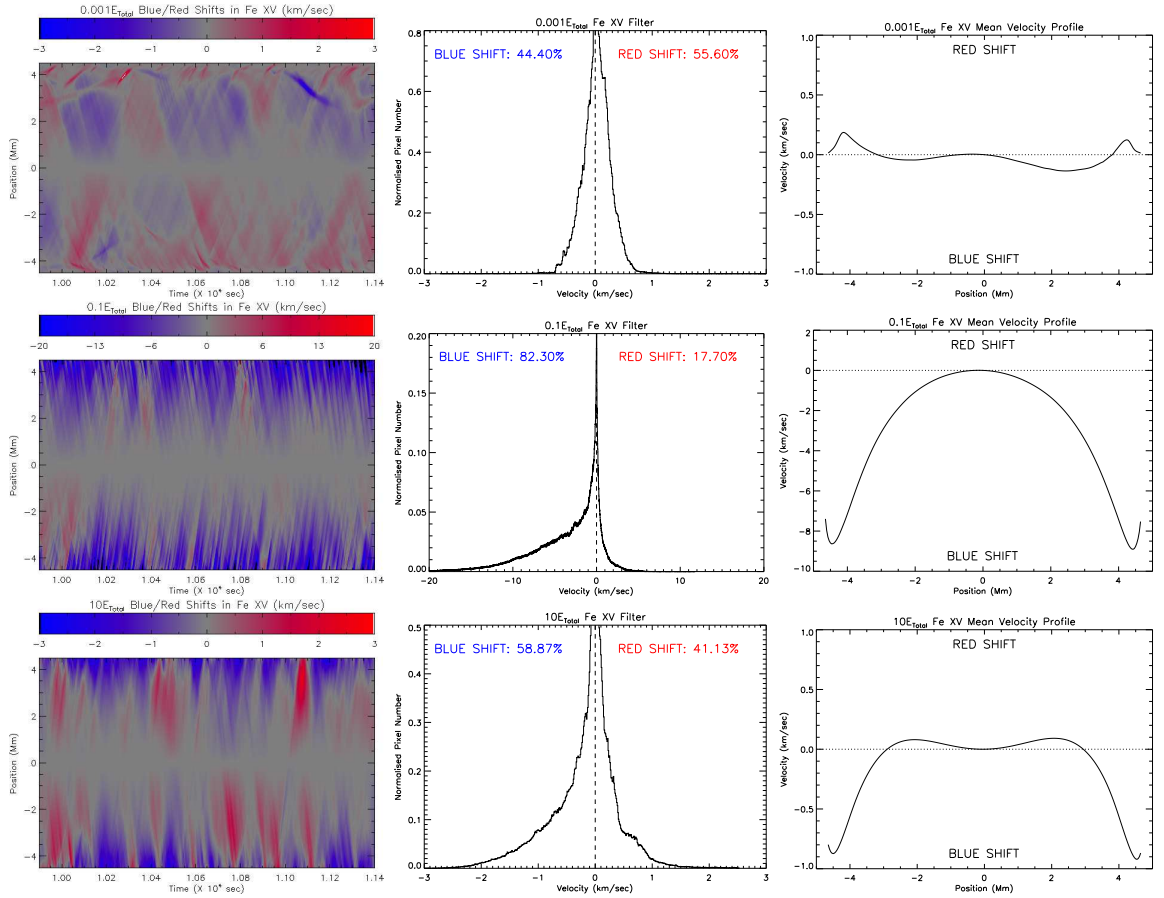


Figure 5.20: Fe XV line-of-sight blue/red shifts for the three selected cases of  $E_{Total}$  (left), their corresponding histograms (centre), and the time-averaged mean blue/red  $V_{cf}$  along the loop (right). The top row of diagrams can be ignored, but are included for completeness. For SUH only.

velocities reaching  $2 \text{ km s}^{-1}$ .

### Fe XV 284.16 Å

Again, the  $0.001E_{Total}$  temperature falls below the temperature range of the Fe XV filter. At  $0.1E_{Total}$ , the loop is predominantly blue shifted (82%), with mean velocities reaching  $9 \text{ km s}^{-1}$  at the footpoints. As the energy is increased to  $10E_{Total}$ , the loop becomes more red shifted, although still has a predominance of blue shift at 59%, and mean blue shift velocities of  $1 \text{ km s}^{-1}$  at the footpoint.

## CHAPTER 5

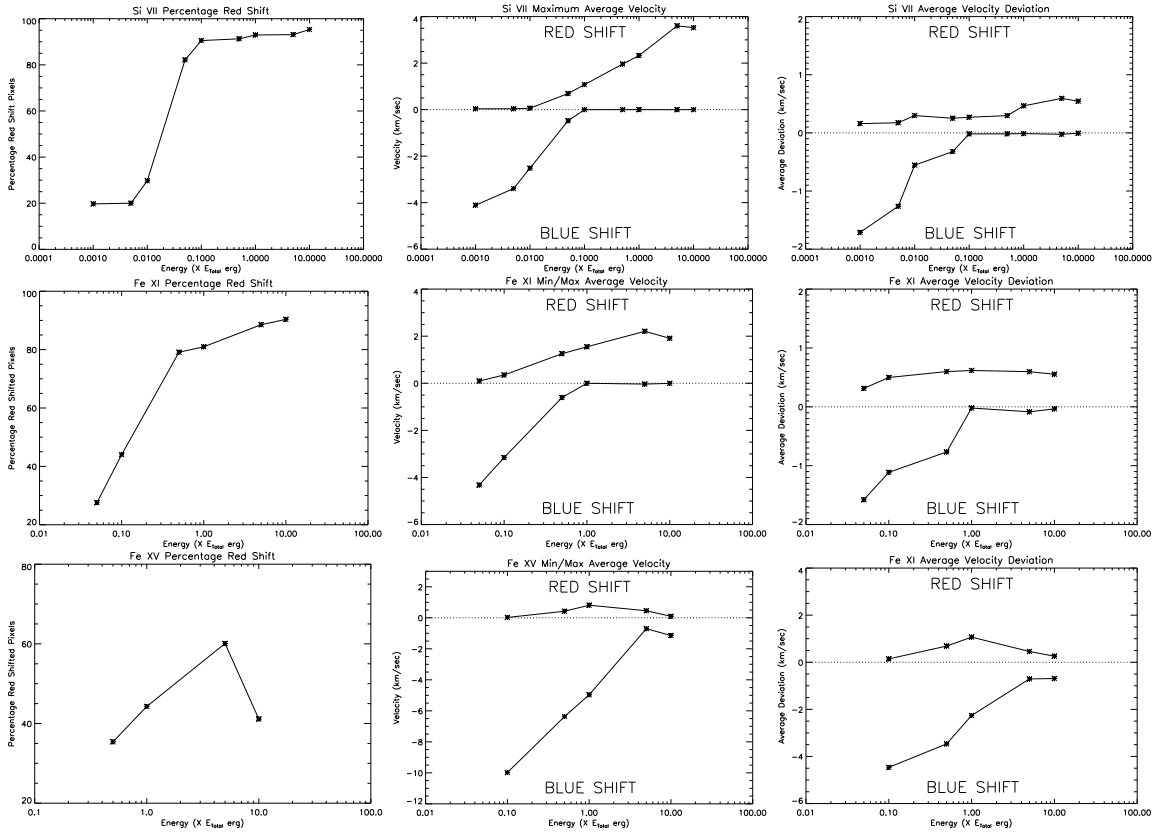


Figure 5.21: Percentage of red shifted pixels (left column), maximum mean velocity ranges (centre column), and average velocity deviation (right column) over a range of total energy inputs, and line filters. From top-to-bottom: Si VII, Fe XI, Fe XV

### 5.3.3 Discussion

Figure 5.21 (left column) displays the percentage of red shift in the loop for each line filter. For all three line filters there is a trend of increasing red shift with increasing energy. The Si VII and Fe XI filters show an increase in red shift velocities and a decrease in blue shift velocities with increasing energy. The Fe XV shows an decrease in both red and blue velocities with increasing temperature. The average deviations show similar trends to the maximum mean velocities.

Figure 5.22 shows another comparison between the simulation velocities and the Tripathi et al. (2009) velocities. The 0.1 and 0.5  $E_{T\text{total}}$  cases represent the closest

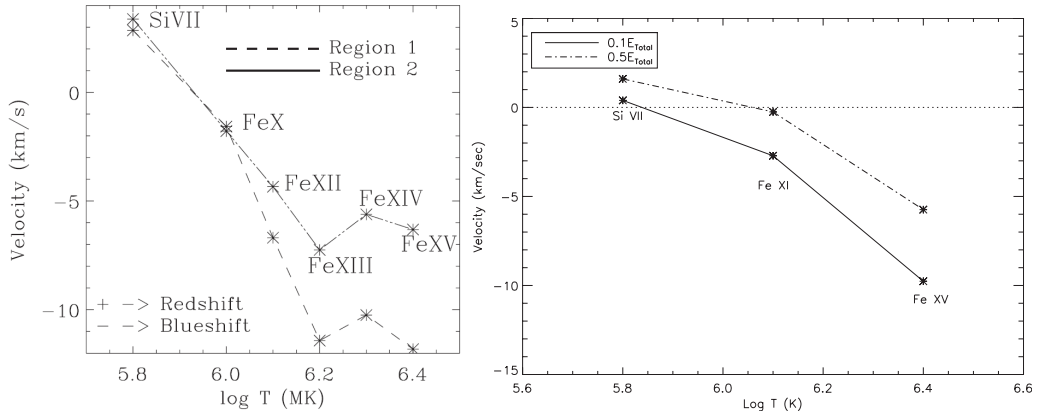


Figure 5.22: Comparison of Tripathi et al. (2009) average footpoint velocities (left) and the average simulation  $V_{cf}$  at  $s = 4.5$  Mm (right) for 0.1 and 0.5  $E_{Total}$

matches to the observations. The velocities do not match exactly, but are within a reasonable limit, and show red shifts where red shifts are expected, and blue shifts where blue shifted are expected. The temperature of the loop at 0.1 and 0.5  $E_{Total}$  matches closely to that of the observed loop. The cool loops (1 MK) observed in Del Zanna (2008) are blue shifted in the footpoints in the Fe XII line filter, matching well with the 1 MK (0.1  $E_{Total}$ ) loop in the Fe XI filter.

## 5.4 Changing the Number of Strands

In this section, the effects of changing the number of strands from 5 up to 2000 will be investigated. The total energy is kept at approximately  $E_{Total}(= 4.5 \times 10^{27}$  erg), and  $\alpha$ , the power law index, is kept approximately fixed at  $\alpha = 2.3$ . Due to the generation of random numbers within the simulation, this is not always possible, but efforts have been made to keep to these figures. Table 5.3 displays the parameters used throughout this section. The number of discrete energy bursts is kept fixed at 57 per strand, but since the number of strands in the loop changes, the energy content of each burst is adjusted accordingly to keep the total energy deposited over the course of the simulation the same. In a 5 stranded loop, the energy released

Table 5.3: Changing the number of strands: simulation parameters

No. Strands	No. Bursts	Total Energy ( $\times E_{Total}$ erg)	Energy Range (erg)	Power Law Index ( $\alpha$ )
1	57	1.06	$5.28 \times 10^{25} - 1.92 \times 10^{26}$	-2.37
5	57	0.96	$1.00 \times 10^{25} - 5.41 \times 10^{25}$	-3.31
45	57	1.01	$4.50 \times 10^{23} - 1.35 \times 10^{25}$	-2.37
125	57	1.00	$1.00 \times 10^{23} - 5.38 \times 10^{24}$	-2.30
500	57	0.98	$5.00 \times 10^{21} - 4.39 \times 10^{23}$	-2.24
1125	57	1.01	$3.31 \times 10^{21} - 7.34 \times 10^{23}$	-2.28
2000	57	1.00	$1.26 \times 10^{21} - 4.80 \times 10^{23}$	-2.34

by each burst is therefore greater than the energy release by a burst from a 2000 stranded loop. SUH is used in each case.

Figure 5.23 shows the energy distribution histograms for three selected cases of strand number.

#### 5.4.1 Effect on Loop Temperature

Figure 5.24 shows the emission measure weighted temperature of the loop apex for the selected cases. As the number of strands increases from 5 to 125 and 2000, the variation in the temperature decreases. Since more energy bursts are occurring with increasing strand number, the loop has less time to cool, than when there are far fewer energy bursts.

The mean temperature along the loop for the three selected cases is displayed in Figure 5.25. This shows an increase in loop temperature as the strand number is increased, and also shows that the temperature gradient along the coronal part of the loop is very similar. The 5 stranded loop profile is somewhat lower than the

## CHAPTER 5

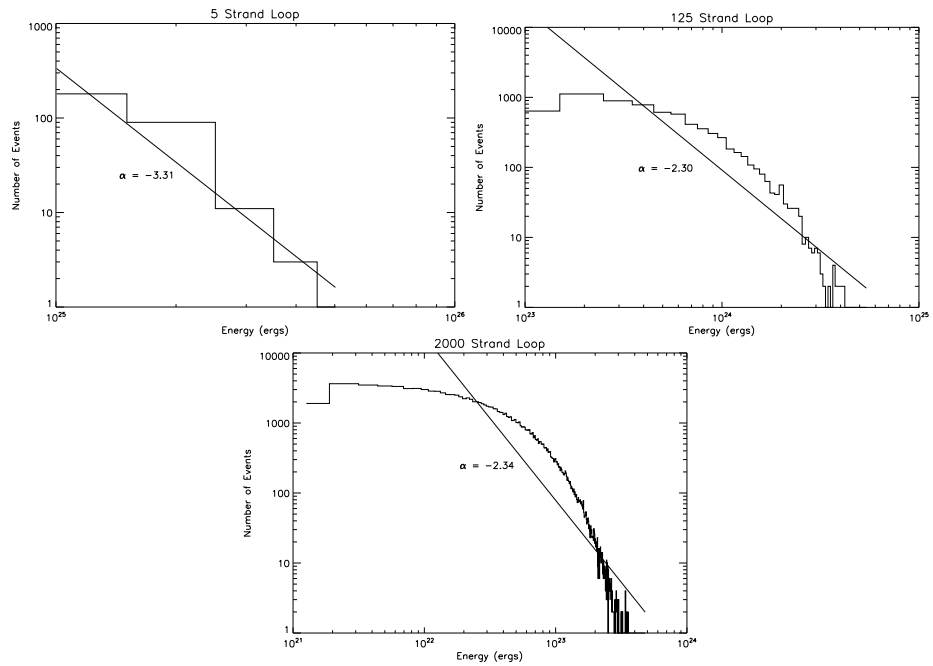


Figure 5.23: Energy histograms for three different cases of strand number, with straight lines fitted to show the power-law slope ( $\alpha$ ).

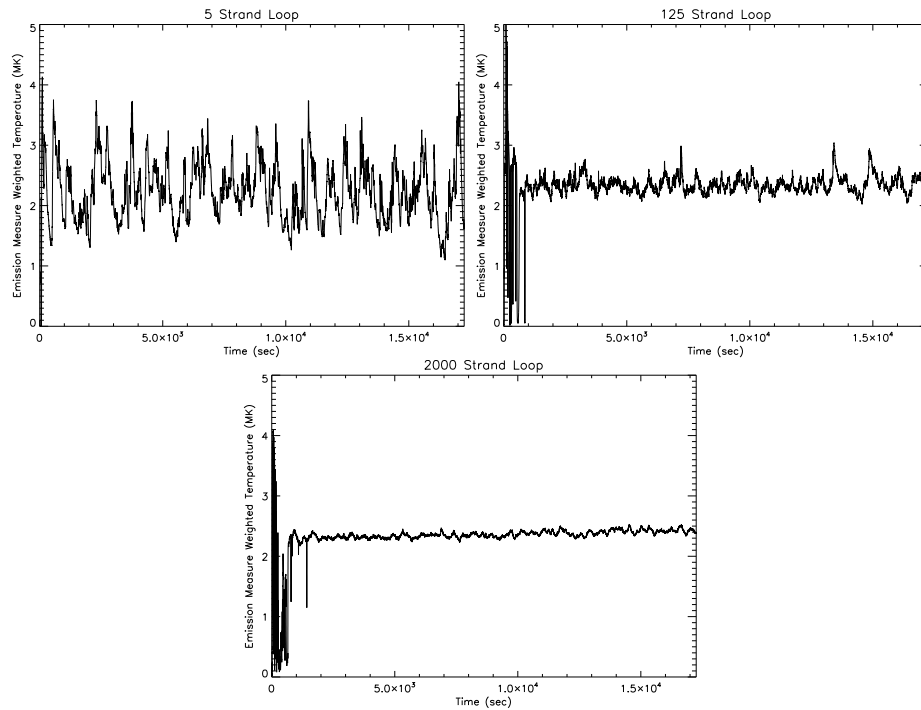


Figure 5.24: Emission measure weighted temperature of the loop apex for 5 strand (left), 125 strand (right) and 2000 strand (bottom) loop.

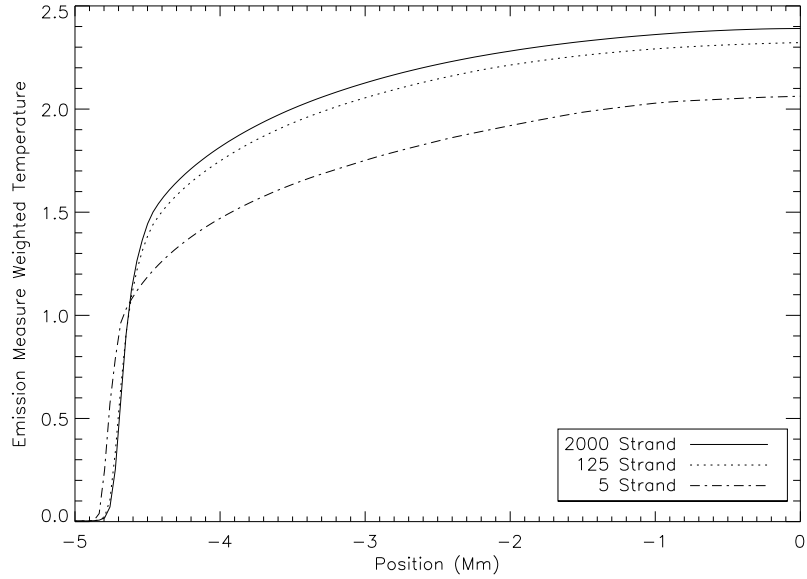


Figure 5.25: Average temperature along the loop of a 5, 125 and 2000 strand loop.

125 and 2000 strand loops. This is in part due to the lower energy deposited in the simulation of  $0.96E_{Total}$ . However, if we take this lower energy into account, and also the error bars (the average deviation), then the average temperature profiles, from all the strand numbers, could quite easily match one another.

The increase in mean apex temperature is again illustrated in Figure 5.26 (left) with the decreasing average deviation shown in Figure 5.26 (right).

### 5.4.2 Effect on Loop Line-of-Sight Velocity

The effects of increasing the number of strands upon the loop velocities can be seen in Figures 5.27 to 5.28. In the Si VII and Fe XI case, increasing the strand number has the effect of increasing the red shift up to close to 100%, and has the effect of smoothing out the appearance of the red shifts. With the Fe XV line filter, the footpoints become more blue shifted with increasing strand number, and again has the effect of smoothing out the appearance. The velocity profiles in the Si VII and Fe XI line filters for the three selected cases show very little change with increasing strand number, however in the Fe XV filter, there appears to be an increase in blue

## CHAPTER 5

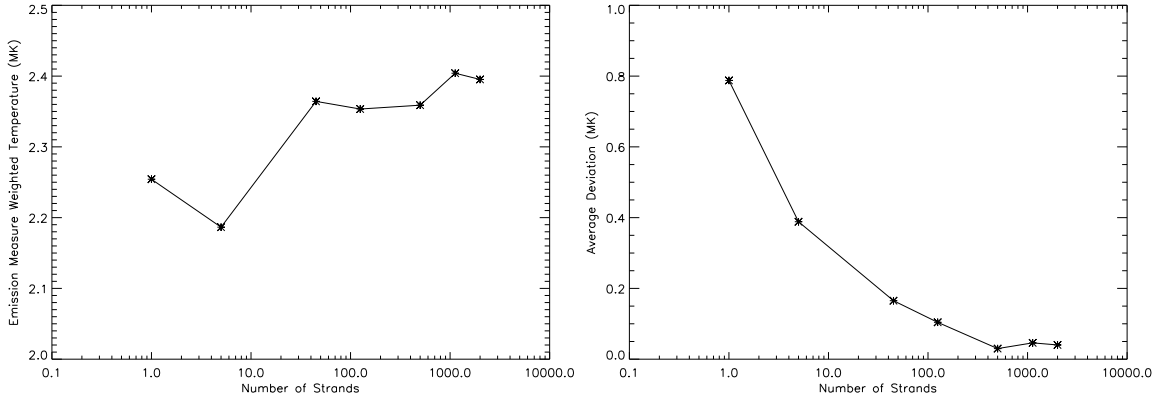


Figure 5.26: Average apex emission measure weighted temperature (left) and the average deviation of the apex temperature (right) as a function of strand number.

shift velocity.

Figure 5.30 displays the percentage of red shifted pixels (left column), the mean maximum velocity ranges for the three line filters (central column) and the average velocity deviation (right column) , as a function of strand number. Again, this illustrates that with increasing strand number, Si VII and Fe XI show a general increase towards red shift.

### 5.4.3 Discussion

The effect of increasing strand number has the effect of increasing the loop temperature slightly, and smoothing over the velocity profiles. Where something is particularly red (blue) shifted, increasing the number of strands will have the effect of making it more red (blue) shifted. This can also lead to an increase in the velocity, since any blue (red) shift velocities removed by the smoothing will therefore increase the mean red (blue) velocity.

## CHAPTER 5

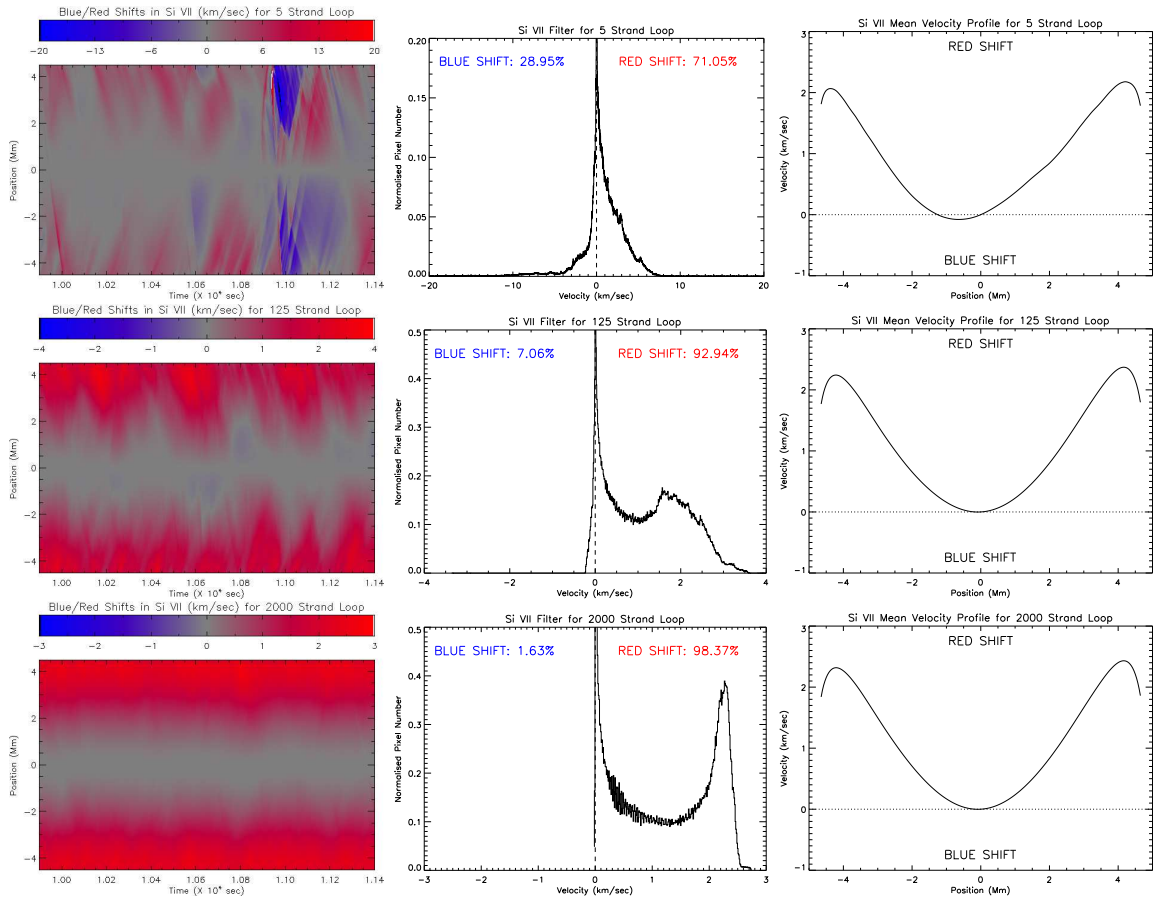


Figure 5.27: Si VII line-of-sight blue/red shifts for the three selected cases of strand number (left), their corresponding histograms (centre), and the time-averaged mean blue/red  $V_{cf}$  along the loop (right).

## CHAPTER 5

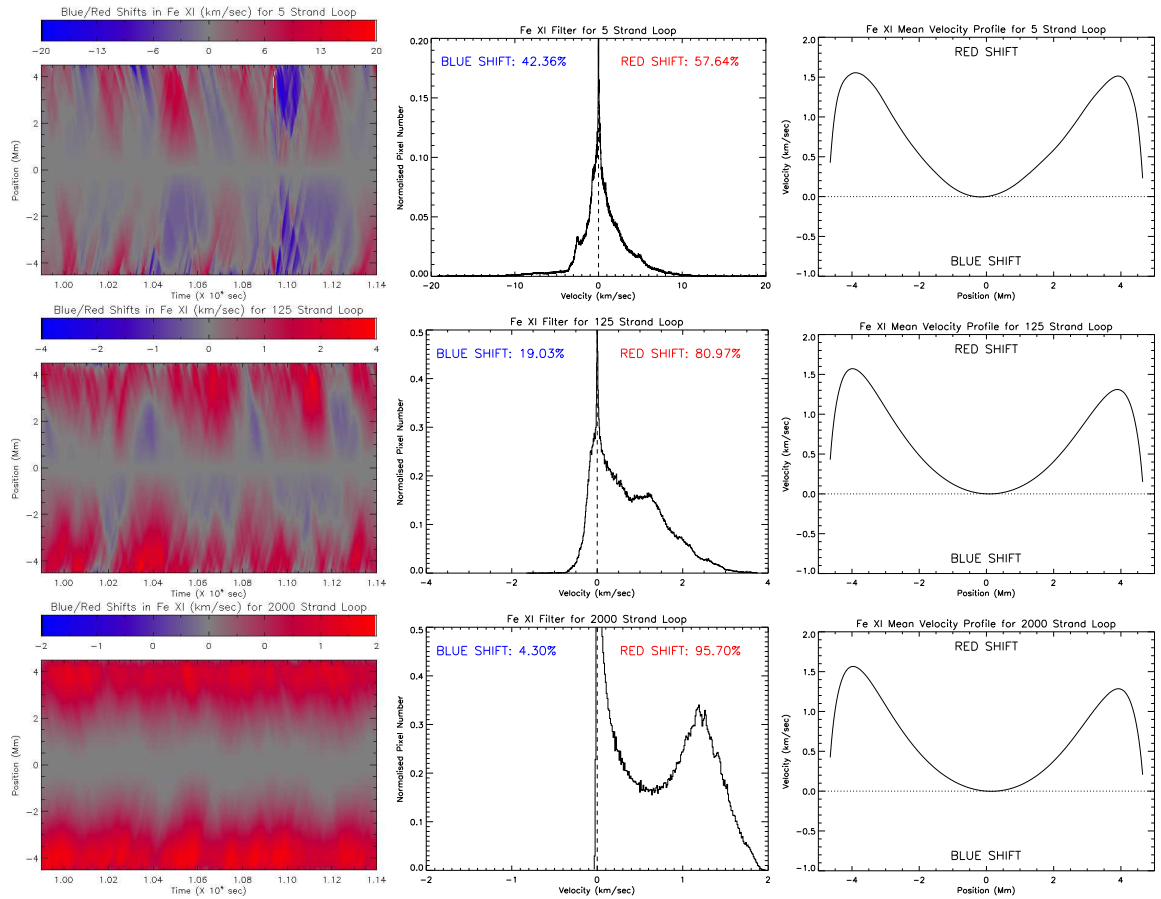


Figure 5.28: Fe XI line-of-sight blue/red shifts for the three selected cases of strand number (left), their corresponding histograms (centre), and the time-averaged mean blue/red  $V_{cf}$  along the loop (right).

## CHAPTER 5

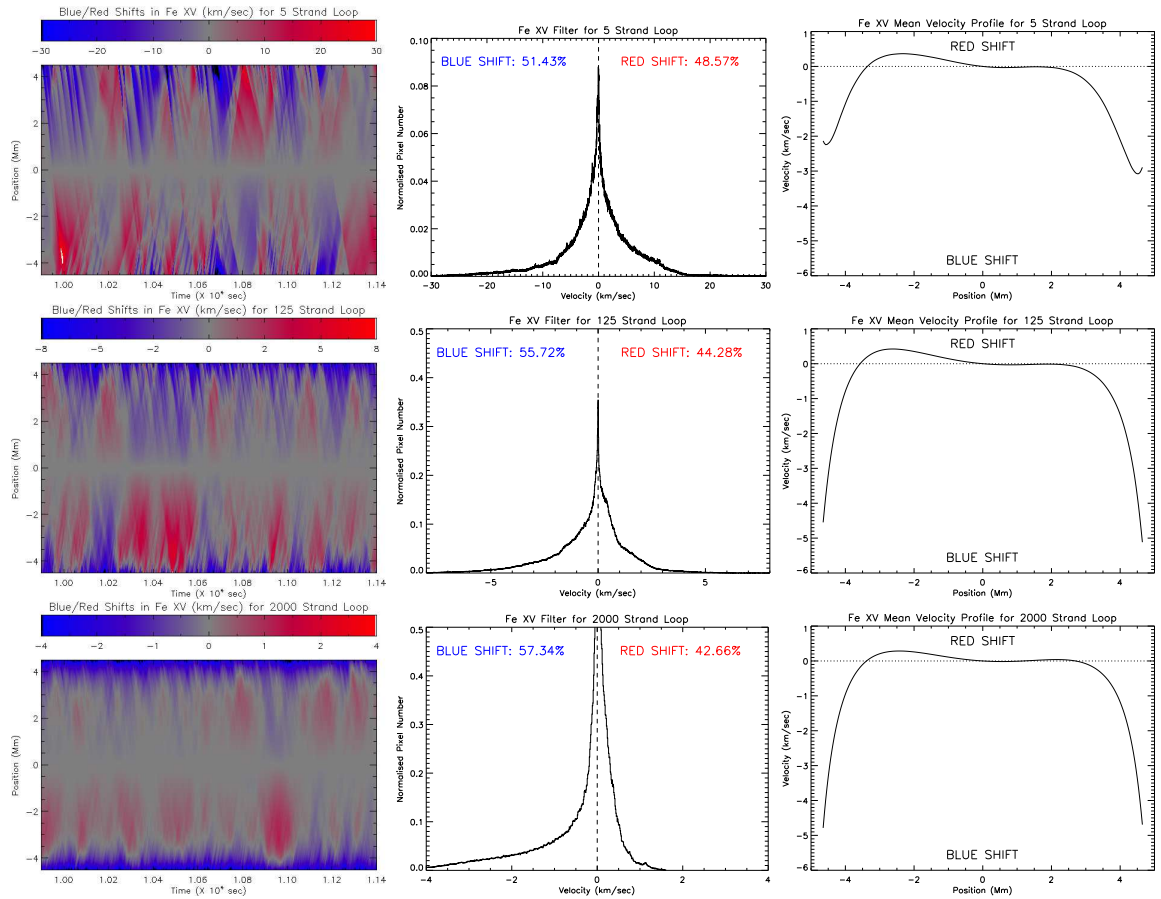


Figure 5.29: Fe XV line-of-sight blue/red shifts for the three selected cases of strand number (left), their corresponding histograms (centre), and the time-averaged mean blue/red  $V_{cf}$  along the loop (right).

# CHAPTER 5

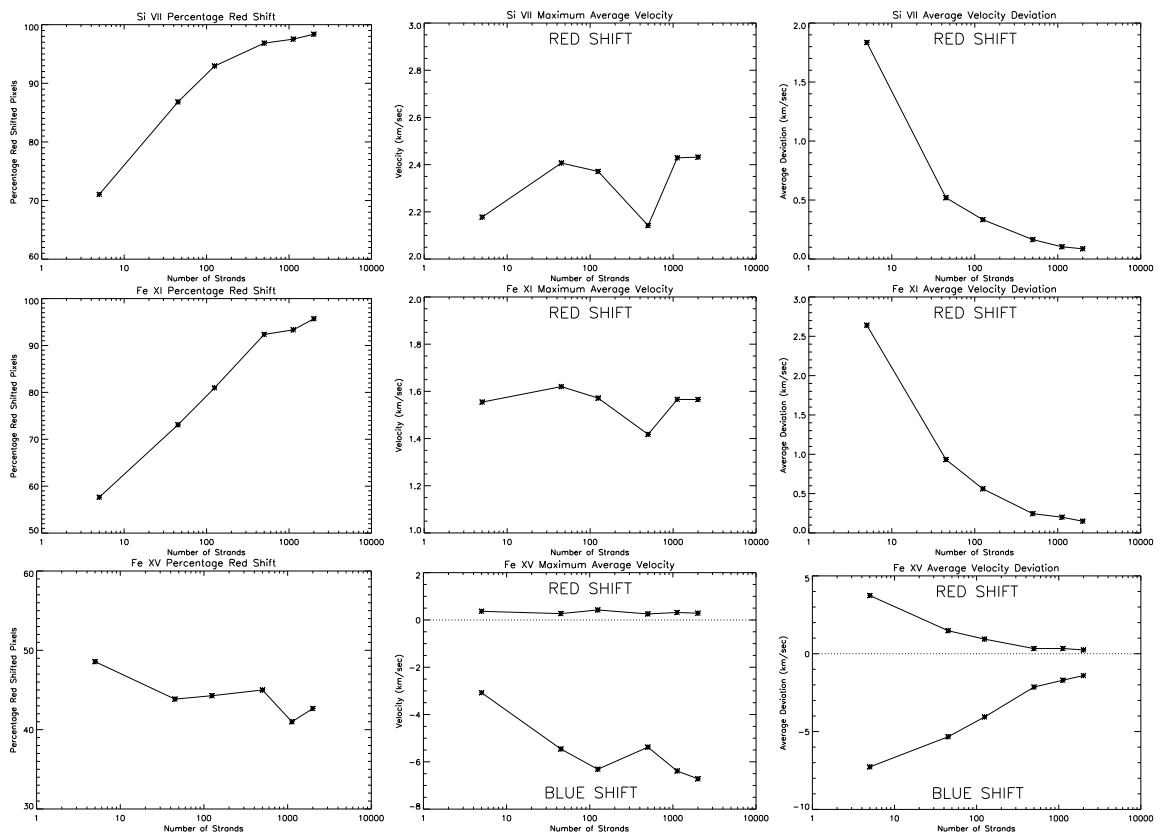


Figure 5.30: Percentage of red shifted pixels (left column), maximum mean velocity ranges (centre column), and average velocity deviation (right column) over a range of number of strands, and line filters. From top-to-bottom: Si VII, Fe XI, Fe XV

Table 5.4: Changing the number of energy bursts: simulation parameters

No. Strands	No. Bursts	Total Energy ( $\times E_{Total}$ erg)	Energy Range (erg)	Power Law Index ( $\alpha$ )
125	11	1.07	$1.11 \times 10^{24} - 2.37 \times 10^{25}$	-2.36
125	57	1.0	$1.00 \times 10^{23} - 5.38 \times 10^{24}$	-2.30
125	114	1.00	$3.76 \times 10^{22} - 2.81 \times 10^{24}$	-2.34
125	570	1.01	$2.65 \times 10^{21} - 6.46 \times 10^{23}$	-2.26
125	1140	1.01	$8.56 \times 10^{20} - 3.38 \times 10^{23}$	-2.31

## 5.5 Changing the Number of Discrete Energy Bursts Per Strand

In the previous section, the number of strands in the loop was changed, whilst keeping the number of energy bursts fixed at 57 per strand. In essence this meant that the number of energy bursts in the global loop system also changed, even though the number of bursts per strand did not. Therefore, in this section, we investigate how changing the number of energy bursts per strand affects the loop temperature and velocity profiles.

Once more, SUH is used, the total energy is kept fixed at approximately  $E_{Total}(= 4.5 \times 10^{27}$  erg) and  $\alpha$  is kept as close to  $-2.3$  as possible (see Figure 5.31 for the three selected cases illustrating the power law slope). Since the number of bursts per strand is changing, the energy of each particular burst must also change in order to keep the total energy the same. Table 5.4 displays the simulation parameters used in this section.

## CHAPTER 5

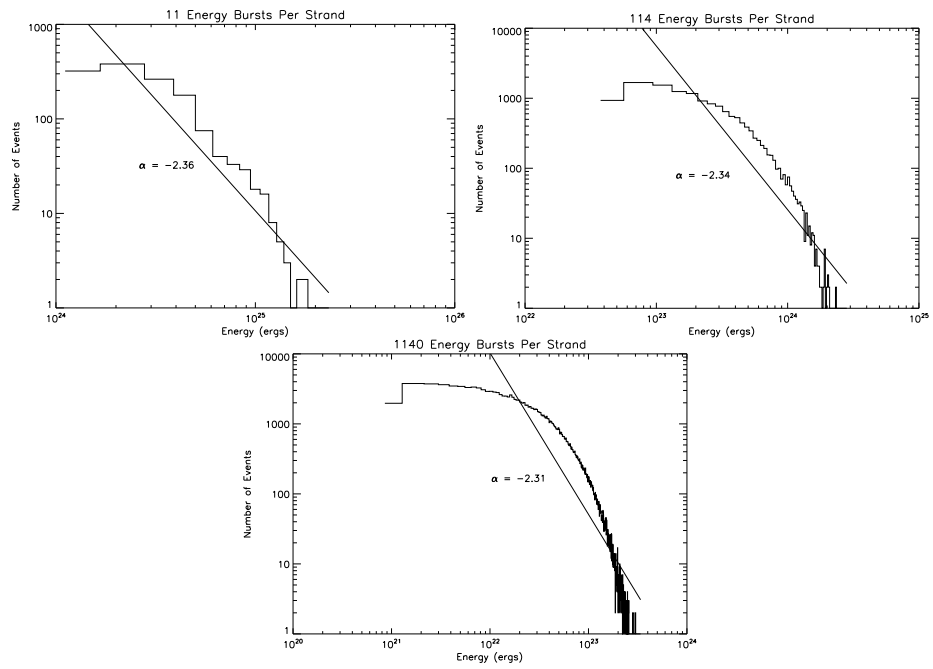


Figure 5.31: Energy histograms for 11, 114 and 1140 energy bursts per strand.

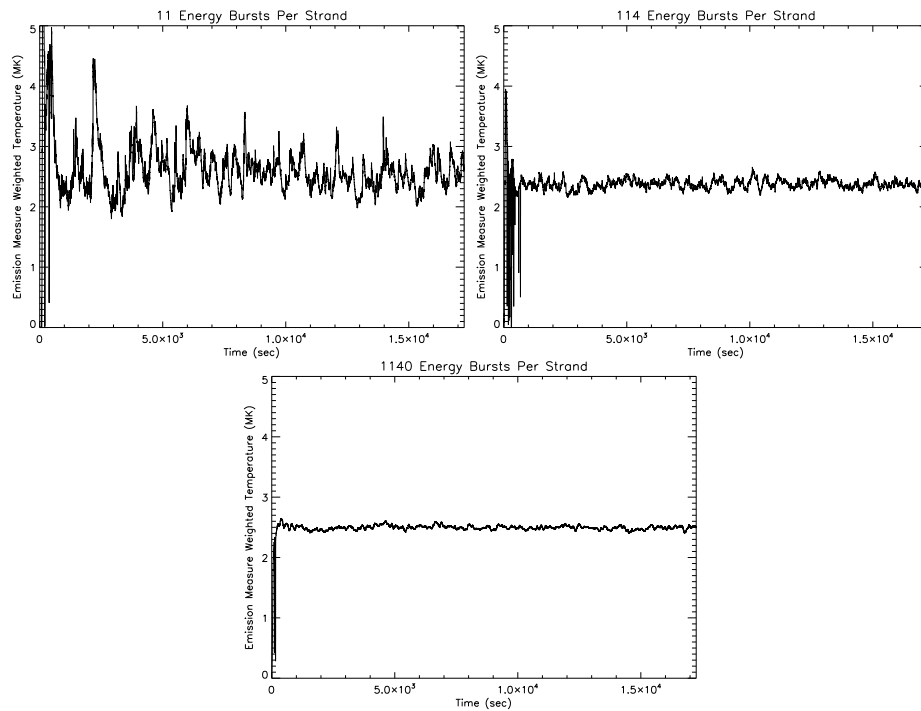


Figure 5.32: Emission measure weighted temperature of the loop apex for 11 energy bursts (left), 114 energy bursts (right) and 1140 energy burst (bottom) per strand in a 125 strand loop.

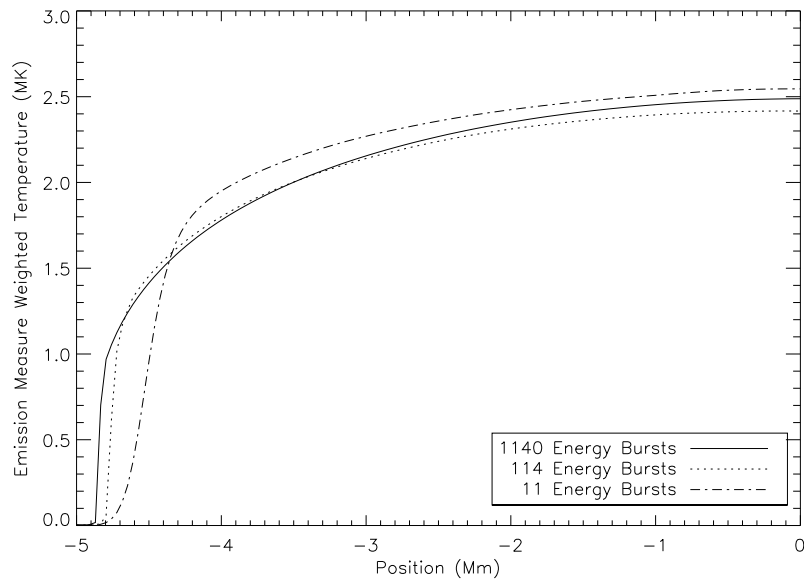


Figure 5.33: Average temperature along a 125 strand loop with 11, 114 and 1140 discrete energy bursts per strand

### 5.5.1 Effect on Loop Temperature

Figure 5.32 shows the emission measure weighted temperature of the loop apex for the three selected cases. With only 11 energy bursts per strand, there are large deviations in the apex temperature compared to that of the 114 and 1140 energy bursts per strand cases. With fewer bursts, in order to maintain the same overall energy in the strand, each particular burst contains more energy than that with more bursts. As such, the loop will be heated more intensely, but also has more time to cool in-between the next burst, thus causing the larger deviations. Conversely, with more energy bursts, each burst contains less energy, but will have less time to cool, since the time between energy bursts is much less. On the other hand, much like in Section 5.4, the error bars show that the average profiles all lie within each other.

Figure 5.33 shows the time-average temperature profile along the loop. The 11 energy bursts per strand loop has the highest average apex temperature of 2.53 MK, although the error on this value is far larger than the other two examples. Also, the

## CHAPTER 5

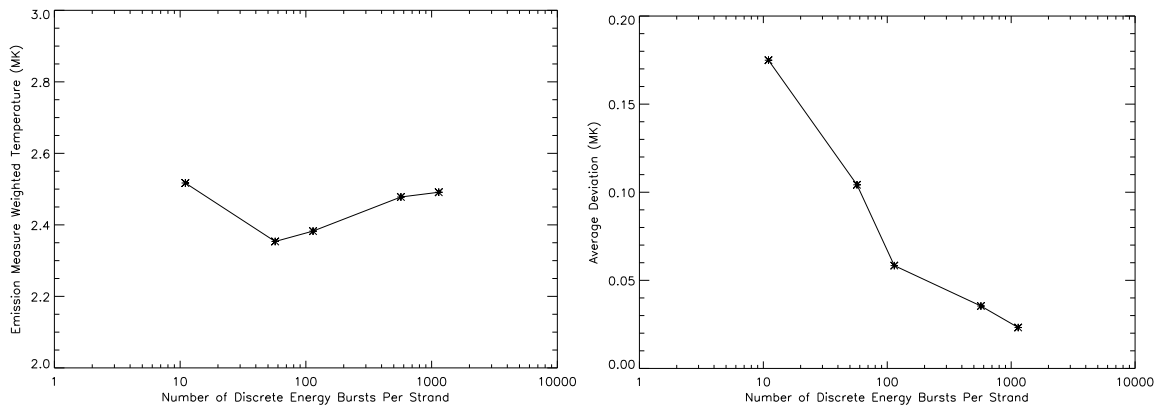


Figure 5.34: Average apex emission measure weighted temperature (left) and the average deviation of the apex temperature (right) as a function of number of energy bursts per strand.

11 bursts per strand loop has a larger amount of energy deposited than in any of the other simulations. The temperature gradient of the 11 energy burst per strand loop is also significantly different. This is because there are only 11 energy bursts along the length of each strand, and will not have as many being released in the footpoint regions as the other examples.

The average apex temperature of the loop as a function of number of bursts per strand is displayed in Figure 5.34 (left). Apart from the 11 energy bursts per strand simulation, there is a general trend of increasing apex temperature with increasing number of energy bursts per strand. Figure 5.34 (right) shows the average deviation of the apex temperature as a function of increasing energy bursts per strand. There is a very clear trend showing a smaller deviation with increasing number of events. This because although the loop is heated more frequently, the energy released is much less, and so there are no big spikes in temperature, whilst the frequency of the bursts is such that there is also much less time to cool between each heating event.

## CHAPTER 5

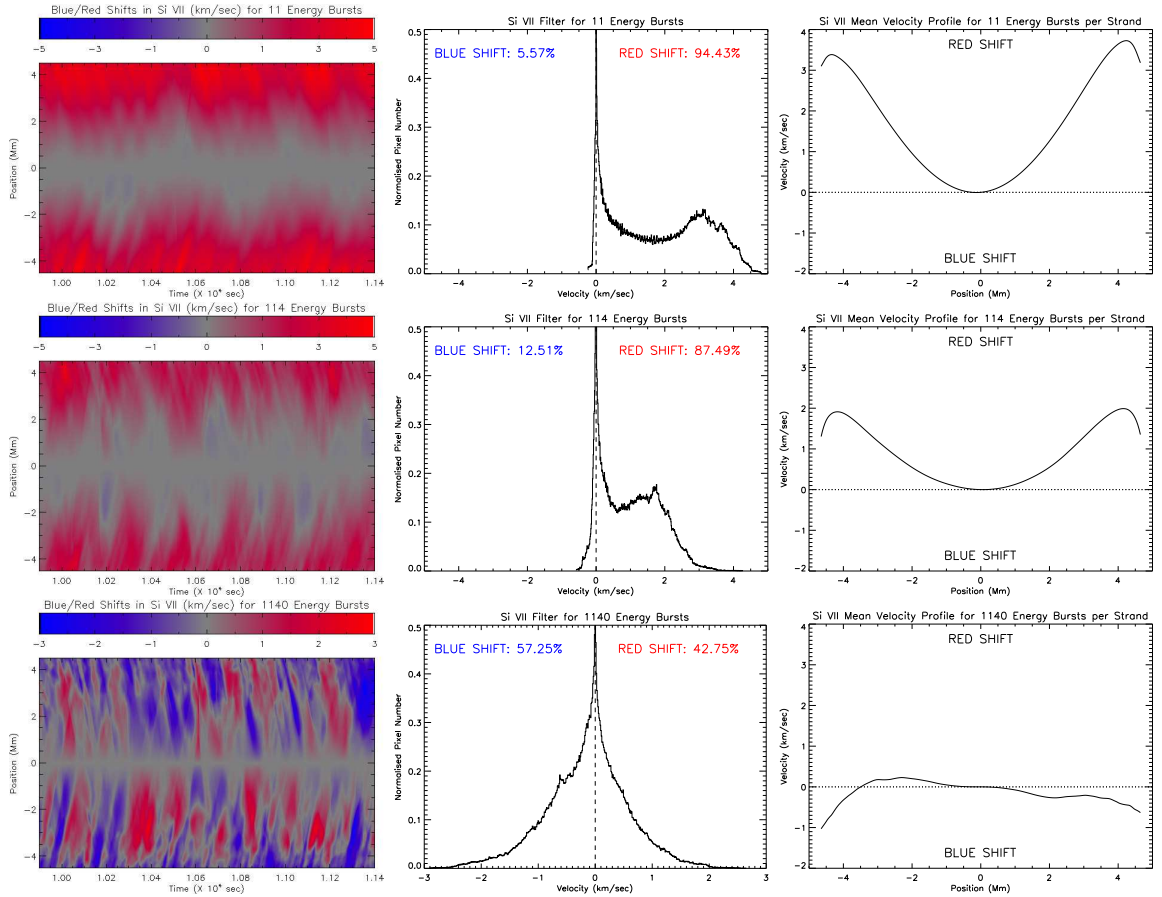


Figure 5.35: Si VII line-of-sight blue/red shifts for the selected cases of number of energy bursts per strand (left), their corresponding histograms (centre), and the time-averaged mean blue/red  $V_{cf}$  along the loop (right).

## CHAPTER 5

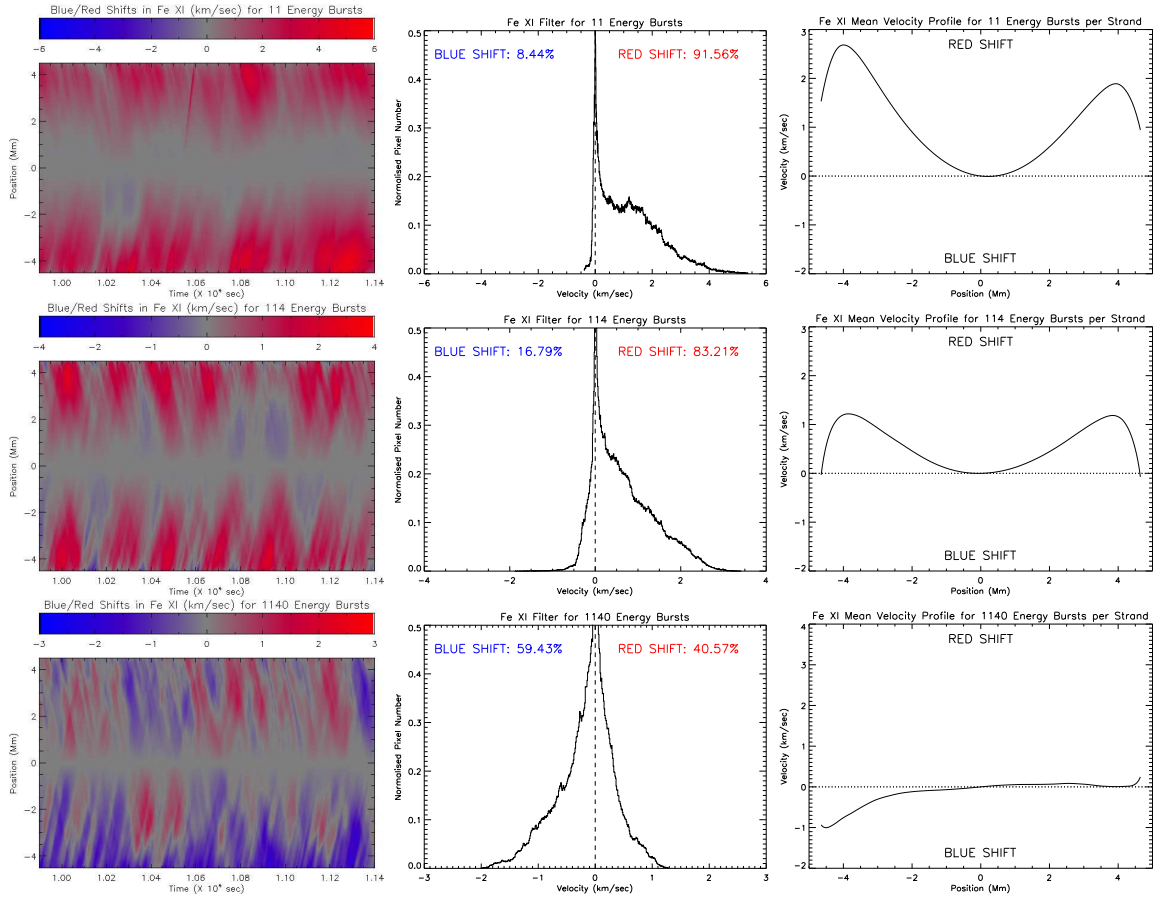


Figure 5.36: Fe XI line-of-sight blue/red shifts for the three cases of spatial heating (left), their corresponding histograms (centre), and the time-averaged mean blue/red  $V_{cf}$  along the loop (right).

## CHAPTER 5

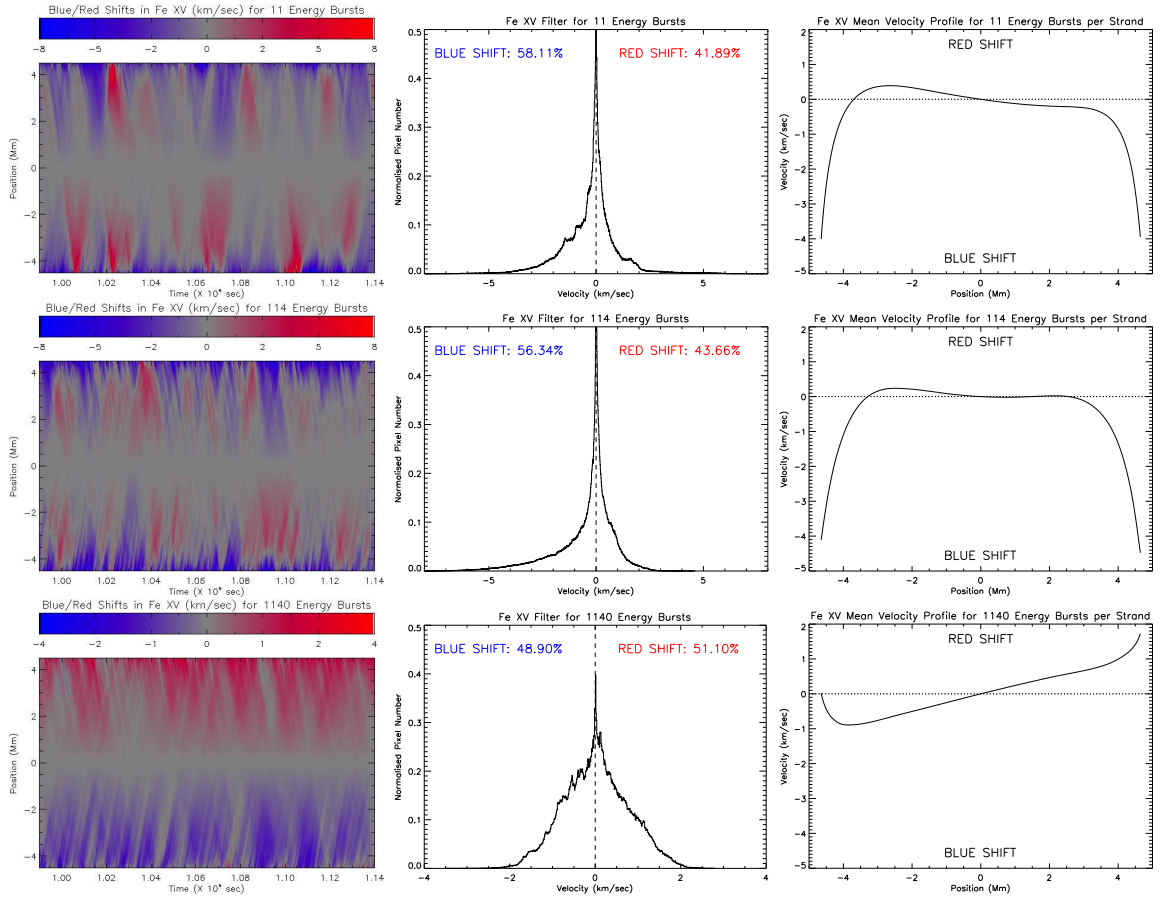


Figure 5.37: Fe XV line-of-sight blue/red shifts for the three cases of spatial heating (left), their corresponding histograms (centre), and the time-averaged mean blue/red  $V_{cf}$  along the loop (right).

## CHAPTER 5

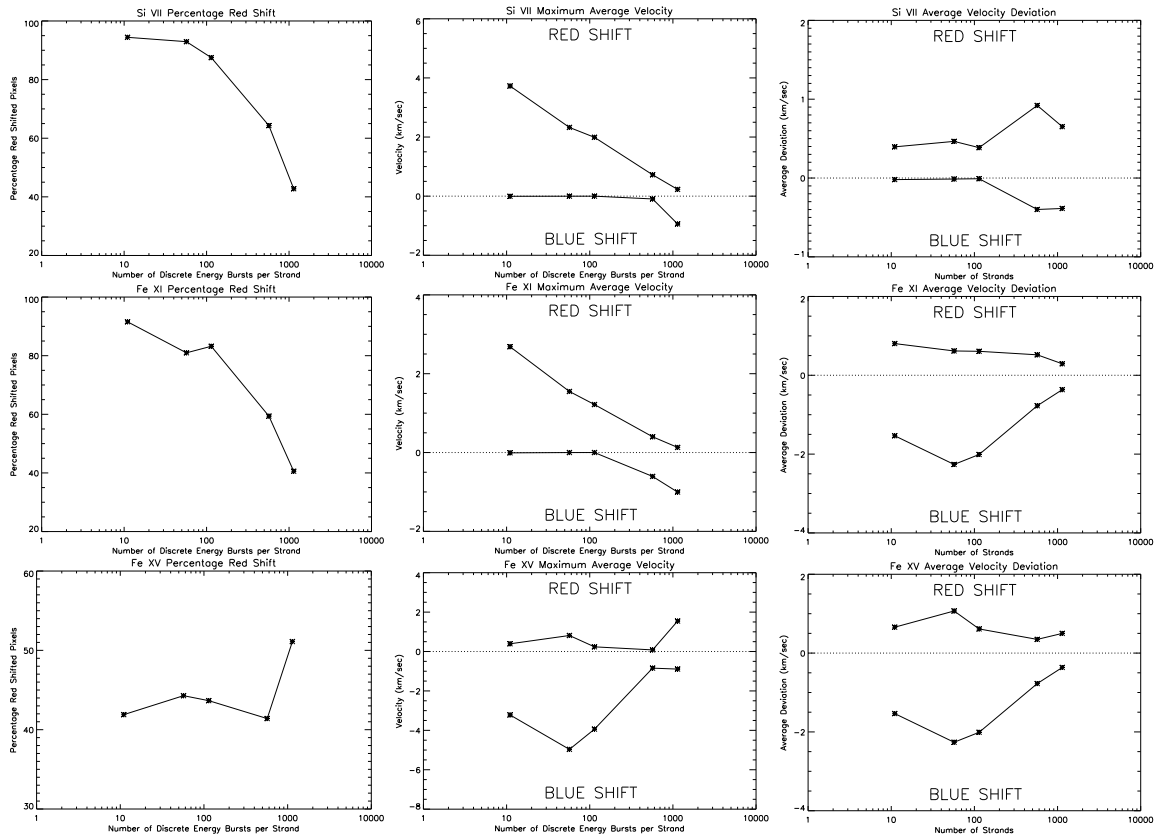


Figure 5.38: Percentage of red shifted pixels (left column), the minimum and maximum velocity (centre column), and the average deviation of the velocity (right column) as a function of energy bursts per strand. From top-to-bottom: Si VII, Fe XI, Fe XV

### 5.5.2 Effect on Loop Line-of-Sight Velocity

In the SI VII and Fe XI line filters (see Figure 5.35 and 5.36), the loop is significantly red shifted with the 11 and 114 bursts per strand. However, with 1140 bursts the loops become more blue shifted, and there appear to be lots of flows from one footpoint to another. In the Fe XV filter, the 1140 bursts per strand creates a predominantly blue shifted left-hand-side of the loop, and a predominantly red shifted right-hand-side of the loop.

Figure 5.38 quantifies the change in red shift, the change in velocity, and the

## CHAPTER 5

change in the average deviation of the velocity for each line filter. In both the Si VII and Fe XI, there is a clear trend of increasing blue shift with increasing number of bursts per strand. With the Fe XV filter there is no clear trend in change in red shift, with the 1140 bursts per strand loop being a notable difference to the results obtained with fewer bursts per strand.

The Si VII and Fe XI line filters show a decrease in red shift velocities, which would be expected with the decrease in the number of red shifted pixels. Therefore, with the increase in the number of blue shifted pixels, it comes as no surprise that the blue shift velocities show an increase with an increasing number of energy bursts per strand. With Fe XV, there appears to be no clear trend in the change in red shift velocities, but there is a decrease in blue shifted velocities with increasing number of events.

The average deviation of the Si VII velocities appear to be show a trend of increasing deviation of both red and blue shift velocities with increasing burst number, whilst the Fe XI and Fe XV line filters show a trend of decreasing red and blue velocity deviations.

### 5.5.3 Discussion

Changing the number of energy bursts per strand throws up some interesting conundrums, particularly where the line filtered velocities are concerned. In terms of the temperature profile, there is a similar pattern to that of changing the number of strands.

In the Si VII and Fe XI line filters, there is a clear trend of increasing blue shift with increasing burst number. In the previous section, the number of strands was changed, which meant that the total number of energy bursts also changed. However, unlike the smoothing effect found from increasing the number of strands, there is a somewhat lack of smoothing. The increase in blue shift could be due to

## CHAPTER 5

a number of things. Firstly, it has been shown previously in Section 5.3, that the loop is predominantly blue shifted in the Si VII filter with a total energy of  $0.001 - 0.01E_{Total}$ . During these simulations, the bursts released energy in the range of  $1 \times 10^{20} - 5 \times 10^{22}$  erg per event, which are similar to the values used in the 1140 bursts case. However, it is more likely that the increase in blue shift is because each strand is being continually heated to a point where there is no, or very little, time when there is not an energy burst being released. The simulation lasts 17,250 seconds, and there are 1140 energy bursts, each lasting between 50 and 150 seconds each, which means there is likely to always be a time where each strand is being continually heated, thus causing more evaporation, and therefore more blue shifts.

### 5.6 Conclusions

The multi stranded coronal loop simulations investigated throughout this chapter have shown some interesting results, and important implications to understanding the general physics of the coronal loop environment. We have shown that by dividing a loop into multiple, thermally isolated strands, and amalgamating to form a single, global loop system, we can produce results which can closely match the properties obtained from loop observations.

The temperature profile of a loop can be simulated efficiently with a multi-strand model heated by discrete energy bursts, where a single stranded model cannot. In addition, we have also shown that the line-of-sight Doppler velocities can also be reproduced with the use of the multi-strand model employed. We have used three line filters, to show that red shifts and blue shifts can be produced, which match general coronal loop observations. Where red shifts are seen from satellite observations, we have shown we can reproduce these red shifts, and similarly for the blue shifts. It must be noted however, that the derived velocities are often lower than the observed velocities by several factors in some cases, although we do show

## CHAPTER 5

good agreement with the velocities observed in Tripathi et al. (2009).

We have simulated a short, 10 Mm loop, and we believe that a longer loop could produce higher velocities. This is discussed in more detail in Chapter 7.

Finally, Table 5.6 summarises the results from this chapter.

Table 5.5: Summary of results in Chapter 5

Parameter	Si VII $V_{cf}$ (blue, red)	Si VII % Red Shift	Fe XI $V_{cf}$ (blue, red)	Fe XI % Red Shift	Fe XV $V_{cf}$ (blue, red)	Fe XV % Red Shift	$V_{cf}$ Deviation (blue, red)	Temperature	Temperature Deviation
Increasing $E_{Total}$	decrease, increase	increase,	decrease, increase	increase	decrease, no trend	no trend	decrease, increase	increase	increase
Increasing No. Strands	n/a, increase	increase	n/a, <sup>1</sup> no trend	increase <sup>1</sup>	increase, no trend	decrease	decrease, decrease	increase	decrease
Increasing No. Bursts	increase, decrease	decrease	increase, decrease	decrease	decrease, no trend	no trend	decrease, <sup>2</sup> decrease <sup>2</sup>	increase	decrease

<sup>1</sup> At cooler temperatures, blue shifts are seen, and are expected to behave similarly to the red shift<sup>2</sup> Si VII shows an increase in deviation

## Chapter 6

# Phase Plane Analysis of the Temperature Structure Along 1-D Hydrostatic Coronal Loops

The concept of the phase plane to study the thermal equilibrium of solar coronal loops has been previously introduced by several authors, including Hood and Priest (1979), Hood and Anzer (1988), Steele and Priest (1990), Steele and Priest (1991), Walsh et al. (1995), and Mendoza-Briceno and Hood (1997).

In the absence of gravity, and with a loop footpoint temperature of 1 MK, Hood and Priest (1979) solved the equations of thermal equilibrium. They concluded that when the radiative term dominated the uniform heating along the loop, a lack of equilibrium occurred, and solutions with cool summit temperatures were possible. The equations of thermal equilibrium were re-examined in Hood and Anzer (1988) to find conditions under which cool condensations could form in the corona. Steele and Priest (1990) extended this work, using the Hildner (1974) radiative losses to numerically solve the thermal equilibrium equations. It was shown that a number of solutions existed:

## CHAPTER 6

1. Hot loops: which have hot summits ( $0.4 - 3.0$  MK), and cool footpoint ( $0.02$  MK).
2. Hot-cool loops: which have footpoints at  $0.2$  MK, and a similar summit temperature, or possibly even lower, but with sections of the loop at coronal temperatures.
3. Cool loops: which have temperatures of  $\sim 0.8$  MK along their entire length.
4. Warm loops: which are similar to cool loops, but have summit temperatures in the region of  $0.08 - 0.4$  MK.

Steele and Priest (1990) suggest that the cool loops could be associated with active region prominences where the magnetic field line lies mainly along the plane of the prominence, and that the global differential emission measure (DEM) can be explained by the hot-cool loop solution. Later, by including changes in the cross-sectional area of the coronal loop, by increasing the area towards the loop apex, Steele and Priest (1991) showed that:

1. the summit temperature of hot-cool loops increased significantly
2. the summit temperature of the warm loops remained unchanged
3. the summit temperature of the hot and cool loops increased slightly

Steele and Priest (1994) then went on to include gravity in the thermal equilibrium equation, meaning that the pressure along the loop fell from the footpoint to the summit. As such, this means that the pressure was now a free parameter, and so rather than a 2-D phase plane, a 3-D phase volume was introduced. The effects of this, meant that the hot-cool loop solutions no longer existed, thus reducing the number of solutions.

## CHAPTER 6

Walsh et al. (1995) also investigated the solution space to analytically solve the thermal equilibrium equation, using a simplified, optically thin, two-range radiative loss function. Again, using a phase plane analysis, Walsh et al. (1995) produced solution where hot, cool, warm and hot-cool solutions are possible, depending on the length of the loop, the footpoint temperature, the base conductive flux and the value of the unknown coronal heating term. This unknown coronal heating term, previously just assumed to be constant along the length of the loop, was investigated in Mendoza-Briceno and Hood (1997), by varying the heating term as a function of the length of the loop. Mendoza-Briceno and Hood (1997) found that there is a critical decay length of the heating below which a hot coronal loop can not exist, and it is thought that this allows the existence of catastrophic cooling after thermal non-equilibrium occurs.

With the above in mind, the work presented in this chapter builds upon the work of Walsh et al. (1995), by analytically solving, and investigating, the solution space of the thermal equilibrium equation, in the absence of gravity, but introduces a new four-range, optically thin, radiative loss function.

### 6.1 Basic Equations

This section will outline the MHD equations, and how with certain assumptions, these can be used to produce the thermal equilibrium equation from which to explore the temperature structure along 1-D hydrostatic coronal loops.

#### Maxwell's Equations

$$\nabla \times \mathbf{B} = \mu \mathbf{j} + \frac{1}{c^2} \frac{\partial \mathbf{E}}{\partial t} \quad (6.1)$$

$$\nabla \cdot \mathbf{B} = 0 \quad (6.2)$$

$$\nabla \times \mathbf{E} = -\frac{\partial \mathbf{B}}{\partial t} \quad (6.3)$$

## CHAPTER 6

$$\nabla \cdot \mathbf{E} = \frac{\rho_e}{\epsilon} \quad (6.4)$$

where  $\mathbf{B}$  is the magnetic field strength,  $\mathbf{E}$  is the electric field strength,  $\mathbf{j}$  is the current density,  $\mu$  is the magnetic permeability,  $t$  is the time,  $\rho_e$  is the charge density,  $c$  is the speed of light in a vacuum, and  $\epsilon$  is the permittivity of free space. These equations can then be simplified under certain assumptions, as discussed in Priest (1982):

- The plasma is assumed to be in thermal equilibrium.
- The plasma is treated as a continuous medium. This assumption is held if the length-scales considered greatly exceed any internal plasma lengthscales.
- The plasma is treated as a single fluid system
- The plasma is assumed to be isotropic, except for the thermal conduction, which is greatest along the magnetic field line.
- Rotational effects of the Sun are neglected, and so an inertial frame of reference is used. The rotational effects can become important when considering very large structures.
- A simplified Ohm's Law is applied:

$$\mathbf{j} = \sigma (\mathbf{E} + \mathbf{v} \times \mathbf{B}) \quad (6.5)$$

where  $\sigma$  is the electrical conductivity and  $\mathbf{v}$  is the plasma velocity.

- $\epsilon$  and  $\mu$  are assumed to be constant, with values taken from a vacuum in the solar context:  $\epsilon_0 = 8.854 \times 10^{-12} \text{ F m}^{-1}$ ;  $\mu_0 = 4\pi \times 10^{-7} \text{ H m}^{-1}$
- Relativistic effects can be ignored, since the sound, Alfvénic and flow velocities are much smaller than the speed of light. Thus, consider

$$v_0 = l_0/t_0,$$

## CHAPTER 6

to be a typical plasma speed, with  $l_0$  and  $t_0$  typical plasma length and timescales respectively. From Equation 6.3, consider also

$$\frac{E_0}{l_0} \approx \frac{B_0}{t_0},$$

where  $B_0$  and  $E_0$  are typical values of  $\mathbf{B}$  and  $\mathbf{E}$  respectively. Thus, by comparing sizes of the terms in Equation 6.1, the second term on the right-hand side has magnitude

$$\frac{E_0}{c^2 t_0} \approx \frac{B_0 l_0}{c^2 t_0^2} = \frac{v_0^2 B_0}{c^2 l_0} \approx \frac{v_0^2}{c^2} |\nabla \times \mathbf{B}|$$

which is much smaller than the left-hand side of Equation 6.1, since  $v_0 \ll c$ . As a result,  $\partial \mathbf{E} / \partial t$  can be neglected. Equation 6.1 can be rewritten as

$$\nabla \times \mathbf{B} = \mu_0 \mathbf{j} \quad (6.6)$$

### The Induction Equation

Equation 6.3 can be rewritten, by using Equation 6.5 to eliminate  $\mathbf{E}$ , to give

$$\frac{\partial \mathbf{B}}{\partial t} = -\nabla \times \left( \frac{\mathbf{j}}{\sigma} - \mathbf{v} \times \mathbf{B} \right). \quad (6.7)$$

Then, by using Equation 6.6, it can be rewritten again as

$$\frac{\partial \mathbf{B}}{\partial t} = -\nabla \times \left( \frac{1}{\mu_0 \sigma} \nabla \times \mathbf{B} - \mathbf{v} \times \mathbf{B} \right). \quad (6.8)$$

The triple vector product (see Equation 6.2 where  $\nabla \cdot \mathbf{B} = 0$ ),

$$\begin{aligned} \nabla \times (\nabla \times \mathbf{B}) &= \nabla(\nabla \cdot \mathbf{B}) - \nabla^2 \mathbf{B} \\ &= -\nabla^2 \mathbf{B} \end{aligned}$$

is then used to with Equation 6.8 to give:

$$\frac{\partial \mathbf{B}}{\partial t} = \nabla \times (\mathbf{v} \times \mathbf{B}) + \eta_0 \nabla^2 \mathbf{B} \quad (6.9)$$

which is known as the induction equation, and it links the evolution of the plasma to the magnetic field.  $\nu_0 = (\mu_0 \sigma)^{-1}$  is the constant magnetic diffusivity.

## CHAPTER 6

### The Plasma Equations

The motion of the magnetic field is coupled to the behaviour of the plasma by the presence of the velocity term in Equation 6.9 and in the equations for mass continuity, motion, and energy.

### Mass Continuity

In an MHD system, the mass must be conserved:

$$\frac{D\rho}{Dt} + \rho\nabla \cdot \mathbf{v} = 0, \quad (6.10)$$

where  $\rho$  is the plasma density and

$$\frac{D}{Dt} = \frac{\partial}{\partial t} + \mathbf{v} \cdot \nabla$$

is the total derivative.

### Motion

The equation of motion for the plasma can be written as

$$\rho \frac{D\mathbf{v}}{Dt} = -\nabla p + \mathbf{j} \times \mathbf{B} + \rho\mathbf{g} + \rho\nu\nabla^2\mathbf{v}, \quad (6.11)$$

where  $p$  is the plasma pressure. The terms on the right-hand side of the equation can be separated as:

- $\nabla p$  is the plasma pressure gradient.
- $\mathbf{j} \times \mathbf{B}$  is the Lorentz force. Using Equation 6.6,

$$\mathbf{j} \times \mathbf{B} = \frac{1}{\mu_0}(\nabla \times \mathbf{B}) \times \mathbf{B}$$

which becomes

$$\mathbf{j} \times \mathbf{B} = (\mathbf{B} \cdot \nabla) \frac{\mathbf{B}}{\mu_0} - \nabla \left( \frac{B^2}{2\mu_0} \right)$$

## CHAPTER 6

when using the triple vector product. The first term on the right-hand side of the equation is a magnetic tension force that is proportional to  $B^2$ . The second term on the right-hand side is a magnetic pressure force, with the magnetic pressure given by  $B^2/2\mu_0$ .

- $\rho\mathbf{g}$  is the effect of gravity, where  $\mathbf{g}$  is the local gravitational acceleration at the surface of the Sun.  $\mathbf{g} \sim 274 \text{ m s}^{-2}$ .
- $\rho\nu\nabla^2\mathbf{v}$  is the effect of viscosity on an incompressible flow.  $\nu$  is the coefficient of kinematic viscosity which is assumed to be uniform throughout the plasma. Spitzer (1962) gives

$$\rho\nu = 2.21 \times 10^{-16} \frac{\text{T}^{5/2}}{\text{Ln}\Lambda} \text{ kg m}^{-1} \text{ s}^{-1},$$

where  $\text{Ln}\Lambda$  is the Coulomb Logarithm, taken to be  $\sim 20$  for the solar corona.

### The Energy Equation

The fundamental energy is expressed as:

$$\frac{\rho^\gamma}{\gamma - 1} \frac{D}{Dt} \left( \frac{p}{\rho^\gamma} \right) = \nabla \cdot (K\nabla T) - L \quad (6.12)$$

where  $\gamma$  is the ratio of specific heats ( $\gamma = 5/3$ ), and  $T$  is the temperature of the plasma.  $K$  is the tensor of thermal conduction. This can be split into components across and along the magnetic field:

$$\nabla_{\parallel} \cdot (\kappa_{\parallel} \nabla_{\parallel} T) + \nabla_{\perp} \cdot (\kappa_{\perp} \nabla_{\perp} T).$$

Conduction along the magnetic fieldlines is mainly by electrons. Braginski (1965) gives  $\kappa_{\parallel} = \kappa_0 T^{5/2} \text{ W m}^{-1} \text{ deg}^{-1}$  with  $\kappa_0 = 10^{-11}$  for the corona. Across the fieldlines, conduction is mainly by ions. At coronal temperatures:

$$\frac{\kappa_{\perp}}{\kappa_{\parallel}} \approx 10^{-12}.$$

## CHAPTER 6

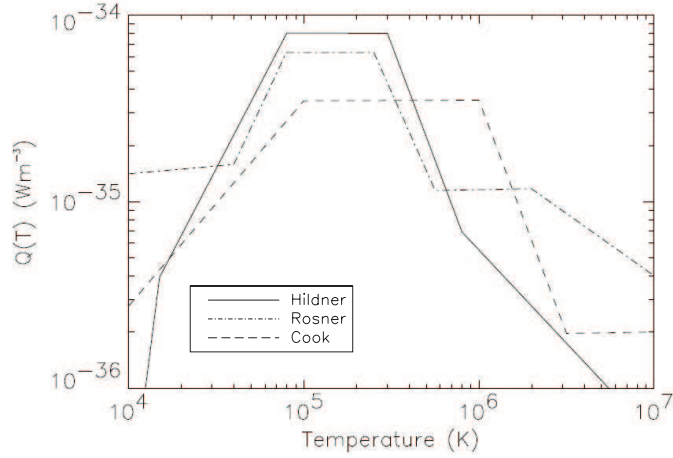


Figure 6.1: Comparison of the radiative loss function  $Q(T)$  from Hildner (1974), Rosner et al. (1978), and Cook et al. (1989).

Therefore, the vast majority of conducted heat occurs along the magnetic field, and as such, the conduction term can be written as:

$$\kappa_{\parallel} \cdot (\kappa_{\parallel} \nabla T) = \kappa_0 \nabla_{\parallel} \cdot (T^{5/2} \nabla_{\parallel} T). \quad (6.13)$$

The loss-gain function,  $W$ , has the form:

$$W(\rho, T) = \rho^2 Q(T) - H \quad (6.14)$$

where  $H$  is the unknown coronal heating term, and  $Q(T)$  is the optically thin radiative loss function, approximated by a piece-wise continuous function:

$$Q(T) = \chi T^{\alpha} \quad (6.15)$$

where  $\alpha$  and  $\chi$  are constant within a particular temperature range of the piecewise fit, and is illustrated, by three examples, in Figure 6.1.

### Perfect Gas Law

The perfect gas law is used:

$$p = \frac{R}{\bar{\mu}} \rho T \quad (6.16)$$

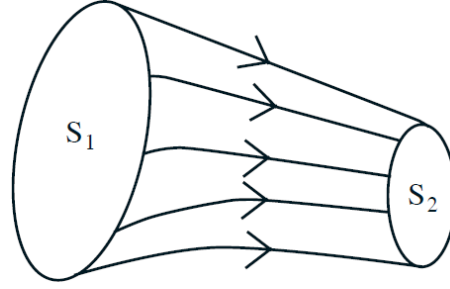


Figure 6.2: An example of a magnetic flux tube through surfaces  $S_1$  and  $S_2$ .

where  $R = 8.3 \times 10^3 \text{ m}^2 \text{ s}^{-2} \text{ K}^{-1}$  is the molar gas constant, and  $\bar{\mu} = 0.6$  in the ionised corona.

### Summary of Equations

Thus, summarising the equations considered so far, we have:

$$\frac{\partial \mathbf{B}}{\partial t} = \nabla \times (\mathbf{v} \times \mathbf{B}) + \eta_0 \nabla^2 \mathbf{B} \quad (6.17)$$

$$\frac{D\rho}{Dt} + \rho \nabla \cdot \mathbf{v} = 0 \quad (6.18)$$

$$\rho \frac{D\mathbf{v}}{Dt} = -\nabla p + \mathbf{j} \times \mathbf{B} + \rho \mathbf{g} + \rho \nu \nabla^2 \mathbf{v} \quad (6.19)$$

$$\frac{\rho^\gamma}{\gamma - 1} \frac{D}{Dt} \left( \frac{p}{\rho^\gamma} \right) = \kappa_0 \nabla_{\parallel} \cdot (T^{5/2} \nabla_{\parallel} T) - \rho^2 \chi T^\alpha + H \quad (6.20)$$

$$p = \frac{R}{\bar{\mu}} \rho T \quad (6.21)$$

### Magnetic Flux Tubes

The volume generated by a set of fieldlines, which intersect a simple, closed curve, is called a magnetic flux tube. Figure 6.2 shows a simple diagram illustrating a typical flux tube. The strength of a flux tube,  $F_s$  is the amount of magnetic flux  $\mathbf{B}$  crossing a particular section,  $S_1$ , of the tube:

$$F_s = \int_{S_1} \mathbf{B} \cdot d\mathbf{S} = \int_{S_1} B_n dS \quad (6.22)$$

where  $B_n$  is the normal component of the field through the section  $S_1$ .

## CHAPTER 6

Coronal loops outline the magnetic field, and are examples of flux tubes. Throughout this chapter, it is assumed that the coronal loops have a constant cross-sectional area, and that the loop structure remains rigid due to the strong magnetic field (i.e. the coronal plasma- $\beta$  is very small).

This also means that Equation 6.17, the induction equation, is no longer required. Also, this means that  $\mathbf{j} \times \mathbf{B} = 0$ , and thus can be omitted from Equation 6.19. All plasma motions are assumed to be along the coronal loop length, and this therefore allows the analysis to be restricted to one-dimensional dynamics. As such, Equations 6.18 to 6.21 are reduced to:

$$\frac{D\rho}{Dt} + \rho \frac{\partial v}{\partial x} = 0 \quad (6.23)$$

$$\rho \frac{Dv}{Dt} = -\frac{\partial p}{\partial x} + \rho g + \rho \nu \frac{\partial^2 v}{\partial x^2} \quad (6.24)$$

$$\frac{\rho^\gamma}{\gamma - 1} \frac{D}{Dt} \left( \frac{p}{\rho^\gamma} \right) = \kappa_0 \frac{\partial}{\partial x} \left( T^{5/2} \frac{\partial T}{\partial x} \right) - \rho^2 \chi T^\alpha + H \quad (6.25)$$

$$p = \frac{R}{\bar{\mu}} \rho T \quad (6.26)$$

where all quantities are along the magnetic field, and  $x$  is the distance along the field line.

### The Isobaric Assumption

Walsh et al. (1996) investigate the validity of the isobaric assumption, by including the inertial terms in the fluid equations. It was found that the temperature structure can be approximated to a high degree, by assuming an isobaric environment, since the temperature changes along a loop are generally governed by the variations in the heating.

So, using Equations 6.23 to 6.26, and neglecting gravity and viscosity, Equation 6.23 (mass continuity) can be rewritten as:

$$\frac{\partial \rho}{\partial t} + v \frac{\partial \rho}{\partial x} + \rho \frac{\partial v}{\partial x} = 0.$$

## CHAPTER 6

Thus,

$$\frac{\partial \rho}{\partial t} + \frac{\partial(\rho v)}{\partial x} = 0. \quad (6.27)$$

Equation 6.24 (motion) can be expressed as:

$$\rho \left( \frac{\partial v}{\partial t} + v \frac{\partial v}{\partial x} \right) = -\frac{\partial p}{\partial x}, \quad (6.28)$$

whilst the left-hand side of Equation 6.25 (energy) can be rewritten as:

$$\begin{aligned} \frac{\rho^\gamma}{\gamma - 1} \frac{D}{Dt} \left( \frac{p}{\rho^\gamma} \right) &= \frac{1}{\gamma - 1} \frac{Dp}{Dt} - \frac{\gamma p}{(\gamma - 1)\rho} \frac{D\rho}{Dt} \\ &= \frac{1}{\gamma - 1} \frac{Dp}{Dt} + \frac{\gamma p}{\gamma - 1} \frac{\partial v}{\partial x} \\ &= \frac{1}{\gamma - 1} \left( \frac{\partial p}{\partial t} + v \frac{\partial p}{\partial x} \right) + \frac{\gamma p}{(\gamma - 1)} \frac{\partial v}{\partial x} \end{aligned} \quad (6.29)$$

by expanding the total derivative. These equations can then be made dimensionless, against typical coronal values, so that:

$$t = t_c \hat{t}, \quad x = l \hat{x}, \quad v = v_c \hat{v} = \frac{l \hat{v}}{t_c}, \quad \rho = \rho_c \hat{\rho}, \quad T = T_c \hat{T}, \quad p = p_c \hat{p}$$

where  $l$  is the length of the field line,  $v_c = l/t_c$  is the conductive velocity,  $T_c = 10^6$  K,  $\rho_c = 8.35 \times 10^{-13}$  kg m<sup>-3</sup>, and  $p_c = R\rho_c T_c / \bar{\mu}$ . The timescale,  $t_c$  is defined as the conduction timescale:

$$t_c = \frac{\gamma p_c l^2}{\kappa_0 (\gamma - 1) T_c^{7/2}} \quad (6.30)$$

Substituting into Equations 6.26 to 6.29, gives:

$$\frac{\partial \hat{\rho}}{\partial \hat{t}} + \frac{\partial(\hat{\rho} \hat{v})}{\partial \hat{x}} = 0 \quad (6.31)$$

$$\frac{\rho_c \hat{\rho} \gamma v_c^2}{c_s^2} \left( \frac{\partial \hat{v}}{\partial \hat{t}} + \hat{v} \frac{\partial \hat{v}}{\partial \hat{x}} \right) + \frac{\partial \hat{p}}{\partial \hat{x}} = 0 \quad (6.32)$$

$$\frac{1}{\gamma} \left( \frac{\partial \hat{p}}{\partial \hat{t}} + \hat{v} \frac{\partial \hat{p}}{\partial \hat{x}} \right) + \hat{p} \frac{\partial \hat{v}}{\partial \hat{x}} = \frac{\partial}{\partial \hat{x}} \left( \hat{T}^{5/2} \frac{\partial \hat{T}}{\partial \hat{x}} \right) - L \left[ \hat{\chi} \hat{p}^2 \hat{T}^{\alpha-2} - \hat{H} \right] \quad (6.33)$$

$$\hat{p} = \hat{\rho} \hat{T} \quad (6.34)$$

where the sound speed squared is defined as  $c_s^2 = \gamma p_c / \rho_c$ , and  $H = H_c \hat{H}$ , with  $H_c = \rho_c^2 \chi_c T_c^{\alpha_c}$  ( $\chi_c$  and  $\alpha_c$  are the values of the temperature dependent parameters when  $T = T_c$ ).

## CHAPTER 6

Also introduced is:

$$L = \frac{\rho_c^2 \chi_c T_c^{\alpha_c} l^2}{\kappa_0 T_c^{7/2}} \quad (6.35)$$

which is the ratio of the conduction and radiative timescales, as well as:

$$\hat{\chi} = \frac{\chi T_c^\alpha}{\chi_c T_c^{\alpha_c}} \quad (6.36)$$

for the piecewise fit of each particular temperature range.

Now, if we consider the case where the conductive velocity,  $v_c$ , is much smaller than the sound speed,  $c_s$ , then Equation 6.32 can be approximated by:

$$\frac{\partial \hat{p}}{\partial x} \approx 0. \quad (6.37)$$

This means that  $\hat{p}$  is constant, and this therefore means the environment is now isobaric. Thus, the radiative timescale is considerably longer than the acoustic timescale, which allows any temperature and density variations to be in pressure equilibrium with their surrounds.

The reduced set of isobaric equation is therefore:

$$\frac{\partial \rho}{\partial t} + \frac{\partial(\rho v)}{\partial x} = 0 \quad (6.38)$$

$$\frac{\partial v}{\partial x} = \frac{\partial}{\partial x} \left( T^{5/2} \frac{\partial T}{\partial x} \right) - L [\chi T^{\alpha-2} - H] \quad (6.39)$$

$$\rho = \frac{1}{T}, \quad (6.40)$$

where all hats have been removed for convenience.

It is assumed the loop is symmetrical, and therefore it is only necessary to consider half the loop length, i.e.  $0 \leq x \leq 0.5$  in non-dimensional coordinates. The boundary conditions are:

$$\frac{\partial T}{\partial x} = 0, \quad \text{at } x = 0 \quad (6.41)$$

$$T = T_e, \quad \text{at } x = 0.5 \quad (6.42)$$

where  $T_e$  is the chromospheric temperature, and with the initial conditions at  $t = 0$  we have:

$$\begin{aligned}v(x) &= 0 \\ T &= T_s(x)\end{aligned}$$

where  $T_s(x)$  is the static temperature profile obtained for a constant value of the heating ( $H = H_0$ ).

## 6.2 Analytical Solutions to the Phase Plane

From the reduced set of isobaric equations, it is now possible to study the thermal equilibrium equation, and introduce a simplified radiative loss function. This allows solutions of the thermal equilibrium equation to be found, by a powerful technique known as phase plane analysis. A phase plane analysis will therefore investigate the solution space to the thermal equilibrium equation.

### 6.2.1 Thermal Equilibrium and the Four Range Radiative Loss Function

By setting the time derivatives and velocity of Equations 6.38 to 6.40 to zero, one is able to obtain the equation of thermal equilibrium. What is left, is a balance between conduction, radiation, and heating:

$$\frac{d}{dx} \left( T^{5/2} \frac{dT}{dx} \right) = L [\chi T^{\alpha-2} - H_0], \quad (6.43)$$

and this chapter will investigate the solution space to this equation.

This is a complicated problem, particularly when considering the radiative losses. Colgan et al. (2008) present the latest optically thin radiative loss calculations in Figure 6.3. Hildner (1974); Rosner et al. (1978); Cook et al. (1989) have previously created the piecewise radiative loss functions, as discussed earlier and shown in

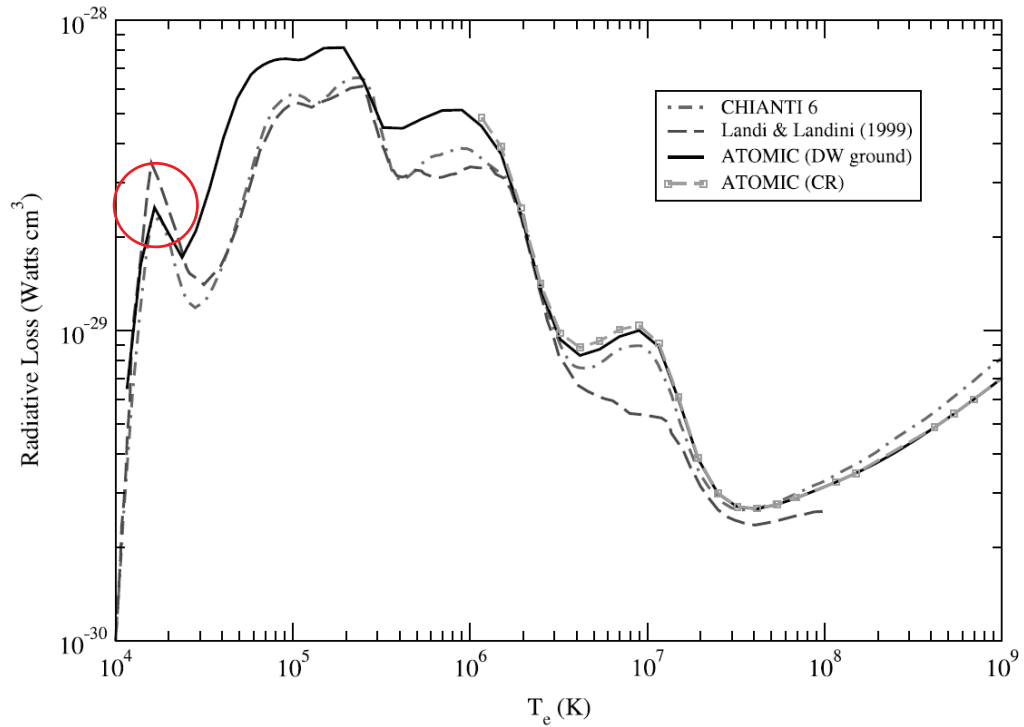


Figure 6.3: From Colgan et al. (2008): Radiative losses from a coronal plasma containing 15 elements. Colgan et al. (2008) compare their ATOMIC calculations (solid line) with those of Landi and Landini (1999) (dashed line) and a calculation made using the most recent version of CHIANTI (dot-dashed line). Also shown is an ATOMIC calculation obtained by solving the full set of collisional-radiative equations, (dashed line with small squares). Losses are given in  $\text{W cm}^3$ , where  $1 \text{ W} = 10^7 \text{ erg s}^{-1}$ . The red circle highlights the significant bump.

## CHAPTER 6

Figure 6.1. Walsh et al. (1995) devised a simplified, two-range radiative loss function. However, these previous functions do not take into consideration the significant bump that is shown at cooler temperatures in Figure 6.3. Therefore, a new four-range radiative loss function is introduced, to investigate the properties of including this extra bump. Also, it can be argued that there are many more dips and rises in the radiative loss function than just the feature being included in this work. But, by just including the one feature, the results of this will have important implications for a fuller treatment of the radiative loss function.

The analytical solutions for the equilibrium states are derived by using this new four-range radiative loss function:

$$\text{where } \chi T^{\alpha-2} = \begin{cases} T^{-7/4}, & T > T_r, & \alpha = 1/4 \\ \frac{T^{7/2}}{T_r^{21/4}}, & T_b \leq T < T_r, & \alpha = 7/2 \\ \frac{T_b^{21/4}}{T_r^{21/4} T^{7/4}}, & T_a \leq T < T_b, & \alpha = 1/4 \\ \frac{T_b^{21/4} T^{7/2}}{T_r^{21/4} T_a^{21/4}}, & T < T_a, & \alpha = 7/2 \end{cases}$$

where  $T_a$  is the temperature at the first peak ( $\sim 0.016$  MK),  $T_b$  is the temperature at the proceeding trough ( $\sim 0.035$  MK), and  $T_r$  is the value at the highest value of the radiation ( $\sim 0.06$  MK). Each temperature interval has a specific value of  $\alpha$  and  $\chi$ , as indicated in the above equation. The four-range function is compared to the two-range function in Walsh et al. (1995), and Hildner (1974) in Figure 6.4.

This simplified function has similar properties to that of the original radiative losses, but allows for simpler, analytical solutions to be calculated, and presented in the form of a phase plane. The radiative losses can only be considered down to chromospheric temperatures (0.01 MK) as at lower temperatures, optically thick effects become important, and so solutions below this temperature will not be considered.

For mathematical ease, Equation 6.43 can now be rewritten as:

$$y'' = \frac{7L}{2} [\chi y^{[2(\alpha-2)]/7} - H_0] \quad (6.44)$$

CHAPTER 6

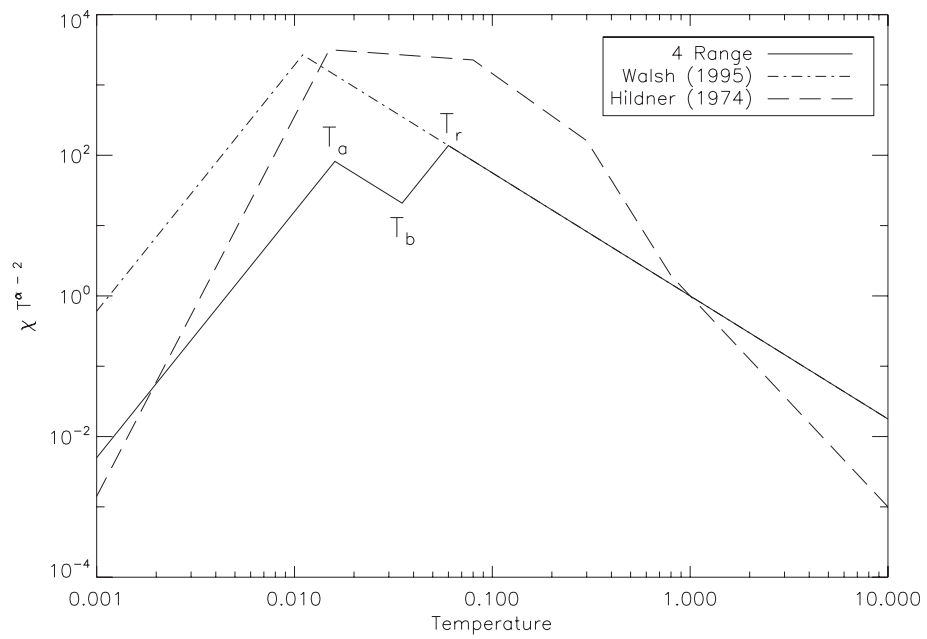


Figure 6.4: Figure showing the non-dimensional four-range radiative loss function (solid line), Walsh et al. (1995) (dot-dash line) and Hildner (1974) (dashed line) optically thin radiative loss functions, with temperature ( $T$ ) displayed in dimensionless units.

## CHAPTER 6

where  $y = T^{7/2}$ . The boundary conditions (Equations 6.41 and 6.42) are now defined as:

$$\frac{dy}{dx} = 0, \text{ at } x = 0 \quad (6.45)$$

$$y = y_e, \text{ at } x = 0.5 \quad (6.46)$$

Furthermore, there exist critical points, which are inherent to the solutions available. By setting:

$$\frac{dy}{dx} = \Psi \quad (6.47)$$

$$\frac{d\Psi}{dx} = \frac{7L}{2} [\chi y^{[2(\alpha-2)]/7} - H_0] \quad (6.48)$$

then the critical points exist when the two derivatives are zero. Therefore, the critical points exist at:

$$y = y_{crit} = \left( \frac{H_0}{\chi} \right)^{7/[2(\alpha-2)]}, \Psi = 0 \quad (6.49)$$

Depending on the value of  $H_0$ , there may be up to four critical points. If we define:

1.  $T_{crit1}$  being the critical temperature for  $T < T_a$ .
2.  $T_{crit2}$  being the critical temperature for  $T_a < T < T_b$ .
3.  $T_{crit3}$  being the critical temperature for  $T_b < T < T_r$ .
4.  $T_{crit4}$  being the critical temperature for  $T > T_r$ .

and so we have:

$$y_{crit1} = \frac{H_0 y_a^{3/2} y_r^{3/2}}{y_b^{3/2}} \quad (6.50)$$

$$y_{crit2} = \left( \frac{H_0 y_r^{3/2}}{y_b^{3/2}} \right)^{-2} \quad (6.51)$$

CHAPTER 6

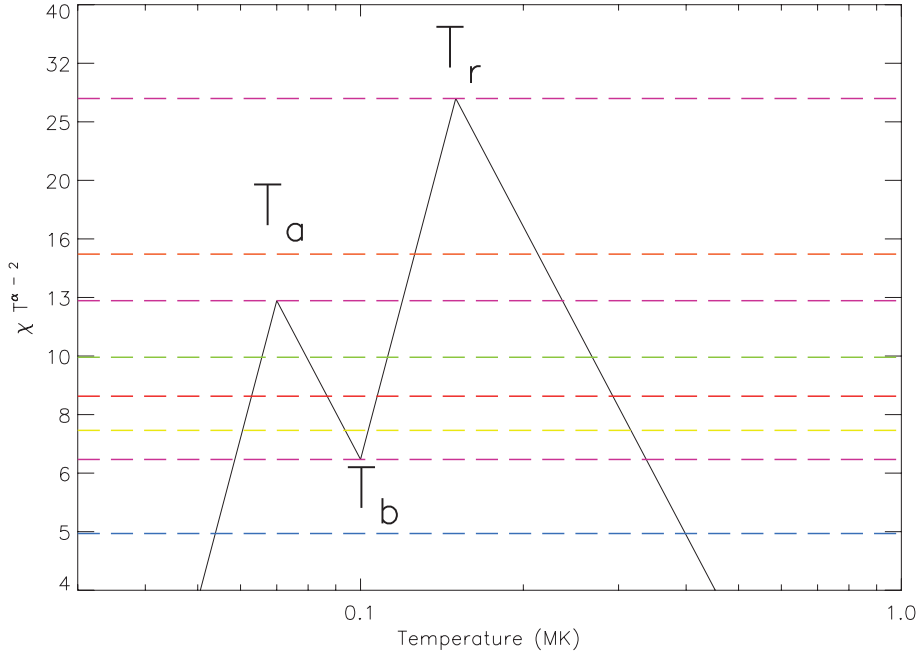


Figure 6.5: Levels of uniform heating for the phase planes displayed in Figures 6.6 to 6.13, for  $T_a = 0.07, T_b = 0.1, T_r = 0.15$ .

$$y_{crit3} = H_0 y_r^{3/2} \quad (6.52)$$

$$y_{crit4} = H_0^{-2} \quad (6.53)$$

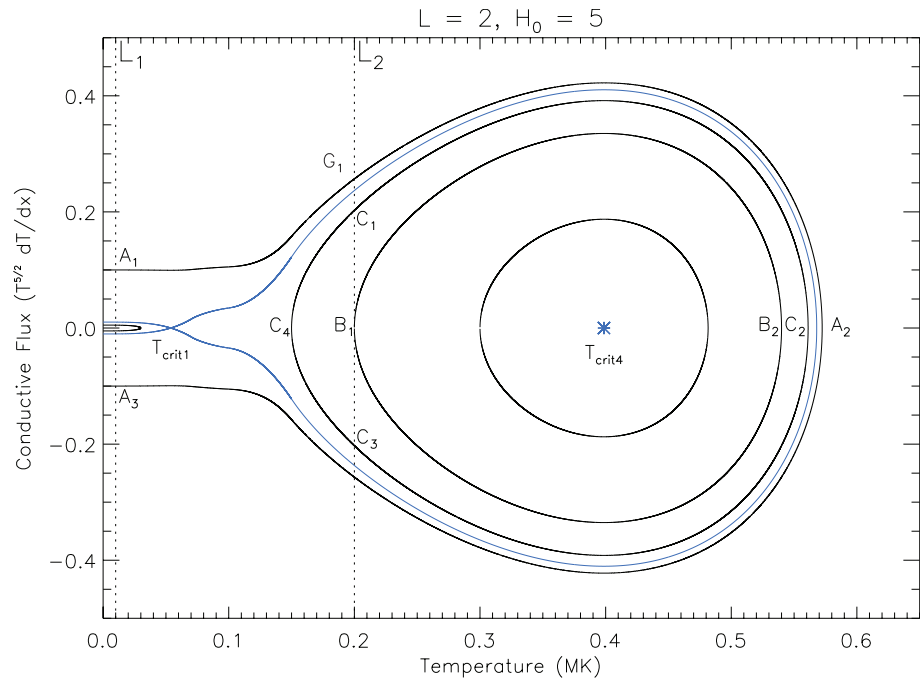
A critical point analysis gives  $(y_{crit1}, 0)$  and  $(y_{crit3}, 0)$  as saddle points, and  $(y_{crit2}, 0)$  and  $(y_{crit4}, 0)$  as centre points (see Appendix A).

Figure 6.5 displays the four-range radiative loss function for values of  $T_a = 0.07, T_b = 0.1$  and  $T_r = 0.15$ . Changing the value of these parameters helps to display the different solutions to the phase plane more clearly, without affecting the physics of the system. The different coloured lines represent the values of  $H_0$  used in the subsequent phase planes, with the colours matching the chosen colours of the separatrix curves.

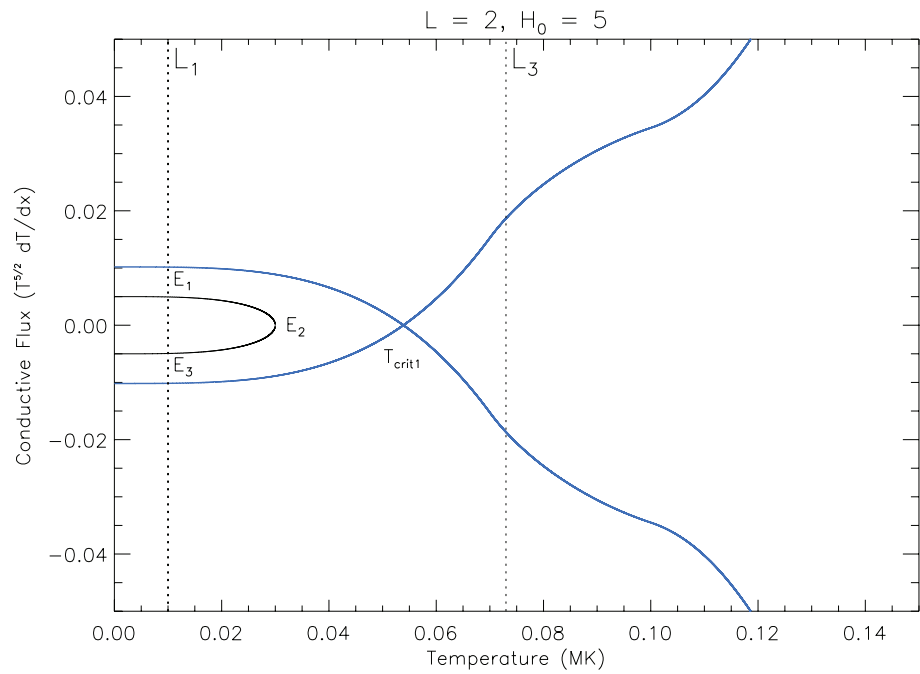
Figures 6.6 to 6.13 display the phase planes for a variety of values of  $H_0$ .  $L = 2$  is used throughout, for analytical expediency.

If we first examine Figure 6.6, the most significant solution is the separatrix

CHAPTER 6



(a) Full solution space.



(b) Zoomed-in cool region.

Figure 6.6: Phase planes for  $H_0 = 5$ .

## CHAPTER 6

curve, which in this diagram is coloured blue. The separatrix curve is fundamental to the solutions in the phase plane, since it separates areas of different topological solutions. This phase plane, for  $H_0 = 5$ , has only two critical points;  $T_{crit1}$  and  $T_{crit4}$ . For example, if we have a loop with a footpoint temperature that lies along the line  $L_1$ , then three unique solution types exist. Firstly, there is the separatrix curve itself, which has the saddle point at  $T = T_{crit1}$ . Secondly, there is the situation where the footpoint (or base) conductive flux is greater than that of the separatrix curve (so that it lies outside of the separatrix curve), then only a hot solution exists. Starting at  $A_1$ , and following the contour clockwise, the contour  $A_1G_1A_2$  gives a loop with a hot summit. Finally if the base conductive flux is less than that of the separatrix curve (and thus lies inside it), then we get the contour  $E_1E_2$  which has a cool summit.

Now, if we have a loop with a footpoint temperature along  $L_2$  and a base conductive flux greater than the separatrix curve, we have the solution  $G_1A_2$ , which is again a hot solution. But, if the base conductive flux is lowered to less than that of the separatrix curve then we get a loop such as  $B_1B_2$ , making sure to follow the contour clockwise. This gives a loop with a hot summit, that is thermally isolated, since the base conductive flux is zero. The summit temperature of the loop is the minimum value for a hot loop solution with this particular footpoint temperature. It is also possible to continue along the contour (e.g.  $B_1B_2B_1$ ), to give a cool summit temperature. This type of a loop is a hot-cool loop, since it is hot along most of its length, but it has a cool summit. The contour  $C_1C_2$  has a hot summit temperature, whilst if the base conductive flux is negative, then cool solutions can occur, such as  $C_3C_4$ , although these cool solutions are normally rejected for being non-physical since the summit temperature is lower than the footpoint temperature.

Figure 6.7 displays the phase plane for  $H_0 \sim 6.69$ . It is at this point that  $T_{crit2}$  and  $T_{crit3}$  suddenly appear at the point  $T = T_b$ . As  $H_0$  is increased past

## CHAPTER 6

this point, four critical points are now observed, with two saddle points, and two centre points. There are therefore now two separatrix curves, as can be seen in Figure 6.8. As  $H_0$  is increased further, there is a point at which the two separatrix curves join together, to form a “double separatrix”, as shown in Figure 6.9, where  $H_0 = \sqrt{\frac{3(y_a^{1/2} - y_b^{1/2})y_b^3}{(y_a^{3/2} - y_b^{3/2})y_r^3}} \sim 8.58$ . As  $H_0$  is again increased, the double separatrix splits into two separate curves, with an example shown for  $H_0 = 10$  in Figure 6.10, which shows the existence of the two separatrix curves, but which offer different properties to those found in Figure 6.8. Increasing  $H_0$  again, begins to merge  $T_{crit1}$  and  $T_{crit2}$  together, which occurs at  $T = T_a$  for  $H_0 \sim 12.49$ , as shown in Figure 6.11, at which point they disappear, and a single separatrix curve remains. This can be seen in Figure 6.12 for  $H_0 = 15$ . As  $H_0$  is increased further, the two critical points  $T_{crit3}$  and  $T_{crit4}$  being to move towards each other, until they reach  $T = T_r$ , at  $H_0 \sim 27.66$ . At this point all the critical values have disappeared, and no separatrix curves exist.

If we now examine the different contours of the phase planes, we notice that there exists different solutions, depending on the value of  $H_0$ . If we take a footpoint temperature along the line  $L_1$ , then we notice that there exists hot solutions in each phase plane, such that the contours  $A_1G_1A_2$ , and  $E_1E_2$  are always possible.<sup>1</sup> Similarly, the same solutions exist in phase planes, until we see in Figure 6.13 at  $H_0 = 27.66$ , where the contours  $C_1C_2$  and  $B_1B_2$ , which include the hot-cool solutions, no longer exist.

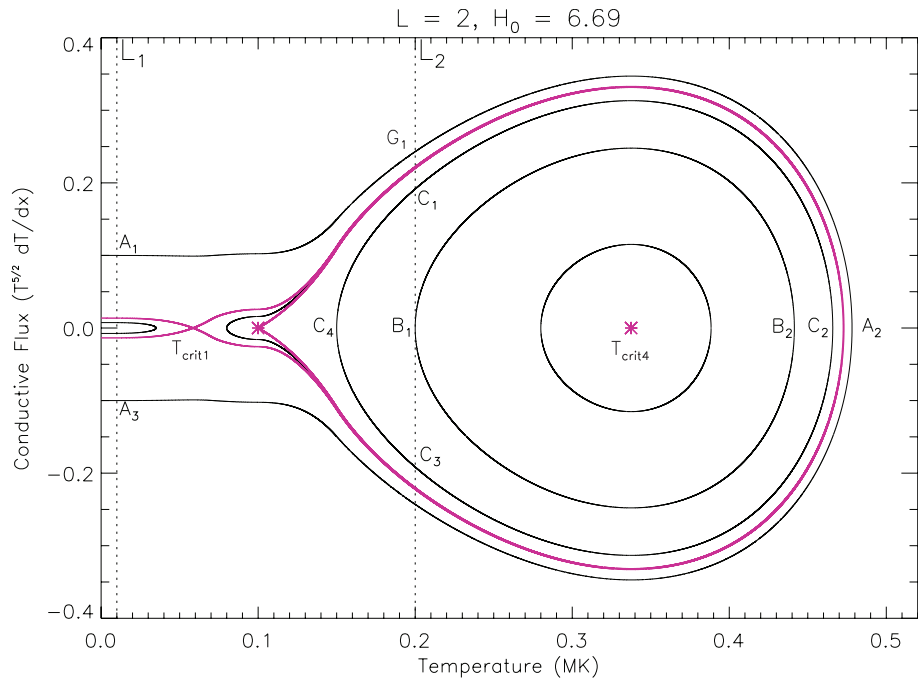
When we examine the phase planes, for footpoint temperatures lying along the line  $L_3$ , we now also see some of the solutions such as  $F_1A_2$ <sup>2</sup> which are capable of the hot-cool and thermally isolated solutions.

Figure 6.14 shows how the phase plane diagram changes with increasing values of  $L$ , which scales as  $L^{1/2}$ . Figure 6.15 shows the maximum and minimum summit temperatures with increasing  $H_0$ . In Region 1, the summit temperature represented

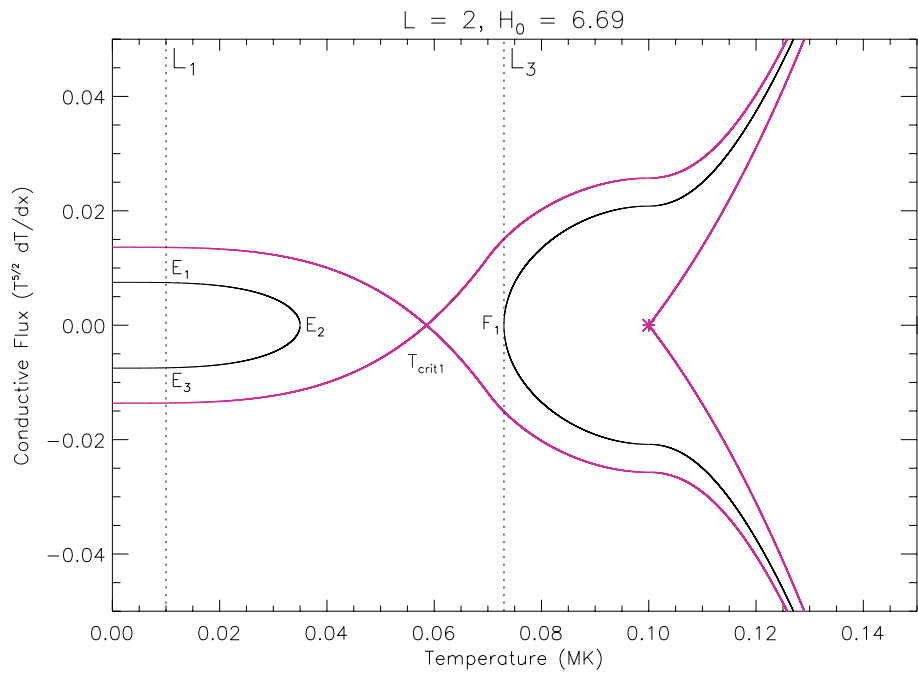
<sup>1</sup>the contours show topologically similar solutions, but the actual solutions are different in each phase plane

<sup>2</sup>in this case, the point  $A_2$  lies directly inside the separatrix curve

CHAPTER 6



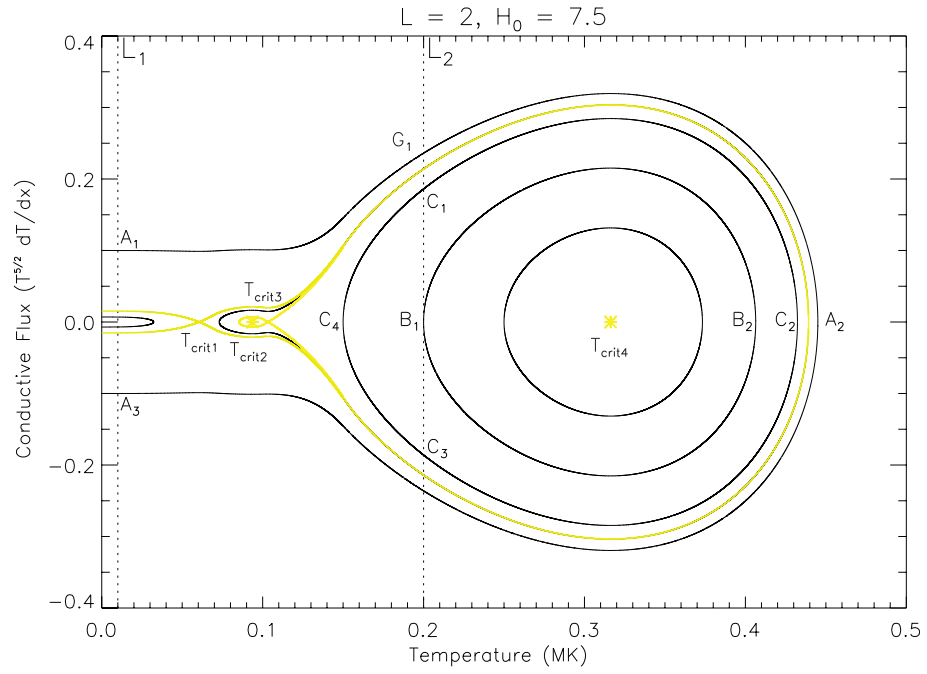
(a) Full solution space.



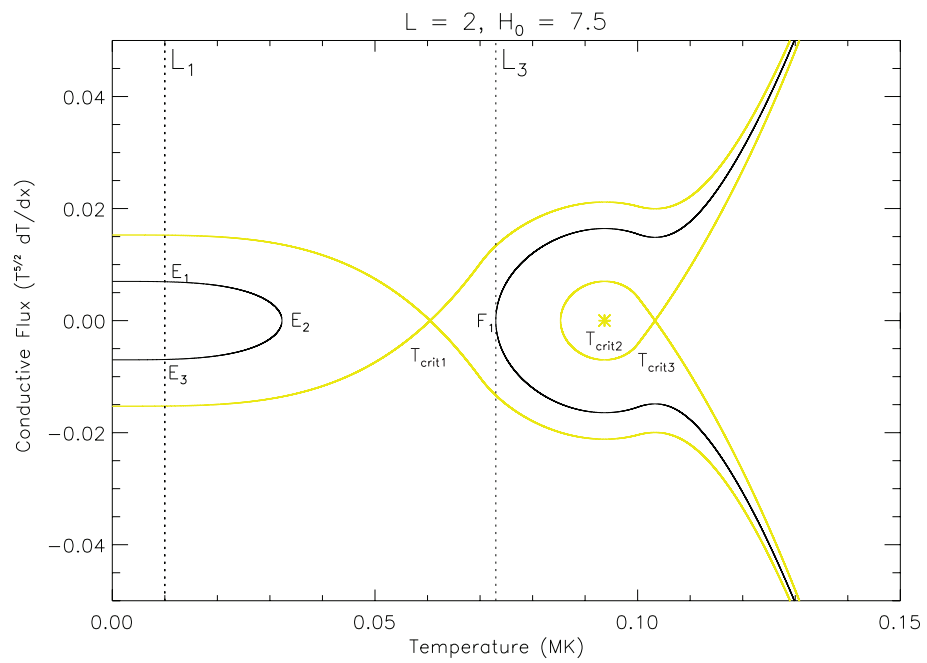
(b) Zoomed in cool region.

Figure 6.7: Phase planes for  $H_0 = 6.69$ .

CHAPTER 6



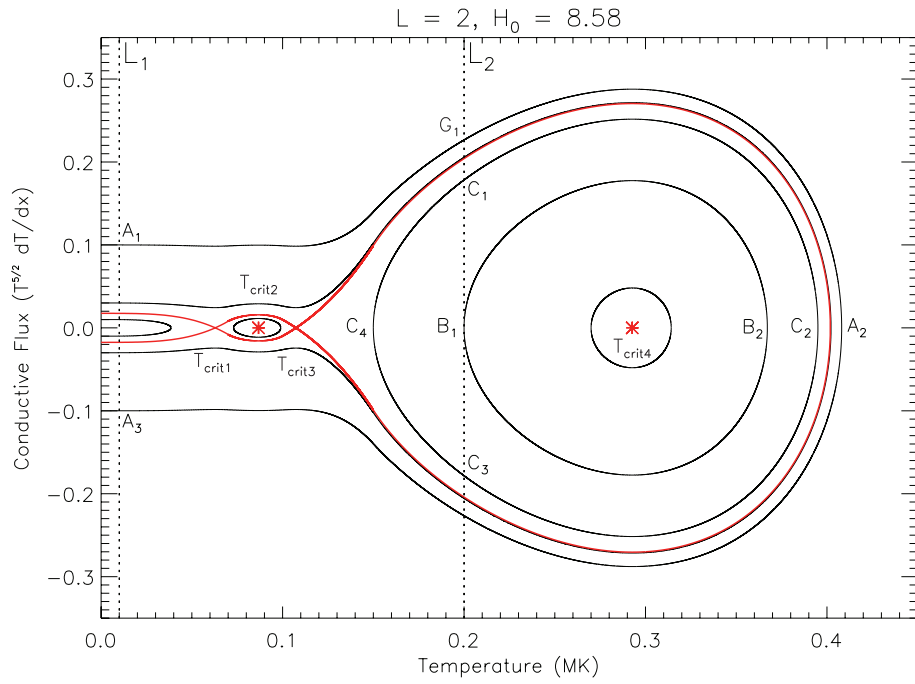
(a) Full solution space.



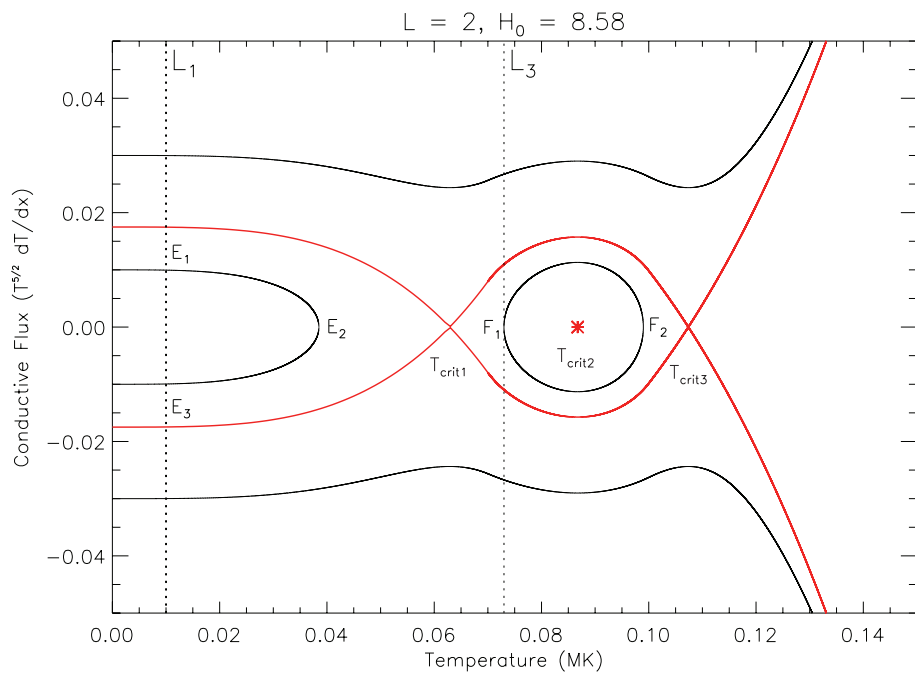
(b) Zoomed in cool region.

Figure 6.8: Phase planes for  $H_0 = 7.5$ .

CHAPTER 6



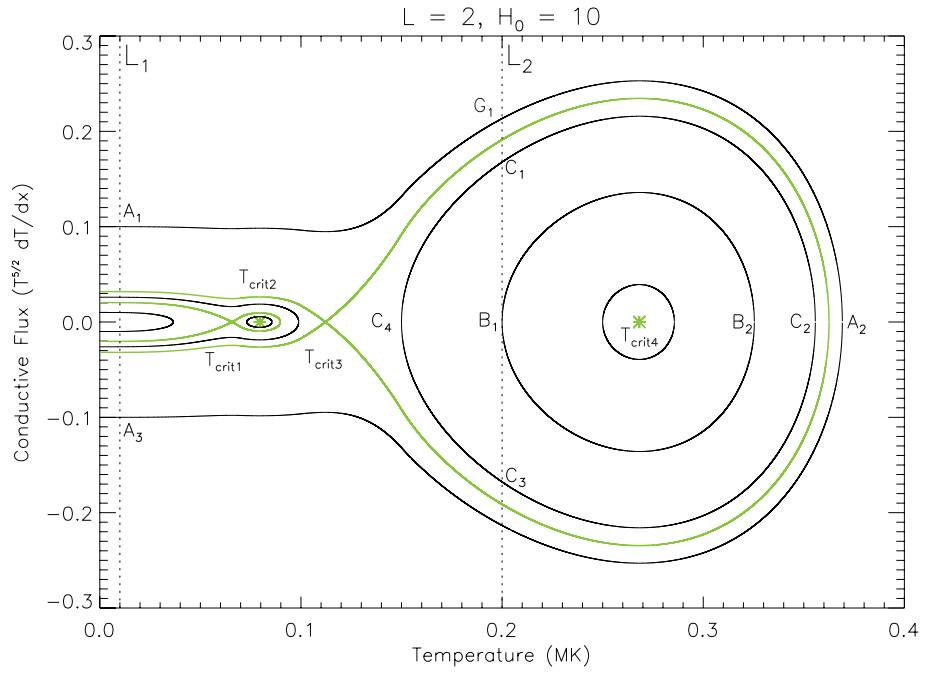
(a) Full solution space.



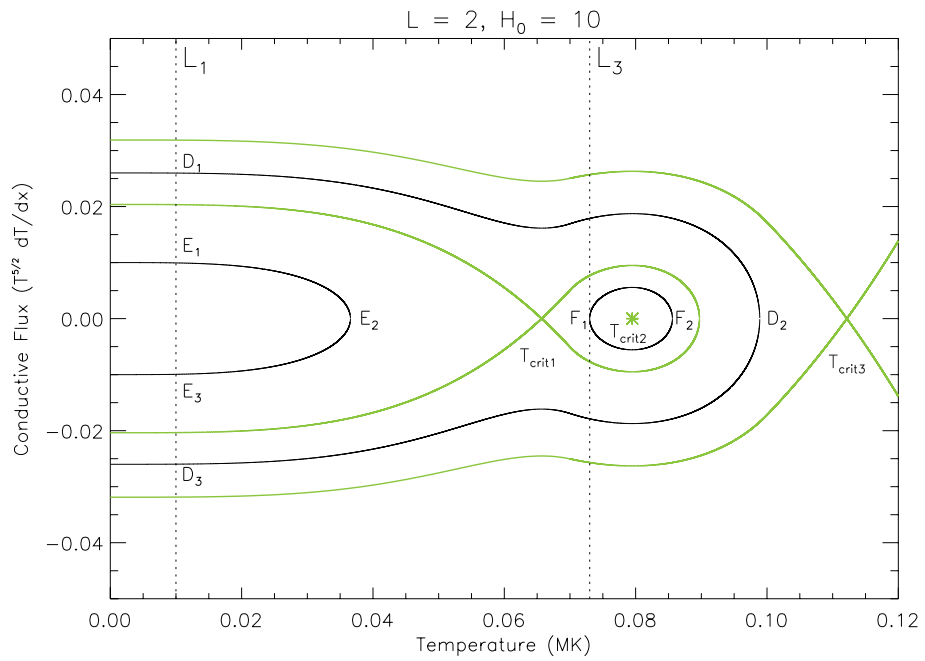
(b) Zoomed in cool region.

Figure 6.9: Phase plane for  $H_0 = \sqrt{\frac{3(y_a^{1/2} - y_b^{1/2})y_b^3}{(y_a^{3/2} - y_b^{3/2})y_r^3}}$

CHAPTER 6



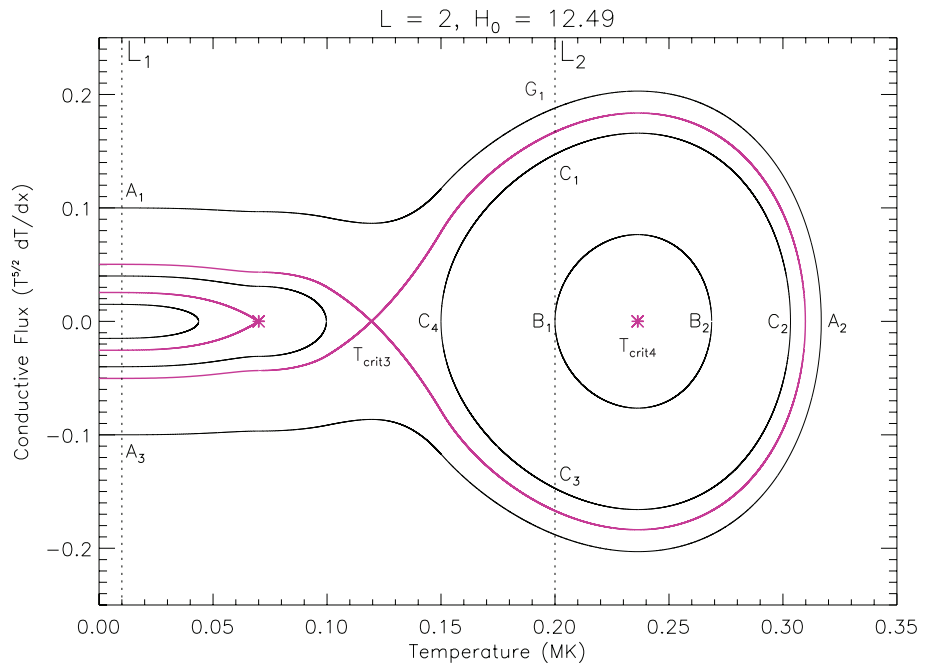
(a) Full solution space.



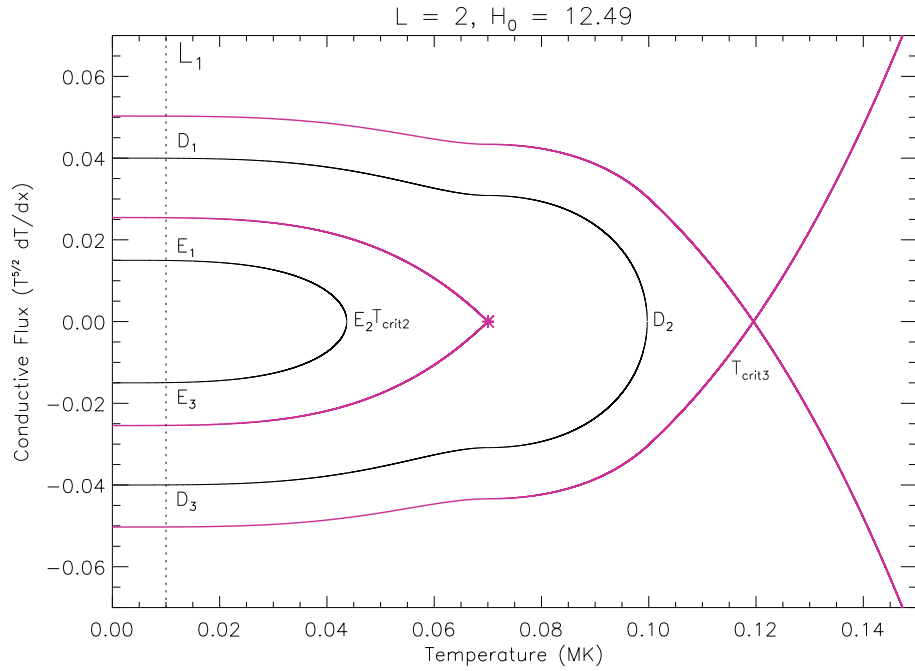
(b) Zoomed in cool region.

Figure 6.10: Phase planes for  $H_0 = 10$

CHAPTER 6



(a) Full solution space.



(b) Zoomed in cool region.

Figure 6.11: Phase plane for  $H_0 = 12.49$ .

CHAPTER 6

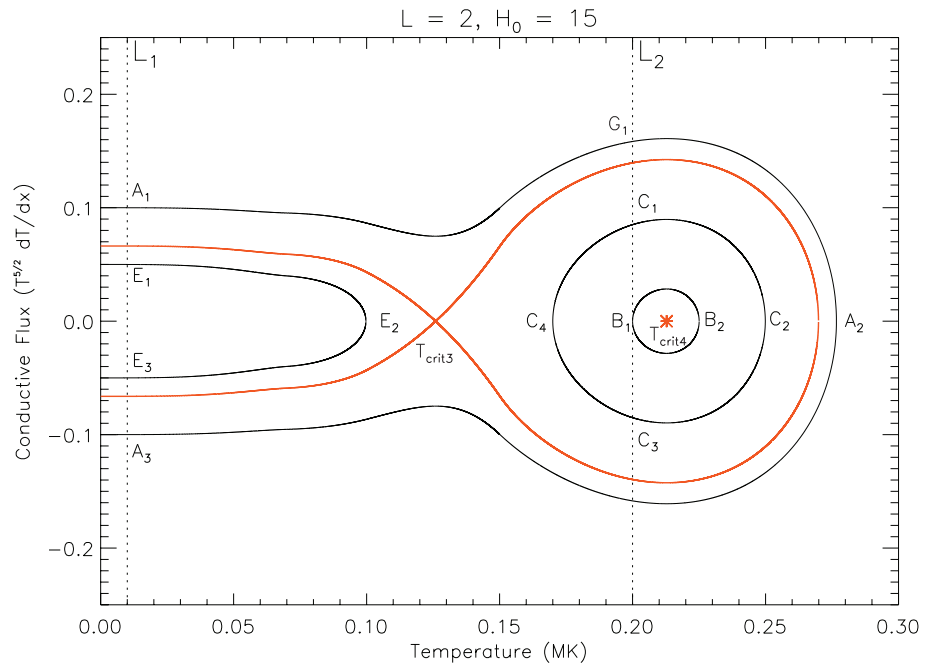


Figure 6.12: Phase plane for  $H_0 = 15$ .

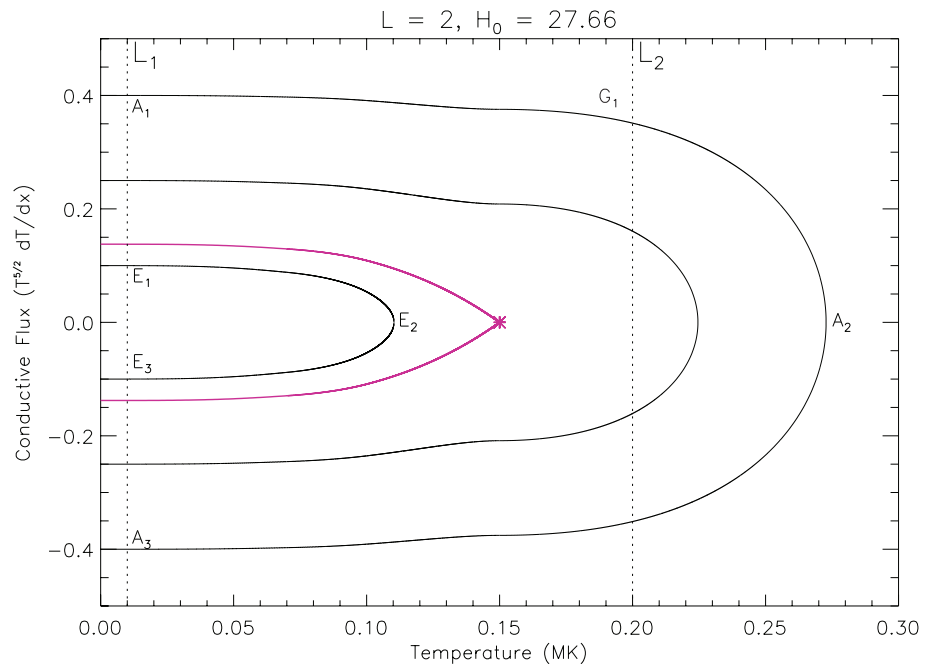


Figure 6.13: Phase plane for  $H_0 = 27.66$ .

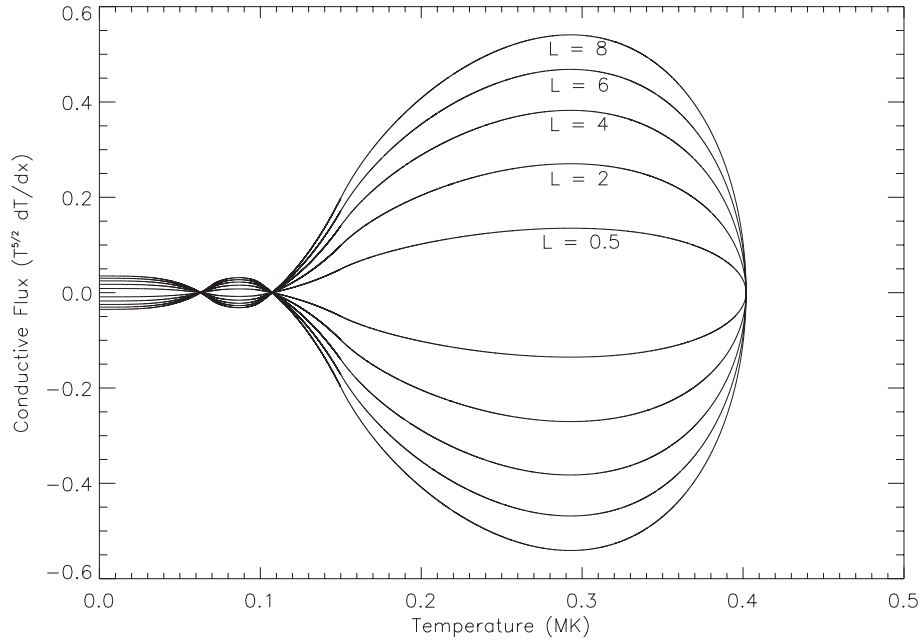


Figure 6.14: Variation of length of loop parameter,  $L$ , for the case with the double separatrix at  $H_0 \sim 8.58$ .

is the maximum summit temperature that can exist, and is the location of the saddle point ( $T_{crit1}$ ). In Region 2, the minimum possible summit temperature is displayed, which represents the summit temperature of the separatrix curve. In Region 3, the maximum summit temperature is displayed, corresponding to  $T_{crit3}$ , whilst the minimum summit temperature in Region 4 is displayed, corresponding to the summit temperature of the separatrix curve in Region 4.

### 6.2.2 Dependence of the summit temperature upon the length of the loop

The two-range radiative loss function (Walsh et al., 1995) was chosen, so that the analytical solutions to the thermal equilibria could be derived. As such, this is the reason that the four-range radiative loss function introduced in this chapter was adapted from this. It is also possible to derive an analytical expression for the

## CHAPTER 6

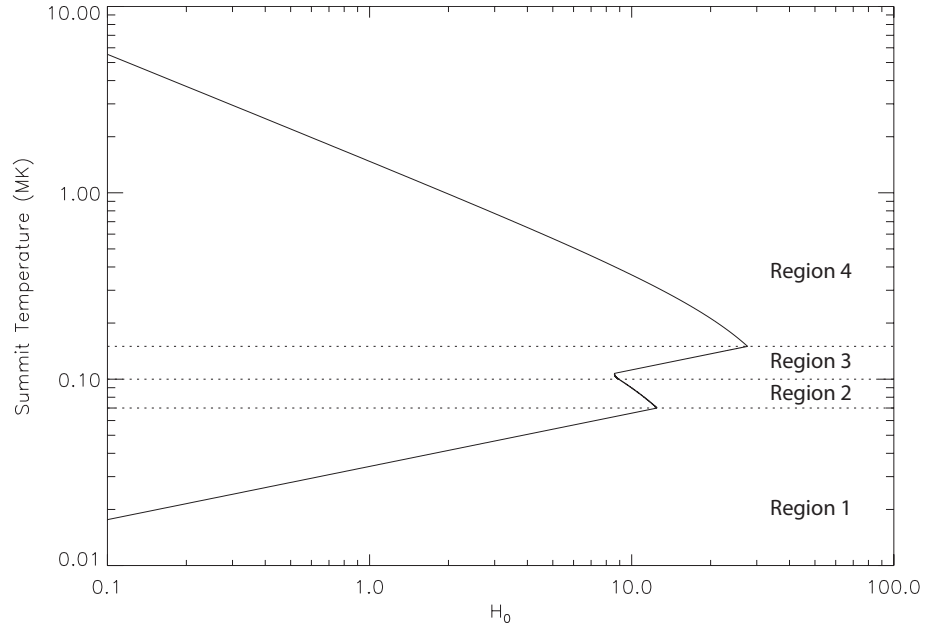


Figure 6.15: Summit temperature for increasing  $H_0$  for loops with a footpoint temperature of  $T_e = 0.01$  MK, and  $L = 2$ , with  $T_a = 0.07$ ,  $T_b = 0.1$ ,  $T_r = 0.15$ .

dependence of the summit temperature ( $T_0$ ), upon the length of the loop variable,  $L$ , for different values of  $H_0$ . There are four sets of solutions, depending upon which temperature region the summit is located at.

**Region 1: For  $T < T_a$**

$$L = \frac{8}{7w} \left( \cosh^{-1} \left( \frac{y_e - \gamma}{y_0 - \gamma} \right) \right)^2 \quad (6.54)$$

where:

$$w = \frac{y_b^{3/2}}{y_r^{3/2} y_a^{3/2}}$$

$$\gamma = \frac{H_0}{w}$$

CHAPTER 6

**Region 2:** For  $T_a \leq T < T_b$

$$\begin{aligned}
 L &= \frac{2}{7} \left[ \left[ (H_0 y_0^{1/2} - z)^2 - (z - H_0 y_a^{1/2})^2 \right]^{1/2} + z \left[ \sin^{-1} \left( \frac{z - H_0 y_a^{1/2}}{H_0 y_0^{1/2} - z} \right) + \frac{\pi}{2} \right] \right. \\
 &\quad \left. + \frac{2}{\sqrt{w}} \ln \left( \frac{C_3 - \sqrt{C_3^2 - 4(C_2^2 - C_1^2)}}{2(C_2 - C_1)} \right) \right]^2 \tag{6.55}
 \end{aligned}$$

where  $z = \frac{y_b^{3/2}}{y_r^{3/2}}$ , and:

$$\begin{aligned}
 C_1 &= \frac{1}{\sqrt{2H_0 w}} \left[ (z - H_0 y_0^{1/2})^2 - (H_0 y_a^{1/2} - z)^2 \right]^{1/2} \\
 C_2 &= \frac{1}{2} \left( y_a - \frac{H_0}{w} \right) \\
 C_3 &= y_e - \frac{H_0}{w}
 \end{aligned}$$

**Region3:** For  $T_b \leq T < T_r$

$$\begin{aligned}
 L &= \frac{2}{7} \left[ \frac{2}{\sqrt{w}} \ln \left[ \frac{C_6 - \sqrt{C_6^2 - 4(C_5^2 - C_4^2)}}{2(C_5 - C_4)} \right] \right. \\
 &\quad \left. + \frac{2\sqrt{2}}{\sqrt{H_0^3}} \left[ z(\theta_c - \theta_d) + \sqrt{E}(\cos \theta_c - \cos \theta_d) \right] \right. \\
 &\quad \left. + 4y_r^{3/4} \cosh^{-1} \left( \frac{y_b - H_0 y_r^{3/2}}{y_0 - H_0 y_r^{3/2}} \right) \right]^2 \tag{6.56}
 \end{aligned}$$

where:

$$\begin{aligned}
 \theta_c &= \sin^{-1} \left[ \frac{z - H_0 y_a^{1/2}}{\sqrt{E}} \right] \\
 \theta_d &= \sin^{-1} \left[ \frac{z - H_0 y_b^{1/2}}{\sqrt{E}} \right]
 \end{aligned}$$

$$\begin{aligned}
 D &= H_0 y_0 - \frac{y_0^2}{2y_r^{3/2}} - \frac{3y_b^2}{2y_r^{3/2}} \\
 E &= H_0 D + z^2
 \end{aligned}$$

CHAPTER 6

$$\begin{aligned}
 C_4 &= \frac{1}{\sqrt{2H_0w}} \left[ E - \left( z - H_0y_a^{1/2} \right)^2 \right]^{1/2} \\
 C_5 &= \frac{1}{2} \left( y_a - \frac{H_0}{w} \right) \\
 C_6 &= y_e - \frac{H_0}{w}
 \end{aligned}$$

**Region 4: For  $T > T_r$**

$$\begin{aligned}
 L &= \frac{2}{7} \left[ \frac{2\sqrt{2}}{\sqrt{H_0^3}} \left( \sin^{-1} \left( \frac{1 - H_0y_r^{1/2}}{\sqrt{G}} \right) + \frac{\pi}{2} + \left[ G - \left( 1 - H_0y_r^{1/2} \right)^2 \right]^{1/2} \right) \right. \\
 &+ 4y_r^{3/4} \ln \left[ \frac{C_9 - \sqrt{C_9^2 - 4(C_8^2 - C_7^2)}}{2(C_8 - C_7)} \right] \\
 &+ \frac{2\sqrt{2}}{\sqrt{H_0^3}} \left[ z(\theta_e - \theta_f) + \sqrt{M}(\cos \theta_e - \cos \theta_f) \right] \\
 &\left. + \frac{2}{\sqrt{w}} \ln \left[ \frac{C_{12} - \sqrt{C_{12}^2 - 4(C_{11}^2 - C_{10}^2)}}{2(C_{11} - C_{10})} \right] \right]^2 \tag{6.57}
 \end{aligned}$$

where:

$$\begin{aligned}
 F &= H_0y_0 - 2y_0^{1/2} \\
 G &= \left( H_0y_0^{1/2} - 1 \right)^2 \\
 J &= \frac{3}{2}y_r^{1/2} + F \\
 K &= J - \frac{3y_b^2}{2y_r^{3/2}} \\
 M &= H_0K + z^2
 \end{aligned}$$

$$\begin{aligned}
 \theta_e &= \sin^{-1} \left[ \frac{z - H_0y_a^{1/2}}{\sqrt{M}} \right] \\
 \theta_f &= \sin^{-1} \left[ \frac{z - H_0y_b^{1/2}}{\sqrt{M}} \right]
 \end{aligned}$$

$$\begin{aligned}
C_7 &= \frac{y_r^{3/4}}{\sqrt{2H_0}} \left[ (1 - H_0 y_0^{1/2})^2 - (1 - H_0 y_r^{1/2})^2 \right]^{1/2} \\
C_8 &= \frac{1}{2} (y_r - H_0 y_r^{3/2}) \\
C_9 &= y_b - H_0 y_r^{3/2} \\
C_{10} &= \frac{1}{\sqrt{2H_0 w}} \left[ M - (z - H_0 y_a^{1/2})^2 \right]^{1/2} \\
C_{11} &= \frac{1}{2} \left( y_a - \frac{H_0}{w} \right) \\
C_{12} &= y_e - \frac{H_0}{w}
\end{aligned}$$

The derivation of these expressions can be found in Appendix B. All four cases are shown in Figure 6.16 for a range of values of  $H_0$ , where it can be seen that the value of  $H_0$  has a large affect on the solution space.

### 6.3 Conclusions

In this chapter, we have analytically solved the thermal equilibrium equation, to produce a phase plane analysis for the temperature structure along hydrostatic coronal loops. Landi and Landini (1999), and Colgan et al. (2008) present optically thin radiative losses which include a significant bump at cooler temperatures, not observed in previous studies by Hildner (1974), Rosner et al. (1978) and Cook et al. (1989). As such, the two-range radiative loss function of Walsh et al. (1995) was adapted to take into account this bump, and a new four-range radiative loss function was introduced.

With this new four-range function, the thermal equilibrium equation was analytically solved, and a new set of solutions to the solution space was observed. The Colgan et al. (2008) radiative losses also show several more dips and peaks (although not quite as prominent), and so the implications are that with a more complex radiative loss function, many more solutions may be possible.

CHAPTER 6

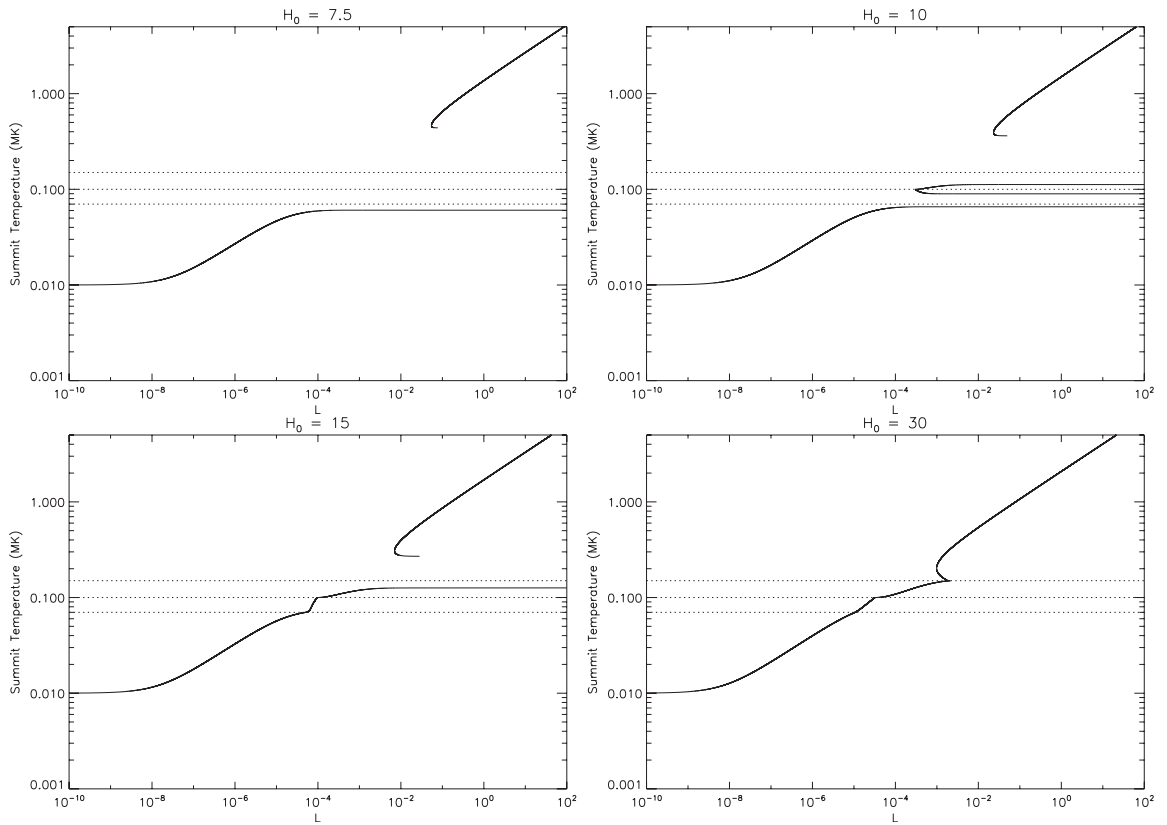


Figure 6.16: Dependence of the summit temperature  $T_0$  (in units of  $10^6$ K upon the parameter  $L$  for different values of  $H_0$ , for a footpoint temperature of  $T_e = 0.01$  MK. The dashed lines (from the bottom upwards) represent where  $T_0 = T_a$ ,  $T_0 = T_b$  and  $T_0 = T_r$ .

# Chapter 7

## Future Work

In this chapter, we outline the work we would like to do, to further increase our understanding of each particular subject.

### 7.1 CME Observations

We would like to analyse many more CME events, and in particular, more slow CMEs, which we are able to obtain in-situ data for, in order to fully understand the propagation of slow CMEs as they travel through the heliosphere. This would hopefully answer some of the questions regarding CME deflections in the heliosphere.

We would also like to use other methods to derive the 3-D position angles, such as using forward modelling, to build up a better understanding of which method works best, with which particular CME type.

Once the 3-D position angles of a CME are known, a plethora of kinematic, energetic, and geometric analysis can be done accurately. We would also strive to include any Thompson scattering effects, which we have so far neglected.

For example, the CME cone models of Michalek et al. (2009) use LASCO CME observations, and derive velocities based upon the latitudinal expansion angle of a CME, using a plane-of-sky assumption. However, if this expansion angle deviates

away from the plane-of-sky, the expansion angle is greatly affected by the angle at which it is propagating, and will therefore have a large impact upon the results.

## 7.2 Multi-Strand Coronal Loop Simulations

Work has already begun on a preliminary investigation to see if it is possible to obtain more accurate velocity results to compare with Tripathi et al. (2009). Figure 7.1 displays the red/blue shifts, their corresponding histograms, and the average velocity profile, for a 1125-strand loop, with 57 energy bursts per strand, for  $0.1E_{Total}$ . We would like to further this work, by increasing the length of the loop to those from the observations. In Tripathi et al. (2009), they observe loops with projected heights of at least 75 Mm, meaning a loop length of  $\sim 250$  Mm. Such a long loop will likely provide different results. For example, the temperature profile may change significantly, since it will take far longer for the heat released by the energy bursts to reach the loop apex. The loop velocities are also expected to change, since the effects of gravity will have a far larger impact upon the plasma in a longer loop.

## 7.3 Phase Planes

We would like to further extend the four-range radiative loss function, into a six-range or even an eight-range function, to investigate the new solution space. We have already seen an increase in the number of solutions when increasing from a two-range to a four-range, so it would be expected that more solutions would indeed exist with a more complex radiative loss function.

At present, gravity is assumed to be constant along the length of the loop. Therefore, we would like to investigate the effects of including gravity upon the thermal equilibrium equation. In doing so, the pressure will be at its greatest at the base of the loop, whilst it will be the least at the loop apex. In order to investigate

## CHAPTER 7

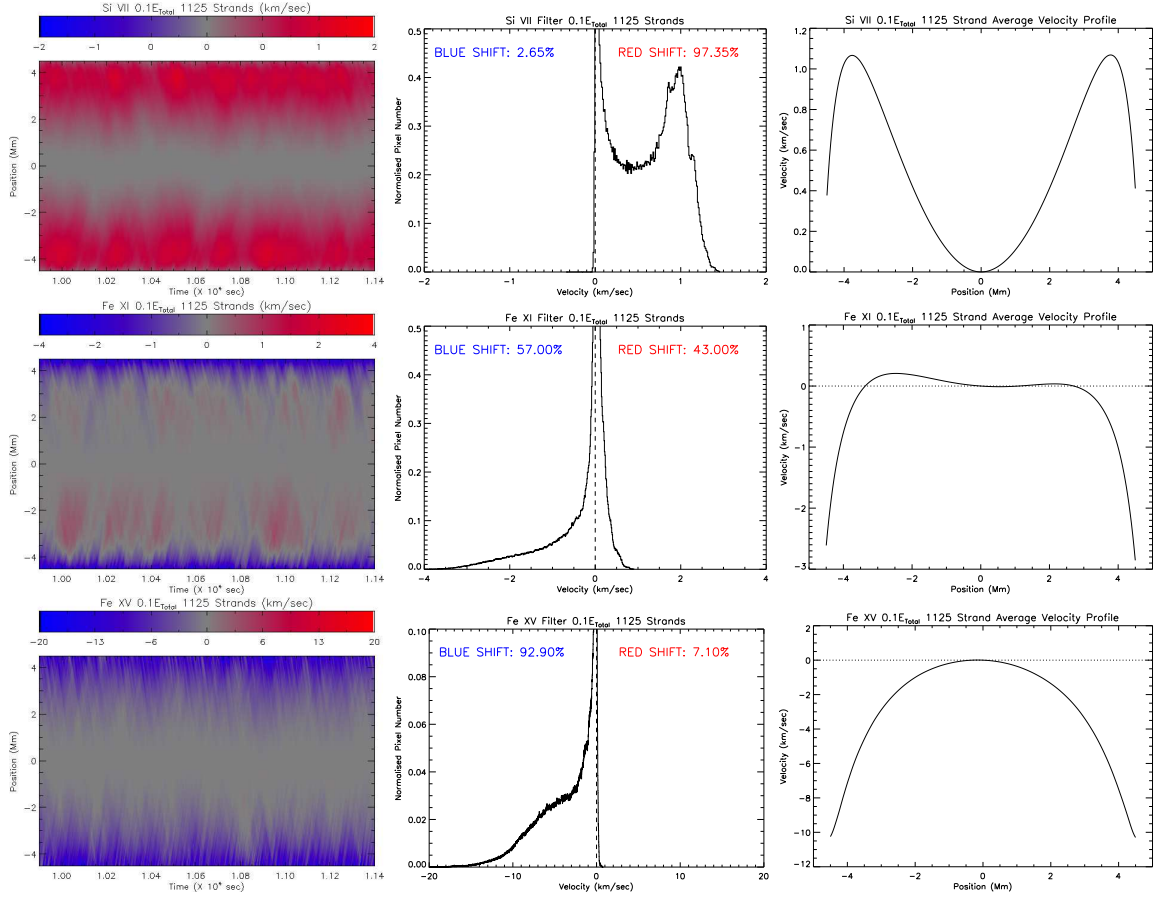


Figure 7.1: Si VII (top row), Fe XI (middle row) and Fe XV (bottom row) line-of-sight blue/red shifts for a 1125 strand loop, with 57 energy bursts per strand and  $0.1E_{Total}$  (left column), their corresponding histograms (centre column), and the time-averaged mean blue/red  $V_{cf}$  along the loop (right column).

## CHAPTER 7

this solution space, a phase volume will need to be constructed, since there is now an extra variable to consider. We believe that the inclusion of gravity will push the critical points together, possibly making them merge together and disappear.

Also, we would like to further investigate the effects of changing the spatial distribution of the coronal heating parameter. Currently, we have only assumed uniform heating, and therefore we would like to investigate using footpoint and apex dominated heating.

A phase volume, consisting of layers of phase planes stacked on top of each other, is presented in Figure 7.2, and shows the separatrix curve for each value of  $H_0$  within the plotted range. When there are two separatrix curves available, only the separatrix curve with the highest summit temperature is plotted.

By taking an angled slice out of the x-y (temperature-conductive flux) plane, it is possible to produce phase plane solutions with heating that varies along the length of the loop (e.g. footpoint or apex dominated heating), dependent upon the gradient of the slice. A slice with a positive gradient with respect to the z-axis, will produce apex heating, whilst a slice with a negative gradient will produce footpoint heating.

CHAPTER 7

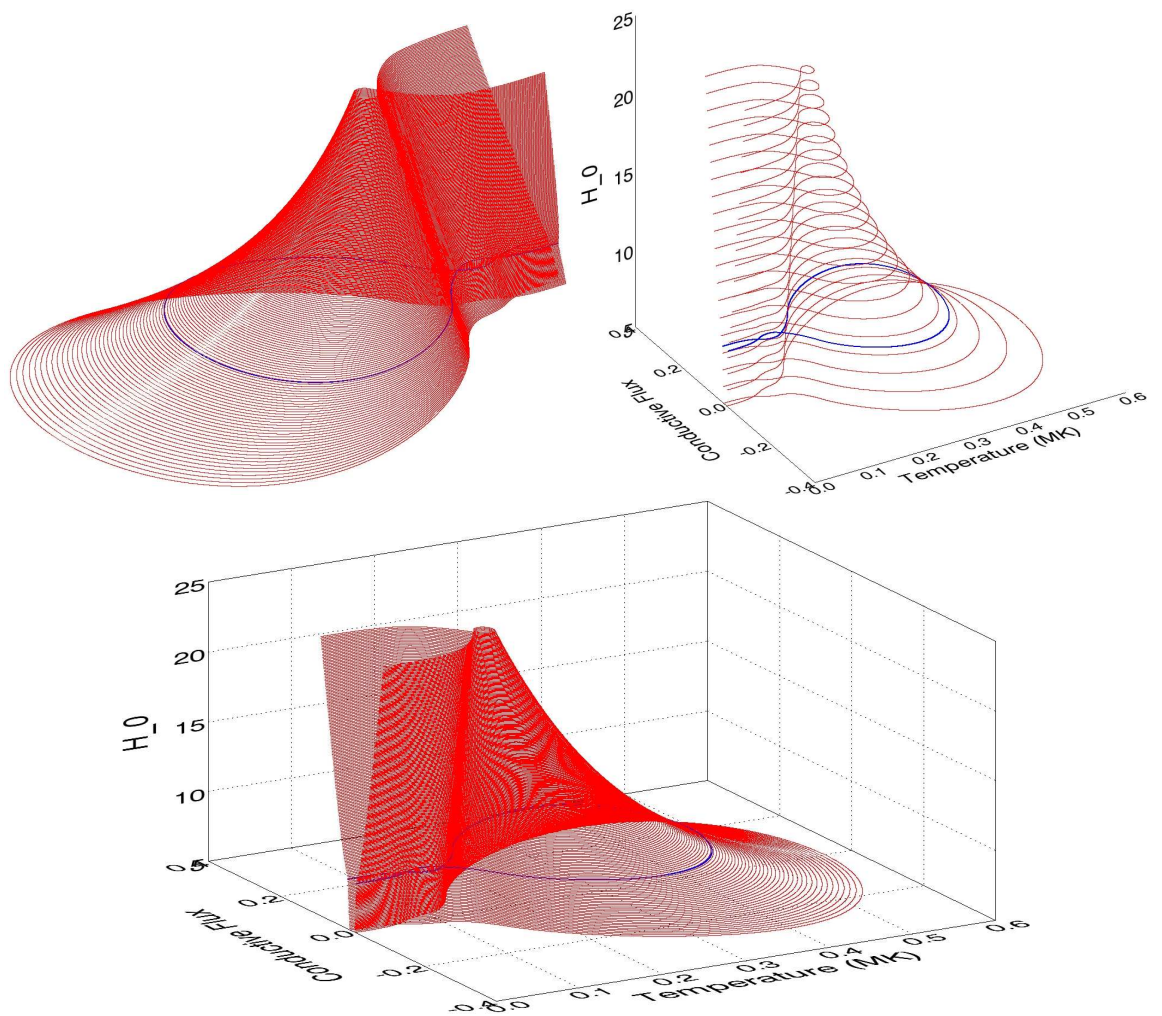


Figure 7.2: Phase volume displaying the separatrix curve for increasing  $H_0$  with  $L = 1$ ,  $T_a = 0.07$ ,  $T_b = 0.1$ , and  $T_r = 0.15$ . The double separatrix is illustrated by the blue contours.

# Appendix A

## Critical Point Analysis

Here, we investigate the nature of the critical points, in the  $(y, \Psi)$  space of the following equations<sup>1</sup>:

$$\frac{dy}{dx} = \Psi \tag{A.1}$$

$$\frac{d\Psi}{dx} = \frac{7L}{2} [\chi y^{2(\alpha-2)/7} - H_0] \tag{A.2}$$

and we have the following critical points:

$$\begin{aligned} y_{crit1} &= \frac{H_0 y_a^{3/2} y_r^{3/2}}{y_b^{3/2}} \\ y_{crit2} &= \left( \frac{H_0 y_r^{3/2}}{y_b^{3/2}} \right)^{-2} \\ y_{crit3} &= H_0 y_r^{3/2} \\ y_{crit4} &= H_0^{-2} \end{aligned}$$

and for convenience, let:

$$\begin{aligned} \chi_a &= \frac{y_a^{3/2} y_r^{3/2}}{y_b^{3/2}} \\ \chi_b &= \frac{y_r^{3/2}}{y_b^{3/2}} \end{aligned} \tag{A.3}$$

---

<sup>1</sup>note: the critical points exist only for certain values of  $H_0$ . For  $H_0 > y_r^{-1/2}$  there exist no critical points.

## A.1 Analysis of $y = y_{crit1}$ and $y = y_{crit3}$

To investigate the local behaviour near  $y = y_{crit1}$  let  $(y_{crit1}, 0) \approx (H_0\chi_a + \epsilon_1, \epsilon_2)$ , where  $\epsilon_1$  and  $\epsilon_2$  are small quantities. Then, approximate Equations A.1 and A.2 by:

$$\dot{\epsilon}_1 \sim \epsilon_2 \quad (\text{A.4})$$

$$\dot{\epsilon}_2 \sim \frac{7L}{2} \left[ \frac{1}{\chi_a} (H_0\chi_a + \epsilon_1) - H_0 \right] \quad (\text{A.5})$$

A Taylor series expansion of the right-hand-side of Equation A.5 about the point  $\epsilon_1 = 0$  gives:

$$\dot{\epsilon}_2 \sim \frac{7L}{2\chi_a} \epsilon_1 \quad (\text{A.6})$$

and dividing Equation A.6 by A.4 we get:

$$\frac{d\epsilon_2}{d\epsilon_1} \sim \frac{7L}{2\chi_a} \frac{\epsilon_1}{\epsilon_2} \quad (\text{A.7})$$

Finally, if we now integrate, we get:

$$\epsilon_2^2 - \frac{7L}{2\chi_a} \epsilon_1^2 = C \quad (\text{A.8})$$

which is the equation of a hyperbola. Hence, the critical value at  $y = y_{crit1}$  is a saddle point.

Similarly, at  $y = y_{crit3}$ , we get:

$$\epsilon_4^2 - \frac{7L}{2y_r^{3/2}} \epsilon_3^2 = C \quad (\text{A.9})$$

## A.2 Analysis of $y = y_{crit2}$ and $y = y_{crit4}$

To investigate the local behaviour near  $y = y_{crit2}$  let  $(y_{crit2}, 0) \approx ((H_0\chi_b)^{-2} + \epsilon_5, \epsilon_6)$ , where  $\epsilon_5$  and  $\epsilon_6$  are small quantities. Then, approximate Equations A.1 and A.2 by:

$$\dot{\epsilon}_5 \sim \epsilon_6 \quad (\text{A.10})$$

$$\dot{\epsilon}_6 \sim \frac{7L}{2} \left[ \frac{1}{\chi_b} \left( (H_0\chi_b)^{-2} + \epsilon_5 \right)^{-1/2} - H_0 \right] \quad (\text{A.11})$$

## CHAPTER A

A Taylor series expansion of the right-hand-side of Equation A.11 about the point  $\epsilon_5 = 0$  gives:

$$\dot{\epsilon}_6 \sim -\frac{7L(H_0\chi_b)^3}{4}\epsilon_5 \quad (\text{A.12})$$

and dividing Equation A.12 by A.10 we get:

$$\frac{d\epsilon_6}{d\epsilon_5} \sim -\frac{7L(H_0\chi_b)^3}{4}\frac{\epsilon_5}{\epsilon_6} \quad (\text{A.13})$$

Finally, if we integrate, we get:

$$\epsilon_6^2 + \frac{7L(H_0\chi_b)^3}{4}\epsilon_5^2 = C \quad (\text{A.14})$$

which is the equation of an ellipse. Therefore, the critical point at  $y = y_{crit2}$  is a centre point.

The direction of rotation of the closed trajectory around the centre is obtained by setting  $\epsilon_6 = 0$  and  $\epsilon_5 > 0$  and checking to see if  $\dot{\epsilon}_6$  is positive or negative. In this particular instance,  $\dot{\epsilon}_6$  is negative, and therefore the rotation is clockwise.

Similarly, for  $y = y_{crit4}$ , we get:

$$\epsilon_8^2 + \frac{7LH_0^3}{4}\epsilon_7^2 = C \quad (\text{A.15})$$

# Appendix B

## Analytical Solutions for the Dependence of the Summit Temperature upon the Length of the Loop

### B.1 Region 1: $T_0 \leq T_a$

Here, we derive the analytical solutions for the dependence of the summit temperature,  $T_0$ , upon the length of the loop parameter,  $L$ . There are four solutions, depending upon the temperature region of the loop.

#### B.1.1 For $T \leq T_a$

Our starting equation is:

$$y'' = \frac{7L}{2} \left[ \frac{y_b^{3/2} y}{y_r^{3/2} y_a^{3/2}} - H_0 \right] \quad (\text{B.1})$$

We can solve this equation by finding the complimentary function ( $y_{cf}$ ) and the

## CHAPTER B

particular integral ( $y_{pi}$ ) :

$$y_{cf_1} = A_1 e^{\lambda x} + B_1 e^{-\lambda x} \quad (\text{B.2})$$

Where  $\lambda = \sqrt{\frac{7Lw}{2}}$ , and  $w = \frac{y_b^{3/2}}{y_r^{3/2} y_a^{3/2}}$

And we have

$$y_{pi_1} = \frac{H_0}{w} \quad (\text{B.3})$$

And thus we have the general solution

$$y = A_1 e^{\lambda x} + B_1 e^{-\lambda x} + \frac{H_0}{w} \quad (\text{B.4})$$

We have the boundary condition that  $y' = 0$  at  $x = 0$ . Thus, since we are starting at this lower temperature range, we have

$$y' = 0 = \lambda A_1 - \lambda B_1$$

And so we have that

$$A_1 = B_1 \quad (\text{B.5})$$

To leave us with

$$\begin{aligned} y &= A_1 e^{\lambda x} + A_1 e^{-\lambda x} + \frac{H_0}{w} \\ &= 2A_1 \cosh(\lambda x) + \frac{H_0}{w} \end{aligned} \quad (\text{B.6})$$

We also have the condition that  $y(0) = y_0$ , which allows us to write

$$y_0 = 2A_1 + \frac{H_0}{w}$$

Thus

CHAPTER B

$$A_1 = \frac{1}{2} \left( y_0 - \frac{H_0}{w} \right) \quad (\text{B.7})$$

The final boundary condition also states that  $y(1/2) = y_e$ , which gives

$$\begin{aligned} y_e &= 2A_1 \cosh(\lambda/2) + \frac{H_0}{w} \\ &= \left( y_0 - \frac{H_0}{w} \right) \cosh(\lambda/2) + \frac{H_0}{w} \end{aligned} \quad (\text{B.8})$$

And by rearranging, we have

$$\lambda = 2 \cosh^{-1} \left( \frac{y_e - \gamma}{y_0 - \gamma} \right) \quad (\text{B.9})$$

Where  $\gamma = H_0/w$

and since  $y(1/2) = y_e$  we have

$$\lambda = 2 \cosh^{-1} \left( \frac{y_e - \gamma}{y_0 - \gamma} \right) = \sqrt{\frac{7Lw}{2}} \quad (\text{B.10})$$

To give

$$L = \frac{8}{7w} \left( \cosh^{-1} \left( \frac{y_e - \gamma}{y_0 - \gamma} \right) \right)^2 \quad (\text{B.11})$$

**B.2 Region 2:  $T_a \leq T_0 \leq T_b$** **B.2.1 For  $T_a \leq T \leq T_b$** 

Our starting equation is

$$y'' = \frac{7L}{2} \left[ \frac{z}{y^{1/2}} - H_0 \right] \quad (\text{B.12})$$

where  $z = \frac{y_b^{3/2}}{y_r^{3/2}}$

Now, if we multiply both sides by  $y'$  and integrate, we get

$$(y')^2 = 7L (2y^{1/2}z - H_0y + C) \quad (\text{B.13})$$

where C is a constant of integration. Now we know that when  $y' = 0$ ,  $y(0) = y_0$ , and this gives us

$$C = H_0y_0 - 2y_0^{1/2}z$$

to give

$$(y')^2 = 7L (2y^{1/2}z - H_0y + H_0y_0 - 2y_0^{1/2}z) \quad (\text{B.14})$$

and this can be rewritten in the form

$$y' = -\sqrt{\frac{7L}{H_0}} \left[ (z - H_0y_0^{1/2})^2 - (z - H_0y^{1/2})^2 \right]^{1/2} \quad (\text{B.15})$$

and it is the negative root we require, since the temperature gradient is always negative. However, we must notice that

$$(z - H_0y_0^{1/2})^2 - (z - H_0y^{1/2})^2 > 0$$

which implies that

$$y > y_0$$

CHAPTER B

which is not possible, and so we must rewrite (B.15) in the form

$$y' = -\sqrt{\frac{7L}{H_0}} \left[ (H_0 y_0^{1/2} - z)^2 - (z - H_0 y^{1/2})^2 \right]^{1/2} \quad (\text{B.16})$$

which we then integrate in the form

$$-\sqrt{\frac{7L}{H_0}} x_a = \int_{y_0}^{y_a} \frac{dy}{\left[ (H_0 y_0^{1/2} - z)^2 - (z - H_0 y^{1/2})^2 \right]^{1/2}} \quad (\text{B.17})$$

where  $y_a = y(x_a)$ . There is a removable singularity in the denominator on the right hand side of (B.17). So set

$$z - H_0 y^{1/2} = (H_0 y_0^{1/2} - z) \sin \theta = A_2 \sin \theta \quad (\text{B.18})$$

and so we have

$$A_2 = H_0 y_0^{1/2} - z \quad (\text{B.19})$$

$$\sin \theta = \frac{z - H_0 y^{1/2}}{H_0 y_0^{1/2} - z} \quad (\text{B.20})$$

and so we have that

$$\begin{aligned} \left[ (H_0 y_0^{1/2} - z)^2 - (z - H_0 y^{1/2})^2 \right]^{1/2} &= [A_2^2 - A_2^2 \sin^2 \theta]^{1/2} \\ &= A_2 \cos \theta \end{aligned} \quad (\text{B.21})$$

Now, we need to find  $\frac{dy}{d\theta} = \frac{dy}{du} \frac{du}{d\theta}$ . So letting  $u = A_2 \sin \theta$  we have

$$\frac{du}{d\theta} = A_2 \cos \theta$$

and from (B.18), we have that

$$y = \left( \frac{z - u}{H_0} \right)^2$$

CHAPTER B

thus

$$\frac{dy}{du} = \frac{-2(z - A_2 \sin \theta) A_2 \cos \theta}{H_0^2}$$

and so

$$dy = \frac{-2A_2(z - A_2 \sin \theta) \cos \theta}{H_0^2} d\theta \quad (\text{B.22})$$

So, if we substitute (B.21) and (B.22) into (B.17) we get

$$\begin{aligned} -\sqrt{\frac{7L}{H_0}} x_a &= -\frac{2}{H_0^2} \int_{-\pi/2}^{\theta_a} (z - A_2 \sin \theta) d\theta \\ &= -\frac{2}{H_0^2} \left( A_2 \cos \theta_a + z \left( \theta_a + \frac{\pi}{2} \right) \right) \end{aligned} \quad (\text{B.23})$$

From (B.19) and (B.20), and by using Pythagoras, we have

$$\cos \theta_a = \frac{\left[ A_2^2 - (z - H_0 y_a^{1/2})^2 \right]^{1/2}}{A_2} \quad (\text{B.24})$$

and also

$$\theta_a = \sin^{-1} \left( \frac{z - H_0 y_a^{1/2}}{A_2} \right) \quad (\text{B.25})$$

and so we have

$$\begin{aligned} x_a &= \frac{2}{\sqrt{7LH_0^3}} \left[ \left[ A_2^2 - (z - H_0 y_a^{1/2})^2 \right]^{1/2} \right. \\ &\quad \left. + z \left[ \sin^{-1} \left( \frac{z - H_0 y_a^{1/2}}{A_2} \right) + \frac{\pi}{2} \right] \right] \end{aligned} \quad (\text{B.26})$$

CHAPTER B

**B.2.2 For  $T \leq T_a$**

Our equation for this section is

$$y'' = \frac{7L}{2} [yw - H_0] \quad (\text{B.27})$$

where  $w = \frac{y_b^{3/2}}{y_r^{3/2} y_a^{3/2}}$ , and this has the general solution

$$y = A_3 e^{\lambda x} + B_3 e^{-\lambda x} + \frac{H_0}{w} \quad (\text{B.28})$$

We know that,  $y(0) = y_a$  for this lower temperature region, and so we have

$$y_a = A_3 + B_3 + \frac{H_0}{w}$$

and so we can define  $B_3$  as

$$B_3 = y_a - A_3 - \frac{H_0}{w} \quad (\text{B.29})$$

and substituting this into B.28 gives us

$$y = A_3 e^{\lambda x} + \left( y_a - A_3 - \frac{H_0}{w} \right) e^{-\lambda x} + \frac{H_0}{w} \quad (\text{B.30})$$

We now need to match the gradient of (B.30) to (B.16), and so differentiating (B.30) yields

$$y' = 2\lambda A_3 - \lambda \left( y_a - \frac{H_0}{w} \right) \quad (\text{B.31})$$

and we need to match this at  $y = y_a$  to (B.16) which gives

$$2\lambda A_3 - \lambda \left( y_a - \frac{H_0}{w} \right) = -\sqrt{\frac{7L}{H_0}} \left[ \left( z - H_0 y_0^{1/2} \right)^2 - \left( H_0 y_a^{1/2} - z \right)^2 \right]^{1/2}$$

and thus we can specify  $A_3$ , and thus also  $B_3$

$$A_3 = \frac{-1}{\sqrt{2H_0 w}} \left[ \left( z - H_0 y_0^{1/2} \right)^2 - \left( H_0 y_a^{1/2} - z \right)^2 \right]^{1/2} + \frac{1}{2} \left( y_a - \frac{H_0}{w} \right) \quad (\text{B.32})$$

## CHAPTER B

And so if we let

$$C_1 = \frac{1}{\sqrt{2H_0w}} \left[ (z - H_0y_0^{1/2})^2 - (H_0y_a^{1/2} - z)^2 \right]^{1/2} \quad (\text{B.33})$$

$$C_2 = \frac{1}{2} \left( y_a - \frac{H_0}{w} \right) \quad (\text{B.34})$$

Then we have that

$$A_3 = C_2 - C_1 \quad (\text{B.35})$$

$$B_3 = C_2 + C_1 \quad (\text{B.36})$$

Now, we have our final boundary condition that  $y(x_e) = y_e$ , we can use (B.28) to write

$$y_e = (C_2 - C_1)e^{\lambda x_e} + (C_2 + C_1)e^{-\lambda x_e} + \frac{H_0}{w} \quad (\text{B.37})$$

Now if we multiply both sides by  $e^{\lambda x_e}$ , we get

$$(C_2 - C_1)e^{2\lambda x_e} - C_3e^{\lambda x_e} + (C_2 + C_1) = 0 \quad (\text{B.38})$$

where

$$C_3 = y_e - \frac{H_0}{w} \quad (\text{B.39})$$

and so (B.38) can be solved by the quadratic formula, (needing only the negative root) to produce

$$x_e = \sqrt{\frac{2}{7Lw}} \ln \left( \frac{C_3 - \sqrt{C_3^2 - 4(C_2^2 - C_1^2)}}{2(C_2 - C_1)} \right) \quad (\text{B.40})$$

Now, since only half the length of the loop is calculated, we have that

$$x_a + x_e = \frac{1}{2} \quad (\text{B.41})$$

## CHAPTER B

And solving for L gives

$$L = \frac{2}{7} \left[ \left[ (H_0 y_0^{1/2} - z)^2 - (z - H_0 y_a^{1/2})^2 \right]^{1/2} + z \left[ \sin^{-1} \left( \frac{z - H_0 y_a^{1/2}}{H_0 y_0^{1/2} - z} \right) + \frac{\pi}{2} \right] \right. \\ \left. + \frac{2}{\sqrt{w}} \ln \left( \frac{C_3 - \sqrt{C_3^2 - 4(C_2^2 - C_1^2)}}{2(C_2 - C_1)} \right) \right]^2 \quad (\text{B.42})$$

### B.3 Region 3: $T_b \leq T_0 \leq T_r$

#### B.3.1 For $T_b \leq T \leq T_r$

Our starting equation is:

$$y'' = \frac{7L}{2} \left[ \frac{y}{y_r^{3/2}} - H_0 \right] \quad (\text{B.43})$$

Like before, we solve this via a complimentary function and a particular integral.

$$y_{cf2} = A_4 e^{\lambda x} + B_4 e^{-\lambda x} \quad (\text{B.44})$$

where  $\lambda = \sqrt{7L/2y_r^{3/2}}$  to give

$$y = A_4 e^{\lambda x} + B_4 e^{-\lambda x} + H_0 y_r^{3/2} \quad (\text{B.45})$$

Now we have that  $y' = 0$  at  $x = 0$ , which gives  $A_4 = B_4$  giving

$$y = 2A_4 \cosh(\lambda x) + H_0 y_r^{3/2} \quad (\text{B.46})$$

We also know that  $y(0) = y_0$  which yields

$$A_4 = \frac{1}{2} (y_0 - H_0 y_r^{3/2}) \quad (\text{B.47})$$

## CHAPTER B

This is true for up to  $y = y_b$ , where it must match the gradient discussed in subsection 3.2. Thus, using (B.46) and substituting  $y(x_b) = y_b$  and rearranging, we have

$$x_b = \sqrt{\frac{2y_r^{3/2}}{7L}} \cosh^{-1} \left( \frac{y_b - H_0 y_r^{3/2}}{y_0 - H_0 y_r^{3/2}} \right) \quad (\text{B.48})$$

### B.3.2 For $T_a \leq T \leq T_b$

For this region, we are now dealing with the equation

$$y'' = \frac{7L}{2} \left[ \frac{y_b^{3/2}}{y^{1/2} y_r^{3/2}} - H_0 \right] \quad (\text{B.49})$$

which we will rewrite for convenience as

$$y'' = \frac{7L}{2} [2y^{-1/2} z - H_0] \quad (\text{B.50})$$

where  $z = \frac{y_b^{3/2}}{y_r^{3/2}}$

As in subsection 2.1, we multiply both sides by  $y'$  and integrate to get

$$(y')^2 = 7L [2y^{1/2} z - H_0 y + D] \quad (\text{B.51})$$

where  $D$  is a constant of integration. This needs to match the gradient at  $y = y_b$  from the previous subsection. Thus we get

$$D = H_0 y_0 - \frac{y_0^2}{2y_r^{3/2}} - \frac{3y_b^2}{2y_r^{3/2}}$$

Thus, by rearranging (B.51), as in subsection 2.1, we have

$$y' = -\sqrt{\frac{7L}{H_0}} \left[ E - (z - H_0 y^{1/2})^2 \right]^{1/2} \quad (\text{B.52})$$

## CHAPTER B

and we then put it in the form

$$-\sqrt{\frac{7L}{H_0}} \int_{x_b}^{x_a} dx = \int_{y_b}^{y_a} \frac{dy}{\left[E - (z - H_0 y^{1/2})^2\right]^{1/2}} \quad (\text{B.53})$$

where  $E = H_0 D + z^2$ . Now this is in the same form as (B.15) and so if we approach this in a similar way we get

$$\begin{aligned} \sin \theta &= \frac{z - H_0 y^{1/2}}{\sqrt{E}} \\ dy &= -\frac{2\sqrt{E} (z - \sqrt{E} \sin \theta) \cos \theta}{H_0^2} d\theta \end{aligned}$$

$$\begin{aligned} \left[E - (z - H_0 y^{1/2})^2\right]^{1/2} &= \left[E - (\sqrt{E} \sin \theta)^2\right]^{1/2} \\ &= \sqrt{E} \cos \theta \end{aligned}$$

and so substituting these into (B.53) we have

$$-\sqrt{\frac{7L}{H_0}} \int_{x_b}^{x_a} dx = -\frac{2}{H_0^2} \int_{\theta_b}^{\theta_a} (z - \sqrt{E} \sin \theta) d\theta \quad (\text{B.54})$$

which can be solved to give

$$x_a = \frac{2}{\sqrt{7LH_0^3}} \left[ z(\theta_a - \theta_b) + \sqrt{E}(\cos \theta_a - \cos \theta_b) \right] + x_b \quad (\text{B.55})$$

$$\text{with } \theta_b = \sin^{-1} \left[ \frac{z - H_0 y_b^{1/2}}{\sqrt{E}} \right], \text{ and } \theta_a = \sin^{-1} \left[ \frac{z - H_0 y_a^{1/2}}{\sqrt{E}} \right]$$

### B.3.3 For $T < T_a$

Now, our equation is

$$y'' = \frac{7L}{2} [yw - H_0] \quad (\text{B.56})$$

where  $w = \frac{y_b^{3/2}}{y_r^{3/2} y_a^{3/2}}$  and this has the general solution

CHAPTER B

$$y = A_5 e^{\lambda x} + B_5 e^{-\lambda x} + \frac{H_0}{w} \quad (\text{B.57})$$

where  $\lambda = \sqrt{\frac{7Lw}{2}}$ , and we have that  $y(0) = y_a$  to give

$$B_5 = \left( y_a - A_5 - \frac{H_0}{w} \right) \quad (\text{B.58})$$

Thus substituting this into (B.57) gives

$$y = A_5 e^{\lambda x} + \left( y_a - A_5 - \frac{H_0}{w} \right) e^{-\lambda x} + \frac{H_0}{w} \quad (\text{B.59})$$

This now has to match the gradient of equation (B.52) at the point  $y = y_a$ , so first we differentiate (B.59) and then set (B.52) equal to this, at  $y = y_a$ , which gives

$$-\sqrt{\frac{7L}{H_0}} \left[ E - (z - H_0 y_a^{1/2})^2 \right]^{1/2} = 2\lambda A_5 - \lambda \left( y_a - \frac{H_0}{w} \right) \quad (\text{B.60})$$

and thus rearranging, we can now specify  $A_5$  as

$$A_5 = -\frac{1}{\sqrt{2H_0w}} \left[ E - (z - H_0 y_a^{1/2})^2 \right]^{1/2} + \frac{1}{2} \left( y_a - \frac{H_0}{w} \right) \quad (\text{B.61})$$

So, if we let

$$\begin{aligned} C_4 &= \frac{1}{\sqrt{2H_0w}} \left[ E - (z - H_0 y_a^{1/2})^2 \right]^{1/2} \\ C_5 &= \frac{1}{2} \left( y_a - \frac{H_0}{w} \right) \end{aligned}$$

Then

$$A_5 = C_5 - C_4$$

$$B_5 = C_5 + C_4$$

## CHAPTER B

Now, our final boundary condition states that  $y(x_e) = y_e$ , thus if we substitute this into (B.57) we get

$$y_e = A_5 e^{\lambda x_e} + B_5 e^{-\lambda x_e} + \frac{H_0}{w}$$

Multiplying by  $e^{\lambda x_e}$ , and substituting for  $A_5$  and  $B_5$  respectively gives

$$(C_5 - C_4) e^{2\lambda x_e} - C_6 e^{\lambda x_e} + (C_5 + C_4) = 0 \quad (\text{B.62})$$

where

$$C_6 = y_e - \frac{H_0}{w}$$

Thus (B.62) is now solvable by the quadratic formula, to give

$$x_e = \sqrt{\frac{2}{7Lw}} \left[ \frac{C_6 - \sqrt{C_6^2 - 4(C_5^2 - C_4^2)}}{2(C_5 - C_4)} \right] \quad (\text{B.63})$$

We can now specify  $L$ , since we know that

$$x_b + x_a + x_e = 1/2$$

Thus we have

$$\begin{aligned} L &= \frac{2}{7} \left[ \frac{2}{\sqrt{w}} \ln \left[ \frac{C_6 - \sqrt{C_6^2 - 4(C_5^2 - C_4^2)}}{2(C_5 - C_4)} \right] \right. \\ &+ \frac{2\sqrt{2}}{\sqrt{H_0^3}} \left[ z(\theta_a - \theta_b) + \sqrt{E}(\cos \theta_a - \cos \theta_b) \right] \\ &+ \left. 4y_r^{3/4} \cosh^{-1} \left( \frac{y_b - H_0 y_r^{3/2}}{y_0 - H_0 y_r^{3/2}} \right) \right]^2 \quad (\text{B.64}) \end{aligned}$$

**B.4 Region 4:  $T_0 \geq T_r$** **B.4.1 For  $T \geq T_r$** 

Our starting equation is

$$y'' = \frac{7L}{2} [y^{-1/2} - H_0] \quad (\text{B.65})$$

Using the same approach as in subsection 2.1, we multiply both sides by  $y'$  and integrate with respect to  $y$ , yielding

$$(y')^2 = 7L (2y^{1/2} - H_0y + F) \quad (\text{B.66})$$

where  $F$  is a constant of integration;

$$F = H_0y_0 - 2y_0^{1/2}$$

since we know that  $y' = 0$  when  $y = y_0$

Rearranging (B.66) we get

$$y' = -\sqrt{\frac{7L}{H_0}} \left[ (1 - H_0y_0^{1/2})^2 - (1 - H_0y^{1/2})^2 \right]^{1/2} \quad (\text{B.67})$$

However, this implies that  $y > y_0$ , and so we must rewrite (B.67) as

$$y' = -\sqrt{\frac{7L}{H_0}} \left[ (H_0y_0^{1/2} - 1)^2 - (1 - H_0y^{1/2})^2 \right]^{1/2} \quad (\text{B.68})$$

Now, if we let

$$G = (H_0y_0^{1/2} - 1)^2$$

CHAPTER B

then we can integrate in the form

$$-\sqrt{\frac{7L}{H_0}} \int_{x_0}^{x_r} dx = \int_{y_0}^{y_r} \frac{dy}{\left[G - (1 - H_0 y^{1/2})^2\right]^{1/2}} \quad (\text{B.69})$$

Now, there is again a removable singularity;

$$1 - H_0 y^{1/2} = \sqrt{G} \sin \theta$$

Now, exactly as in subsection 2.1, we apply the same method to get

$$dy = \frac{-2\sqrt{G} (1 - \sqrt{G} \sin \theta) \cos \theta}{H_0^2} d\theta \quad (\text{B.70})$$

$$\left[G - (\sqrt{G} \sin \theta)^2\right]^{1/2} = \sqrt{G} \cos \theta \quad (\text{B.71})$$

So, when we substitute (B.70) and (B.71) into (B.69), we get

$$\begin{aligned} -\sqrt{\frac{7L}{H_0}} x_r &= -\frac{2}{H_0^2} \int_{-\pi/2}^{\theta_r} (1 - \sqrt{G} \sin \theta) d\theta \\ &= -\frac{2}{H_0^2} \left( \sqrt{G} \cos \theta_r + \theta_r + \frac{\pi}{2} \right) \end{aligned} \quad (\text{B.72})$$

where

$$\begin{aligned} \theta_r &= \sin^{-1} \left( \frac{1 - H_0 y_r^{1/2}}{\sqrt{G}} \right) \\ \cos \theta_r &= \frac{\left[G - (1 - H_0 y_r^{1/2})^2\right]^{1/2}}{\sqrt{G}} \end{aligned}$$

and thus we have

$$x_r = \frac{2}{\sqrt{7LH_0^3}} \left[ \sin^{-1} \left( \frac{1 - H_0 y_r^{1/2}}{\sqrt{G}} \right) + \frac{\pi}{2} + \left[G - (1 - H_0 y_r^{1/2})^2\right]^{1/2} \right] \quad (\text{B.73})$$

## CHAPTER B

### B.4.2 For $T_b \leq T \leq T_r$

In this subsection, we are dealing with the equation

$$y'' = \frac{7L}{2} \left[ \frac{y}{y_r^{3/2}} - H_0 \right] \quad (\text{B.74})$$

which has the general solution

$$y = A_6 e^{\lambda x} + B_6 e^{-\lambda x} + H_0 y_r^{3/2} \quad (\text{B.75})$$

where  $\lambda = \sqrt{7L/2y_r^{3/2}}$ . Now, for this subsection, we know that  $y(0) = y_r$  which therefore allows us to write

$$A_6 + B_6 + H_0 y_r^{3/2} = y_r$$

thus we can now specify  $B_6$ ;

$$B_6 = y_r \left( 1 - H_0 y_r^{1/2} \right) - A_6 \quad (\text{B.76})$$

Thus, substituting (B.76) into (B.75) gives

$$y = A_6 e^{\lambda x} - A_6 e^{-\lambda x} + y_r \left( 1 - H_0 y_r^{1/2} \right) e^{-\lambda x} + H_0 y_r^{3/2} \quad (\text{B.77})$$

We now need to differentiate (B.77), so as to match the gradient at (B.68), and so we have

$$y' = \lambda A_6 \left( e^{\lambda x} + e^{-\lambda x} \right) - \lambda y_r \left( 1 - H_0 y_r^{1/2} \right) e^{-\lambda x}$$

CHAPTER B

Thus, matching this to (B.68) where we know that  $y(0) = y_r$ . This gives

$$2\lambda A_6 - \lambda y_r (1 - H_0 y_r^{1/2}) = -\sqrt{\frac{7L}{H_0}} \left[ (1 - H_0 y_0^{1/2})^2 - (1 - H_0 y_r^{1/2})^2 \right]^{1/2}$$

Rearranging, and substituting in  $\lambda = \sqrt{7L/2y_r^{1/2}}$  we get

$$A_6 = -\frac{y_r^{3/4}}{\sqrt{2H_0}} \left[ (1 - H_0 y_0^{1/2})^2 - (1 - H_0 y_r^{1/2})^2 \right]^{1/2} + \frac{1}{2} (y_r - H_0 y_r^{3/2}) \quad (\text{B.78})$$

So, if we let

$$C_7 = \frac{y_r^{3/4}}{\sqrt{2H_0}} \left[ (1 - H_0 y_0^{1/2})^2 - (1 - H_0 y_r^{1/2})^2 \right]^{1/2} \quad (\text{B.79})$$

$$C_8 = \frac{1}{2} (y_r - H_0 y_r^{3/2}) \quad (\text{B.80})$$

Thus

$$A_6 = C_8 - C_7$$

$$B_6 = C_8 + C_7$$

Since  $y(x_b) = y_b$ , we can use (B.75) to write

$$y_b = A_6 e^{\lambda x_b} + B_6 e^{-\lambda x_b} + H_0 y_r^{3/2}$$

Multiplying both sides by  $e^{\lambda x_b}$ , and rearranging, we have

$$(C_8 - C_7) e^{2\lambda x_b} - C_9 e^{\lambda x_b} + (C_8 + C_7) = 0 \quad (\text{B.81})$$

where  $C_9 = y_b - H_0 y_r^{3/2}$

and we can now use the quadratic formula to give us  $x_b$ ;

$$x_b = \sqrt{\frac{2y_r^{3/2}}{7L}} \ln \left[ \frac{C_9 - \sqrt{C_9^2 - 4(C_8^2 - C_7^2)}}{2(C_8 - C_7)} \right] \quad (\text{B.82})$$

### B.4.3 For $T_a \leq T \leq T_b$

For this particular region, we are using

$$y'' = \frac{7L}{2} \left[ \frac{z}{y^{1/2}} - H_0 \right] \quad (\text{B.83})$$

where  $z = y_b^{3/2}/y_r^{3/2}$ , and we will use the same approach as in subsection 3.2.

So, if we multiply both sides of (ref4.3start) and integrate, we get

$$(y')^2 = 7L \left[ 2y^{1/2}z - H_0y + K \right] \quad (\text{B.84})$$

where  $K$  is a constant of integration. We can now find  $K$ , by matching the gradient from (B.74) at  $y = y_b$ . This means first of all, that we must multiply both sides of (B.74) by  $y'$  and integrate, and match that gradient to that of (B.66) at  $y = y_r$ .

So, first of all, multiplying both sides of (B.74) by  $y'$  and integrating yields

$$(y')^2 = 7L \left[ \frac{y^2}{2y_r^{3/2}} - H_0y + J \right] \quad (\text{B.85})$$

and thus if we match this to (B.66) at  $y = y_r$  we get

$$\begin{aligned} J &= \frac{3}{2}y_r^{1/2} + F \\ &= \frac{3}{2}y_r^{1/2} - 2y_0^{1/2} + H_0y_0 \end{aligned}$$

CHAPTER B

where  $F = H_0 y_0 - 2y_0^{1/2}$

Thus we can now specify  $K$  by matching the gradients of (B.85) and (B.84) at  $y = y_b$  to give us

$$\begin{aligned} K &= J - \frac{3y_b^2}{2y_r^{3/2}} \\ &= \frac{3}{2}y_r^{1/2} - 2y_0^{1/2} + H_0 y_0 - \frac{3y_b^2}{2y_r^{3/2}} \end{aligned}$$

Thus we can rewrite (B.84) as

$$y' = -\sqrt{\frac{7L}{H_0}} \left[ (H_0 K + z^2) - (z - H_0 y^{1/2})^2 \right]^{1/2} \quad (\text{B.86})$$

or, more conveniently as

$$y' = -\sqrt{\frac{7L}{H_0}} \left[ M - (z - H_0 y^{1/2})^2 \right]^{1/2} \quad (\text{B.87})$$

where  $M = H_0 K + z^2$ .

This is now in exactly the same form as (B.52), and thus we can therefore write

$$x_a = \frac{2}{\sqrt{7LH_0^3}} \left[ z(\theta_c - \theta_d) + \sqrt{M}(\cos \theta_c - \cos \theta_d) \right] + x_b \quad (\text{B.88})$$

## CHAPTER B

where

$$\begin{aligned}\theta_c &= \sin^{-1} \left[ \frac{z - H_0 y_a^{1/2}}{\sqrt{M}} \right] \\ \theta_d &= \sin^{-1} \left[ \frac{z - H_0 y_b^{1/2}}{\sqrt{M}} \right]\end{aligned}$$

### B.4.4 For $T \leq T_a$

Finally, we are looking at

$$y'' = \frac{7L}{2} [yw - H_0] \quad (\text{B.89})$$

where  $w = \frac{y_b^{3/2}}{y_r^{3/2} y_a^{3/2}}$

If we now follow the same method as in subsection 3.3, we get

$$\begin{aligned}C_{10} &= \frac{1}{\sqrt{2H_0 w}} \left[ M - (z - H_0 y_a^{1/2})^2 \right]^{1/2} \\ C_{11} &= \frac{1}{2} \left( y_a - \frac{H_0}{w} \right) \\ C_{12} &= y_e - \frac{H_0}{w}\end{aligned}$$

and therefore

$$x_e = \sqrt{\frac{2}{7Lw}} \ln \left[ \frac{C_{12} - \sqrt{C_{12}^2 - 4(C_{11}^2 - C_{10}^2)}}{2(C_{11} - C_{10})} \right] \quad (\text{B.90})$$

We can now specify  $L$  for this region since

CHAPTER

$$x_r + x_b + x_a + x_e = \frac{1}{2} \quad (\text{B.91})$$

Finally, we therefore have

$$\begin{aligned} L &= \frac{2}{7} \left[ \frac{2\sqrt{2}}{\sqrt{H_0^3}} \left( \sin^{-1} \left( \frac{1 - H_0 y_r^{1/2}}{\sqrt{G}} \right) + \frac{\pi}{2} + \left[ G - (1 - H_0 y_r^{1/2})^2 \right]^{1/2} \right) \right. \\ &+ 4y_r^{3/4} \ln \left[ \frac{C_9 - \sqrt{C_9^2 - 4(C_8^2 - C_7^2)}}{2(C_8 - C_7)} \right] \\ &+ \frac{2\sqrt{2}}{\sqrt{H_0^3}} \left[ z(\theta_c - \theta_d) + \sqrt{M}(\cos \theta_c - \cos \theta_d) \right] \\ &\left. + \frac{2}{\sqrt{w}} \ln \left[ \frac{C_{12} - \sqrt{C_{12}^2 - 4(C_{11}^2 - C_{10}^2)}}{2(C_{11} - C_{10})} \right] \right]^2 \quad (\text{B.92}) \end{aligned}$$

# Bibliography

- Amari, T., J. F. Luciani, Z. Mikic, and J. Linker (2000). A Twisted Flux Rope Model for Coronal Mass Ejections and Two-Ribbon Flares. *Astrophys. J.*, 529, L49–L52.
- Antiochos, S. K., C. R. DeVore, and J. A. Klimchuk (1999). A Model for Solar Coronal Mass Ejections. *Astrophys. J.*, 510, 485–493.
- Arber, T. D., A. W. Longbottom, C. L. Gerrard, and A. M. Milne (2001). A staggered grid, lagrangian-eulerian remap code for 3-d mhd simulations. *Journal of Computational Physics* 171(1), 151 – 181.
- Aschwanden, M. J. (2005, December). *Physics of the Solar Corona. An Introduction with Problems and Solutions (2nd edition)*.
- Aschwanden, M. J. (2009, August). 4-D modeling of CME expansion and EUV dimming observed with STEREO/EUVI. *Annales Geophysicae* 27, 3275–3286.
- Aschwanden, M. J., J. Wülser, N. V. Nitta, and J. R. Lemen (2008, May). First Three-Dimensional Reconstructions of Coronal Loops with the STEREO A and B Spacecraft. I. Geometry. *Astrophys. J.*, 679, 827–842.
- Bewsher, D., D. S. Brown, C. J. Eyles, B. J. Kellett, G. J. White, and B. Swinyard (2010, July). Determination of the Photometric Calibration and Large-Scale Flatfield of the STEREO Heliospheric Imagers: I. HI-1. *Solar Phys.*, 264, 433–460.

## CHAPTER

Billings, D. E. (1966). *A guide to the solar corona*.

Braginski, S. I. (1965). Transport processes in a plasma. *Reviews of Plasma Physics 1*, 205–311.

Brown, D. S., D. Bewsher, and C. J. Eyles (2009). Calibrating the Pointing and Optical Parameters of the STEREO Heliospheric Imagers. *Solar Phys.*, *254*, 185–225.

Brueckner, G. E., R. A. Howard, M. J. Koomen, C. M. Korendyke, D. J. Michels, J. D. Moses, D. G. Socker, K. P. Dere, P. L. Lamy, A. Llebaria, M. V. Bout, R. Schwenn, G. M. Simnett, D. K. Bedford, and C. J. Eyles (1995). The Large Angle Spectroscopic Coronagraph (LASCO). *Solar Phys.*, *162*, 357–402.

Buffington, A., B. V. Jackson, and C. M. Korendyke (1996). Wide-angle stray-light reduction for a spaceborne optical hemispherical imager. *Appl. Opt.* *35*(34), 6669–6673.

Byrne, J. P., S. A. Maloney, R. T. J. McAteer, J. M. Refojo, and P. T. Gallagher (2010, October). Propagation of an Earth-directed coronal mass ejection in three dimensions. *ArXiv e-prints*.

Cargill, P. J. (1994, February). Some implications of the nanoflare concept. *Astrophys. J.*, *422*, 381–393.

Cargill, P. J. and J. A. Klimchuk (1997, March). A Nanoflare Explanation for the Heating of Coronal Loops Observed by YOHKOH. *Astrophys. J.*, *478*, 799–+.

Cargill, P. J. and J. A. Klimchuk (2004, April). Nanoflare Heating of the Corona Revisited. *Astrophys. J.*, *605*, 911–920.

Carmichael, H. (1964). A Process for Flares. *NASA Special Publication 50*, 451–+.

## CHAPTER

- Chen, J. (2001). Physics of Coronal Mass Ejections: A New Paradigm of Solar Eruptions. *Space Sci. Rev.*, *95*, 165–190.
- Colaninno, R. C. and A. Vourlidas (2009, June). First Determination of the True Mass of Coronal Mass Ejections: A Novel Approach to Using the Two STEREO Viewpoints. *Astrophys. J.*, *698*, 852–858.
- Colgan, J., J. Abdallah, Jr., M. E. Sherrill, M. Foster, C. J. Fontes, and U. Feldman (2008, December). Radiative Losses of Solar Coronal Plasmas. *Astrophys. J.*, *689*, 585–592.
- Cook, J. W., C. Cheng, V. L. Jacobs, and S. K. Antiochos (1989, March). Effect of coronal elemental abundances on the radiative loss function. *Astrophys. J.*, *338*, 1176–1183.
- Cremades, H. and V. Bothmer (2004, July). On the three-dimensional configuration of coronal mass ejections. *Astron. Astrophys.*, *422*, 307–322.
- Davies, J. A., R. A. Harrison, A. P. Rouillard, N. R. Sheeley, C. H. Perry, D. Bewsher, C. J. Davis, C. J. Eyles, S. R. Crothers, and D. S. Brown (2009). A synoptic view of solar transient evolution in the inner heliosphere using the Heliospheric Imagers on STEREO. *Geophys. Res. Lett.*, *36*, 2102–+.
- Davis, C. J., J. A. Davies, M. Lockwood, A. P. Rouillard, C. J. Eyles, and R. A. Harrison (2009). Stereoscopic imaging of an Earth-impacting solar coronal mass ejection: A major milestone for the STEREO mission. *Geophys. Res. Lett.*, *36*, 8102–+.
- Davis, C. J., J. Kennedy, and J. A. Davies (2010). Assessing the Accuracy of CME Speed and Trajectory Estimates from STEREO Observations Through a Comparison of Independent Methods. *Solar Phys.*, *61*–+.

## CHAPTER

- Del Zanna, G. (2008, April). Flows in active region loops observed by Hinode EIS. *Astron. Astrophys.*, *481*, L49–L52.
- Delaboudinière, J., G. E. Artzner, J. Brunaud, A. H. Gabriel, J. F. Hochedez, F. Millier, X. Y. Song, B. Au, K. P. Dere, R. A. Howard, R. Kreplin, D. J. Michels, J. D. Moses, J. M. Defise, C. Jamar, P. Rochus, J. P. Chauvineau, J. P. Marioge, R. C. Catura, J. R. Lemen, L. Shing, R. A. Stern, J. B. Gurman, W. M. Neupert, A. Maucherat, F. Clette, P. Cugnon, and E. L. van Dessel (1995, December). EIT: Extreme-Ultraviolet Imaging Telescope for the SOHO Mission. *Solar Phys.*, *162*, 291–312.
- Dere, K. P., E. Landi, H. E. Mason, B. C. Monsignori Fossi, and P. R. Young (1997). CHIANTI - an atomic database for emission lines. *Astron. Astrophys. Suppl.*, *125*, 149–173.
- Driesman, A., S. Hynes, and G. Cancro (2008, April). The STEREO Observatory. *Space Sci. Rev.*, *136*, 17–44.
- Elmore, D. F., J. T. Burkepile, J. A. Darnell, A. R. Lecinski, and A. L. Stanger (2003). Calibration of a ground-based solar coronal polarimeter. In S. Fineschi (Ed.), *Society of Photo-Optical Instrumentation Engineers (SPIE) Conference Series*, Volume 4843 of *Society of Photo-Optical Instrumentation Engineers (SPIE) Conference Series*, pp. 66–75.
- Eyles, C. J., G. M. Simnett, M. P. Cooke, B. V. Jackson, A. Buffington, P. P. Hick, N. R. Waltham, J. M. King, P. A. Anderson, and P. E. Holladay (2003). The Solar Mass Ejection Imager (Smei). *Solar Phys.*, *217*, 319–347.
- Forbes, T. G. and P. A. Isenberg (1991). A catastrophe mechanism for coronal mass ejections. *Astrophys. J.*, *373*, 294–307.

## CHAPTER

- Freeland, S. L. and B. N. Handy (1998). Data Analysis with the SolarSoft System. *Solar Phys.*, 182, 497–500.
- Gibson, E. G. (1973). *The quiet sun*.
- Gopalswamy, N., M. Shimojo, W. Lu, S. Yashiro, K. Shibasaki, and R. A. Howard (2003, March). Prominence Eruptions and Coronal Mass Ejection: A Statistical Study Using Microwave Observations. *Astrophys. J.*, 586, 562–578.
- Guo, W. P. and S. T. Wu (1998). A Magnetohydrodynamic Description of Coronal Helmet Streamers Containing a Cavity. *Astrophys. J.*, 494, 419–+.
- Hara, H., T. Watanabe, L. K. Harra, J. L. Culhane, P. R. Young, J. T. Mariska, and G. A. Doschek (2008, May). Coronal Plasma Motions near Footpoints of Active Region Loops Revealed from Spectroscopic Observations with Hinode EIS. *Astrophys. J.*, 678, L67–L71.
- Harrison, R. A. (1986). Solar coronal mass ejections and flares. *Astron. Astrophys.*, 162, 283–291.
- Hildner, E. (1974, March). The Formation of Solar Quiescent Prominences by Condensation. *Solar Phys.*, 35, 123–136.
- Hirayama, T. (1974, February). Theoretical Model of Flares and Prominences. I: Evaporating Flare Model. *Solar Phys.*, 34, 323–338.
- Hood, A. and U. Anzer (1988, March). Thermal condensations in coronal magnetic fields. *Solar Phys.*, 115, 61–80.
- Hood, A. W. and E. R. Priest (1979, August). The equilibrium of solar coronal magnetic loops. *Astron. Astrophys.*, 77, 233–251.
- Howard, R. A., J. D. Moses, A. Vourlidas, J. S. Newmark, D. G. Socker, S. P. Plunkett, C. M. Korendyke, J. W. Cook, A. Hurley, J. M. Davila, W. T. Thompson,

## CHAPTER

- O. C. St Cyr, E. Mentzell, K. Mehalick, J. R. Lemen, J. P. Wuelser, D. W. Duncan, T. D. Tarbell, C. J. Wolfson, A. Moore, R. A. Harrison, N. R. Waltham, J. Lang, C. J. Davis, C. J. Eyles, H. Mapson-Menard, G. M. Simnett, J. P. Hain, J. M. Defise, E. Mazy, P. Rochus, R. Mercier, M. F. Ravet, F. Delmotte, F. Auchere, J. P. Delaboudiniere, V. Bothmer, W. Deutsch, D. Wang, N. Rich, S. Cooper, V. Stephens, G. Maahs, R. Baugh, D. McMullin, and T. Carter (2008). Sun Earth Connection Coronal and Heliospheric Investigation (SECCHI). *Space Science Reviews* 136, 67–115.
- Hudson, H. S. (1991, June). Solar flares, microflares, nanoflares, and coronal heating. *Solar Phys.*, 133, 357–369.
- Hundhausen, A. (1999). Coronal Mass Ejections. In K. T. Strong, J. L. R. Saba, B. M. Haisch, & J. T. Schmelz (Ed.), *The many faces of the sun: a summary of the results from NASA's Solar Maximum Mission.*, pp. 143–+.
- Inhester, B. (2006, December). Stereoscopy basics for the STEREO mission. *ArXiv Astrophysics e-prints*.
- Kivelson, M. G. and C. T. Russell (1995, April). *Introduction to Space Physics*.
- Klimchuk, J. A. (1990). Shear-induced inflation of coronal magnetic fields. *Astrophys. J.*, 354, 745–754.
- Klimchuk, J. A. (2001). Theory of Coronal Mass Ejections. *Space Weather (Geophysical Monograph 125)*, ed. P. Song, H. Singer, G. Siscoe (Washington: Am. Geophys. Un.), 143 (2001) 125, 143–+.
- Klimchuk, J. A. and P. J. Cargill (2001, May). Spectroscopic Diagnostics of Nanoflare-heated Loops. *Astrophys. J.*, 553, 440–448.
- Kopp, R. A. and G. W. Pneuman (1976, October). Magnetic reconnection in the corona and the loop prominence phenomenon. *Solar Phys.*, 50, 85–98.

## CHAPTER

- Kosugi, T., K. Matsuzaki, T. Sakao, T. Shimizu, Y. Sone, S. Tachikawa, T. Hashimoto, K. Minesugi, A. Ohnishi, T. Yamada, S. Tsuneta, H. Hara, K. Ichimoto, Y. Suematsu, M. Shimojo, T. Watanabe, S. Shimada, J. M. Davis, L. D. Hill, J. K. Owens, A. M. Title, J. L. Culhane, L. K. Harra, G. A. Doschek, and L. Golub (2007, June). The Hinode (Solar-B) Mission: An Overview. *Solar Phys.*, *243*, 3–17.
- Krall, J., J. Chen, and R. Santoro (2000). Drive Mechanisms of Erupting Solar Magnetic Flux Ropes. *Astrophys. J.*, *539*, 964–982.
- Landi, E. and M. Landini (1999, July). Radiative losses of optically thin coronal plasmas. *Astron. Astrophys.*, *347*, 401–408.
- Liewer, P. C., E. M. de Jong, J. R. Hall, R. A. Howard, W. T. Thompson, J. L. Culhane, L. Bone, and L. van Driel-Gesztelyi (2009). Stereoscopic Analysis of the 19 May 2007 Erupting Filament. *Solar Phys.*, *256*, 57–72.
- Liu, Y., A. Thernisien, J. G. Luhmann, A. Vourlidas, J. A. Davies, R. P. Lin, and S. D. Bale (2010, October). Reconstructing Coronal Mass Ejections with Coordinated Imaging and in Situ Observations: Global Structure, Kinematics, and Implications for Space Weather Forecasting. *Astrophys. J.*, *722*, 1762–1777.
- Low, B. C. (1996). Solar Activity and the Corona. *Solar Phys.*, *167*, 217–265.
- Lyot, B. (1939). The study of the solar corona and prominences without eclipses (George Darwin Lecture, 1939). *Mon. Not. Roy. Astron. Soc.*, *99*, 580–+.
- Maloney, S. A., P. T. Gallagher, and R. T. J. McAteer (2009). Reconstructing the 3-D Trajectories of CMEs in the Inner Heliosphere. *Solar Phys.*, *256*, 149–166.
- Mendoza-Briceno, C. A. and A. W. Hood (1997, September). The effect of spatially dependent heating on the thermal equilibria of coronal loops. *Astron. Astrophys.*, *325*, 791–802.

## CHAPTER

- Michalek, G., N. Gopalswamy, and S. Yashiro (2009, December). Expansion Speed of Coronal Mass Ejections. *Solar Phys.*, *260*, 401–406.
- Mierla, M., B. Inhester, A. Antunes, Y. Boursier, J. P. Byrne, R. Colaninno, J. Davila, C. A. de Koning, P. T. Gallagher, S. Gissot, R. A. Howard, T. A. Howard, M. Kramar, P. Lamy, P. C. Liewer, S. Maloney, C. Marqué, R. T. J. McAteer, T. Moran, L. Rodriguez, N. Srivastava, O. C. St. Cyr, G. Stenborg, M. Temmer, A. Thernisien, A. Vourlidas, M. J. West, B. E. Wood, and A. N. Zhukov (2010, January). On the 3-D reconstruction of Coronal Mass Ejections using coronagraph data. *Annales Geophysicae* *28*, 203–215.
- Moon, Y., K. S. Cho, Z. Smith, C. D. Fry, M. Dryer, and Y. D. Park (2004, November). Flare-Associated Coronal Mass Ejections with Large Accelerations. *Astrophys. J.*, *615*, 1011–1020.
- Ogawara, Y. (1987). The Solar-A mission. *Solar Phys.*, *113*, 361–370.
- Parker, E. N. (1958, November). Dynamics of the Interplanetary Gas and Magnetic Fields. *Astrophys. J.*, *128*, 664–+.
- Parker, E. N. (1988, July). Nanoflares and the solar X-ray corona. *Astrophys. J.*, *330*, 474–479.
- Parnell, C. E. and P. E. Jupp (2000, January). Statistical Analysis of the Energy Distribution of Nanoflares in the Quiet Sun. *Astrophys. J.*, *529*, 554–569.
- Patsourakos, S. and J. A. Klimchuk (2005, August). Coronal Loop Heating by Nanoflares: The Impact of the Field-aligned Distribution of the Heating on Loop Observations. *Astrophys. J.*, *628*, 1023–1030.
- Pauluhn, A. and S. K. Solanki (2007, January). A nanoflare model of quiet Sun EUV emission. *Astron. Astrophys.*, *462*, 311–322.

## CHAPTER

- Pitz, E., C. Leinert, H. Link, and N. Salm (1976). HELIOS zodiacal light experiment. In H. Elsaesser & H. Fechtig (Ed.), *Interplanetary Dust and Zodiacal Light*, Volume 48 of *Lecture Notes in Physics*, Berlin Springer Verlag, pp. 19–23.
- Priest, E. R. (1982). *Solar magneto-hydrodynamics*.
- Reale, F. (2010, November). Coronal Loops: Observations and Modeling of Confined Plasma. *Living Reviews in Solar Physics* 7, 5–+.
- Rosner, R., W. H. Tucker, and G. S. Vaiana (1978, March). Dynamics of the quiescent solar corona. *Astrophys. J.*, 220, 643–645.
- Rouillard, A. P., J. A. Davies, R. J. Forsyth, A. Rees, C. J. Davis, R. A. Harrison, M. Lockwood, D. Bewsher, S. R. Crothers, C. J. Eyles, M. Hapgood, and C. H. Perry (2008). First imaging of corotating interaction regions using the STEREO spacecraft. *Geophys. Res. Lett.*, 35, 10110–+.
- Rouillard, A. P., J. A. Davies, B. Lavraud, R. J. Forsyth, N. P. Savani, D. Bewsher, D. S. Brown, N. R. Sheeley, C. J. Davis, R. A. Harrison, R. A. Howard, A. Vourlidas, M. Lockwood, S. R. Crothers, and C. J. Eyles (2010). Intermittent release of transients in the slow solar wind: 1. Remote sensing observations. *Journal of Geophysical Research (Space Physics)* 115, 4103–+.
- Rouillard, A. P., B. Lavraud, J. A. Davies, N. P. Savani, L. F. Burlaga, R. J. Forsyth, J. Sauvaud, A. Opitz, M. Lockwood, J. G. Luhmann, K. D. C. Simunac, A. B. Galvin, C. J. Davis, and R. A. Harrison (2010). Intermittent release of transients in the slow solar wind: 2. In situ evidence. *Journal of Geophysical Research (Space Physics)* 115, 4104–+.
- Rouillard, A. P., N. P. Savani, J. A. Davies, B. Lavraud, R. J. Forsyth, S. K. Morley, A. Opitz, N. R. Sheeley, L. F. Burlaga, J. Sauvaud, K. D. C. Simunac, J. G. Luhmann, A. B. Galvin, S. R. Crothers, C. J. Davis, R. A. Harrison, M. Lockwood,

## CHAPTER

- C. J. Eyles, D. Bewsher, and D. S. Brown (2009). A Multispacecraft Analysis of a Small-Scale Transient Entrained by Solar Wind Streams. *Solar Phys.*, 256, 307–326.
- Saito, K., A. I. Poland, and R. H. Munro (1977). A study of the background corona near solar minimum. *Solar Phys.*, 55, 121–134.
- Sarkar, A. and R. W. Walsh (2008, August). Hydrodynamic Simulation of a Nanoflare-heated Multistrand Solar Atmospheric Loop. *Astrophys. J.*, 683, 516–526.
- Sarkar, A. and R. W. Walsh (2009, July). Extreme-Ultraviolet Observational Consequences of the Spatial Localization of Nanoflare Heating within a Multistranded Atmospheric Loop. *Astrophys. J.*, 699, 1480–1486.
- Scherrer, P. H., R. S. Bogart, R. I. Bush, J. T. Hoeksema, A. G. Kosovichev, J. Schou, W. Rosenberg, L. Springer, T. D. Tarbell, A. Title, C. J. Wolfson, I. Zayer, and MDI Engineering Team (1995, December). The Solar Oscillations Investigation - Michelson Doppler Imager. *Solar Phys.*, 162, 129–188.
- Sheeley, N. R., J. H. Walters, Y. Wang, and R. A. Howard (1999). Continuous tracking of coronal outflows: Two kinds of coronal mass ejections. *J. Geophys. Res.*, 104, 24739–24768.
- Sockett, D. G., R. A. Howard, C. M. Korendyke, G. M. Simnett, and D. F. Webb (2000). NASA Solar Terrestrial Relations Observatory (STEREO) mission heliospheric imager. In S. Fineschi, C. M. Korendyke, O. H. Siegmund, & B. E. Woodgate (Ed.), *Society of Photo-Optical Instrumentation Engineers (SPIE) Conference Series*, Volume 4139 of *Society of Photo-Optical Instrumentation Engineers (SPIE) Conference Series*, pp. 284–293.
- Spitzer, L. (1962). *Physics of Fully Ionized Gases*.

## CHAPTER

- Steele, C. D. C. and E. R. Priest (1990, May). Thermal equilibria of coronal magnetic arcades. *Solar Phys.*, *127*, 65–94.
- Steele, C. D. C. and E. R. Priest (1991, April). Thermal equilibria of coronal magnetic loops with non-constant cross-sectional area. *Solar Phys.*, *132*, 293–306.
- Steele, C. D. C. and E. R. Priest (1994, December). Thermal equilibria in solar coronal magnetic loops: Gravitational considerations. *Astron. Astrophys.*, *292*, 291–303.
- Strong, K., M. Bruner, T. Tarbell, A. Title, and C. J. Wolfson (1994, October). Trace - The transition region and coronal explorer. *Space Sci. Rev.*, *70*, 119–122.
- Sturrock, P. A. (1966, August). Model of the High-Energy Phase of Solar Flares. *Nature*, *211*, 695–697.
- Tappin, S. J., A. Buffington, M. P. Cooke, C. J. Eyles, P. P. Hick, P. E. Holladay, B. V. Jackson, J. C. Johnston, T. Kuchar, D. Mizuno, J. B. Mozer, S. Price, R. R. Radick, G. M. Simnett, D. Sinclair, N. R. Waltham, and D. F. Webb (2004). Tracking a major interplanetary disturbance with SMEI. *Geophys. Res. Lett.*, *31*, 2802–+.
- Temmer, M., S. Preiss, and A. M. Veronig (2009, May). CME Projection Effects Studied with STEREO/COR and SOHO/LASCO. *Solar Phys.*, *256*, 183–199.
- Thernisien, A., A. Vourlidas, and R. A. Howard (2009). Forward Modeling of Coronal Mass Ejections Using STEREO/SECCHI Data. *Solar Phys.*, *256*, 111–130.
- Thompson, W. T. (2006). Coordinate systems for solar image data. *Astron. Astrophys.*, *449*, 791–803.
- Thompson, W. T. and N. L. Reginald (2008). The Radiometric and Pointing Calibration of SECCHI COR1 on STEREO. *Solar Phys.*, *250*, 443–454.

## CHAPTER

- Thompson, W. T. and K. Wei (2010, January). Use of the FITS World Coordinate System by STEREO/SECCHI. *Solar Phys.*, *261*, 215–222.
- Tripathi, D., H. E. Mason, B. N. Dwivedi, G. del Zanna, and P. R. Young (2009, April). Active Region Loops: Hinode/Extreme-Ultraviolet Imaging Spectrometer Observations. *Astrophys. J.*, *694*, 1256–1265.
- Vršnak, B., D. Sudar, and D. Ruždjak (2005, June). The CME-flare relationship: Are there really two types of CMEs? *Astron. Astrophys.*, *435*, 1149–1157.
- Walsh, R. W., G. E. Bell, and A. W. Hood (1995, October). Time-Dependent Heating of the Solar Corona. *Solar Phys.*, *161*, 83–102.
- Walsh, R. W., G. E. Bell, and A. W. Hood (1996, November). Validity of the Isobaric Assumption to the Solar Corona. *Solar Phys.*, *169*, 33–45.
- Wang, Y., C. Shen, S. Wang, and P. Ye (2004). Deflection of coronal mass ejection in the interplanetary medium. *Solar Phys.*, *222*, 329–343.
- Williams, A. O., J. A. Davies, S. E. Milan, A. P. Rouillard, C. J. Davis, C. H. Perry, and R. A. Harrison (2009). Deriving solar transient characteristics from single spacecraft stereo/hi elongation variations: a theoretical assessment of the technique. *Annales Geophysicae* *27*(12), 4359–4368.
- Wolfson, R. and S. Saran (1998). Energetics of Coronal Mass Ejections: Role of the Streamer Cavity. *Astrophys. J.*, *499*, 496–+.
- Wuelser, J., J. R. Lemen, T. D. Tarbell, C. J. Wolfson, J. C. Cannon, B. A. Carpenter, D. W. Duncan, G. S. Gradwohl, S. B. Meyer, A. S. Moore, R. L. Navarro, J. D. Pearson, G. R. Rossi, L. A. Springer, R. A. Howard, J. D. Moses, J. S. Newmark, J. Delaboudiniere, G. E. Artzner, F. Auchere, M. Bougnet, P. Bouyries, F. Bridou, J. Clotaire, G. Colas, F. Delmotte, A. Jerome, M. Lamare, R. Mercier,

## CHAPTER

- M. Mullet, M. Ravet, X. Song, V. Bothmer, and W. Deutsch (2004). EUVI: the STEREO-SECCHI extreme ultraviolet imager. In S. Fineschi & M. A. Gummin (Ed.), *Society of Photo-Optical Instrumentation Engineers (SPIE) Conference Series*, Volume 5171 of *Society of Photo-Optical Instrumentation Engineers (SPIE) Conference Series*, pp. 111–122.
- Young, P. R., G. Del Zanna, E. Landi, K. P. Dere, H. E. Mason, and M. Landini (2003). CHIANTI-An Atomic Database for Emission Lines. VI. Proton Rates and Other Improvements. *Astrophys. J.*, *144*, 135–152.
- Zhang, J., K. P. Dere, R. A. Howard, M. R. Kundu, and S. M. White (2001, September). On the Temporal Relationship between Coronal Mass Ejections and Flares. *Astrophys. J.*, *559*, 452–462.
- Zhang, J., K. P. Dere, R. A. Howard, and A. Vourlidas (2004, March). A Study of the Kinematic Evolution of Coronal Mass Ejections. *Astrophys. J.*, *604*, 420–432.
- Zhang, M. and B. C. Low (2004). Magnetic Energy Storage in the Two Hydromagnetic Types of Solar Prominences. *Astrophys. J.*, *600*, 1043–1051.